

SIMULATIONS FOR UPCOMING AND PROPOSED EXOPLANET SURVEYS  
AS PATHFINDERS FOR DIRECT IMAGING MISSIONS

by

Patrick D Newman

A Dissertation

Submitted to the

Graduate Faculty

of

George Mason University

In Partial fulfillment of

The Requirements for the Degree

of

Doctor of Philosophy

Astronomy

Committee:

\_\_\_\_\_  
Dr. Peter Plavchan, Dissertation Director

\_\_\_\_\_  
Dr. Peter Becker, Committee Member

\_\_\_\_\_  
Dr. Joseph Weingartner, Committee Member

\_\_\_\_\_  
Dr. Jennifer Burt, Committee Member

\_\_\_\_\_  
Dr. Ernest Barreto, Department Chair

\_\_\_\_\_  
Dr. Gerald L. R. Weatherspoon, Associate  
Dean for Undergraduate and Graduate  
Affairs, College of Science

\_\_\_\_\_  
Dr. Cody W. Edwards, Dean,  
College of Science

Date: \_\_\_\_\_ Fall Semester 2025  
George Mason University  
Fairfax, VA

Simulations for Upcoming and Proposed Exoplanet Surveys as Pathfinders for Direct Imaging Missions

A dissertation submitted in partial fulfillment of the requirements for the degree of Doctor of Philosophy at George Mason University

By

Patrick D Newman  
Bachelor of Science  
University of Missouri, Kansas City, 2015

Director: Dr. Peter Plavchan, Professor  
Department of Department of Physics and Astronomy

Fall Semester 2025  
George Mason University  
Fairfax, VA

Copyright © 2025 by Patrick D Newman  
All Rights Reserved

## **Dedication**

I dedicate this thesis to my parents Geof and Sheila for encouraging my interest in Astronomy.

## **Acknowledgments**

I would like to thank dissertation committee, including the chair and my advisor, Peter Plavchan. This work would not have been possible without the opportunities he gave me.

## Table of Contents

	Page
List of Tables . . . . .	viii
List of Figures . . . . .	x
Abstract . . . . .	0
1 Introduction to Exoplanets and RV Survey Simulations . . . . .	1
1.1 Background . . . . .	1
1.1.1 Exoplanets and Radial Velocities . . . . .	1
1.1.2 Photometric Systems . . . . .	4
1.2 Outline . . . . .	5
2 Simulations for Planning Next-Generation Exoplanet Radial Velocity Surveys (published paper) . . . . .	6
2.1 Introduction . . . . .	6
2.1.1 Planet Detection Figure of Merit . . . . .	8
2.2 Survey Simulation Description . . . . .	9
2.2.1 The Dispatch Scheduler . . . . .	10
2.2.2 RV Model . . . . .	14
2.2.3 Exposure Time Calculations . . . . .	15
2.2.4 Architectures: Telescopes and Spectrographs . . . . .	16
2.2.5 Target Star Lists . . . . .	21
2.2.6 Other Simulation Inputs . . . . .	26
2.2.7 Simulation Outputs . . . . .	28
2.3 Results: Architecture Exposure Times and Cadences . . . . .	31
2.3.1 Per-Architecture Comments . . . . .	32
2.3.2 Example Architecture Results . . . . .	34
2.4 Results: Architecture Comparison . . . . .	38
2.4.1 P-mode Oscillation timescale . . . . .	45
2.5 Discussion . . . . .	46
2.5.1 Survey simulation assumptions and their effects . . . . .	48
2.6 Conclusions . . . . .	50

2.7	Appendix: Architecture Results . . . . .	52
3	Joint Radial Velocity and Direct Imaging Planet Yield Calculations. II: Radial Velocity Scheduling and Cadence (draft) . . . . .	71
3.1	Introduction . . . . .	71
3.1.1	History . . . . .	71
3.1.2	Motivation . . . . .	72
3.2	Simulation Inputs . . . . .	74
3.2.1	Target Catalogs . . . . .	74
3.2.2	Telescope and Instrument Parameters . . . . .	75
3.3	Radial Velocities . . . . .	76
3.3.1	Stellar Properties . . . . .	76
3.3.2	Exposure Time/Precision . . . . .	81
3.3.3	Exposure Time Estimation . . . . .	82
3.3.4	Atmospheric Effects . . . . .	83
3.3.5	Stellar Activity . . . . .	84
3.4	Dispatch Scheduler (Survey Simulations) . . . . .	85
3.4.1	Target Weighting . . . . .	88
3.5	Results (Overview) . . . . .	89
3.5.1	Figure of merit: planet semi-amplitude sensitivity and detection SNR	89
3.5.2	Example Timeseries . . . . .	90
3.6	Results (HWO target list) . . . . .	91
3.6.1	Exposure Times and Observations . . . . .	91
3.6.2	Exposure Times and Stellar Parameters . . . . .	93
3.6.3	Right Ascension and Declination . . . . .	94
3.6.4	Telluric Corrections . . . . .	95
3.7	Results (HabEx target list) . . . . .	96
3.8	Results (EPRV target list) . . . . .	102
3.9	Discussion . . . . .	107
3.9.1	Exposure Time Considerations . . . . .	107
3.9.2	Comparisons to Other Exposure Time Calculators . . . . .	107
3.9.3	Dispatch Scheduler considerations . . . . .	111
3.9.4	Target Weighting . . . . .	112
3.9.5	Do the different P-mode calculation methods affect yields? . . . . .	115
3.9.6	Target List Comparison/Target Star Selection . . . . .	121

3.9.7	Other/Uncompensated Noise . . . . .	124
3.10	Conclusions . . . . .	124
4	Orbital Photometric Light-source Simulations . . . . .	127
4.1	Motivation . . . . .	127
4.2	Project History/My Part . . . . .	127
4.3	Simulation Parameters . . . . .	128
4.4	Procedure/Equations . . . . .	129
4.4.1	Blackbody . . . . .	129
4.4.2	LED . . . . .	129
4.4.3	Filters . . . . .	129
4.4.4	F-lambda, Janskys, and Magnitudes . . . . .	132
4.5	Example Graphs . . . . .	132
4.6	Light Source Selection . . . . .	133
4.7	Conclusions . . . . .	140
5	Overall Conclusions . . . . .	141
5.1	EPRV Survey Simulations Conclusions . . . . .	141
5.1.1	Paper 1 . . . . .	141
5.1.2	Paper 2 . . . . .	142
5.2	Orbiting Photometric Light-Source Conclusions . . . . .	143
	Bibliography . . . . .	144

## List of Tables

Table	Page
1.1 Table of semi-amplitudes for example planets in relatively circular orbits. The solar system cases are assumed to be at 0 degrees inclination. . . . .	3
2.1 The seven architectures' facility and instrumental properties. Architectures not listed (III, IV, VII) were dropped from direct consideration in earlier simulations. Architectures with a/b variants have different sizes/numbers of telescopes, but identical instruments for each variant. . . . .	17
2.2 Peak system throughputs for current EPRV spectrographs. These are higher than the averages used in the various simulated architectures, as they largely do not account for performance variations from varying seeing conditions and as a function of wavelength. . . . .	18
2.3 Stars in the “green prime” list. Name (HIP number), spectral type, which hemispheres they were observed in, the properties used in the simulations, and their sources are included. Mass and radius for all stars are estimated from other properties. . . . .	24
2.4 Notional detector properties derived from NEID’s CCDs as a representative example. These values were used for all architecture simulation spectrograph assumptions, both the defined and baseline instruments. . . . .	27
3.1 Peak system throughputs for current EPRV spectrographs. These are higher than the averages used in the various architectures, as they largely do not account for performance variations from varying seeing and wavelength.	76
3.2 The HabEx stars and their properties used in these simulations. . . . .	78
3.3 The HWO stars and their properties used in these simulations. (1/2) . . .	79
3.4 The HWO stars and their properties used in these simulations. (2/2) . . .	80
3.5 The primary telescope and spectrograph combinations considered. While specific telescopes are listed, these are nominal ones chosen as representative 4/8/12 m class observatories. The collecting area of the 2x8.4 m is simulated as a single 11.78 m telescope. . . . .	81

4.1	A listing of all filters used in the various simulations. For ease of reading, all wavelengths have been converted into Angstroms. Aside from WFI, these are all for ground-based telescopes. . . . .	130
4.2	A listing of all filters used in the various simulations. For ease of reading, all wavelengths have been converted into Angstroms. The JWST filters are most-all NIRCam, while the “NGRST” ones are mostly a repeat of the WFI instrument (though with one filter from GRS and one from PRS added). . .	131

## List of Figures

Figure	Page
1.1 <b>Left:</b> Cumulative detections of exoplanets from 1992 to 2024, with the different methods shown. <b>Right:</b> A graph of period vs mass for known exoplanets, with the different detection methods shown. . . . .	2
2.1 Outline of the simulation pipeline, including the exposure time calculator (ETC) and dispatch scheduler. . . . .	11
2.2 Site locations . . . . .	12
2.3 Nightly weather probabilities for each site included in our simulations. . . . .	13
2.4 The locations on the sky of all green and yellow list stars. Open circles represent green list targets, color coded by effective temperature, while the yellow list stars are depicted by the grey points. While the thin disk of nearby stars is effectively isotropic on the sky, the green prime list of 101 nearby bright stars shows some minor clustering on the sky which can impact RV survey efficiency. . . . .	23
2.5 Representative illustration of number and diameter of telescope in the architectures. . . . .	27
2.6 Observations of HIP 73184 (HD 131977) in the the architecture I simulation at Siding Spring Observatory. Local sunrise/set, star rise/set, and observation times for each day are shown. . . . .	28
2.7 Simulated RV time-series for HIP 73184 (HD 131977) for Architecture I as observed by the three telescopes in its hemisphere (one each at Las Campanas, Sutherland, and Siding Spring). This star was chosen, as it has the median number of observations (2724) for the architecture. Note, only “white” noise is included in this simulation, despite the apparent correlated noise by eye during some seasons. The appearance of correlated noise could be partially due to the variable single measurement uncertainties from airmass extinction for a fixed exposure time over the course of a season. . . . .	29

2.8	Simulated observation cadence and nightly availability for HIP 73184 (HD 131977) for Architecture I observed by three telescopes (one each at Las Campanas, Sutherland, and Siding Spring). Observations here are binned into 30.4375 day “months”; actual observations were never more than 1/night.	30
2.9	Histograms of how often a given star was observed. Individual sites are shown (top), as well as groupings of different sites (bottom), with the 6 telescope grouping being the full architecture. . . . .	35
2.10	Top: Histograms of exposure times per star calculated individually at each site. Bottom: how “efficiently” each star was observed. That is, for what fraction of nights where a star could be observed from at least one site it was observed at least once. . . . .	36
2.11	Histograms of our sensitivity calculations from the observations. Top: smallest semi-amplitude $K$ for which a planet with a period much shorter than our 10 year survey could be found at an SNR-detect of 10. Bottom: The SNR-detect at which a planet with a period much shorter than our 10 year survey could be detected at if it had a semi-amplitude of 10 cm/s. In both cases, these values are calculated from equation 2.1. . . . .	37

2.12 Top Left, Top Right, Bottom left: Comparison of the distribution of the number of observations between each architecture presented in §2.2.4 for the three spectrograph assumptions respectively: the architecture-defined spectrograph with a RV precision photon noise requirement and no minimum SNR-phot per spectral resolution element requirement (Top Left), the architecture-defined spectrograph with both a RV precision photon noise requirement and a minimum SNR-phot per spectral resolution element requirement (Top Right), and the baseline instrument spectrograph with only a RV precision photon noise requirement and no minimum SNR-phot per spectral resolution element requirement (Bottom Right). The boxes show the 25th/75th percentile, with the median marked in orange. The whiskers extend from the 5th to the 95th percentile, and the circles the stars below the 5th or above the 95th percentile. For all architectures, the number of observations is summed across all telescopes for the specified architecture. Bottom Right: Comparison of the median number of observations between each architecture presented in §2.2.4 for the three spectrograph and survey requirements combination assumptions considered: the architecture-defined spectrograph with both a RV precision photon noise requirement and a minimum SNR-phot per spectral resolution element requirement (red line), the architecture-defined spectrograph with only a RV precision photon noise requirement and no minimum SNR-phot per spectral resolution element requirement (blue line), and a baseline instrument spectrograph with only a RV precision photon noise requirement and no minimum SNR-phot per spectral resolution element requirement (black line). The number of observations from an effective cadence of once per night per architecture (3653 epochs) is shown as a dashed horizontal line. . . . .



2.16	Comparison across architecture simulations and P-mode oscillation assumptions for median number of observations (top), and minimum reflex velocity semi-amplitude sensitivity (bottom). The 5 minute (left) and 10 minute (right) graphs use the same vertical scale for ease of comparison. . . . .	46
2.17	Same as figure 2.9, but for architecture IIa. . . . .	53
2.18	Same as figure 2.10, but for architecture IIa. . . . .	54
2.19	Same as figure 2.11, but for architecture IIa. . . . .	55
2.20	Same as figure 2.9, but for architecture IIb. . . . .	56
2.21	Same as figure 2.10, but for architecture IIb. . . . .	57
2.22	Same as figure 2.11, but for architecture IIb. . . . .	58
2.23	Same as figure 2.9, but for architecture V. . . . .	59
2.24	Same as figure 2.10, but for architecture V. . . . .	60
2.25	Same as figure 2.11, but for architecture V. . . . .	61
2.26	Same as figure 2.9, but for architecture VI. . . . .	62
2.27	Same as figure 2.10, but for architecture VI. . . . .	63
2.28	Same as figure 2.11, but for architecture VI. . . . .	64
2.29	Same as figure 2.9, but for architecture VIIIa. . . . .	65
2.30	Same as figure 2.10, but for architecture VIIIa. . . . .	66
2.31	Same as figure 2.11, but for architecture VIIIa. This includes using equation 2.2 for finding the sensitivity due to the varying precision of the measurements. . . . .	67
2.32	Same as figure 2.9, but for architecture VIIIb. . . . .	68
2.33	Same as figure 2.10, but for architecture VIIIb. . . . .	69
2.34	Same as figure 2.11, but for architecture VIIIb. This includes using equation 2.2 for finding the sensitivity due to the varying precision of the measurements. . . . .	70
3.1	Monthly WIYN observing and weather statistics from 1999 to 2006. Adapted from <a href="http://www-kpno.kpno.noao.edu/Images/wiynWeather_stats.jpeg">http://www-kpno.kpno.noao.edu/Images/wiynWeather_stats.jpeg</a>	87
3.2	Example survey results from a 5 years/100% time with Super NEID (3 cm/s) on the WIYN. The top graph shows target rise and set times, sunrise and sunset times, and target observations over the course of the survey. The bottom graph shows potential aliasing/false planet signals from the distribution of observations over various orbital periods. Patterns in observations as a result of long exposure times and changing weighting are visible, as well sensitivity limitations for some planets. . . . .	91

3.3	Exposure times as histograms (left) and cumulative distribution functions (right) for every star in our telescope/instrument combinations. There is a tail of stars with very long exposure times (and which are therefore difficult to observe at high precision). The PDF appears the same for all 3 sets of stars due to the current bin size of 20 minutes, as whatever chosen p-mode correction has little effect beyond that. Due to finer bin sizes, the CDFs do show that the exact distribution of exposure times is shuffled around somewhat, though the effect is again small (and largely confined to telescope/instrument/precision combinations that skew to shorter exposure times). . . . .	92
3.4	Histograms of total number of observations for the different telescope/instrument combinations as both PDFs (left) and CDFs (right). Differences between different architectures are quite obvious, though the ones between different p-mode compensation methods are subtle (and not apparent for the architectures with longer exposure times and fewer observations). . . . .	92
3.5	Total number of observations (left) and total time spent observing (right) for each star and telescope/instrument combination as a function of exposure time. . . . .	93
3.6	Exposure times as a function of effective temperature (left), and rotational velocity (right), for the gravity/effective temperature P-mode compensation. While we see clear trends of hotter/faster rotating stars being harder to observe, the choice of telescope/instrument/precision usually has a larger effect. . . . .	93
3.7	Total number of observations per star as a function of Right Ascension (left) and Declination (right). There is a clear trend in right ascension, we believe from a combination of night length and weather (though it is suppressed for longer exposure time telescope/instrument/precision combinations). That the larger peak corresponds with stars that have the longest time above the horizon in late summer (around 300-330 degrees) and not winter/early spring (when the weather is better and nights longer) is surprising. Declination does not show a clear trend, with number of observations per star being relatively flat north of about -40 degrees. Below that, stars are never observed. . . .	94

3.8	CDFs of minimum detectable reflex velocity (K, in cm/s) of a planet at SNR = 10 over our telescope/instrument combinations at multiple scales. The results with no microtellurics are shown as solid lines, while the telluric noise are the dotted lines. . . . .	95
3.9	CDFs of minimum detectable reflex velocity (K, in cm/s) of a planet at SNR = 10 over our telescope/instrument combinations at multiple scales. The results with no microtellurics are shown as solid lines, while the telluric noise are the dotted lines. . . . .	96
3.10	Exposure times as histograms (left) and cumulative distribution functions (right) for every star in our telescope/instrument combinations. There is a tail of stars with very long exposure times (and which are therefore difficult to observe at high precision). The PDF appears the same for all 3 sets of stars due to the current bin size of 20 minutes, as whatever chosen p-mode correction has little effect beyond that. Due to finer bin sizes, the CDFs do show that the exact distribution of exposure times is shuffled around somewhat, though the effect is again small (and largely confined to telescope/instrument/precision combinations that skew to shorter exposure times). In all cases, there is a “tail” of stars that have relatively long exposure times, even for favorable telescope/instrument/precision combinations. For less favorable ones, this “tail” can mean that around half of all stars have exposure times of over two hours (and so are difficult to observe). . . . .	97
3.11	Histograms of total number of observations for the different telescope/instrument combinations as both PDFs (left) and CDFs (right). Differences between different architectures are quite obvious, though the ones between different p-mode compensation methods are subtle (and not apparent for the architectures with longer exposure times and fewer observations). Because of the details of the target list (both position and exposure times), between around 25 and 40% percent of the target stars are never observed. . . . .	97

3.12 Total number of observations (left) and total time spent observing (right) for each star and telescope/instrument combination as a function of exposure time. Number of observations decrease slowly with increasing exposure time (while time spent on a given star increases) until around 300 minutes, and which point both rapidly decrease as the stars become increasingly impractical to observe. . . . .	98
3.13 Exposure time as a function of effective temperature (left), and rotational velocity (right). This target list shows a clear trend of increasing observation difficulty for hotter stars, though choice of telescope, instrument, and target precision are more important for GKM stars. One star (Altair), is off the top-right corner of the vsini plot, due to its unphysically long exposure times at our desired precisions and having a rotational velocity of 211 km/s. . . . .	99
3.14 Total number of observations per star as a function of Right Ascension (top) and Declination (bottom). There is a clear trend in right ascension, we believe from a combination of night length and weather (though it is suppressed for longer exposure time telescope/instrument/precision combinations). That the peak corresponds with stars that have the longest time above the horizon in late summer (around 300-330 degrees) and not winter or early spring (when the weather is better and nights longer) is surprising. Declination does not show a clear trend, with number of observations per star being relatively flat north of about -40 degrees. Below that, stars are never observed. . . . .	100
3.15 How our detection heuristic changes from no microtellurics (solid lines) to nominal microtelluric noise (dotted lines). <b>Left:</b> CDFs for the minimum detectable reflex velocity ( $K$ , in cm/s) for a planet at $\text{SNR} = 10$ . <b>Right:</b> CDFs for the SNR for a detection of a $K = 10$ cm/s planet. . . . .	100
3.16 Histograms/PDFs (left) and CDFs (right) of the number of observations (top), SNR of a nominal 10 cm/s planet detection (middle), and minimum detectable reflex velocity $k$ of a nominal $\text{SNR} = 10$ planet detection (bottom).	103

3.17 Exposure time as a function of effective temperature (left), and rotational velocity (right). This target list shows a clear trend of increasing observation difficulty for hotter stars, though choice of telescope, instrument, and target precision are more important for GKM stars. There is no clear trend in exposure time for $v\sin i$ , possible due to all stars in this sample being slow rotators. . . . .	104
3.18 Total number of observations per star as a function of Right Ascension (left) and Declination (right). There is a clear trend in right ascension, we believe from a combination of night length and weather (though it is suppressed for longer exposure time telescope/instrument/precision combinations). That the peak corresponds with stars that have the longest time above the horizon in late summer (300-330 degrees) and not winter/early spring (when the weather is better and nights longer) is surprising. Declination does not show a clear trend, with number of observations per star being relatively flat north of about -40 degrees. Below that, stars are never observed. . . . .	105
3.19 How our detection heuristic changes from no microtellurics (solid lines) to nominal microtelluric noise (dotted lines). <b>Left:</b> CDFs for the minimum detectable reflex velocity ( $K$ , in cm/s) for a planet at $\text{SNR} = 10$ . <b>Right:</b> CDFs for the SNR for a detection of a $K = 10$ cm/s planet. . . . .	105
3.20 <b>Left:</b> Nominal exposure times at 3 RV precisions on NEID for synthetic stars that have an apparent V-magnitude of 4.83 as a function of effective temperature (so an unrealistic approximately constant luminosity, thus showing RV information content for a more or less constant number of photons as a function of temperature). The values are calculated with NEID's official ETC over their modeled range (2700 to 6300 K). Lower values are "better" (higher precision). <b>Right:</b> Equivalent synthetic stars stars (apparent magnitude 4.83, constant $v\sin i$ , metallicity, and $\log(g)$ , but with varying effective temperature) with exposure times calculated by our ETC. Both show similar trends, though the exact times are offset from each-other by about an order of magnitude. Given that none of these stars are especially real, such an offset is not concerning. . . . .	109

3.21 **Left:** Exposure times for the stars in our 3 target lists for a nominal single exposure at 40 cm/s, using the NEID ETC. Stars with exposure times longer than one hour are not shown. Depending on the target list, there can be a trend towards shorter exposures for hotter stars, but this is not always the case and it is relatively flat for stars hotter than around 4500-5000 K. If one wanted to choose a target list with a specific exposure time cutoff, they could do so while having stars across a broad temperature range. **Right:** The same target lists at the same scale are shown with our own exposure calculator. The higher “floor” in our times is from our p-mode compensation, and the upwards scatter at high temperatures is from increased  $vsini$ . . . . . 110

3.22 PDFs (left), and CDFs (right) of all stars in the HWO target list for different precisions and a large variety of observation weighting strategies. Here we look at 3 main strategies: a simplistic hour-angle weighting, a time since last observation weighting (do not observe the object again at all within the time limit, and then ramp up the weighting), and a combined hour-angle and time since last observation weighting. The last two are relatively similar (especially for shorter exposure times), but we find that the combined weighting is the “best”. . . . . 113

3.23 Plots of the distribution of results for different precisions and a variety of weighting strategies. We compare median (x-axis) with mean (y-axis) and standard deviation (error bars). Here we look at 3 main strategies: a simplistic hour-angle weighting, a time since last observation weighting (do not observe the object again at all within the time limit, and then ramp up the weighting), and a combined hour-angle and time since last observation weighting. The last two are relatively similar (especially for shorter exposure times), and unlike the broader distributions, it looks like pure time since last observation is the “best”. Notably, for 3 cm/s, we are unable to observe the majority of the stars, hence a median of 0. . . . . 114

3.24 All minimum p-mode times across all target lists as a function of effective temperature. Most are shorter than 5 minutes and the vast majority are shorter than 10. The remainder include stars that a direct observation mission may wish to pass over (eg: subgiants). . . . . 115

3.25 Comparison of the exposure time distributions for four kinds of p-mode oscillation compensation measures: fixed 5-minute versus fixed 10-minute versus two kinds of variable (mass-radius and effective temperature-surface gravity). The telescope/precision combinations that otherwise give the shortest exposures (11.8 m and 40 cm/s) and longest exposures (3.5 m and 3 cm/s) using NEID are used. In the CDF graphs (**top**), the p-values for a null result between the two variable exposure modes (the mass-radius and temperature-gravity using distributions are the same) are given in the figure keys. The **bottom** panels show 'percent difference' between the two variable p-mode timescale distributions. The two fixed timescale distributions are not considered, as they are different by inspection (though overlap in some ways with the other distributions). The K-S test does not show these two distributions as statistically different (the p-value for the 40 cm/s case is  $>0.05$ , and for the 3 cm/s case is around 1). . . . .

116

3.26 Comparison of the same 6 datasets in observation distribution. The left graph is the CDF of the distributions, while the middle is the percent difference for the two variable p-modes, and the right is the percent difference between all combinations for the short exposure time case. Notably unlike the exposure time distributions, these are in some cases distinguishable from each-other. . . . .

117

3.27 Comparison of the same 6 datasets in their distributions for our K/SNR detection heuristic (semi-amplitude sensitivity at an SNR of 10 is top, SNR for a fixed semi-amplitude of 10 cm/s is bottom). The left graphs are the CDF of the distributions, while the middle are the percent difference for the two variable p-modes, and the right is the percent difference between all combinations for the short exposure time case. Using a cutoff of  $p < 0.05$ , we find that the two variable p-mode calculations cannot be distinguished from each-other, nor the mass-radius method from a 5-minute cutoff. All others can be, as can usually be seen by offsets in their CDFs (which appear as peaks/troughs in the percent difference). . . . .

118

3.28 Comparison of the exposure time distributions for four kinds of p-mode oscillation compensation measures: fixed 5-minute versus fixed 10-minute versus two kinds of variable (mass-radius and effective temperature-surface gravity). The telescope/precision combinations that are “canonical” and give the shortest exposures (3.5 m and 27 cm/s) and longest exposures (3.5 m and 3 cm/s) using NEID are used. In the CDF graphs ( <b>top</b> ), the p-values for a null result between the two variable exposure modes (the mass-radius and temperature-gravity using distributions are the same) are given in the figure keys. The <b>bottom</b> panels show ‘percent difference’ between the two variable p-mode timescale distributions. The two fixed timescale distributions are not considered, as they are different by inspection (though overlap in some ways with the other distributions). The K-S test does not show these two distributions as statistically different (with p-values of near to or exactly 1). . . . .	119
3.29 Comparison of the same 6 datasets in observation distribution. The left graph is the CDF of the distributions, while the middle is the percent difference for the two variable p-modes, and the right is the percent difference between all combinations for the short exposure time case. The variable p-modes remain indistinguishable from each-other, though the fixed 5-minute is somewhat distinguishable from either. The fixed 10-minute p-mode has a statistically significant and visible offset distribution from the rest. . . . .	120
3.30 Comparison of the same 6 datasets in their distributions for our K/SNR detection heuristic (semi-amplitude sensitivity at an SNR of 10 is top, SNR for a fixed semi-amplitude of 10 cm/s is bottom). The left graphs are the CDF of the distributions, while the middle are the percent difference for the two variable p-modes, and the right is the percent difference between all combinations for the short exposure time case. Using a cutoff of $p < 0.05$ , we find no p-mode compensation method is different from any other. This is supported by the overlapping CDFs. . . . .	120
3.31 A comparison of our 3 target lists in the parameter spaces used for p-mode compensation. . . . .	122

3.32 A comparison of our 3 target lists (HWO, EPRV, HabEx), for typical high and low precisions using the NEID spectrograph on a 3.5 m telescope. ( <b>top</b> : CDFs of exposure times and observation counts, <b>bottom</b> : CDFs of our K/SNR detection heuristic). . . . .	123
4.1 Two typical graphs of light source simulations. The left shows what would be seen at the Vera Rubin Observatory from a distant satellite with a 100 W incandescent (black body) source diffused over $\pi$ steradians. The right shows results from a 755 nm 0.1 W LED source in GEO by several different filters and for several different dispersions. . . . .	133
4.2 Graphs from the initial runs/parameters, looking at a 100 W, 2700 K incandescent source in Vera Rubin Observatory's ugrizy filters at a large range of distances. Despite it being an 8-meter class telescope, the very faint magnitudes (often $\geq 20$ ), pushed us towards other designs. . . . .	134
4.3 Graphs from the initial runs/parameters, looking at a 100 W, 6500 K incandescent source in Vera Rubin Observatory's ugrizy filters at a large range of distances. While the hotter source is substantially brighter in visible light, this would be difficult to do as a true blackbody. . . . .	135
4.4 A typical LED (532 nm 1 W source), at varying collimations and distances comparable to the incandescent sources. Filters from all of the instruments that we considered that could plausibly detect that wavelength are shown. Again, isotropic emission ( $4\pi$ sr), a stand-in for a bare fibre or possibly an integrating sphere ( $\pi$ sr), and a highly collimated beam ( $1 \mu\text{sr}$ ) are shown. While LEDs offer order of magnitude increases in photons per watt in this wavelength range, the uncollimated beams are again quite faint (below 20th magnitude at the longer distances considered). . . . .	137
4.5 Graphs from later runs. Here, the craft would be in GEO (35,768 km), with an LED emitter. Four dispersions were looked at: 338 microradians, 0.1 degrees, 5.42 degrees, and (depending on the run) $2/\sqrt{\pi}$ radians. At this point, multiple kinds of optics were being considered to get a range of apparent magnitudes, depending on what would be observing the light source.	139

## Abstract

SIMULATIONS FOR UPCOMING AND PROPOSED EXOPLANET SURVEYS AS PATHFINDERS FOR DIRECT IMAGING MISSIONS

Patrick D Newman, PhD

George Mason University, 2025

Dissertation Director: Dr. Peter Plavchan

Orbital direct imaging missions (eg: HabEx, LUVOIR, HWO), expect to have great yields in exoplanet characterization, but limited flight times that could be best used if not spent on detection. Ground-based EPRV can provide target lists and best observation times for a fraction of the cost and in a short enough time-frame to be ready before launch. These missions in turn represent a significant resource investment and should be arranged to maximize planet detection and orbit/mass characterization. For these I present: 1) A code to simulate radial velocity surveys, along with a project using it in proposed next generation RV surveys, and 2) More general characterization of RV survey parameters and yields for differing target lists and prioritization strategies. These results are used to provide partial characterization, and survey program recommendations. Additionally, existing photometric measurements of stars have high relative precision, though much lower absolute precision. Flying a light source with known properties can provide high precision calibration that includes atmospheric effects. For these I present: an outline of simulations of the apparent brightness of diode and black-body light sources through the filters of current and upcoming ground and space based observatories at realistic distances. From these results, I present recommendations for selecting light sources and orbits.

# Chapter 1: Introduction to Exoplanets and RV Survey Simulations

## 1.1 Background

### 1.1.1 Exoplanets and Radial Velocities

Exoplanets (planets outside of the solar system), are a rapidly advancing field. As of 2025-09-17, over 6000 have been discovered[1], and work to characterize them is ongoing.

There have been multiple direct and indirect methods by which exoplanets have been discovered to date. Herein we highlight some of the most common methods.[2,3] This listing is far from exhaustive.

While the very first were found with pulsar timing[4], Most exoplanet discoveries were initially performed via the radial velocity (RV) method[5]. In terms of number of planets found, this has been superseded by the transit method[6–9], though both probe different portions of the orbital period-mass (and inclination) parameter space. Direct imaging[10] is a third method that has historically been used for distant giant planets from the ground, though with an ultimate goal of being able to detect and characterize earth-like planets (in terms of both mass and orbit) from a space based platform. Direct imaging can provide atmospheric information, but provides little to none of planetary masses (which are needed to better than 10-20% accuracy to constrain atmospheric models).

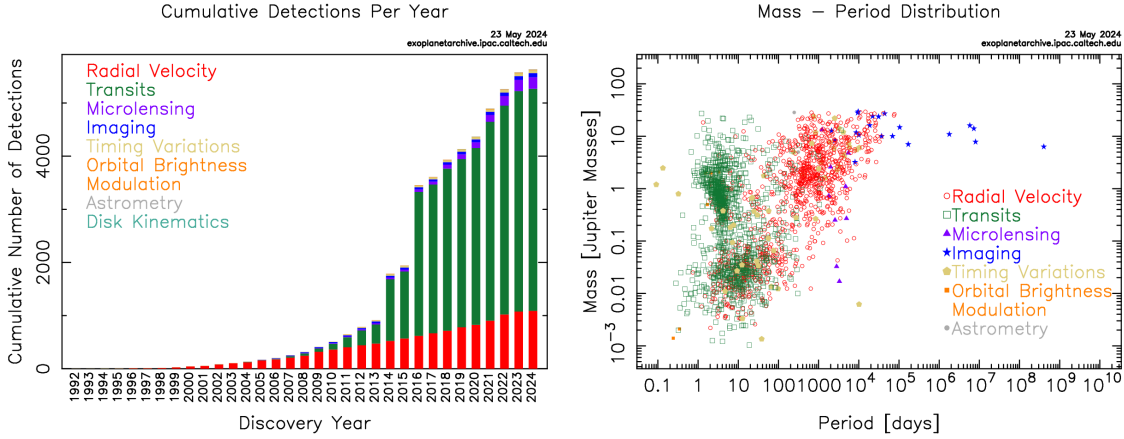


Figure 1.1: **Left:** Cumulative detections of exoplanets from 1992 to 2024, with the different methods shown. **Right:** A graph of period vs mass for known exoplanets, with the different detection methods shown.

Future, ground-based, extreme precision radial velocity (EPRV) surveys aim to detect Earth-mass analogs orbiting nearby Sun-like stars, many of which will overlap with the potential survey samples of a future direct imaging mission derived from studies such as HabEx and LUVOIR [11–15]. The National Academies Exoplanet Science Strategy (ESS) report in 2018 recommended that “NASA and NSF should establish a strategic initiative in extremely precise radial velocities (EPRVs) to develop methods and facilities for measuring the masses of temperate terrestrial planets orbiting Sun-like stars” [16]. In response, NASA and the NSF established the EPRV Working Group in 2019 to “recommend a ground-based program architecture and implementation plan accounting for the full scope of the ESS report findings.” [17]. Herein, “architecture” refers to an observatory or set of observatories and spectrographs, target lists and survey strategies to meet the goal of the ESS recommendation, and we will use the term architecture throughout this paper in this context.

Consideration of different architectures necessitates an assessment through simulation of the potential yield of a future EPRV survey. Historically,  $1 \text{ m s}^{-1}$  RV survey yields have been based upon theoretical photon noise approximations from the number of targets, number of observations, survey duration, and single measurement precision [18–21]. However, cadence sampling biases, weather and other realistic observatory and spectrograph factors

Table 1.1: Table of semi-amplitudes for example planets in relatively circular orbits. The solar system cases are assumed to be at 0 degrees inclination.

Planet	RV signal strength
51 Peg b	56 m/s
Jupiter	12 m/s
Earth	9 cm/s

can impact actual survey yields [22]. Current and next-generation EPRV instrumentation aims for an order of magnitude improvement in detection sensitivity compared to the era of 1 m s<sup>-1</sup> RV surveys. Achieving these gains in detection sensitivity will require a minimum of two orders of magnitude increase in photon counts and thus aperture and/or observing time based upon photon noise statistics alone. Thus it is important to first establish what minimum observational resources are necessary.

$$K = \frac{m_2 \cdot \sin(i) \sqrt{G}}{\sqrt{m_1 + m_2} \sqrt{a} \sqrt{1 - e^2}} = \frac{m_2 \cdot \sin(i) (2\pi G)^{1/3}}{(m_1 + m_2)^{2/3} T^{1/3} \sqrt{1 - e^2}} \quad (1.1)$$

The figure of merit for a planet's observability with RV surveys is its semi-amplitude K(1.1). This is linearly proportional to the planet's mass, and (sub-linearly) inversely proportional to its semi-major axis/period and the host star's mass. A 1 m/s sensitivity is small by the standards of previous surveys and an order of magnitude better than what is needed detecting giant planets. At the same time, it puts earth analogs around M and K-dwarfs at the edge of detection, and is an order of magnitude too insensitive to find earth analogs around solar analogs.

Additionally, stellar activity has impacted EPRV exoplanet detection sensitivity and, consequently, survey yields [19, 23–33]. Stellar atmospheres are variable environments, with a number of effects (eg: pulsation, granulation, spots/plages, flares) that can add, alter, or hide signals at the few m/s level over a very large range of timescales (minutes to years). There has been one community challenge to date taking HARPS cadence measurements for individual targets and testing the injection and recovery of planetary systems for modeling

and accounting for stellar activity correlated noise [34, 35].

More recently, [36] carried out a EPRV survey simulation for the HARPS3 spectrometer. They considered three different cadences, four different possible planetary architectures, instrument white noise, and star spot correlated noise around a G6V star. They found that some common survey cadences would be insufficient to accurately find/characterize earth-mass habitable zone planets, though more aggressive ones often are. Similarly, [37] investigated the impact of realistic cadence aliases mixing with stellar activity in producing false-positive EPRV signals for the Kepler 20 and 131 systems.

Imperfectly modeled stellar activity can generate spurious signals of planets [38], and biases in sampling can also cause large discrepancies in the properties of a planet. [39] However, current mitigation techniques should be able to mitigate stellar activity and detect planets at the 1-2 m/s level. [40, 41] Failure to properly account for stellar activity also can result in overly optimistic techniques that do not come to fruition. The MINERVA survey predicted a yield of  $15 \pm 4$  planets between 0.8 and 3 m/s. [42] They found 0.

### 1.1.2 Photometric Systems

While relative photometry of astronomical sources has become extremely precise, absolute photometry has stalled out at around 1% precision. A great deal of “standard” sources trace back to reference objects that impose additional uncertainty. The Hubble Space Telescope started with three pure hydrogen white dwarfs for absolute flux calibration [43–45]. The Sloan Digital Sky Survey has nominal absolute flux standards [46, 47], but uses a 4th pure hydrogen white dwarf, which is in turn calibrated from the Hubble white dwarfs [48]. More recent work has expanded the number of standard white dwarfs and wavelength ranges for HST, JWST, etc. [49, 50], and while they may reach 0.1% with respect to each-other and in time, they remain in the 1% absolute precision range. The Johnson-Cousins system has its own sets of standard stars, and its own limitations from the comparatively complicated atmospheres and in some cases surrounding environments of Vega, Sirius, etc. [51]

## 1.2 Outline

In this thesis I present: my existing published survey simulation research (chapter 2), a draft of additional but currently unpublished survey simulation work (chapter 3), and simulations for planning a photometric absolute calibration mission (chapter 4).

## Chapter 2: Simulations for Planning Next-Generation Exoplanet Radial Velocity Surveys (published paper)

### 2.1 Introduction

Future, ground-based, extreme precision radial velocity (EPRV) surveys aim to detect Earth-mass analogs orbiting nearby Sun-like stars, many of which will overlap with the potential survey samples of future direct imaging mission studies such as HabEx and LUVOIR [11–15]. The National Academies Exoplanet Science Strategy (ESS) report in 2018 recommended that “NASA and NSF should establish a strategic initiative in extremely precise radial velocities (EPRVs) to develop methods and facilities for measuring the masses of temperate terrestrial planets orbiting Sun-like stars” [16]. In response, NASA and the NSF established the EPRV Working Group in 2019 to “recommend a ground-based program architecture and implementation plan accounting for the full scope of the ESS report findings.” [17]. Herein, “architecture” refers to an observatory or set of observatories and spectrographs, target lists and survey strategies to meet the goal of the ESS recommendation, and we will use the term architecture throughout this paper in this context.

Consideration of different architectures necessitates an assessment through simulation of the potential yield of a future EPRV survey. Historically,  $1 \text{ m s}^{-1}$  RV survey yields have been based upon theoretical photon noise approximations from the number of targets, number of observations, survey duration, and single measurement precision [18–21]. However, cadence sampling biases, weather and other realistic observatory and spectrograph factors can impact actual survey yields [22]. Current and next-generation EPRV instrumentation aims for an order of magnitude improvement in detection sensitivity compared to the era of  $1 \text{ m s}^{-1}$  RV surveys. Achieving these gains in detection sensitivity will require a minimum

of two orders of magnitude increase in photon counts and thus aperture and/or observing time based upon photon noise statistics alone. Thus it is important to first establish what minimum observational resources are necessary. Additionally, stellar activity has impacted EPRV exoplanet detection sensitivity and, consequently, survey yields [19, 23–33]. There has been one community challenge to date taking HARPS cadence measurements for individual targets and testing the injection and recovery of planetary systems for modeling and accounting for stellar activity correlated noise [34, 35].

More recently, [36] carried out a EPRV survey simulation for the HARPS3 spectrometer. They considered three different cadences, four different possible planetary architectures, instrument white noise, and star spot correlated noise around a G6V star. They found that some common survey cadences would be insufficient to accurately find/characterize earth-mass habitable zone planets, though more aggressive ones often are. Similarly, [37] investigated the impact of realistic cadence aliases mixing with stellar activity in producing false-positive EPRV signals for the Kepler 20 and 131 systems.

Imperfectly modeled stellar activity can generate spurious signals of planets [38], and biases in sampling can also cause large discrepancies in the properties of a planet. [39] However, current mitigation techniques should be able to mitigate stellar activity and detect planets at the 1-2 m/s level. [40, 41]

In this chapter, we simulate and make available the tools and output to the community<sup>1</sup> possible dedicated EPRV surveys to search nearby stars to detect and characterize Earth-mass analogs as input targets prior to the launch of a direct imaging mission such as HabEx or LUVOIR [17]. The architectures considered herein are all potential next-generation EPRV global networks of observatories assumed to be operational prior to the launch of a direct imaging mission. Our goal herein is to evaluate survey cadences for these potential architectures for their ability detect Earth-like planets around Sun-like stars. For this, we choose a characteristic figure of merit of a 10 cm/s semi-amplitude stellar reflex velocity

---

<sup>1</sup>[https://github.com/pdn4kd/dispatch\\_scheduler](https://github.com/pdn4kd/dispatch_scheduler)   [https://github.com/pdn4kd/reimagined\\_palm\\_tree](https://github.com/pdn4kd/reimagined_palm_tree)

measured at a minimum SNR of 10 (§2.1.1). This RV semi-amplitude is representative of an edge-on Earth-mass planet in Habitable Zone (HZ) of a Sun-like star. A great many hidden variables can change this value by approximately a factor of 2 – e.g. inclination, eccentricity, HZ location, stellar mass, etc. Due to the approximate nature of this figure of merit, we explicitly look at distributions of our survey sensitivity and do not treat it as a simple cut-off. We do not consider temporally correlated noise from stellar activity or otherwise, and this is the subject of a companion paper by [52]. We restrict the analysis herein to the consideration of sensitivity guided by uncorrelated measurement photon noise statistics [18]. We do however include the impact of stellar activity from a spectroscopic perspective by incorporating a minimum spectral SNR requirement in addition to an RV precision requirement for the spectral characterization of stellar activity – e.g. such as performed in line-by-line analyses [53–56] No injection and recovery tests with realistic exoplanet populations and stellar activity are performed on the resulting simulated data, but such efforts could be the subject of future work.

In §2.2, we describe the simulations, and the features therein that we consider and ignore for a set of plausible observatory and spectrograph architectures. In §2.3, we show the results for each architecture. In §2.4, we compare the figures of merit across architectures. In §2.5, we present a discussion of the results and limitations and effects of survey simulations, and in §2.6 we present our conclusions.

### 2.1.1 Planet Detection Figure of Merit

We use the theoretical best-case scenario for estimating the detection significance achieved for a  $1 M_{\oplus}$  planet in an edge-on, circular, 1 au orbit around a  $1 M_{\odot}$  Sun-like star with unknown orbital phase.[18]

$$SNR - detect = \frac{K}{\sigma} \sqrt{\frac{N_{\text{obs}}}{2}} \quad (2.1)$$

Here  $K$  is the stellar reflex velocity semi-amplitude due to the orbiting exoplanet,  $\sigma$  is

the typical single measurement precision, and  $N_{\text{obs}}$  is the number of observations realized from our simulations over the survey duration, which is assumed to be greater than the exoplanet orbital periods of interest. We note that Equation 2.1 formally assumes uniform cadence in phase. For the large number of observations that we find are required for a robust detection, this is an excellent approximation for most cases, with the exception being planets with periods very close to one year.[57] Both the instrument and photon noise are added in quadrature for  $\sigma$ . In cases of instruments operating at different precisions (Architecture VIII), it can be shown that the equation is expanded to:

$$SNR - \text{detect} = K \sqrt{\frac{1}{2} \left( \frac{N_{\text{obs1}}}{2\sigma_1^2} + \frac{N_{\text{obs2}}}{2\sigma_2^2} \right)} \quad (2.2)$$

Throughout this analysis we assume stellar activity can be perfectly modeled and subtracted from observed RVs. All of these assumptions lead to increased sensitivity (and planet yield) compared with more detailed/realistic considerations of stellar noise and injection/recovery tests. As signal to noise values can move by multiple standard deviations from our assumptions, directly calculating false alarm probabilities herein is not warranted.

## 2.2 Survey Simulation Description

In this section, we outline the survey simulations and the components and assumptions that went into these simulations (Figure 2.1). At the top level we simulate multiple radial velocity surveys to benchmark against one another. Each simulated radial velocity survey consists of a set of telescopes in a global network with different spectrographs and telescope specifications, which we call “architectures” (see §2.2.4), along with other additional miscellaneous simulation inputs (§2.2.6). Then for each telescope site, we simulate the observations of a set of targets (see §2.2.5) using a dispatch schedule that takes into account a variety of observational constraints and target prioritization (§2.2.1). The RV precision (§2.2.2) and exposure times are then simulated, and we conclude with describing

the outputs from the simulations in §2.2.7.

### 2.2.1 The Dispatch Scheduler

All survey simulations were carried out using a dispatch scheduler that selects which target to observe next “on the fly”, instead of following a preset observing schedule. The dispatch scheduler simulates a survey in moderate detail to provide a realistic observation time series. Our version<sup>2</sup> is derived from the MINERVA scheduler [42, 58]. The scheduler takes a list of targets with name, right ascension, declination, and estimated observation times as inputs, and generates a time series of observations for each target (as well as rise and set times for the Sun and each of the potential targets). It also generates a nightly summary file containing the start and end times of the night, the simulated weather, the number of times each star was observed, the amount of time spent on each star which is impacted by the airmass at the time of observation, and whether the star was considered to be observable given our constraints. Constraints define the ordering and prioritization of targets to observe and can be divided into: weather, other natural constraints, observatory constraints, and prioritization weights. We discuss each of these in turn below. For simplicity, we do not take into account variable throughput from changing seeing conditions. However, the dispatch scheduler does account for airmass attenuation from Rayleigh-scattering.

---

<sup>2</sup>Available at [https://github.com/pdn4kd/dispatch\\_scheduler](https://github.com/pdn4kd/dispatch_scheduler)

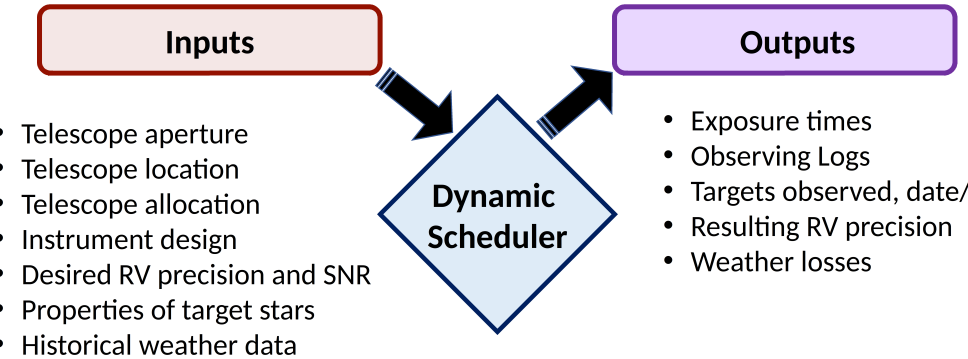


Figure 2.1: Outline of the simulation pipeline, including the exposure time calculator (ETC) and dispatch scheduler.

## Site Locations and Weather

A representative set of six locations were chosen to achieve a global network of facilities. In the final round of simulations, these locations were: Mauna Kea, Kitt Peak, and Calar Alto in the North, along with Las Campanas, Sutherland, and Siding Spring in the South (Figure 2.2). All of the architectures used all six sites. For the architectures with heterogeneous telescope compositions, the largest aperture telescopes were located at Mauna Kea and Las Campanas in our simulations.

We use available historical weather records for all observatory sites in order to determine the weather during our simulated survey. Specifically: Mauna Kea used a site survey [59], Calar Alto and Sutherland used telescope operations reports [60, 61], and Kitt Peak, Las Campanas, and Siding Spring used information from the observatory websites.<sup>3</sup> For each site, we compiled either monthly, or by semester in the case of Sutherland and yearly for Siding Spring, statistics for the fraction of clear nights (Figure 2.2.1). For Siding Spring and Sutherland, monthly statistics were not readily available. Finally, all surveys were assumed to span 10 years in duration (2020-01-01 to 2030-01-01).

---

<sup>3</sup>[http://www-kpno.kpno.noao.edu/Images/wiynWeather\\_stats.jpeg](http://www-kpno.kpno.noao.edu/Images/wiynWeather_stats.jpeg)    <https://www.eso.org/sci/facilities/lasilla/astclim/weather/tablemr.html> <https://aat.anu.edu.au/about-us/AAT>

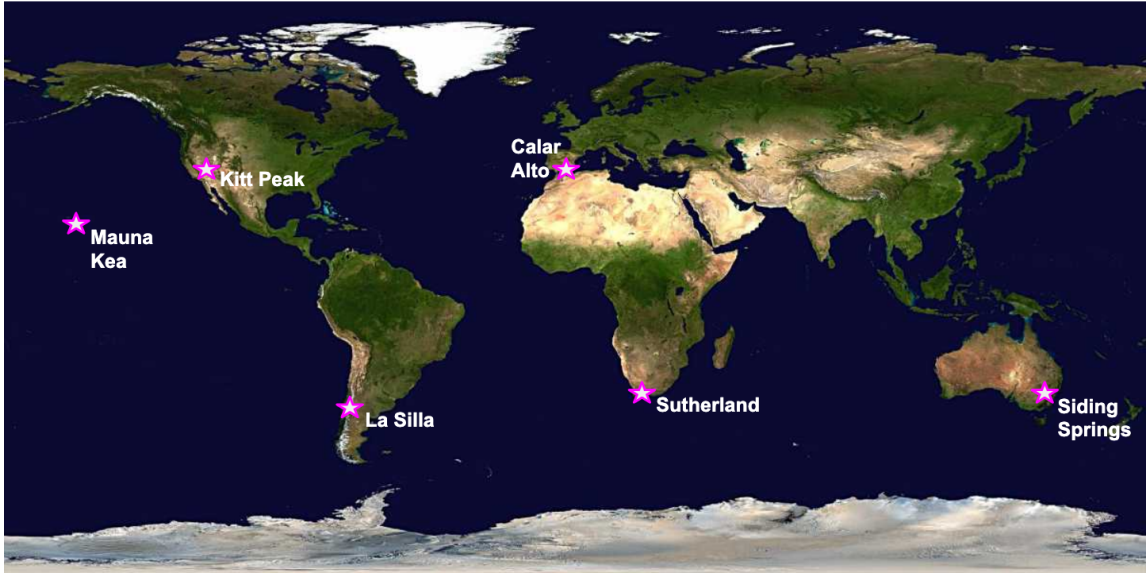


Figure 2.2: Site locations

We make the simplification that each night is assumed to be either entirely clear or entirely unusable, so there are no partial nights. Whether or not a night is lost due to weather is determined randomly at the start of the night, with the probabilities drawn from the historical monthly average. When monthly historical weather averages were not available, we instead used yearly averages for Siding Spring and semester averages for Sutherland. For simplification, we assume that nights lost due to weather do not exhibit night-to-night correlations, even though in reality it is typical to lose multiple nights in a row from weather patterns.

### Other Natural Constraints

To further determine each target star's availability for observation we consider the telescope's latitude, longitude, and elevation, the time required for target acquisition, and the local horizon. Calculated sun-rise/set times are used to determine astronomical twilight which is when we allow observations to begin, and a minimum distance from the Moon (10 degrees for our surveys) that is required for a star to be targeted. The effects of Moon avoidance angle on survey cadence are not explored herein, although these effects would be

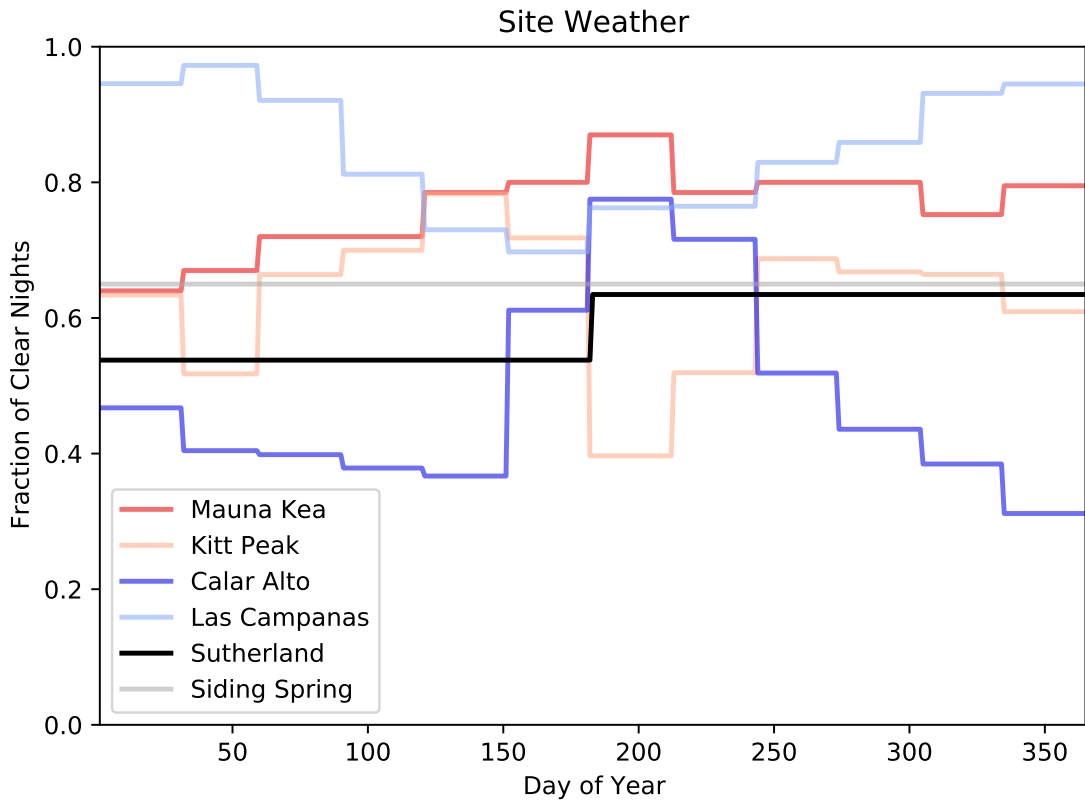


Figure 2.3: Nightly weather probabilities for each site included in our simulations.

a possible avenue for future research. Ephemerides for all objects are found via Astropy.

### Observatory Constraints

For the observatory constraints, we consider telescope pointing limits (set to 30 degrees above the physical horizon), time for telescope slews between targets and for target acquisition (five minutes used for all observations), and total open shutter and detector readout times.

### Target Prioritization

Finally, as per the name, we use a dispatch scheduler prioritization scheme. The scheduler determines target choices from a user provided list of stars between each observation, rather

than executing a preset observing order. Targets are ranked using a combination of hour angle (highest weight at zenith), and time since last observation. We assume a minimum separation between observations of two hours (e.g. within that time the target is at a minimum priority), with linearly increasing weight thereafter. The relative weighting of these two factors can be adjusted, and we fixed the relative weighting to produce cadences that spread the observations approximately evenly between the targets [62].

The dispatch scheduler assumes a single fixed observatory site. For handling up to the six telescope sites, a separate independent simulation was run. As such, we do not implement a mechanism for different telescope sites to coordinate prioritization of target observations with each other. In other words, we make the simplifying assumption that the telescope schedules are decoupled. On average, the different sites will randomly compensate for each others weather losses, but this is not optimized.

Despite the architectures in this survey having specified cadence goals/requirements, the dispatch scheduler does not attempt to reach any specific cadence. Rather, it observes every star in a given site’s target list as frequently as possible, given the above constraints and weightings. As shown in the results, not all architectures can achieve their desired cadences. Reaching the cadences specified for each architecture below would require sculpting/optimizing the target list iteratively, which is beyond the scope and capability of these simulations.

### 2.2.2 RV Model

RV precision and exposure times were calculated<sup>4</sup> using an implementation of the formalism presented in [63]. This RV model uses a set of BT Settl synthetic stellar spectra over the user specified instrument wavelength range, and a set of pre-calculated RV precision values for each wavelength and temperature bin in units of 1 photon per m/s in each 100 Å wavelength bin. Correction factors for the RV content are used to account for variations in stellar surface gravity ( $\log(g)$ ), metallicity, and projected rotational velocity ( $v \cdot \sin(i)$ ).

---

<sup>4</sup> Available at <https://github.com/pdn4kd/reimagined-palm-tree>.

Synthetic spectra for M dwarfs in particular are known to underestimate the RV information content at red-optical wavelengths (e.g. there are more, deeper, sharper absorption lines), and overestimate the RV information content in the J and H bands [64][65][e.g. there are fewer, shallower, broader absorption lines, Fig 3, ]. However, this is a relatively small effect ( $\sim 25\%$ ) for what we are considering herein for M dwarfs, and additionally there are no M dwarfs in our simulated survey sample (§2.2.5).

The finite size and throughput of the spectrograph (in both resolution and pixels) is considered, though optical details beyond those are not. Instrument noise in the forms of dark current and readout noise are considered. The important changes in our implementation are: allowing the spectrographs defined in Section 2.2.4 to be in any wavelength range instead of just three specific ranges, and a simple atmospheric scattering model (Rayleigh plus a baseline). No telluric absorption lines are included, so our resulting RV precision estimates should be considered optimistic, especially in the near-infrared. Stellar activity similarly is not directly modeled, and thus we are simulating a bounding best-case scenario of a photon-noise limited survey with “perfect” stellar activity correction. Additional details on the model and its calibration are in [62]. Consideration of the impact of correlated noise on our analysis is considered explicitly in [52].

### 2.2.3 Exposure Time Calculations

Exposure times at each observing site are calculated with an exposure time calculator (ETC) in two steps. First, the RV and SNR-phot are found for an observation that is just long enough to saturate the CCD at the star’s peak brightness (approximated using Wein’s Law) within the spectral grasp of the spectrograph as defined in Section 2.2.4. Second, this exposure time is scaled to the desired RV and SNR-phot precision based upon an assumption that we are purely photon-noise limited (RV uncertainty  $\sim \text{SNR-phot}^{-1} \sim t^{-1/2}$ ). This scaling dictates how many individual exposures (co-adds) are needed, and is combined with the instrumental readout time of co-add of 30 seconds<sup>2.4</sup> to give a cumulative (“clock”) observation time. The SNR (SNR-phot) we use for the ETC is a per-pixel raw

spectrum photon-noise measurement unrelated to the SNR-detect from Equation 2.1 of the velocity semi-amplitude we calculate as a planet detection heuristic later in our analysis.

In order to average over short term stellar pulsation modes or p-mode oscillations, we implement a minimum clock observation time of 5 minutes and execute additional exposures as needed to achieve this minimum. For simplicity, we do not adjust this minimal time to account for the estimated p-mode oscillation time as a function of individual spectral type and surface gravity for each individual target (eg: [66]). This assumption, and its impact, is investigated (verses a 10 minute minimum) in 2.4.1. Finally, we assume that the observatory does not move onto the next target until the final co-add is read out; conversely, this can be thought of as an additional 30-second penalty on the assumed 5 minutes for target slews and acquisition overhead.

#### 2.2.4 Architectures: Telescopes and Spectrographs

We consider a set of architectures of dedicated telescopes of different diameters equipped with high-resolution spectrometers to enable a next-generation global EPRV survey to search for and detect Earth-mass twins. We consider realistic telescope diameters that are representative of existing or proposed EPRV facilities and telescopes. All architectures we consider utilized the same notional “baseline instrument” design: a high resolution, optical band pass, extreme precision RV spectrograph loosely based on the design of NN-Explore’s NEID spectrograph located on the 3.5 m WIYN telescope [67, 68]. For all architectures, we also consider a “defined instrument” variation to these spectrograph parameters, motivated by the given telescope diameter or configuration. In the following sub-sections, we describe each architecture in detail.

Table 2.1: The seven architectures' facility and instrumental properties. Architectures not listed (III, IV, VII) were dropped from direct consideration in earlier simulations. Architectures with a/b variants have different sizes/numbers of telescopes, but identical instruments for each variant.

Architecture	I	IIa	IIb
Telescopes	6x2.4 m	2x6 m and 4x4 m	6x4 m
Collecting area by aperture	$2.4 \text{ m} = 4.2 \text{ m}^2$	$4 \text{ m} = 9.5 \text{ m}^2; 6 \text{ m} = 27 \text{ m}^2$	$4 \text{ m} = 9.5 \text{ m}^2$
Time allocation	100%	100%	100%
Wavelength coverage	380-930 nm	380 - 930 nm	380 - 930 nm
Spectral resolution	180 000	180 000	180 000
Total system efficiency	6%	6%	6%
instrument noise floor	10 cm/s	5 cm/s	5 cm/s
Required (peak) SNR/pix	300	300	300
Required RV precision	10 cm/s	10 cm/s	10 cm/s
Observation cadence per star	1 / night	3 / night	3 / night

Architecture	V	VI
Telescopes	6x3 m	6x arrays of 1 m
Collecting area by aperture	$3 \text{ m} = 6.3 \text{ m}^2$	$0.61 \text{ m}^2 \text{ each; array is } 9.5 \text{ m}^2$
Time allocation	100%	100%
Wavelength coverage	500-1700 nm	500-800 nm
Spectral resolution	180 000	150 000
Total system efficiency	7%	6%
instrument noise floor	10 cm/s	10 cm/s
Required (peak) SNR/pix	300	300
Required RV precision	10 cm/s	10 cm/s
Observation cadence per star	2 / telescope / night	1/night

Architecture	VIIia
Telescopes	2x10 m and 4x 3.5 m
Collecting area by aperture	$10 \text{ m} = 75 \text{ m}^2; 3.5 \text{ m} = 9.5 \text{ m}^2$
Time allocation	25% of 10 m; 100% of 3.5m
Wavelength coverage	380-930 nm
Spectral resolution	180 000
Total system efficiency	6%
instrument noise floor	5 cm/s
Required (peak) SNR/pix	1000 for the 10 m; 300 for 3.5 m
Required RV precision	15 cm/s on 3.5 m; 5 cm/s on 10 m
Observation cadence per star	1/week on 10 m; 1/night on 3.5 m

Architecture	VIIib
Telescopes	2x10 m and 6x2.4 m
Collecting area by aperture	$10 \text{ m} = 75 \text{ m}^2; 2.4 \text{ m} = 4.2 \text{ m}^2$
Time allocation	25% of 10 m; 100% of 2.4 m
Wavelength coverage	380-930 nm
Spectral resolution	180 000
Total system efficiency	6%
instrument noise floor	5cm/s
Required (peak) SNR/pix	1000 for the 10 m; 300 for 2.4 m
Required RV precision	15 cm/s on 2.4 m; 5 cm/s on 10 m
Observation cadence per star	1/week on 10 m, <sup>7</sup> 1/night on 2.4 m

Table 2.2: Peak system throughputs for current EPRV spectrographs. These are higher than the averages used in the various simulated architectures, as they largely do not account for performance variations from varying seeing conditions and as a function of wavelength.

Spectrograph	Throughput	Source
ESPRESSO	10%	[69]
EXPRES	9-15%	[70]
MAROON-X	7-8%, 11.5%	[71]
NEID	6%	[72]

## Architecture I

This architecture utilizes a network of six identical, dedicated robotic 2.4-m telescopes, each of which is paired with one of the standardized EPRV spectrographs described above. The telescopes in this architecture spend 100% of nightly observations on the EPRV survey (the survey targets are described in 2.2.5). An example of such an observatory in existence today is the Automated Planet Finder telescope [73]; the APF is a fully automated, robotic facility that has been executing precise RV surveys since 2014, and is the largest aperture robotic RV telescope currently in operation.

As with most architectures described herein, the telescopes are spread across both longitude and latitude - three in the northern hemisphere (Mauna Kea in Hawaii, Kitt Peak in Arizona, and Calar Alto in Spain) and three in the southern hemisphere (La Silla in Chile, Sutherland in South Africa, and Siding Springs in Australia). This architecture could potentially save costs from the identical telescope hardware. Alternatively, given the large number of existing (and sometimes underutilized) telescopes in this size class, a heterogeneous variant could re-purpose one or more.

## Architecture II

Architecture II employs facilities at the same locations as Architecture I but uses larger aperture telescopes. It consists of two sub-architecture variations: IIa places 6-m telescopes at Mauna Kea and Las Campanas, and 4-m telescopes at the remaining locations, while

IIb uses 4-m telescopes at all six sites. Like the telescopes in architecture I, all facilities in Architecture II are dedicated and spend the entirety of their observing time working on this particular survey. Given the number of existing 4-m and 6-m class telescopes around the globe, this architecture may more easily re-purpose existing observatories, with the caveat that only a handful of telescopes of their aperture are currently dedicated to obtaining PRVs.

### Architectures III and IV

Architecture III consists of two 10-m class telescopes, one in the Northern hemisphere and one in the South, each of which has 50% of its time assigned to carrying out this EPRV survey, matching the 10-m portion of Architecture VIII. Examples of analogous telescopes currently in operation include but are not limited to Keck and Gemini observatories. Architecture IV is a copy of Architecture VIII, with a small fraction of additional time on one or two  $\geq 25$ -m class telescopes [eg: Thirty Meter Telescope or Giant Magellan Telescope [74]] that is used exclusively for RV follow-up, and not for the primary RV survey being simulated herein. Thus, the simulated RV survey performances of Architectures III and IV can be evaluated from the simulated performance of Architecture VIII.

### Architecture V

The distinguishing feature of architecture V is the spectrograph, which would use adaptive optics to inject light into single mode fibers, and extends farther into the near-infrared than its counterparts. Examples of current or planned single-mode fiber PRV spectrometers include PARVI, iLocater, and HISPEC [75–77]. Many of the unique advantages and challenges of this architecture are simulated at low fidelity herein, or are outside of the scope of these simulations. For example, we assume a spectral grasp that will extend into the visible with sufficient AO-corrections for efficient throughput coupling into the fibers than has currently been demonstrated on sky. We also do not consider differences in detector noise properties at the NIR wavelengths relative to visible CCDs, in part because the dark

current and read noise for H4RG, are reaching a level that is comparable to present CCD sensors.[78–80] For the simulations, we assume six 3-m telescopes are used.

## Architecture VI

This architecture uses a fiber multi-plexed array of small (notionally 1-m) telescopes at each telescope site to get the light gathering power equivalent of a larger aperture at potentially lower cost. As simulated, each array is considered to be the same as a single 4-m class telescope (equivalent to architecture IIb). The spectrograph suffers from reduced spectral grasp and lower spectral resolution due to the penalty of multiple fibers for each telescope in the array, and drives the difference in the assumed instrument parameters. The heritage for this architecture is conceptually a scaled-up version of the MINERVA and MINERVA-Australis PRV telescope arrays [42, 81].

## Architecture VIII

Architecture VIII is explicitly a hybrid architecture. It combines a pair of 10-m class telescopes operating at high precision and limited time allocation, one in each hemisphere, and a larger number (4-6) of smaller telescopes at lower precision and 100% dedicated time allocation to the EPRV survey. Architecture VIII is the only architecture simulated with varying precision and/or varying amounts of allocated survey time available at each telescope site. The VIIIa variant has four 3.5-m telescopes (comparable to architectures IIa/b and VI) located at four other locations distinct from the two 10-m telescopes. The VIIIb variant has six 2.4 m telescopes (similar to architecture I). We simulate two telescopes each (one 10-m and one 2.4-m) at both Mauna Kea and Las Campanas. In reality, these pairs of telescopes at Mauna Kea and Las Campanas would suffer identical weather losses. However, since we simulate each telescope independently, the telescopes at the same site have independently drawn weather losses. We reuse the 10-m simulations for all of Architectures VIIIa, VIIIb, and III.

### 2.2.5 Target Star Lists

Future exoplanet direct imaging NASA mission concept studies have produced prioritized target lists of nearby, bright stars. To identify a set of stars that would constitute a reasonable set of targets for a future EPRV survey of direct imaging targets, we cross-matched the HabEx and LUVOIR-A, LUVOIR-B, and Starshade Rendezvous[82] target lists [11, 12], and gathered archival information on stellar properties relevant to each star’s RV information content (i.e., spectral type, effective temperature, apparent magnitude, rotational velocity, metallicity and surface gravity). We first divide the stellar sample into three target prioritization levels listed below. All stars on the green and yellow lists must satisfy the criteria that 1) planets in the habitable zone would be visible to future direct imaging efforts, and 2) the host stars themselves are amenable to EPRV observations:

- Green targets
  - Spectral types F7-K9
  - $vsini < 5$  km/s
  - HabEx deep or nearest 50 or appearing on  $N \geq 2$  lists (including LUVOIR-A, LUVOIR-B, HabEx, Starshade Rendezvous)
  - 106 stars
- Yellow targets
  - Spectral types F7-M
  - $vsini < 10$  km/s
  - Appears on at least one direct imaging mission concept list, but not a “green” target
  - 123 stars
- Red targets
  - Spectral type hotter than F7

- $v\sin i > 10$  km/s

- 78 stars

An additional five stars were removed from the green target list to generate a final “green prime” list of 101 stars. These five stars possessed the longest (in the green list) estimated exposure times from §1.4 to reach the desired RV precision, primarily due to a combination of spectral type and rotational velocity (e.g. these were corner cases). The resulting “green prime” star list of 101 stars and associated stellar properties are listed in Table 2, shown distributed on the sky in Figure 2.4, and constitute the sample used for our RV survey simulations. The yellow stars were both less favored by the direct imaging surveys, somewhat fainter, and in some cases had less RV information content due to rotational broadening, and thus were excluded from our simulations here. Similar the red targets were excluded due to their insufficient RV information content.

The green prime list of targets was in turn broken into a northern hemisphere sub-set ( $\geq -5^\circ$  dec, 51 stars), and a southern hemisphere sub-set ( $\leq +5^\circ$  dec, 58 stars) for observing with telescopes in their respective hemispheres, with 9 stars near the celestial equator appearing on both lists for cross-comparison. Since our simulations do not coordinate telescope target optimization, we did not dynamically optimize which stars were observed by which telescopes (e.g. a fluid declination cutoff that is optimized for each observing site and time of year). These particular declination cuts were chosen to have  $\sim 10\%$  overlap between the target lists of both hemispheres.

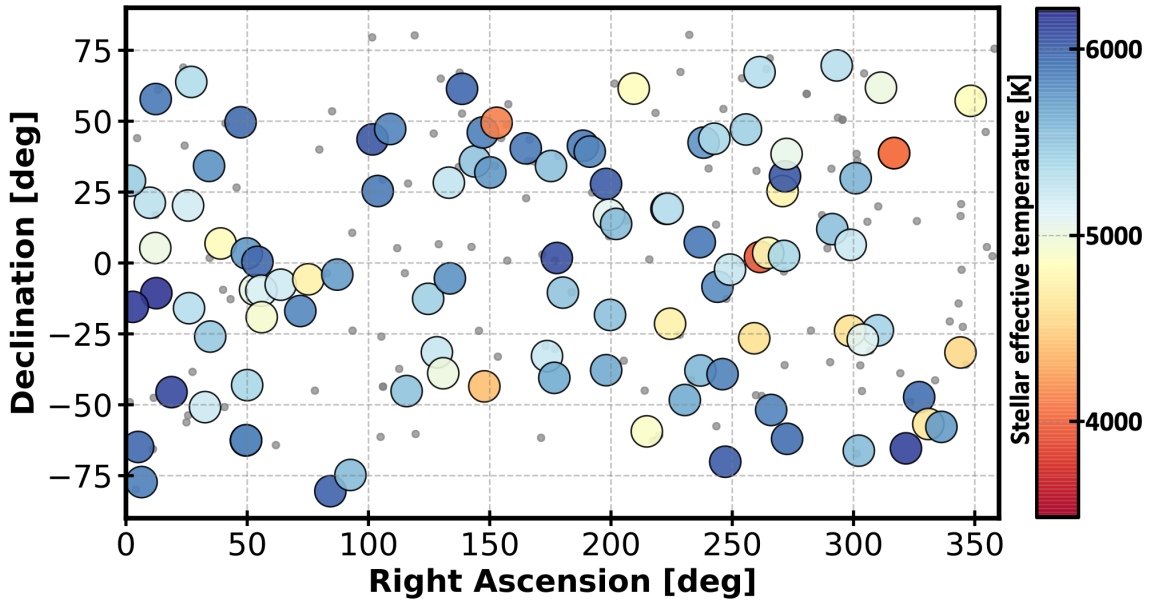


Figure 2.4: The locations on the sky of all green and yellow list stars. Open circles represent green list targets, color coded by effective temperature, while the yellow list stars are depicted by the grey points. While the thin disk of nearby stars is effectively isotropic on the sky, the green prime list of 101 nearby bright stars shows some minor clustering on the sky which can impact RV survey efficiency.

Table 2.3: Stars in the “green prime” list. Name (HIP number), spectral type, which hemispheres they were observed in, the properties used in the simulations, and their sources are included. Mass and radius for all stars are estimated from other properties.

HIP	RA	Declination	Dist (pc)	$v\sin i$	Spectral Type	$T_{eff}$	$\log(g)$	[Fe/H]	Mass	Radius
10138	02:10:24.00	-50:49:31.1	10.787 <sup>a</sup>	1.9 <sup>b</sup>	K1.5V <sup>c</sup>	5217 <sup>d</sup>	4.56 <sup>d</sup>	-0.23 <sup>d</sup>	0.82	0.755
101997	20:40:11.44	-23:46:30.0	14.677 <sup>a</sup>	1.8 <sup>b</sup>	G7.5IV-V <sup>c</sup>	5414 <sup>e</sup>	4.46 <sup>e</sup>	-0.31 <sup>e</sup>	0.95	0.951
102422	20:45:17.27	+61:50:12.5	14.265 <sup>f</sup>	1.7 <sup>b</sup>	K0IV <sup>c</sup>	5002 <sup>g</sup>	3.43 <sup>g</sup>	-0.09 <sup>g</sup>	1.23	10.188
104214	21:06:50.84	+38:44:29.4	3.497 <sup>a</sup>	1.8 <sup>b</sup>	K5V <sup>c</sup>	4339 <sup>h</sup>	4.43 <sup>h</sup>	-0.33 <sup>h</sup>	0.68	1.019
104217	21:06:52.19	+38:44:03.9	3.495 <sup>a</sup>	1.8 <sup>b</sup>	K7V <sup>c</sup>	4045 <sup>h</sup>	4.53 <sup>h</sup>	-0.38 <sup>h</sup>	0.63	0.809
105858	21:26:26.49	-65:22:05.3	9.262 <sup>f</sup>	3.4 <sup>b</sup>	F9V Fe-1.4 CH-0.7 <sup>i</sup>	6150 <sup>d</sup>	4.35 <sup>d</sup>	-0.66 <sup>d</sup>	1.14	1.225
10644	02:17:02.42	+34:13:29.4	11.008 <sup>a</sup>	2 <sup>b</sup>	G0.5V Fe-0.5 <sup>c</sup>	5786 <sup>d</sup>	4.29 <sup>d</sup>	-0.53 <sup>d</sup>	1.08	1.406
107649	21:48:15.61	-47:18:10.4	15.561 <sup>a</sup>	1.8 <sup>b</sup>	G0V Fe+0.4 <sup>i</sup>	5946 <sup>e</sup>	4.48 <sup>e</sup>	0.01 <sup>e</sup>	1.08	0.908
10798	02:18:58.65	-25:56:48.4	12.834 <sup>a</sup>	2.7 <sup>b</sup>	G8V <sup>i</sup>	5476 <sup>d</sup>	4.61 <sup>d</sup>	-0.45 <sup>d</sup>	0.94	0.673
108870	22:03:17.44	-56:46:47.3	3.639 <sup>a</sup>	1.4 <sup>b</sup>	K4V(k) <sup>i</sup>	4649 <sup>d</sup>	4.63 <sup>d</sup>	-0.19 <sup>d</sup>	0.72	0.643
110649	22:24:56.19	-57:47:47.8	20.454 <sup>a</sup>	1.8 <sup>b</sup>	G2IV-V <sup>i</sup>	5739 <sup>j</sup>	4.15 <sup>j</sup>	0.05 <sup>j</sup>	1.02	1.941
113283	22:56:23.83	-31:33:54.6	7.608 <sup>a</sup>	2.6 <sup>b</sup>	K4Ve <sup>c</sup>	4555 <sup>k</sup>	4.53 <sup>k</sup>	-0.01 <sup>k</sup>	0.72	0.809
114622	23:13:14.74	+57:10:03.5	6.532 <sup>a</sup>	1.8 <sup>b</sup>	K3V <sup>c</sup>	4833 <sup>d</sup>	4.59 <sup>d</sup>	0 <sup>d</sup>	0.75	0.705
12114	02:36:03.83	+06:53:00.1	7.235 <sup>a</sup>	1.3 <sup>b</sup>	K3V <sup>c</sup>	4829 <sup>l</sup>	4.6 <sup>l</sup>	-0.16 <sup>l</sup>	0.75	0.689
14632	03:09:02.88	+49:36:48.6	10.541 <sup>f</sup>	3.6 <sup>b</sup>	G0V <sup>c</sup>	5968 <sup>d</sup>	4.19 <sup>d</sup>	0.08 <sup>d</sup>	1.08	1.770
15330	03:17:44.47	-62:34:36.8	12.039 <sup>a</sup>	2.7 <sup>b</sup>	G2.5V Hdell <sup>c</sup>	5712 <sup>d</sup>	4.48 <sup>d</sup>	-0.24 <sup>d</sup>	1.01	0.908
15371	03:18:11.14	-62:30:28.6	12.046 <sup>a</sup>	2.7 <sup>b</sup>	G1V <sup>c</sup>	5852 <sup>d</sup>	4.43 <sup>d</sup>	-0.25 <sup>d</sup>	1.07	1.019
15457	03:19:21.54	+03:22:11.9	9.14 <sup>f</sup>	4.5 <sup>b</sup>	G5V <sup>c</sup>	5749 <sup>m</sup>	4.51 <sup>m</sup>	0.08 <sup>m</sup>	0.98	0.847
15510	03:19:53.22	-43:04:17.6	6.043 <sup>f</sup>	0.9 <sup>b</sup>	G6V <sup>c</sup>	5398 <sup>e</sup>	4.41 <sup>e</sup>	-0.41 <sup>e</sup>	0.97	1.067
1599	00:20:01.91	-64:52:39.4	8.587 <sup>f</sup>	4.9 <sup>b</sup>	F9.5V <sup>i</sup>	5977 <sup>n</sup>	4.51 <sup>n</sup>	-0.18 <sup>n</sup>	1.11	0.847
16537	03:32:56.42	-09:27:29.9	3.216 <sup>f</sup>	1.9 <sup>b</sup>	K2V <sup>c</sup>	5050 <sup>h</sup>	4.6 <sup>h</sup>	-0.09 <sup>h</sup>	0.78	0.689
16852	03:36:52.52	+00:24:10.2	13.963 <sup>f</sup>	3.7 <sup>b</sup>	F9IV-V <sup>c</sup>	5971 <sup>d</sup>	4.06 <sup>d</sup>	-0.09 <sup>d</sup>	1.14	2.388
17378	03:43:14.96	-09:45:54.7	9.041 <sup>f</sup>	1 <sup>b</sup>	K0+IV <sup>c</sup>	5144 <sup>o</sup>	3.95 <sup>o</sup>	0 <sup>o</sup>	0.87	3.077
17420	03:43:55.15	-19:06:40.6	13.955 <sup>a</sup>	3 <sup>b</sup>	K2.5V <sup>i</sup>	4930 <sup>p</sup>	4.41 <sup>p</sup>	-0.17 <sup>p</sup>	0.76	1.067
19849	04:15:17.64	-07:38:40.4	4.985 <sup>f</sup>	0.9 <sup>b</sup>	K0.5V <sup>i</sup>	5202 <sup>d</sup>	4.55 <sup>d</sup>	-0.28 <sup>d</sup>	0.86	0.773
2021	00:25:39.20	-77:15:18.1	7.459 <sup>f</sup>	3.4 <sup>b</sup>	G0V <sup>i</sup>	5873 <sup>h</sup>	3.98 <sup>h</sup>	-0.04 <sup>h</sup>	1.08	2.871
22263	04:47:36.21	-16:56:05.5	13.241 <sup>a</sup>	2.9 <sup>b</sup>	G1.5V CH-0.5 <sup>i</sup>	5840 <sup>q</sup>	4.5 <sup>q</sup>	0.03 <sup>q</sup>	1.04	0.867
23311	05:00:48.68	-05:45:03.5	8.848 <sup>a</sup>	1.4 <sup>b</sup>	K3+V <sup>r</sup>	4745 <sup>d</sup>	4.57 <sup>d</sup>	0.19 <sup>d</sup>	0.75	0.738
26394	05:37:08.79	-80:28:18.0	18.28 <sup>a</sup>	2.7 <sup>b</sup>	G0V <sup>i</sup>	6003 <sup>n</sup>	4.42 <sup>n</sup>	0.09 <sup>n</sup>	1.08	1.042
27435	05:48:34.90	-04:05:38.7	15.255 <sup>a</sup>	2.7 <sup>b</sup>	G2V <sup>r</sup>	5733 <sup>n</sup>	4.51 <sup>n</sup>	-0.22 <sup>n</sup>	1.02	0.847
29271	06:10:14.20	-74:45:09.1	10.215 <sup>a</sup>	2.3 <sup>b</sup>	G7V <sup>i</sup>	5569 <sup>d</sup>	4.43 <sup>d</sup>	0.11 <sup>d</sup>	0.96	1.019
3093	00:39:22.09	+21:15:04.9	11.137 <sup>a</sup>	1.8 <sup>b</sup>	K0.5V <sup>c</sup>	5303 <sup>d</sup>	4.56 <sup>d</sup>	0.18 <sup>d</sup>	0.86	0.755
32480	06:46:44.34	+43:34:37.3	16.648 <sup>a</sup>	3.6 <sup>b</sup>	F9V <sup>r</sup>	6064 <sup>j</sup>	4.33 <sup>j</sup>	0.12 <sup>j</sup>	1.14	1.283
32984	06:52:18.37	-05:10:25.3	8.749 <sup>a</sup>	2.7 <sup>b</sup>	K3.5V <sup>r</sup>	4758 <sup>j</sup>	4.5 <sup>s</sup>	-0.07 <sup>t</sup>	0.79	0.867
33277	06:55:18.69	+25:22:32.3	17.47 <sup>a</sup>	2.9 <sup>b</sup>	G0V <sup>r</sup>	5891 <sup>j</sup>	4.36 <sup>j</sup>	-0.18 <sup>j</sup>	1.08	1.197
35136	07:15:50.11	+47:14:25.5	16.867 <sup>a</sup>	2.9 <sup>b</sup>	F9V <sup>r</sup>	5849 <sup>u</sup>	4.26 <sup>u</sup>	-0.33 <sup>u</sup>	1.14	1.507
37606	07:42:57.16	-45:10:18.4	22.473 <sup>a</sup>	4.3 <sup>v</sup>	G8IV-V <sup>i</sup>	5526 <sup>w</sup>	4.1 <sup>w</sup>	0.19 <sup>w</sup>	0.94	2.178
3765	00:48:22.53	+05:17:00.2	7.435 <sup>a</sup>	1.8 <sup>b</sup>	K2V <sup>r</sup>	5015 <sup>d</sup>	4.6 <sup>d</sup>	-0.31 <sup>d</sup>	0.78	0.689
3821	00:49:05.10	+57:48:59.6	5.953 <sup>f</sup>	3.4 <sup>b</sup>	F9V <sup>c</sup>	5904 <sup>m</sup>	4.32 <sup>m</sup>	-0.25 <sup>m</sup>	1.14	1.312
3909	00:50:07.72	-10:38:37.6	15.88 <sup>a</sup>	3.9 <sup>b</sup>	F7V <sup>r</sup>	6203 <sup>x</sup>	4.27 <sup>x</sup>	-0.15 <sup>x</sup>	1.21	1.473
40693	08:18:23.78	-12:37:47.2	12.564 <sup>a</sup>	2.2 <sup>b</sup>	G8+V <sup>i</sup>	5442 <sup>d</sup>	4.53 <sup>d</sup>	-0.02 <sup>d</sup>	0.93	0.809
41926	08:32:52.26	-31:30:09.7	12.182 <sup>a</sup>	1.8 <sup>b</sup>	K1V <sup>c</sup>	5243 <sup>n</sup>	4.46 <sup>n</sup>	-0.41 <sup>n</sup>	0.85	0.951
42808	08:43:18.26	-38:52:59.5	11.186 <sup>a</sup>	2.7 <sup>b</sup>	K2.5V(k) <sup>i</sup>	5005 <sup>d</sup>	4.61 <sup>d</sup>	-0.01 <sup>d</sup>	0.76	0.673
43587	08:52:36.13	+28:19:53.0	12.59 <sup>a</sup>	2.2 <sup>b</sup>	K0IV-V <sup>r</sup>	5270 <sup>p</sup>	4.31 <sup>p</sup>	0.31 <sup>p</sup>	0.95	1.343
43726	08:54:18.19	-05:26:04.3	16.85 <sup>a</sup>	2.4 <sup>b</sup>	G2V <sup>c</sup>	5781 <sup>e</sup>	4.44 <sup>e</sup>	0.12 <sup>e</sup>	1.02	0.996
45333	09:14:20.55	+61:25:24.2	19.659 <sup>a</sup>	4.8 <sup>b</sup>	G0IV-V <sup>r</sup>	5973 <sup>d</sup>	4.13 <sup>d</sup>	0.05 <sup>d</sup>	1.08	2.033
47080	09:35:40.03	+35:48:38.8	11.203 <sup>a</sup>	2.3 <sup>b</sup>	G8Va <sup>c</sup>	5511 <sup>d</sup>	4.46 <sup>d</sup>	0.28 <sup>d</sup>	0.94	0.951
48113	09:48:35.18	+46:01:16.4	18.904 <sup>a</sup>	2.9 <sup>b</sup>	G0.5Va <sup>c</sup>	5872 <sup>d</sup>	4.1 <sup>d</sup>	0.09 <sup>d</sup>	1.08	2.178
48331	09:51:06.68	-43:30:05.9	11.285 <sup>a</sup>	0.9 <sup>b</sup>	K6V(k) <sup>i</sup>	4400 <sup>e</sup>	4.36 <sup>e</sup>	-0.26 <sup>e</sup>	0.65	1.197
49081	10:01:01.02	+31:55:29.0	14.926 <sup>a</sup>	1.8 <sup>b</sup>	G3Va Hdell1 <sup>c</sup>	5753 <sup>m</sup>	4.3 <sup>m</sup>	0.26 <sup>m</sup>	1	1.374
49908	10:11:23.36	+49:27:19.7	4.869 <sup>a</sup>	2.7 <sup>b</sup>	K7V <sup>y</sup>	4131 <sup>z</sup>	4.61 <sup>aa</sup>	0.24 <sup>z</sup>	0.63	0.673
53721	10:59:28.22	+40:25:48.4	13.802 <sup>a</sup>	3.1 <sup>b</sup>	G1-V Fe-0.5 <sup>c</sup>	5894 <sup>d</sup>	4.3 <sup>d</sup>	0.02 <sup>d</sup>	1.07	1.374
544	00:06:36.53	+29:01:19.0	13.779 <sup>a</sup>	3.6 <sup>b</sup>	G8V <sup>r</sup>	5458 <sup>d</sup>	4.52 <sup>d</sup>	0.14 <sup>d</sup>	0.94	0.828
56452	11:34:29.95	-32:50:00.0	9.544 <sup>a</sup>	0.9 <sup>b</sup>	K0-V <sup>i</sup>	5241 <sup>d</sup>	4.59 <sup>d</sup>	-0.37 <sup>d</sup>	0.88	0.705
56997	11:41:03.03	+34:12:09.2	9.579 <sup>a</sup>	2.3 <sup>b</sup>	G8V <sup>c</sup>	5528 <sup>d</sup>	4.53 <sup>d</sup>	-0.05 <sup>d</sup>	0.94	0.809
57443	11:46:32.25	-40:30:04.8	9.292 <sup>a</sup>	2.7 <sup>b</sup>	G2V <sup>i</sup>	5655 <sup>d</sup>	4.44 <sup>d</sup>	-0.29 <sup>d</sup>	1.02	0.996
57757	11:50:41.29	+01:45:55.4	10.929 <sup>f</sup>	3.6 <sup>b</sup>	F9V <sup>ab</sup>	6083 <sup>h</sup>	4.08 <sup>h</sup>	0.24 <sup>h</sup>	1.14	2.281
58576	12:00:44.37	-10:26:41.4	12.697 <sup>a</sup>	1.8 <sup>b</sup>	G8IV <sup>i</sup>	5510 <sup>u</sup>	4.33 <sup>u</sup>	0.25 <sup>u</sup>	0.94	1.283
5862	01:15:10.57	-45:31:55.5	15.177 <sup>a</sup>	4.7 <sup>b</sup>	F9V Fe+0.4 <sup>i</sup>	6111 <sup>ac</sup>	4.36 <sup>ac</sup>	0.17 <sup>ac</sup>	1.14	1.197
61317	12:33:45.09	+41:21:24.4	8.44 <sup>f</sup>	2.8 <sup>b</sup>	G0V <sup>c</sup>	5887 <sup>m</sup>	4.34 <sup>m</sup>	-0.2 <sup>m</sup>	1.08	1.253
62207	12:44:59.68	+39:16:42.9	17.565 <sup>a</sup>	1.8 <sup>b</sup>	F9V Fe-0.3 <sup>r</sup>	5842 <sup>u</sup>	4.33 <sup>u</sup>	-0.5 <sup>u</sup>	1.14	1.283
64394	13:11:52.92	+27:52:33.7	9.129 <sup>f</sup>	4.5 <sup>b</sup>	F9.5V <sup>c</sup>	6034 <sup>m</sup>	4.44 <sup>m</sup>	0.06 <sup>m</sup>	1.11	0.996
64408	13:12:03.47	-37:48:11.3	20.295 <sup>a</sup>	2.7 <sup>b</sup>	G4IV <sup>i</sup>	5670 <sup>o</sup>	3.9 <sup>o</sup>	0.16 <sup>o</sup>	0.99	3.452
64797	13:16:50.67	+17:01:04.1	10.985 <sup>a</sup>	3.3 <sup>b</sup>	K2.5V(k) <sup>r</sup>	5081 <sup>d</sup>	4.62 <sup>d</sup>	-0.16 <sup>d</sup>	0.76	0.658
64924	13:18:24.97	-18:18:31.0	8.555 <sup>f</sup>	1.8 <sup>b</sup>	G6.5V <sup>c</sup>	5537 <sup>e</sup>	4.38 <sup>e</sup>	-0.03 <sup>e</sup>	0.97	1.143
65721	13:28:25.95	+13:46:48.7	17.91 <sup>a</sup>	3 <sup>b</sup>	G4V-IV <sup>ad</sup>	5559 <sup>o</sup>	4.05 <sup>o</sup>	-0.06 <sup>o</sup>	0.99	2.444
68184	13:57:32.10	+61:29:32.4	10.078 <sup>a</sup>	2 <sup>ap</sup>	K3V <sup>ae</sup>	4851 <sup>d</sup>	4.58 <sup>d</sup>	0.11 <sup>d</sup>	0.75	0.721
69972	14:19:05.36	-59:22:37.4	11.841 <sup>a</sup>	0.9 <sup>b</sup>	K3IV <sup>i</sup>	4903 <sup>j</sup>	4.69 <sup>j</sup>	0.32 <sup>j</sup>	0.83	0.560
72659	14:51:23.28	+19:06:02.3	6.733 <sup>a</sup>	3.5 <sup>b</sup>	G7V <sup>r</sup>	5527 <sup>u</sup>	4.6 <sup>u</sup>	-0.13 <sup>u</sup>	0.96	0.689
72848	14:53:24.04	+19:09:08.2	11.51 <sup>f</sup>	3.9 <sup>b</sup>	K0.5V <sup>c</sup>	5291 <sup>u</sup>	4.55 <sup>u</sup>	0.08 <sup>u</sup>	0.86	0.773

HIP	RA	Declination	Dist (pc)	$v\sin i$	Spectral Type	$T_{eff}$	$\log(g)$	[Fe/H]	Mass	Radius
73184	14:57:27.35	-21:24:40.6	5.882 <sup>a</sup>	3.5 <sup>b</sup>	K4V <sup>c</sup>	4744 <sup>j</sup>	4.76 <sup>j</sup>	0.12 <sup>j</sup>	0.72	0.477
75181	15:21:49.57	-48:19:01.1	14.688 <sup>a</sup>	2.4 <sup>b</sup>	G2-V <sup>i</sup>	5664 <sup>n</sup>	4.39 <sup>n</sup>	-0.34 <sup>n</sup>	1.02	1.117
77257	15:46:26.75	+07:21:11.7	11.819 <sup>a</sup>	3.3 <sup>b</sup>	G0-V <sup>c</sup>	5900 <sup>d</sup>	4.17 <sup>d</sup>	-0.01 <sup>d</sup>	1.09	1.854
77358	15:47:29.41	-37:54:56.9	15.26 <sup>a</sup>	1.8 <sup>b</sup>	G7IV-V <sup>i</sup>	5584 <sup>e</sup>	4.4 <sup>e</sup>	0.08 <sup>e</sup>	0.96	1.092
77760	15:52:40.19	+42:27:00.0	15.832 <sup>a</sup>	3.4 <sup>b</sup>	G0V Fe-0.8 CH-0.5 <sup>r</sup>	5776 <sup>u</sup>	3.83 <sup>u</sup>	-0.51 <sup>u</sup>	1.08	4.056
79248	16:10:24.21	+43:49:06.1	17.942 <sup>a</sup>	2.6 <sup>b</sup>	K0V <sup>c</sup>	5388 <sup>j</sup>	4.52 <sup>j</sup>	0.46 <sup>j</sup>	0.87	0.828
79672	16:15:37.13	-08:22:05.7	14.131 <sup>a</sup>	2.7 <sup>b</sup>	G2Va <sup>c</sup>	5814 <sup>q</sup>	4.45 <sup>q</sup>	0.06 <sup>q</sup>	1.02	0.973
7981	01:42:29.95	+20:16:12.5	7.605 <sup>a</sup>	0.1 <sup>b</sup>	K1V <sup>c</sup>	5196 <sup>u</sup>	4.5 <sup>u</sup>	-0.01 <sup>u</sup>	0.85	0.867
80337	16:24:01.24	-39:11:34.8	12.908 <sup>a</sup>	2.2 <sup>b</sup>	G1V CH-0.4 <sup>i</sup>	5858 <sup>n</sup>	4.5 <sup>n</sup>	0.03 <sup>n</sup>	1.07	0.867
80686	16:28:27.80	-70:05:04.8	12.177 <sup>a</sup>	2.4 <sup>b</sup>	F9V <sup>i</sup>	6030 <sup>d</sup>	4.43 <sup>d</sup>	-0.08 <sup>d</sup>	1.14	1.019
8102	01:44:05.13	-15:56:22.4	3.65 <sup>f</sup>	0.9 <sup>b</sup>	G8V <sup>c</sup>	5331 <sup>h</sup>	4.44 <sup>h</sup>	-0.49 <sup>h</sup>	0.94	0.996
81300	16:36:21.18	-02:19:25.8	9.92 <sup>a</sup>	1.6 <sup>b</sup>	K0V(k) <sup>i</sup>	5248 <sup>d</sup>	4.55 <sup>d</sup>	0.01 <sup>d</sup>	0.87	0.773
83389	17:02:36.30	+47:04:47.3	18.294 <sup>a</sup>	1.8 <sup>b</sup>	G8V <sup>af</sup>	5442 <sup>ag</sup>	4.39 <sup>ag</sup>	-0.13 <sup>ag</sup>	0.94	1.117
8362	01:47:44.06	+63:51:11.2	10.043 <sup>a</sup>	0.9 <sup>b</sup>	G9V <sup>r</sup>	5354 <sup>d</sup>	4.53 <sup>d</sup>	0.03 <sup>d</sup>	0.9	0.809
84478	17:16:13.68	-26:32:36.3	5.95 <sup>a</sup>	3.3 <sup>b</sup>	K5V(k) <sup>i</sup>	4600 <sup>d</sup>	4.7 <sup>d</sup>	-0.34 <sup>d</sup>	0.68	0.547
85235	17:25:00.90	+67:18:24.1	12.793 <sup>a</sup>	1.3 <sup>b</sup>	K0V <sup>af</sup>	5327 <sup>d</sup>	4.56 <sup>d</sup>	-0.42 <sup>d</sup>	0.87	0.755
85295	17:25:45.57	+02:06:51.5	7.715 <sup>a</sup>	3.5 <sup>b</sup>	K7V <sup>ah</sup>	3941 <sup>ai</sup>	4.68 <sup>aj</sup>	0.19 <sup>z</sup>	0.63	0.573
86400	17:39:17.02	+03:33:19.7	11 <sup>f</sup>	1.5 <sup>b</sup>	K3-V <sup>c</sup>	4808 <sup>d</sup>	4.56 <sup>d</sup>	-0.08 <sup>d</sup>	0.75	0.755
86796	17:44:08.72	-51:50:00.9	15.605 <sup>a</sup>	3.8 <sup>b</sup>	G3IV-V <sup>i</sup>	5845 <sup>h</sup>	4.27 <sup>h</sup>	0.35 <sup>h</sup>	1	1.473
88601	18:05:27.21	+02:30:08.8	5.123 <sup>a</sup>	3.7 <sup>b</sup>	K0-V <sup>c</sup>	5394 <sup>d</sup>	4.56 <sup>d</sup>	0.07 <sup>d</sup>	0.88	0.755
88745	18:07:01.61	+30:33:42.7	15.739 <sup>a</sup>	2.8 <sup>b</sup>	F9V mw <sup>ak</sup>	6049 <sup>d</sup>	4.18 <sup>d</sup>	-0.58 <sup>d</sup>	1.14	1.812
88972	18:09:37.65	+38:27:32.1	11.096 <sup>a</sup>	0.6 <sup>b</sup>	K2V <sup>r</sup>	5048 <sup>d</sup>	4.55 <sup>d</sup>	-0.2 <sup>d</sup>	0.78	0.773
89042	18:10:26.26	-62:00:10.0	17.753 <sup>a</sup>	4.2 <sup>b</sup>	G0V <sup>i</sup>	5950 <sup>al</sup>	4.31 <sup>al</sup>	0.01 <sup>al</sup>	1.08	1.343
910	00:11:15.91	-15:28:02.4	17.99 <sup>a</sup>	4.8 <sup>b</sup>	F8V Fe-0.8 CH-0.5 <sup>i</sup>	6169 <sup>u</sup>	4.07 <sup>u</sup>	-0.34 <sup>u</sup>	1.18	2.334
95447	19:24:57.77	+11:56:34.3	14.959 <sup>a</sup>	1.9 <sup>b</sup>	G7IV Hdell <sup>c</sup>	5530 <sup>o</sup>	4.05 <sup>o</sup>	0.34 <sup>o</sup>	0.95	2.444
96100	19:32:20.59	+69:39:55.4	5.755 <sup>f</sup>	1.8 <sup>b</sup>	K0V <sup>c</sup>	5318 <sup>u</sup>	4.59 <sup>u</sup>	-0.15 <sup>u</sup>	0.87	0.705
97944	19:54:17.82	-23:56:24.3	14.107 <sup>a</sup>	1.8 <sup>b</sup>	K2IV(k) <sup>i</sup>	4600 <sup>am</sup>	4.56 <sup>am</sup>	0.25 <sup>an</sup>	0.9	0.755
98036	19:55:18.77	+06:24:28.6	13.699 <sup>f</sup>	2.7 <sup>b</sup>	G8IV <sup>c</sup>	5223 <sup>o</sup>	3.86 <sup>o</sup>	-0.17 <sup>o</sup>	0.94	3.785
98767	20:03:36.95	+29:53:53.1	16.014 <sup>a</sup>	0.8 <sup>b</sup>	G7IV-V <sup>i</sup>	5606 <sup>ao</sup>	4.44 <sup>ao</sup>	0.25 <sup>ao</sup>	0.96	0.996
99240	20:08:41.86	-66:10:45.6	6.108 <sup>f</sup>	2 <sup>b</sup>	G8IV <sup>i</sup>	5566 <sup>e</sup>	4.24 <sup>e</sup>	0.32 <sup>e</sup>	0.94	1.578
99825	20:15:16.58	-27:01:57.1	8.799 <sup>a</sup>	0.6 <sup>b</sup>	K2+V <sup>i</sup>	5104 <sup>d</sup>	4.54 <sup>d</sup>	0.06 <sup>d</sup>	0.77	0.791

## 2.2.6 Other Simulation Inputs

We specify telescope size, available survey time (in fractions of a year), and the following instrument parameters: wavelength range, spectrograph resolution, overall efficiency, target RV precision photon noise, and target spectroscopic SNR-phot per resolution element in Table 2.1. The remaining parameters, all related to the detectors such as read noise and dark current (see Table 2.4), were kept the same across architectures. From these parameters, we calculated estimated exposure times for all stars for each telescope/site/instrument combination at an airmass of 1.0154 (10 degrees off zenith) as an intermediate step. These estimated exposure times were then scaled by the dispatch scheduler to calculate realized exposure times to achieve the desired precision. We calculated two sets of exposure times – one that accounted for only the desired photon noise RV precision, and one that met both the desired photon noise RV precision and the spectroscopic SNR-phot per resolution element (whichever was longer), to determine which requirement was driving the simulated exposure times and consequently the achieved survey cadence. The former is driven by the required RV precision, whereas the latter is driven by the spectroscopic (as opposed to temporal) characterization of stellar activity – e.g. individual spectral line analyses.

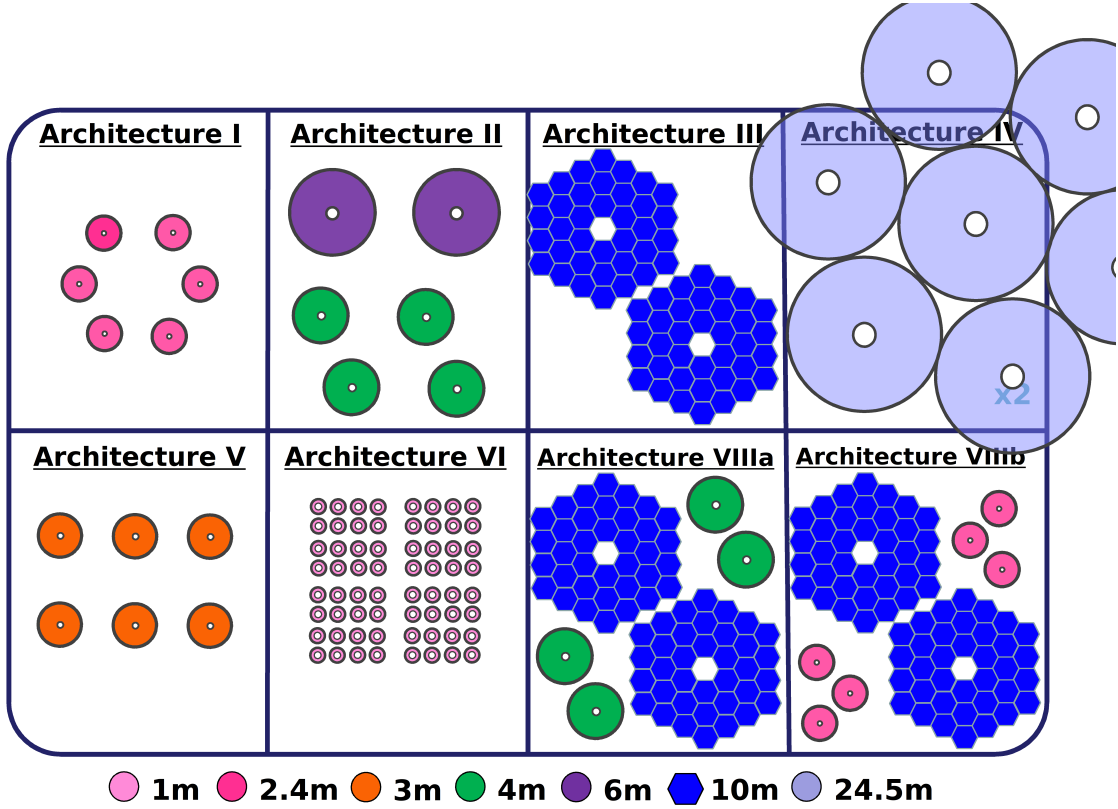


Figure 2.5: Representative illustration of number and diameter of telescope in the architectures.

Table 2.4: Notional detector properties derived from NEID’s CCDs as a representative example. These values were used for all architecture simulation spectrograph assumptions, both the defined and baseline instruments.

Well Depth	Gain	Read Noise	Dark Current	Resolution Element	Readout
90000 e-	0.704225 ADU/e-	4.5 e-	3 e-/hour	5 pixels	30 s

<sup>a</sup>[83], <sup>b</sup>[84], <sup>c</sup>[85], <sup>d</sup>[86], <sup>e</sup>[87], <sup>f</sup>[88], <sup>g</sup>[89], <sup>h</sup>[90], <sup>i</sup>[91], <sup>j</sup>[92], <sup>k</sup>[93], <sup>l</sup>[94], <sup>m</sup>[95], <sup>n</sup>[96], <sup>o</sup>[97], <sup>p</sup>[98], <sup>q</sup>[99], <sup>r</sup>[100], <sup>s</sup>[101], <sup>t</sup>[93], <sup>u</sup>[102], <sup>v</sup>[103], <sup>w</sup>[104], <sup>x</sup>[105], <sup>y</sup>[106], <sup>z</sup>[107], <sup>aa</sup>[108], <sup>ab</sup>[109], <sup>ac</sup>[110], <sup>ad</sup>[111], <sup>ae</sup>[112], <sup>af</sup>[113], <sup>ag</sup>[114], <sup>ah</sup>[115], <sup>ai</sup>[116], <sup>aj</sup>[117], <sup>ak</sup>[118], <sup>al</sup>[119], <sup>am</sup>[120], <sup>an</sup>[121], <sup>ao</sup>[122], <sup>ap</sup> Assumed

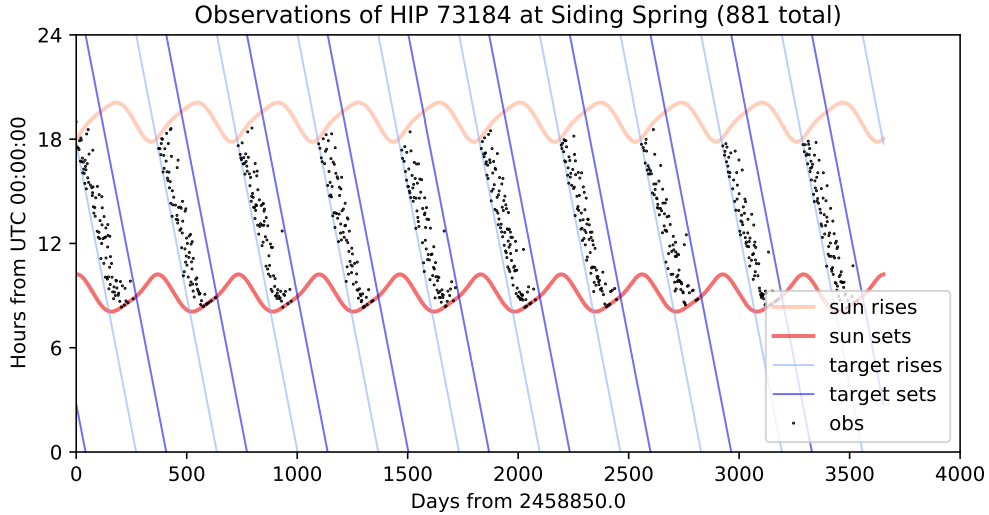


Figure 2.6: Observations of HIP 73184 (HD 131977) in the the architecture I simulation at Siding Spring Observatory. Local sunrise/set, star rise/set, and observation times for each day are shown.

### 2.2.7 Simulation Outputs

We generate outputs from both the exposure time calculator (ETC) and the dispatch scheduler. The ETC outputs are: Time observing with the shutter open, total time on a target including readouts, the number of exposures, and expected RV precision and SNR-phot given its inputs and constraints. The dispatch scheduler outputs are: local rise/set times of the sun and target stars, site weather conditions (if a night was usable or not), and observation timeseries of the target stars.

Radial velocity time-series can be generated from the observation times of each star, although that was not done here for all architectures and telescope combinations. In Figures 2.6, 2.7, and 2.8, we show a representative cadence and RV time-series. The full data outputs are available upon request

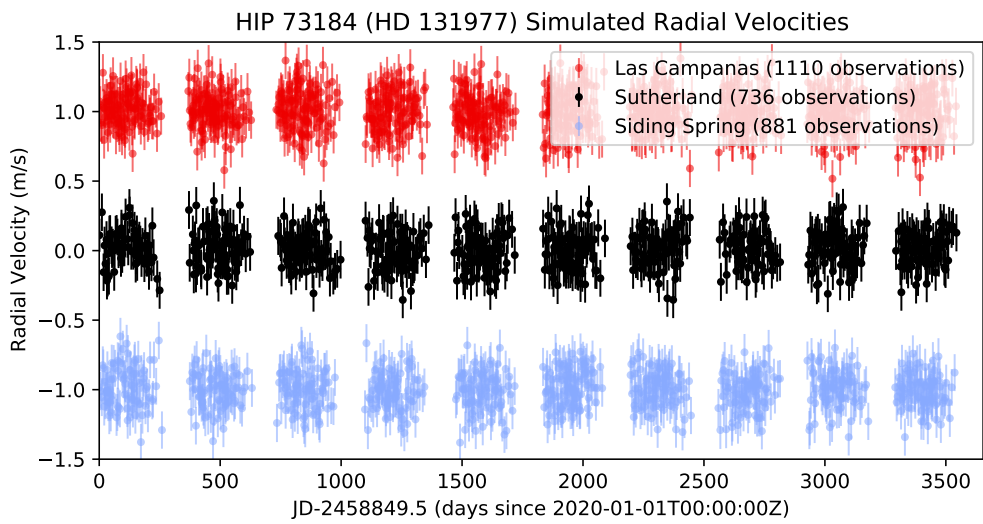


Figure 2.7: Simulated RV time-series for HIP 73184 (HD 131977) for Architecture I as observed by the three telescopes in its hemisphere (one each at Las Campanas, Sutherland, and Siding Spring). This star was chosen, as it has the median number of observations (2724) for the architecture. Note, only “white” noise is included in this simulation, despite the apparent correlated noise by eye during some seasons. The appearance of correlated noise could be partially due to the variable single measurement uncertainties from airmass extinction for a fixed exposure time over the course of a season.

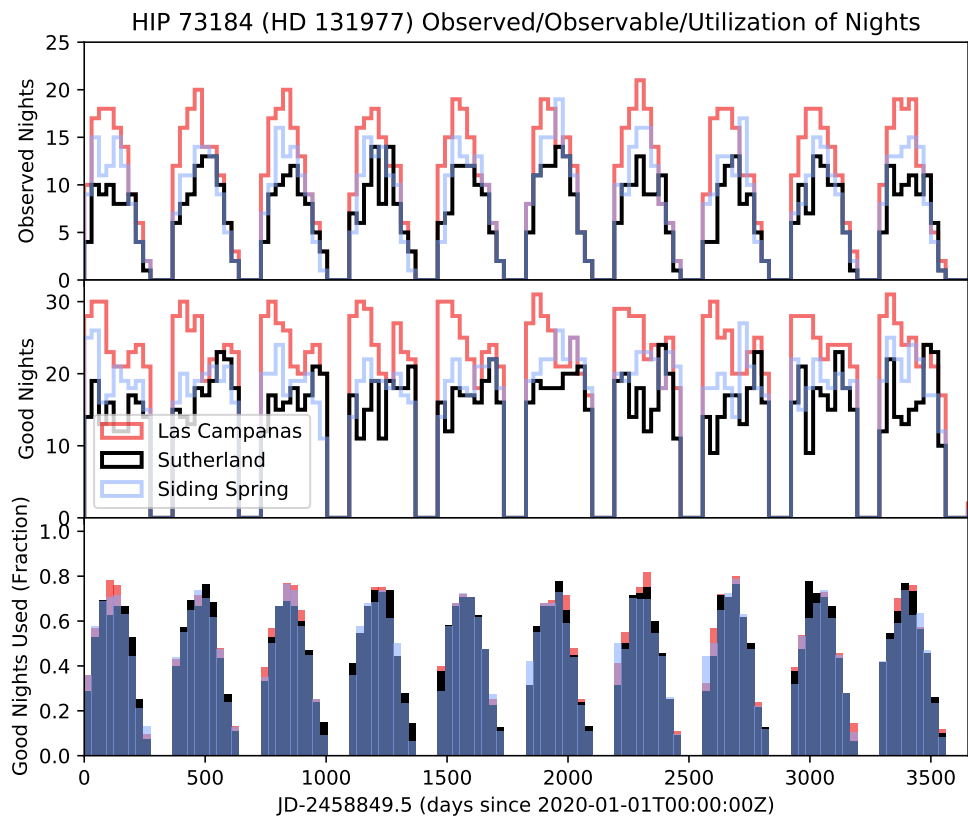


Figure 2.8: Simulated observation cadence and nightly availability for HIP 73184 (HD 131977) for Architecture I observed by three telescopes (one each at Las Campanas, Sutherland, and Siding Spring). Observations here are binned into 30.4375 day “months”; actual observations were never more than 1/night.

## 2.3 Results: Architecture Exposure Times and Cadences

In this Section, we present summaries of the simulated radial velocity surveys for each of the architectures in turn. For each architecture, we present PDFs and CDFs of the stellar exposure times and number of observations of each star. These PDFs and CDFs are presented both for each telescope individually, and for certain combinations of telescopes within a given architecture. The 2/4/6 telescope combinations use the same number of telescopes in each hemisphere (1, 2, or 3), and we select the “best” ones first, e.g. those with the highest number of observations per star due to the different weather statistics. The best two sites are Mauna Kea and Las Campanas, then Kitt Peak and Sutherland, then Calar Alto and Siding Spring based upon the assumed weather statistics in Figure 2.2.1. This appeared to be consistent across all simulations of all architectures.

Second, we include PDFs and CDFs of the fraction of observable days during which each target star was observed. We bin by Julian date as opposed to the local “night”, which varies for each site in the global network.

Third, we compute and present theoretically optimal estimates of the achievable SNR-detect for the detection of a  $K = 0.1$  m/s planet, and the corresponding theoretical minimum detectable velocity semi-amplitude (for an SNR-detect = 10) of a planet as per Equation 2.1. For SNR-detect=10, the false alarm probability is formally vanishingly small, and thus one may presume too conservative: assuming a normal distribution about  $K \pm \sigma'$ , where  $\sigma' = \sigma/\sqrt{N_{\text{obs}}/2}$  from Equation 2.1, and evaluating the probability that  $K \leq 0$ . However, SNR-detect=10 is nonetheless a good approximate order-of-magnitude heuristic for evaluating whether or not we have a statistically robust detection; for example, the *Kepler* mission used a SNR=7.1 threshold for photometric transit detection threshold to balance the number of false-positives to bona-fide signals while still maintaining sensitivity to smaller planets, albeit with a sample size several orders of magnitude larger [123, 124]. Additionally, SNR-detect=10 in the velocity semi-amplitude is the precision recommended for a 10-20% mass determination for interior and atmospheric characterization [125, 126].

Furthermore, these estimates follow the idealized circular orbit and uniform cadence as described in §2.1, with the photon noise and instrument noise added in quadrature for the  $\sigma$  term. Future injection and recovery tests, combined with stellar activity models, could explore the impact our realistic cadences have on survey sensitivity, but are beyond the scope of the analysis presented herein. [52] in particular explores the impact of correlated noise from stellar activity on our results. Finally, for all of the above, we compute summary statistics for the distribution of these values within an architecture (e.g. median, quartiles, 5<sup>th</sup> and 95<sup>th</sup> percentiles), which we use for the overall comparisons of the performance across all architectures in §2.4.

### 2.3.1 Per-Architecture Comments

For architecture IIa, we only simulate the 6-m telescopes at Mauna Kea and Las Campanas. For the 4-m telescopes (Kitt Peak, Calar Alto, Sutherland, And Siding Spring), we re-use the simulations from architecture IIb; hence the identical PDFs and CDFs.

For architecture VIIIA, not all combinations of large and small telescopes are shown. In particular, the 2 and 4 small telescope cases (with and without large telescopes) are not shown to reduce clutter.

The higher RV precision requirements of the 10-m telescopes result in fairly similar exposure times compared to the 3.5-m apertures with lower RV precision requirements. Consequently, the 10-m apertures have a similar number of observations per star per usable night, despite the larger apertures. However, given the smaller time allocation available on the 10-m apertures, this results in an overall lower number of observations per star for those telescopes.

Architecture VIIIB is broadly similar to architecture VIIIA, though the small telescopes are six 2.4 m telescopes (comparable to architecture I), instead of four 3.5 m telescopes (comparable to architecture IIa). For legibility, in the plots that follow, only the small (2.4-m) telescopes are shown in the exposure time plots. The simulations of the 10-m telescopes from architecture VIIIA are reused here. Again as in architecture VIIIA, not all large/small

telescope combinations are shown. Additionally, the detection calculations consider the differing instrument sensitivities using equation 2.2.

### **2.3.2 Example Architecture Results**

For clarity, only the results from Architecture I are shown here. The results from all other architectures are in Appendix [2.7](#).

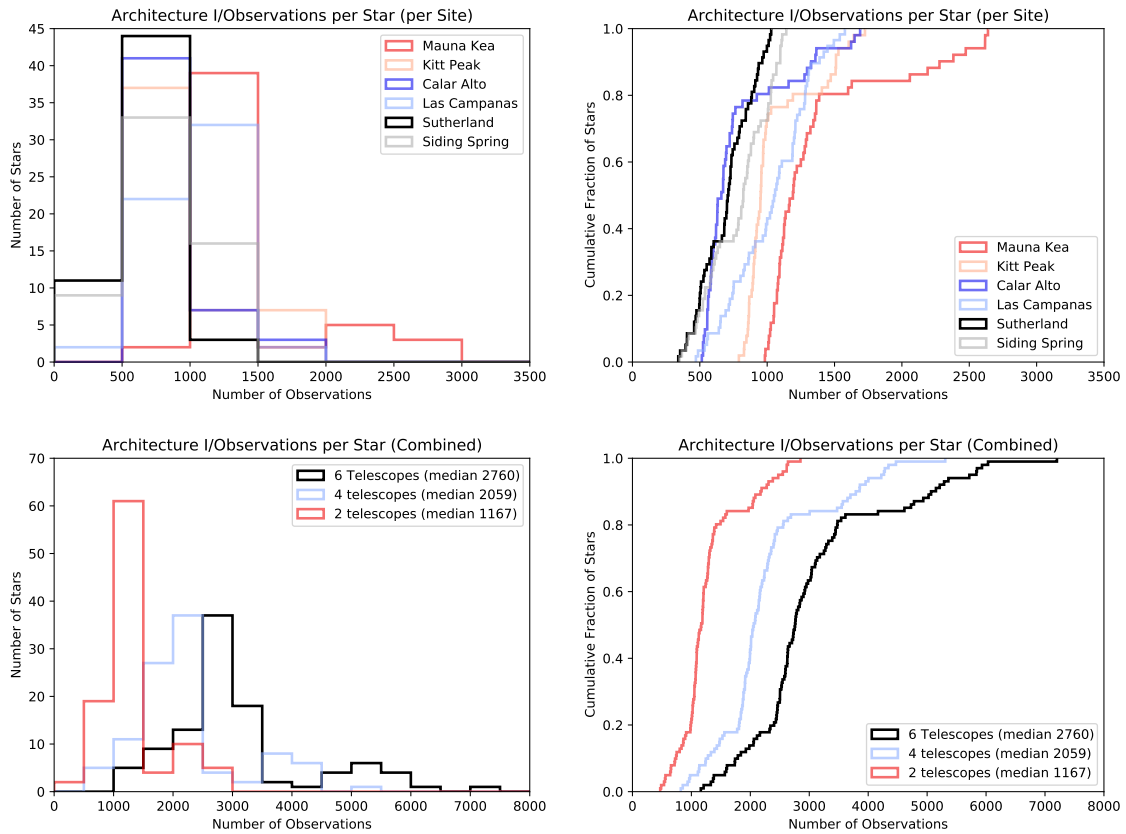


Figure 2.9: Histograms of how often a given star was observed. Individual sites are shown (top), as well as groupings of different sites (bottom), with the 6 telescope grouping being the full architecture.

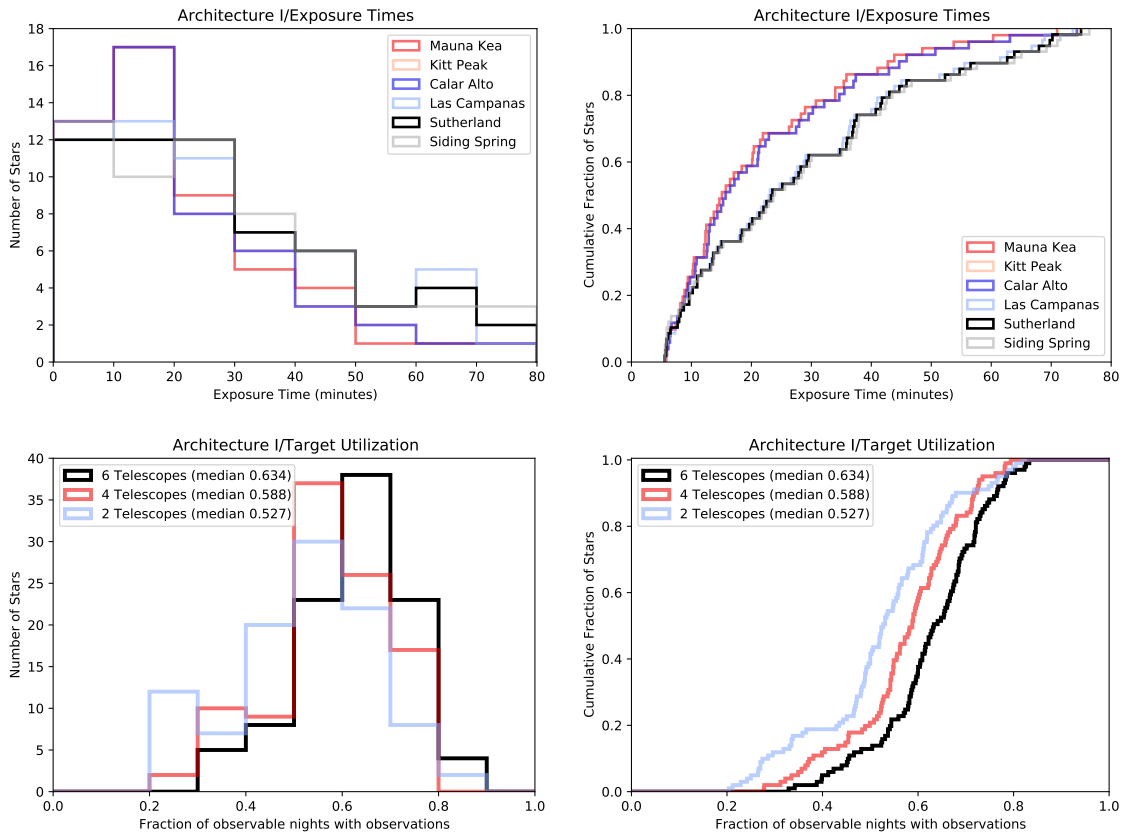


Figure 2.10: Top: Histograms of exposure times per star calculated individually at each site. Bottom: how “efficiently” each star was observed. That is, for what fraction of nights where a star could be observed from at least one site it was observed at least once.

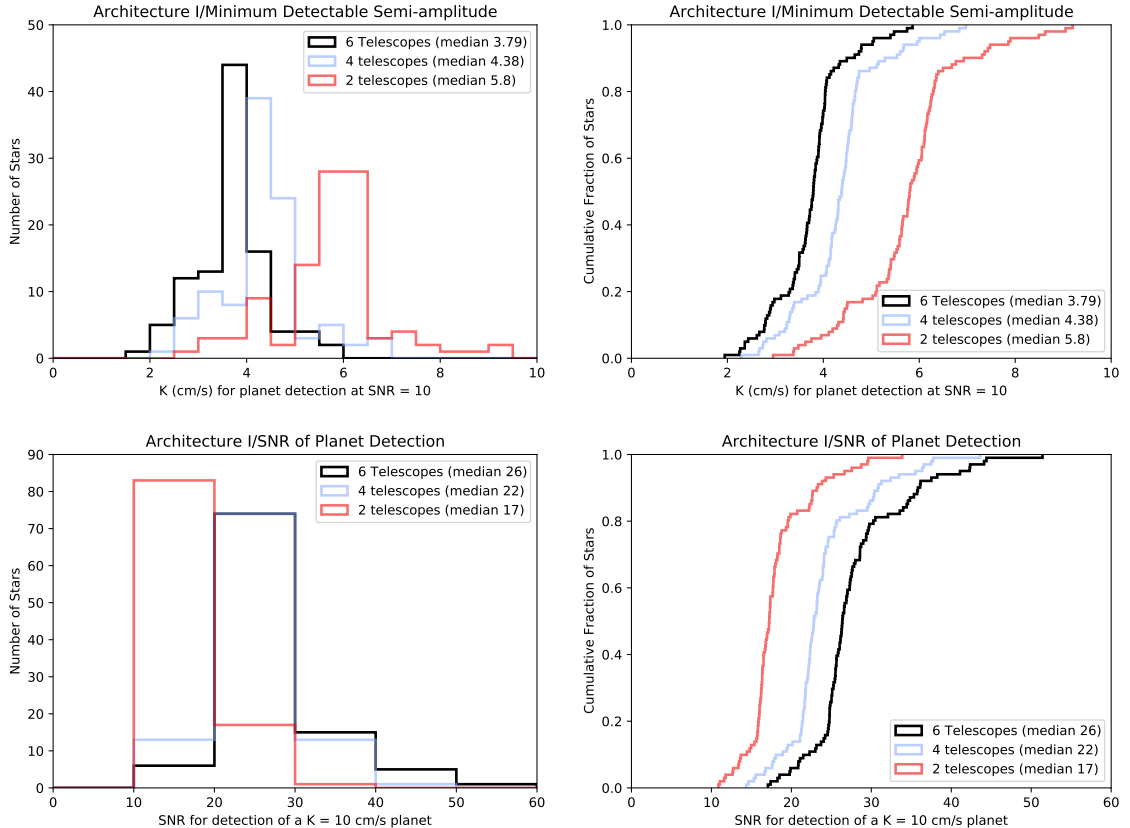


Figure 2.11: Histograms of our sensitivity calculations from the observations. Top: smallest semi-amplitude  $K$  for which a planet with a period much shorter than our 10 year survey could be found at an SNR-detect of 10. Bottom: The SNR-detect at which a planet with a period much shorter than our 10 year survey could be detected at if it had a semi-amplitude of 10 cm/s. In both cases, these values are calculated from equation 2.1.

## 2.4 Results: Architecture Comparison

In this section we present our key findings from a comparison between architectures in our survey simulations. First, we present a summary of the number of observations per star for each architecture, summed across all telescopes within an architecture (Figure 2.12). The baseline case with the baseline spectrometer can be considered as an (aperture  $\times$  time allocation) figure of merit, while the others leverage particular defined spectrograph specifications and SNR-phot and RV precision optimizations as listed in table 2.1.

Second, we present a cross-architecture summary of the fraction of observable days during which each target star was observed; we use the same binning procedure as in section 3. This figure of merit represents the effective achieved cadences of each architecture given the size of the target list. Third, we present a cross-architecture summary of the maximum (photon noise) SNR-detect for the detection of a  $K = 0.1$  m/s planet, and minimum (photon noise) detectable semi-amplitude for an SNR-detect = 10 planet, per equations 2.1 and 2.2. This simple photon noise metric we have adopted represents a theoretical optimistic limit to what can be achieved in a real survey impacted by instrumental systematics, stellar activity, and other RV noise terms, but offers the most straightforward and direct means for assessing how the number of observations per star achieved for a given architecture maps to exoplanet sensitivity. The impacts of correlated noise on RV survey detection efficiency is the subject of follow-on work. Finally, in Figure 2.14 we show the median detectable semi-amplitude  $K$  and median SNR-detect for a  $K = 0.1$  m/s for each architecture. These are directly anti-correlated and correlated with the achieved number of observations per star for a given architecture in Figure 2.12, as might be expected.

From these figures of merit, we can reach several conclusions. First, the minimum SNR-phot per spectral resolution element requirements (for spectroscopic characterization of stellar activity from line-by-line analyses) did not significantly increase exposure times relative to the required photon noise single measurement RV precision. In other words, they were approximately equivalent requirements. Second, whether or not an architecture

achieves nightly cadence is determined largely by the collective telescope aperture, as might be expected. In the case of architecture VIIIb, the differences in specified surveys RV photon noise precision and time allocation of the 10-m telescopes also had significant effects. All architectures come close to or slightly exceed achieving an effectively nightly cadence for the specified target list, but that requires three telescope per hemisphere in order to do so; e.g. the typical cadence for a single telescope site within an architecture  $\sim 3$  days, given the assumptions, target list size, and this level of desired RV precision. Third, the differences in number of observations between sites in a given hemisphere correlates with number of clear nights, as might be expected. Future optimizations of a simulated RV survey could sculpt target lists and dynamically set priorities on a given telescope in a given hemisphere depending on the weather conditions at other sites.

Fourth, some stars are rarely observed for various reasons (right ascension, declination, and/or long exposure time), and they are least observed by telescopes with limited time allocation; e.g. the minimum outliers in the box-and-whiskers plots of Figures 2.12 and 2.13. In this case, adding more telescopes increased the fraction of observable nights used. A more complex target prioritization scheme than the simple combination combination of hour angle and time since last observation metric used here will be necessary for some targets in order to achieve a more uniform number of observations per star. By comparison, architectures that were “efficient” with short exposure times were able to observe almost every available star every night. In that case, adding more sites increased the number of observations, but not the fraction of observable nights used.

Finally, an efficient RV survey will need to minimize target slew and acquisition time, particularly for larger aperture telescopes. We consider the following limiting survey case: if all of the exposure times are limited by p-mode oscillation time-scales and not photon noise or SNR-phot exposure time requirements, then each star would have a five minute target dwell time (see §2.2.3). Taking into consideration weather losses, slew and acquisition overhead, this limiting scenario would result in a survey with approximately  $\sim 2500$  observations on average per star per telescope. Thus, for a typical architecture with three

telescopes per hemisphere, a p-mode oscillation time-scale limited exposure time survey would achieve  $\sim$ 7500 observations per star. This number of observations is achieved for some of the most frequently observed targets in the architectures with  $>4$ -m apertures (IIa, IIb and VIIIa, VIIIb); for these telescopes and targets, the RV survey performance is limited by their minimum dwell times. However, we see that for the majority of the survey targets and architectures, even for the larger apertures, we are not limited by target dwell time, but rather the photon noise precision and SNR-phot per resolution element exposure time requirements at this level of RV precision. This is distinctly different than the era of 1–3 m/s RV surveys, where the desired photon noise precision on large-aperture telescopes can be achieved within five minutes for most nearby, bright stars.

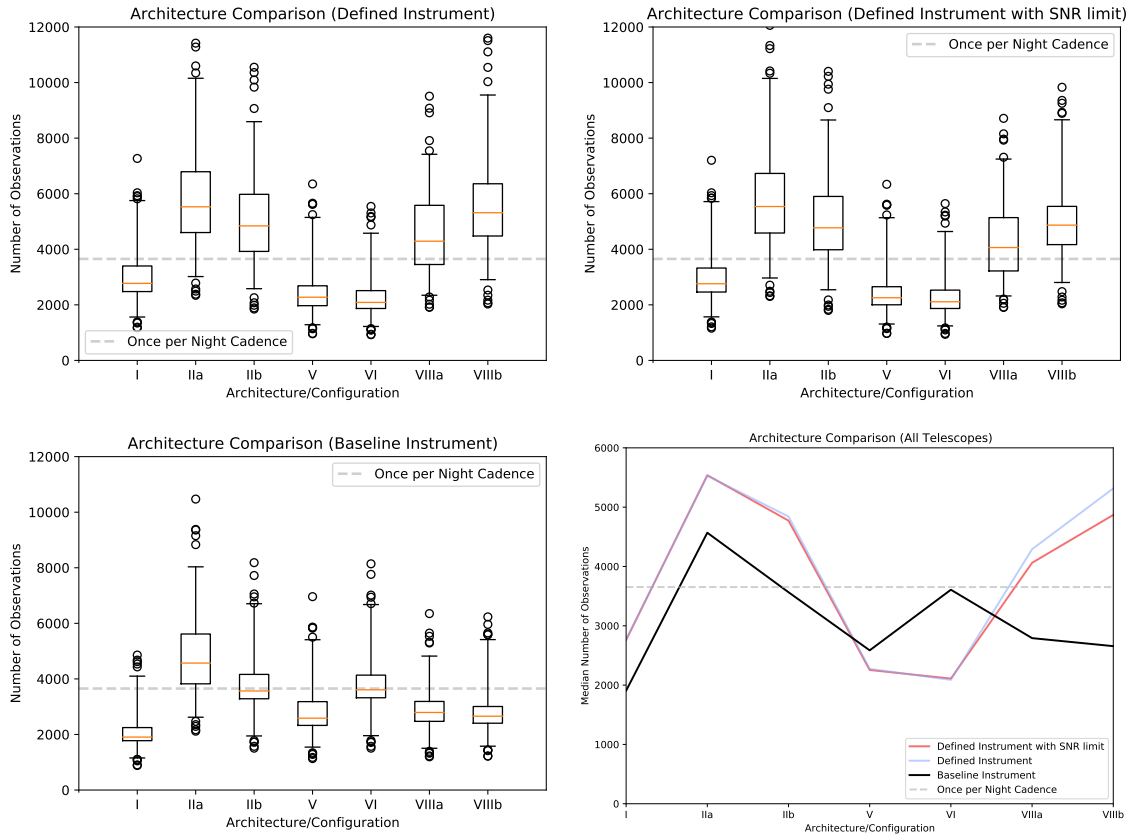


Figure 2.12: Top Left, Top Right, Bottom left: Comparison of the distribution of the number of observations between each architecture presented in §2.2.4 for the three spectrograph assumptions respectively: the architecture-defined spectrograph with a RV precision photon noise requirement and no minimum SNR-phot per spectral resolution element requirement (Top Left), the architecture-defined spectrograph with both a RV precision photon noise requirement and a minimum SNR-phot per spectral resolution element requirement (Top Right), and the baseline instrument spectrograph with only a RV precision photon noise requirement and no minimum SNR-phot per spectral resolution element requirement (Bottom Right). The boxes show the 25th/75th percentile, with the median marked in orange. The whiskers extend from the 5th to the 95th percentile, and the circles the stars below the 5th or above the 95th percentile. For all architectures, the number of observations is summed across all telescopes for the specified architecture. Bottom Right: Comparison of the median number of observations between each architecture presented in §2.2.4 for the three spectrograph and survey requirements combination assumptions considered: the architecture-defined spectrograph with both a RV precision photon noise requirement and a minimum SNR-phot per spectral resolution element requirement (red line), the architecture-defined spectrograph with only a RV precision photon noise requirement and no minimum SNR-phot per spectral resolution element requirement (blue line), and a baseline instrument spectrograph with only a RV precision photon noise requirement and no minimum SNR-phot per spectral resolution element requirement (black line). The number of observations from an effective cadence of once per night per architecture (3653 epochs) is shown as a dashed horizontal line.

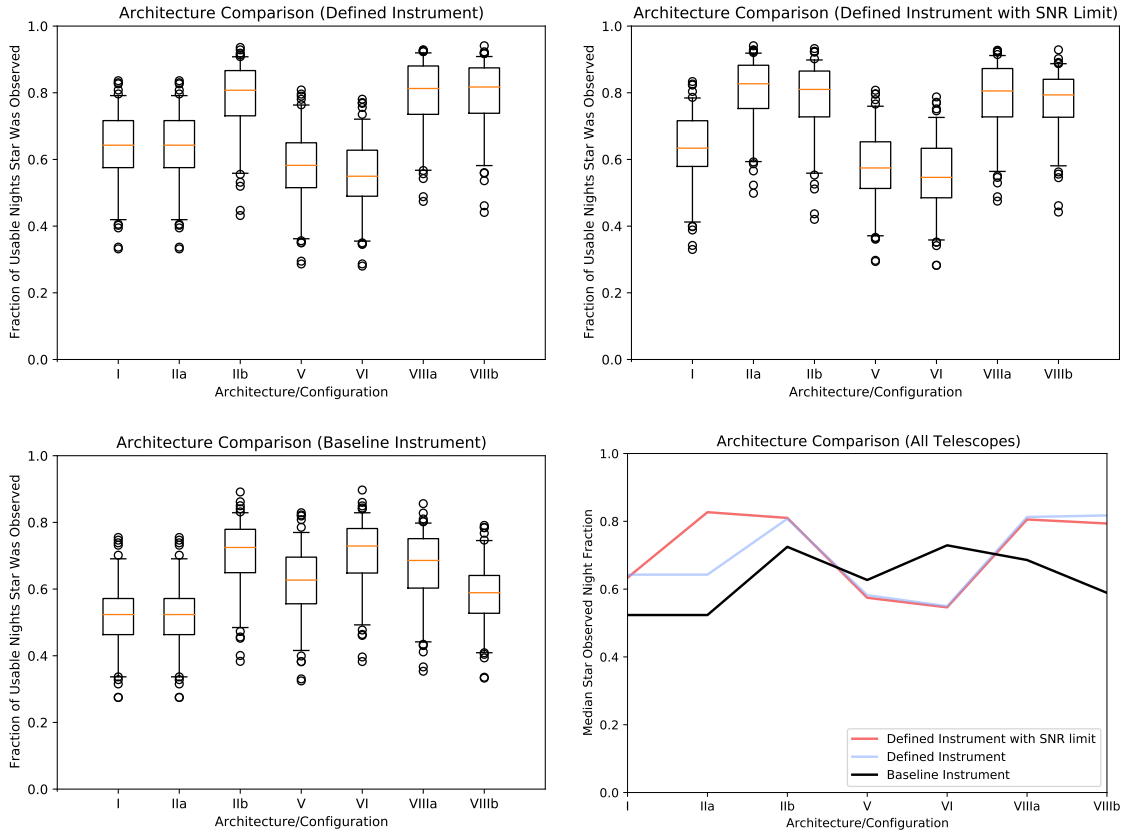


Figure 2.13: Comparison across architecture simulations for the observable nights fraction: the number of nights in which a star is observed divided by the number of nights that star could be observed. A value of 1 means that for every night a star is observable by at least 1 telescope (e.g.:a telescope had time allocated, was not weathered out, and the star was above the pointing limits), at least 1 or more of the telescopes in the architecture does observe it in our simulations. If more than 1 telescope observes the same star on the same night, that star does not get double-counted, so the maximum possible fraction is 1.0. Given that each telescope site is modeled independently, we do not optimize this quantity (e.g., we do not prioritize a particular star at a given telescope higher if the other 2–5 telescopes are weathered out). The three box plots are for the distribution of observation fractions under different spectrograph instrument configurations as in Figure 2.12, while the line graph shows the medians for all. The color scheme is the same as Figure 2.12 as well. The observable nights fraction is an approximate comparison of the survey efficiency for the given target list. No star in any architecture is observed for 100% of possible nights.

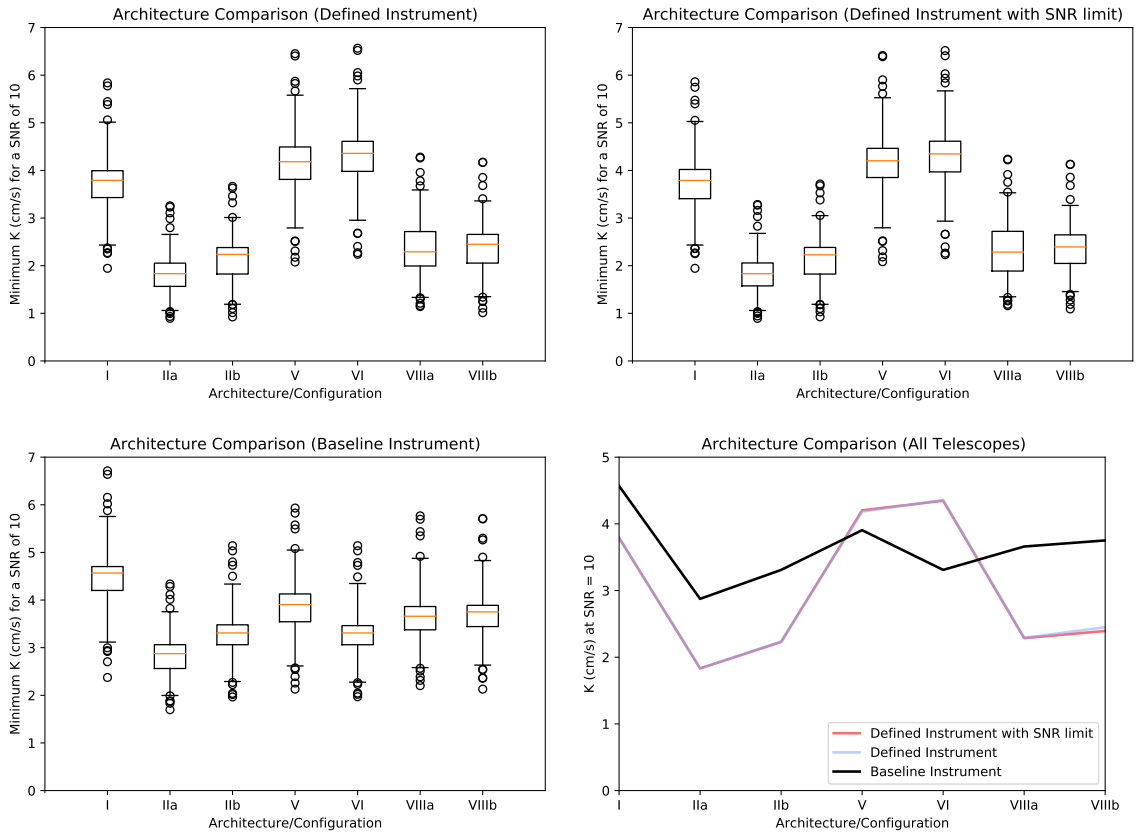


Figure 2.14: Comparison across architecture simulations for minimum reflex velocity semi-amplitude sensitivity at a nominal SNR-detect of 10, as inferred from equations 2.1 and 2.2 for the number of observations per star and architecture single measurement precision. The box plots show the distribution of target stars under the different instrument configurations, while the line graph shows just the medians for all configurations, in the same layout as in Figure 2.12. Lower values are better, as they indicate sensitivity to smaller and/or more distant planets.

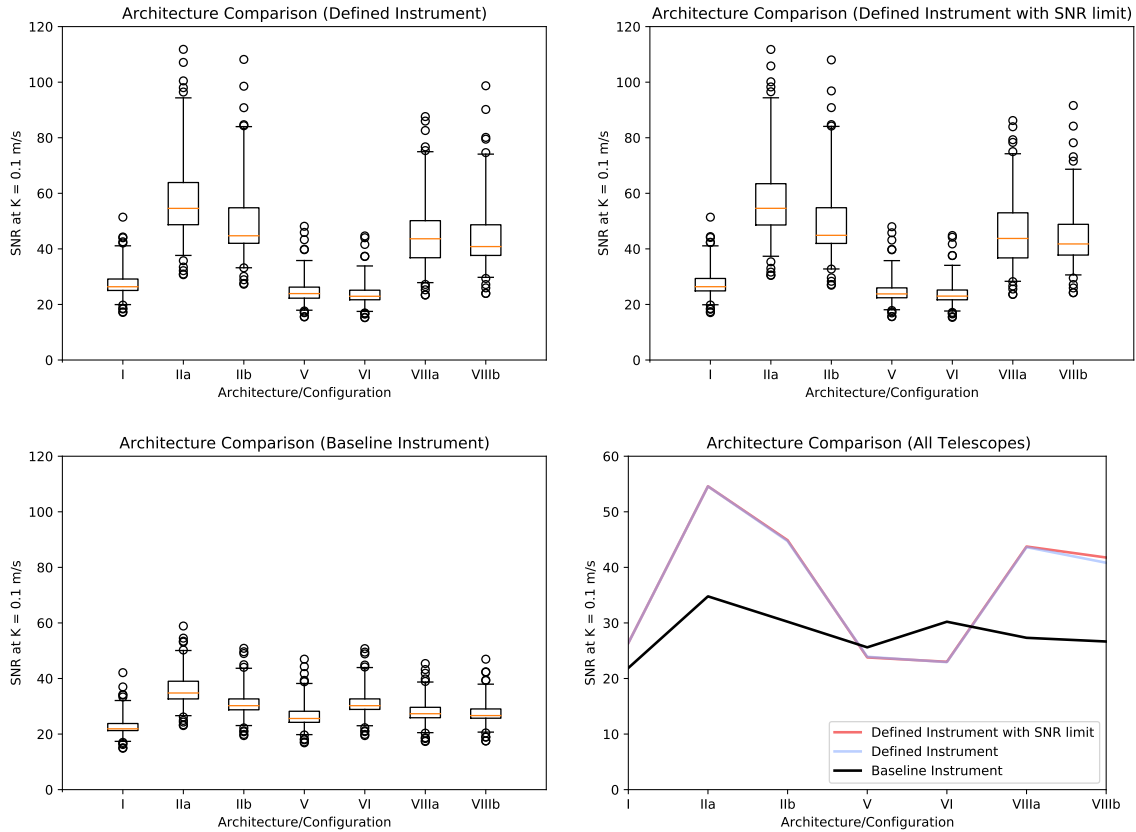


Figure 2.15: Comparison across architecture simulations for the maximum signal to noise ratio (SNR-detect) for a planet detection at a nominal reflex velocity semi-amplitude of 0.1 m/s, as inferred from equations 2.1 and 2.2. The box plots show the distribution of target stars under the different instrument configurations, while the line graph shows just the medians for all configurations, as in Figure 2.12. Higher values are better, as they indicate stronger detections of a planet at the nominal semi-amplitude.

### 2.4.1 P-mode Oscillation timescale

In the above analysis, we did not take the p-mode oscillation time into account as a function of spectral type. To investigate the effect that varying p-mode oscillation times have on our results, we re-ran the simulations with the minimum exposure time set to 10 minutes. One would naively think that doubling the p-mode oscillation time would halve the number of observations per target. However, because of the 5-minute overhead time for slewing and target acquisition, a better naive assumption would be a decrease of 33% when sufficient photons are available to reach the desired precision/SNR-phot within the oscillation time.

Smaller telescope architectures see minimal impact on the number of observations per target, as they already have longer exposure times. For the larger architectures (6 and 10 m class), we observe a change of about 25% in the median number of observations per star. This is because many of our fainter stars already have exposure times between 5 and 10 minutes. Last, even with a 25% change in the number of observations per target, this results in only a  $\sim$ 5-10% effect in semi-amplitude sensitivity, as this goes with the square root of the number of observations. As a consequence, our results are relatively insensitive to choice of p-mode oscillation timescale to within a factor of about 10%.

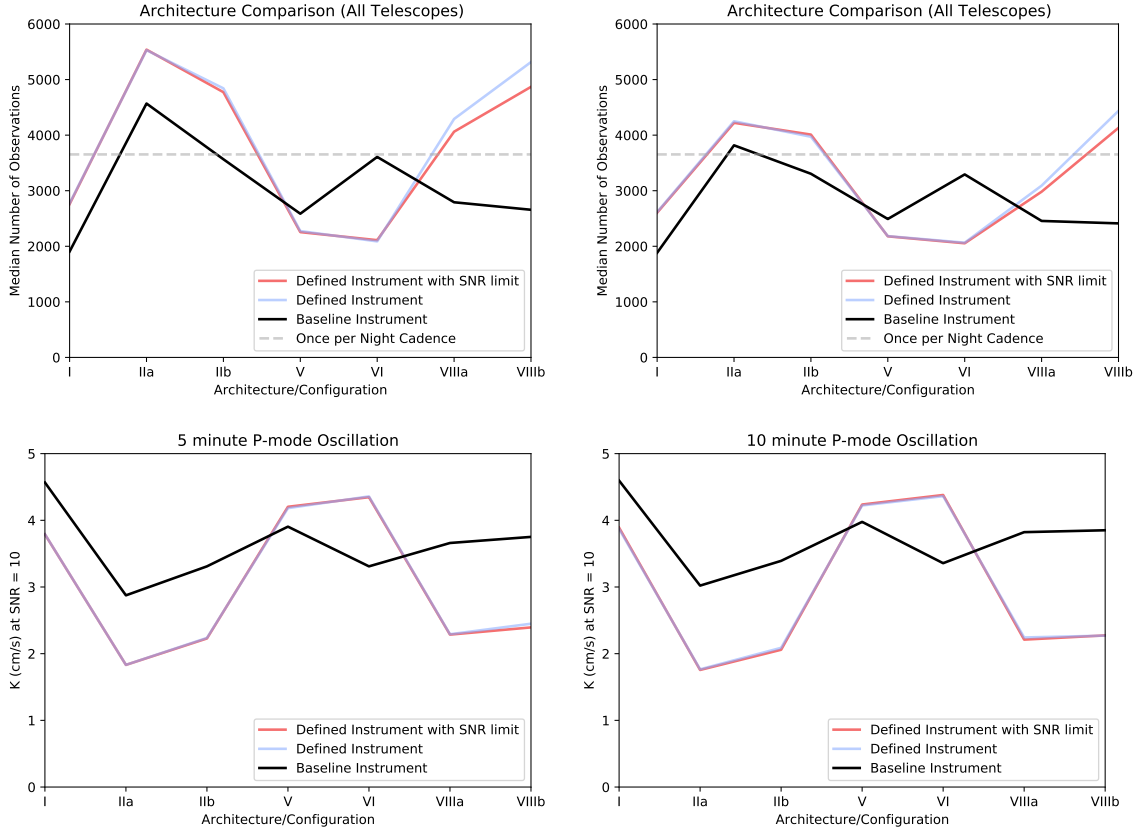


Figure 2.16: Comparison across architecture simulations and P-mode oscillation assumptions for median number of observations (top), and minimum reflex velocity semi-amplitude sensitivity (bottom). The 5 minute (left) and 10 minute (right) graphs use the same vertical scale for ease of comparison.

## 2.5 Discussion

In this section, we discuss the relative performance of the architectures simulated herein, and we present an assessment in §2.5.1 of the impact of our survey simulation assumptions on our results. First, using the baseline instrument spectrograph for all architectures, architecture IIa has the largest median number of observations per star due to having the largest collecting area (on average). Architectures IIb and VI are close behind, with I, V, and VIII resulting in the fewest median number of observations per star. The sensitivity and SNR-detect estimates follow from the number of observations per star; however the differences are more muted from these on account of the scaling with the square root of the

number of observations. For the architecture-defined instruments, precision and wavelength coverage choices can have a large (about factor of 2) effect on number of observations per star. Including the instrument variations increase the spread in the number of observations per star and sensitivity estimates, with the architectures forming two distinct groups. Architectures IIa, IIb, VIIa, and VIIb are all in the high cadence/efficient/high sensitivity group, while architectures I, V, and VI are in the low sensitivity group for the reasons that vary between them – telescope aperture, spectrograph efficiency, spectral grasp, etc. As might be expected, larger apertures can compensate for lower throughput and/or spectral grasp, and vice-versa.

Second, efficient (close to nightly cadence) observations are improved with additional telescopes at additional sites, up to a point. The peak achieved median survey cadence appears to be a bit above 80% across the architectures considered, with all architecture achieving much lower cadences for some outlier stars. Presumably, a more sophisticated dispatch scheduler that coordinates the observing sequences across telescopes within an architecture could achieve a higher and more uniform cadence. This is an interesting topic for future study.

Third, all architectures considered were able to exceed the SNR-detect and semi-amplitude sensitivities sufficient to find “earth-mass planets in the habitable zone around sun-like stars” for most of the targets in the survey in the optimistic photon noise limiting scenario. This is due to a combination of: some of the assumptions being optimistic (see section 2.5.1), the relatively large number of telescopes compared to prior single-telescope RV surveys, most (and aside from architecture VIII, all) telescopes are assumed to be fully dedicated facilities, and the long survey duration of ten years. While several architectures failed to reach the equivalent of nightly cadence for most stars, even the down-scoped cases (less than 6 telescopes) had several hundred observations per target. While stellar activity and correlated noise would reduce detection sensitivity, and especially mass characterization [52], these architectures would gather sufficient data to enable the application of sophisticated stellar activity modeling and have sufficient excess sensitivity that the detection goals

remain plausible.

### 2.5.1 Survey simulation assumptions and their effects

A number of simplifying assumptions were made for the survey simulations. In this subsection, we categorize their effects as rendering these simulations optimistic, pessimistic, or neutral/ambiguous. We defer to a future work to quantify the impact of these assumptions.

Optimistic assumptions:

- Instrument design requirements can be achieved, including efficiency and instrumental noise as specified
- There is no degradation in throughput over the decade-long survey due to, e.g., dust accumulation on the optics. [127]
- Stellar activity can be mitigated completely, as no correlated noise models are included herein. This is investigated in [52].
- Tellurics can be perfectly corrected.
- The atmospheric model does not consider line absorption. As such, it assumes that more light is available than in reality, as well as there being no noise from telluric absorption
- Telescopes do not have significant downtime besides weather losses.
- Weather losses continue at historical rates; climate change effects may be increasing clouds/haze at most sites. [128]
- Weather conditions night-to-night are uncorrelated, which will significantly impact any injection and recovery tests which are not explored herein.
- Time allocation is uniform; bright time gives additional limitations on when stars can be observed and introduce additional correlated sampling.

- Our 10 degree moon avoidance angle is the value employed in the MINERVA survey [42], whereas some other surveys may use larger moon avoidance angles. Future generation EPRV spectrographs such as NEID and ESPRESSO have added sky fibers for the subtraction of scattered Sun-light and Moon-light. This may permit future optimization of the Moon avoidance angle due to general reduction in noise. [129] We additionally assume that adaptive optics for Architecture V will minimize sky noise due to the smaller PSFs, and therefore even less background light reaches the spectrograph.
- Infrared detector characteristics (including readout noise and dark current) are equivalent to those of optical detectors.

Pessimistic assumptions:

- Observatories at different sites do not coordinate and optimize target lists and prioritization.
- Telescope sizes, particularly for the architectures with the 4, 6, and 8 meter class observatories, are at the smaller end of each size class specified. For example, 3.5-m apertures are simulated for the architectures with 4-m class telescopes.
- Pointing limits; many telescopes can go below the 2 airmass/30 degree above the horizon limit that we assumed, which can extend the observing season duration of targets and minimize annual gaps.
- Site selection does not include any options in eastern Europe or Asia, and only existing sites were simulated.
- Target Selection: While the target list is consistent between architectures and all stars on it are “good”, no attempt to further optimize the list to increase cadence/sensitivity or number of stars at a fixed cadence/sensitivity was done.

Ambiguous Assumptions:

- Throughput/efficiency in existing instruments is assumed to be constant as a function of wavelength, and across varying designs. We assume a median throughput instead of peak throughput to account for this effect, and accurately reflects system throughput. See Table 2.2 for existing EPRV spectrographs.
- Constant spectrograph resolution. As with throughputs, we assume an intermediate value to reflect the overall system spectral resolution to account for this effect.
- NEID is the assumed baseline specifications for future instruments, particular for the detectors and spectral grasp.
- Site selection: a number of the chosen sites have alternatives far enough away to impact weather and declination effects, which were not optimized. Additionally, the large number and spread of sites mitigates the effects of any one site being good/bad.
- Survey timing: A ten year survey with all dedicated instruments mitigates any effects from a specific site having an unusually good/bad year in terms of open-dome time.

## 2.6 Conclusions

Next-generation EPRV surveys, with goal of detecting Earth-mass analogs at approximately 10 cm/s velocity semi-amplitudes, will require a two order-of-magnitude increase in the necessary observational resources compared to prior generation 1 m s<sup>-1</sup> RV surveys of bright, nearby stars, by virtue of consideration of the photon noise statistics alone. We have developed tools and simulations available to the community of a set possible next-generation global-network RV surveys with realistic site and instrument parameters. We gathered the parameters for a nominal target list of nearby, bright stars common to future direct imaging mission concepts, several existing and potential observatory sites, and a set of telescope/instrument combinations. We generated exposure times for a given star based on its temperature, radius, distance, metallicity, surface gravity, and rotational velocity, as well as

the properties of the telescope and instrument measuring it. We then ran simulations of observing runs using the exposure times, site locations, and astronomical/weather conditions. Through the results of these simulations, we estimated the distributions of observations per star, target observation frequency as a function of available nights, and approximate estimates of planet detection sensitivity. As expected, we find that the achieved cadences generally scaled with the collective telescope aperture. We find that most architectures considered herein can achieve the theoretical minimum (optimistic bound) number of observations required to detect at SNR-detect=10 an Earth-mass analog producing a 9 cm/s stellar reflex velocity for all targets, with some margin to spare particularly for architectures II and VIII. We incorporated the impact of the spectroscopic characterization of stellar activity from line-by-line analyses through the imposition of a minimum SNR-phot per spectral resolution element, which resulted in exposure times comparable to those from the desired RV photon noise single measurement precision. While we did not explore the impact of correlated noise on detection sensitivity, this is explored in the companion paper to this work in [52]. Finally, we considered the major assumptions of the survey and how they could affect our results, which along with cost considerations can be explored in future work.

## **2.7 Appendix: Architecture Results**

In this Appendix, we present detailed architecture survey simulation results for the other architectures not presented in the main text.

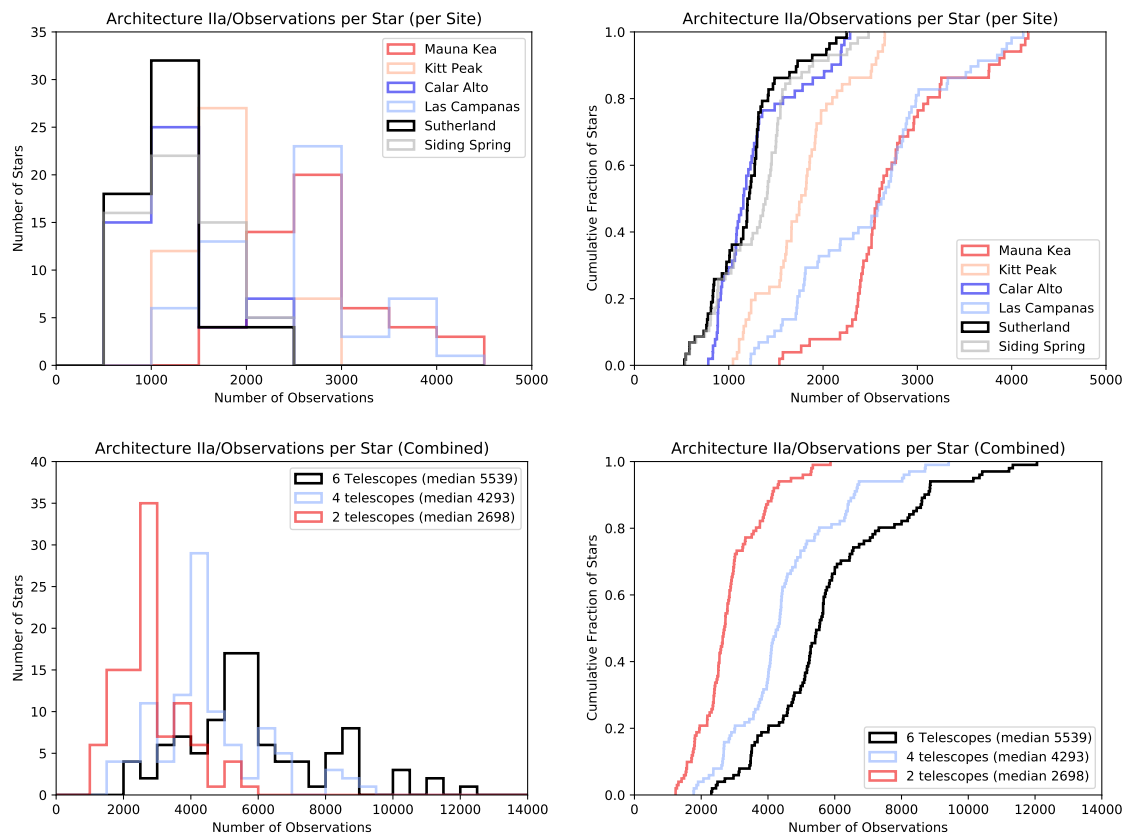


Figure 2.17: Same as figure 2.9, but for architecture IIa.

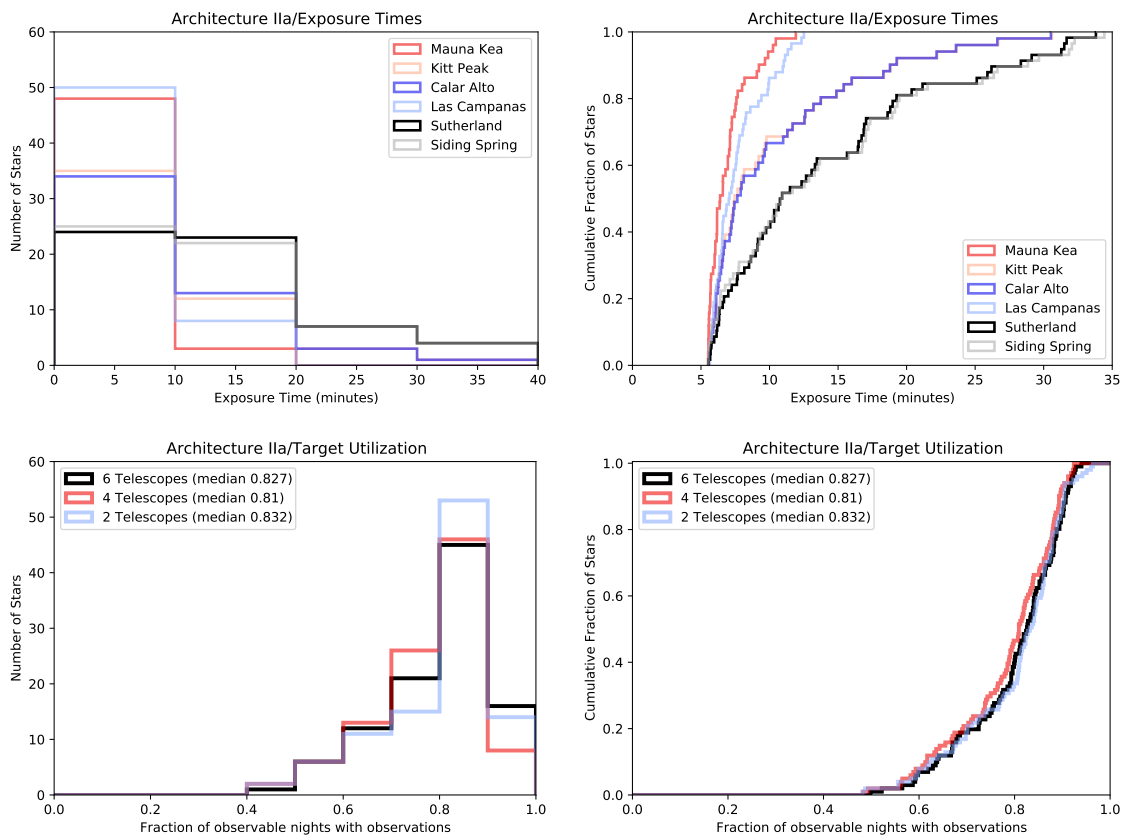


Figure 2.18: Same as figure 2.10, but for architecture IIa.

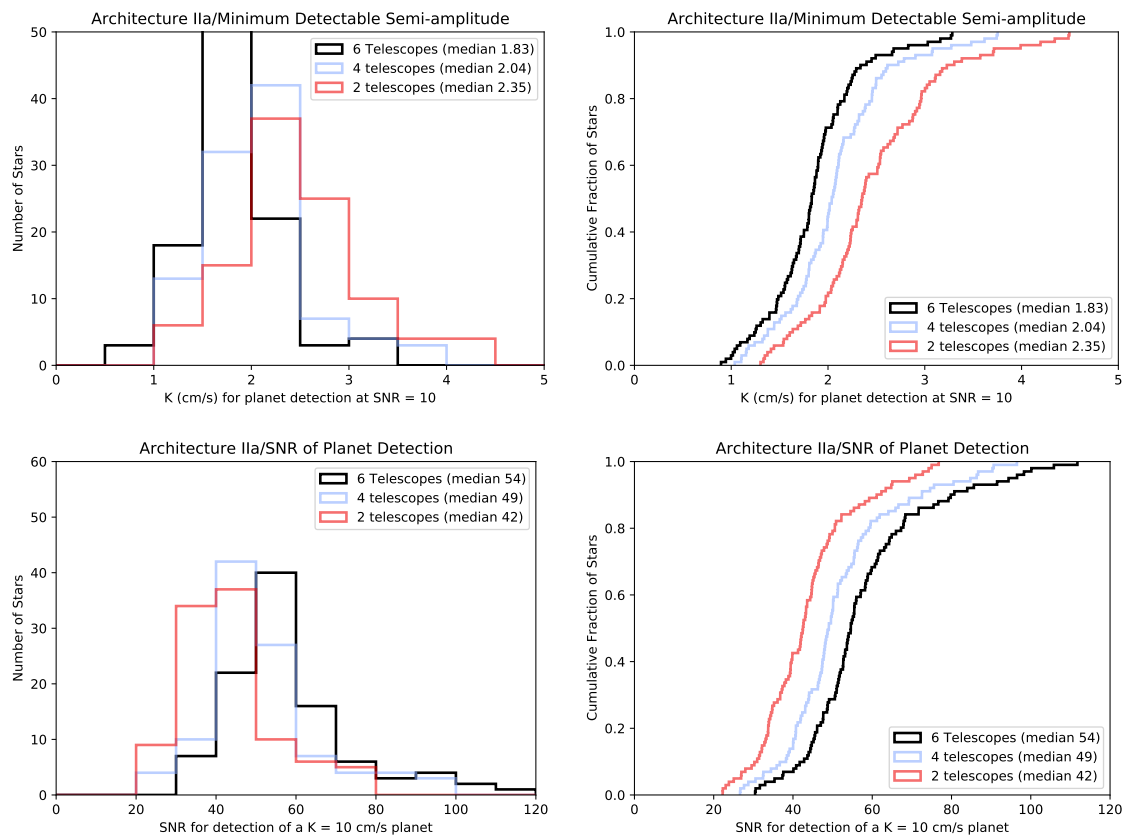


Figure 2.19: Same as figure 2.11, but for architecture IIa.

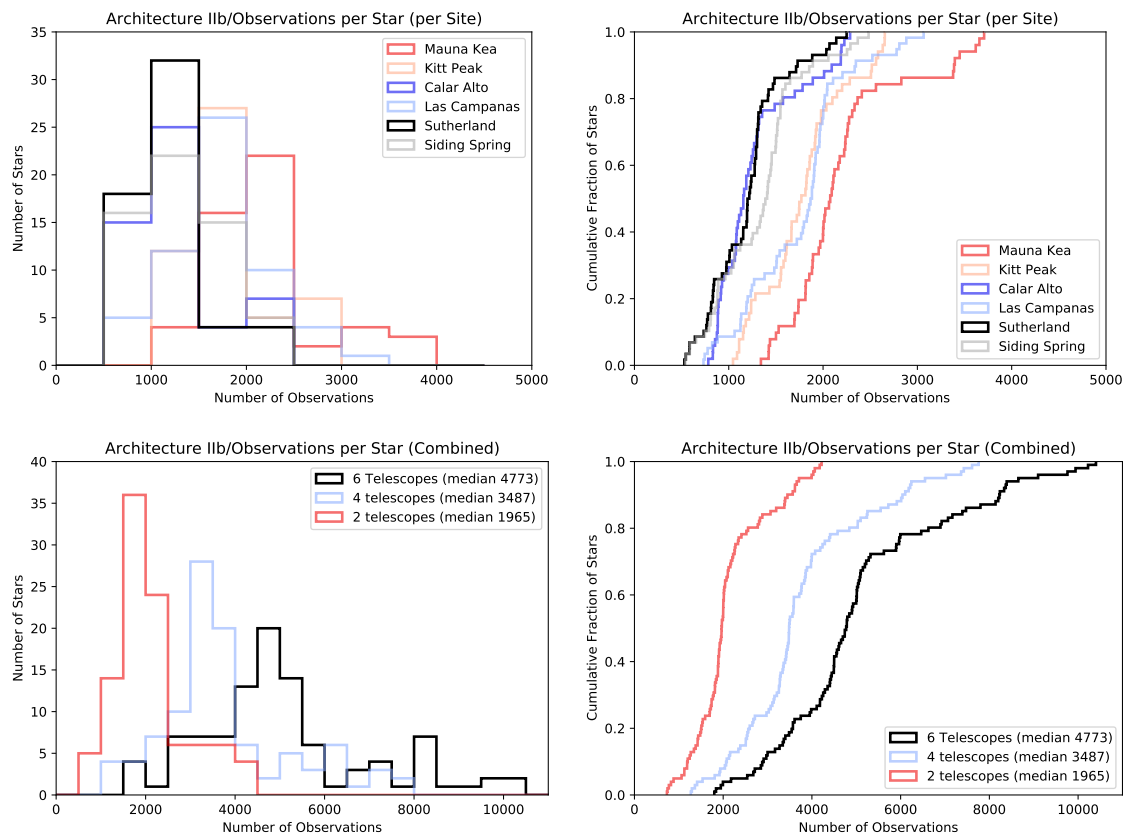


Figure 2.20: Same as figure 2.9, but for architecture IIb.

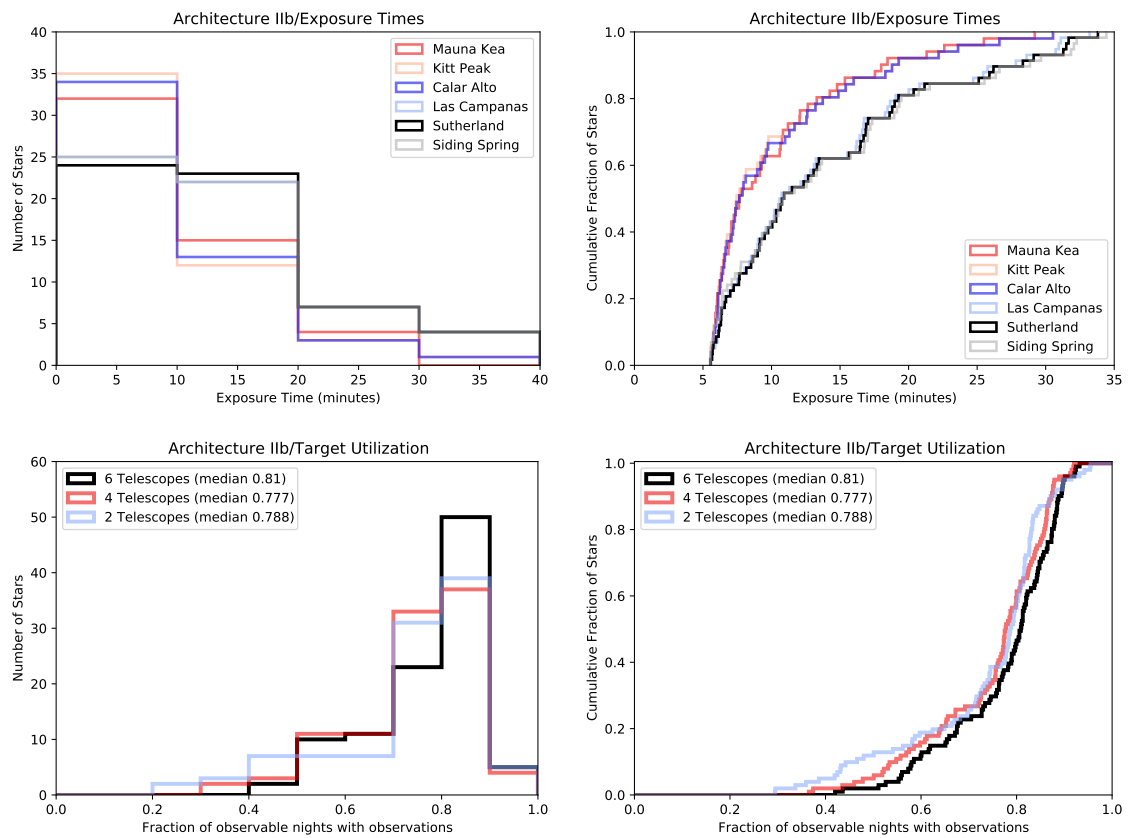


Figure 2.21: Same as figure 2.10, but for architecture IIb.

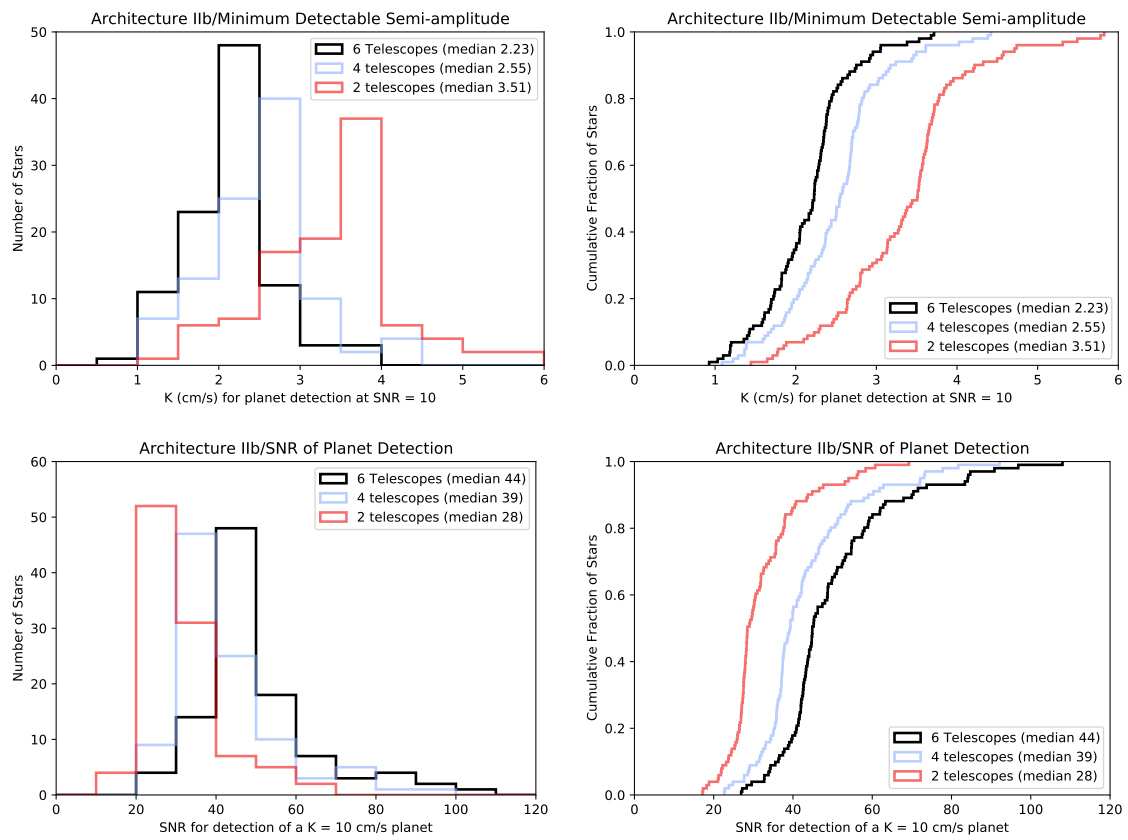


Figure 2.22: Same as figure 2.11, but for architecture IIb.

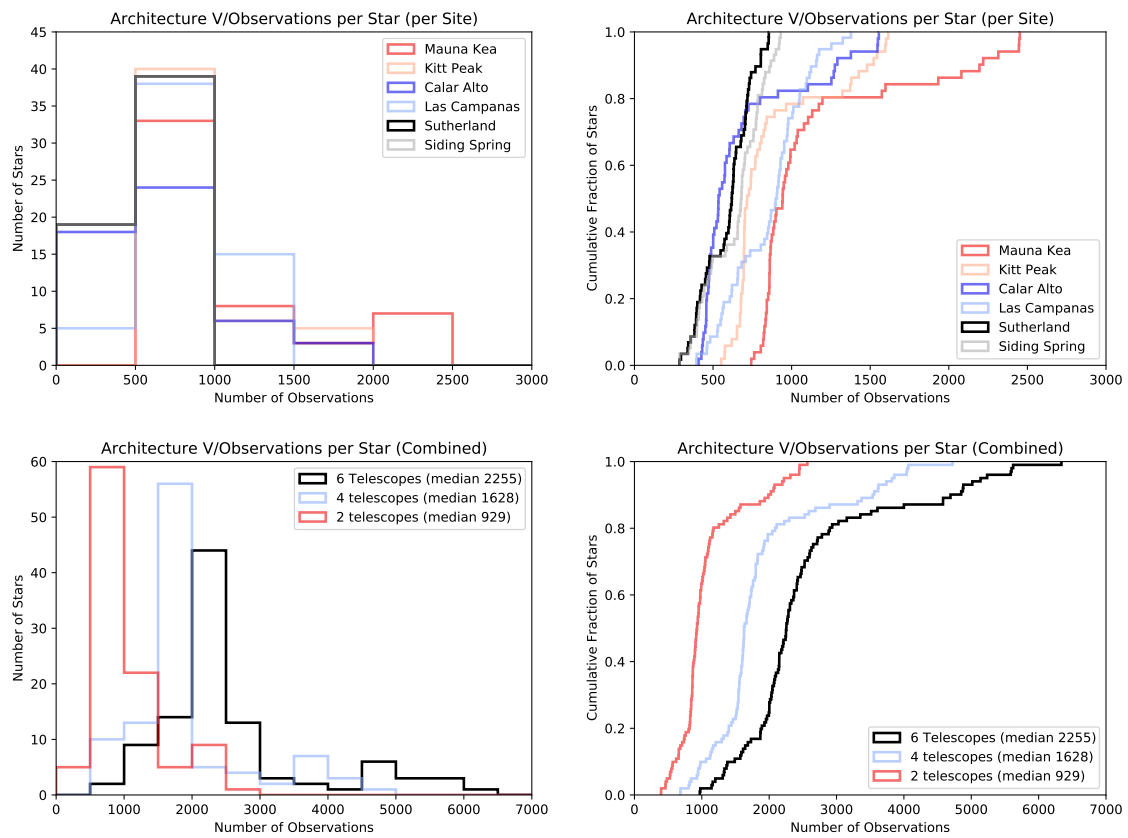


Figure 2.23: Same as figure 2.9, but for architecture V.

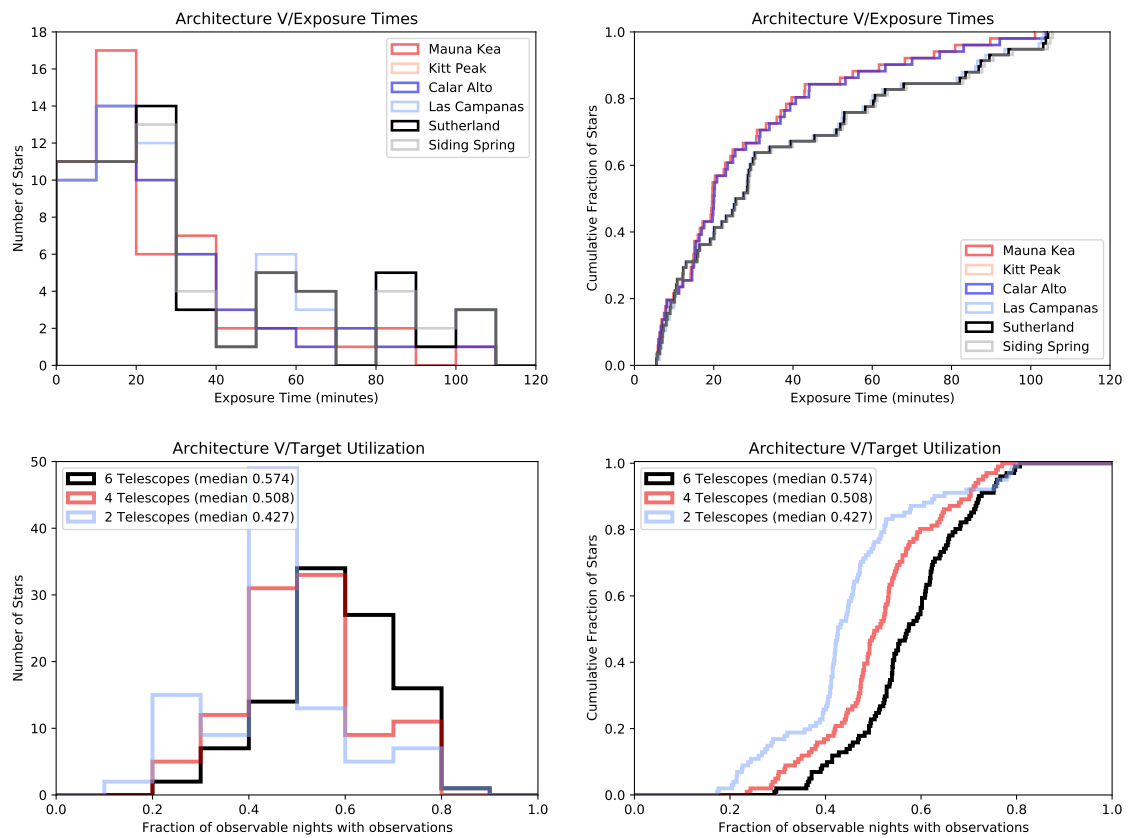


Figure 2.24: Same as figure 2.10, but for architecture V.

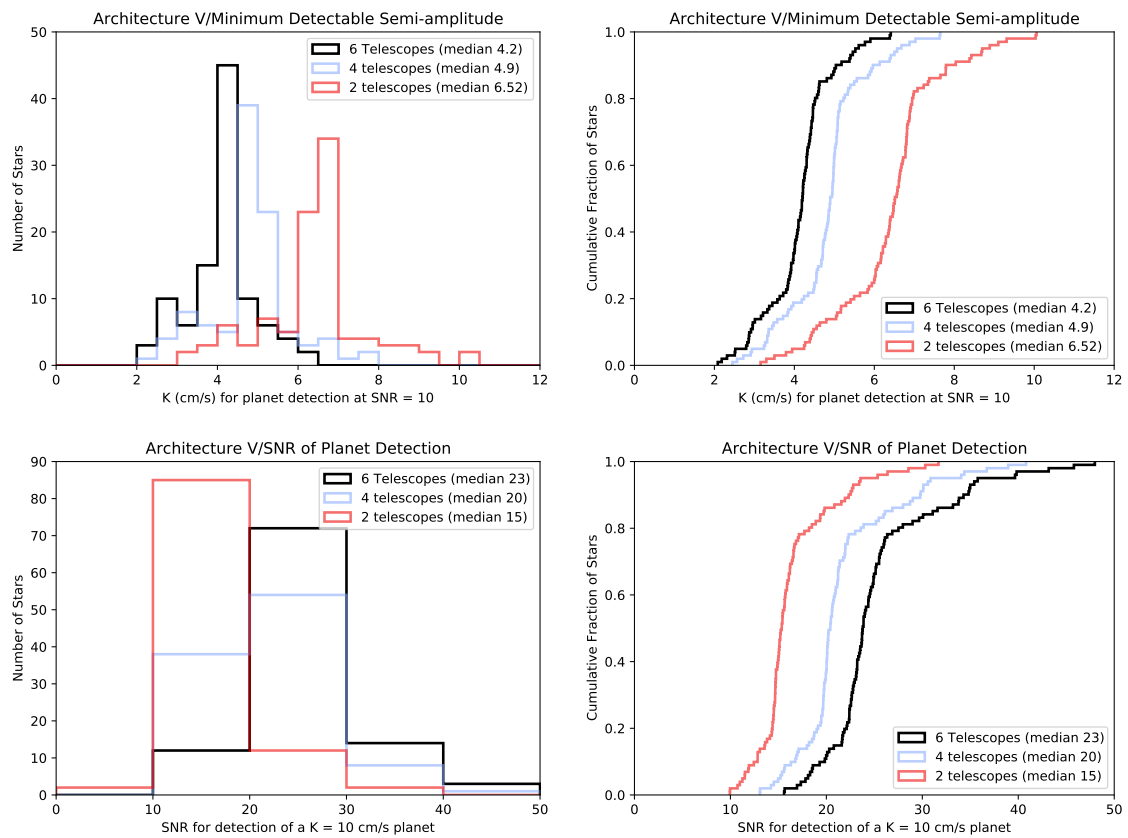


Figure 2.25: Same as figure 2.11, but for architecture V.

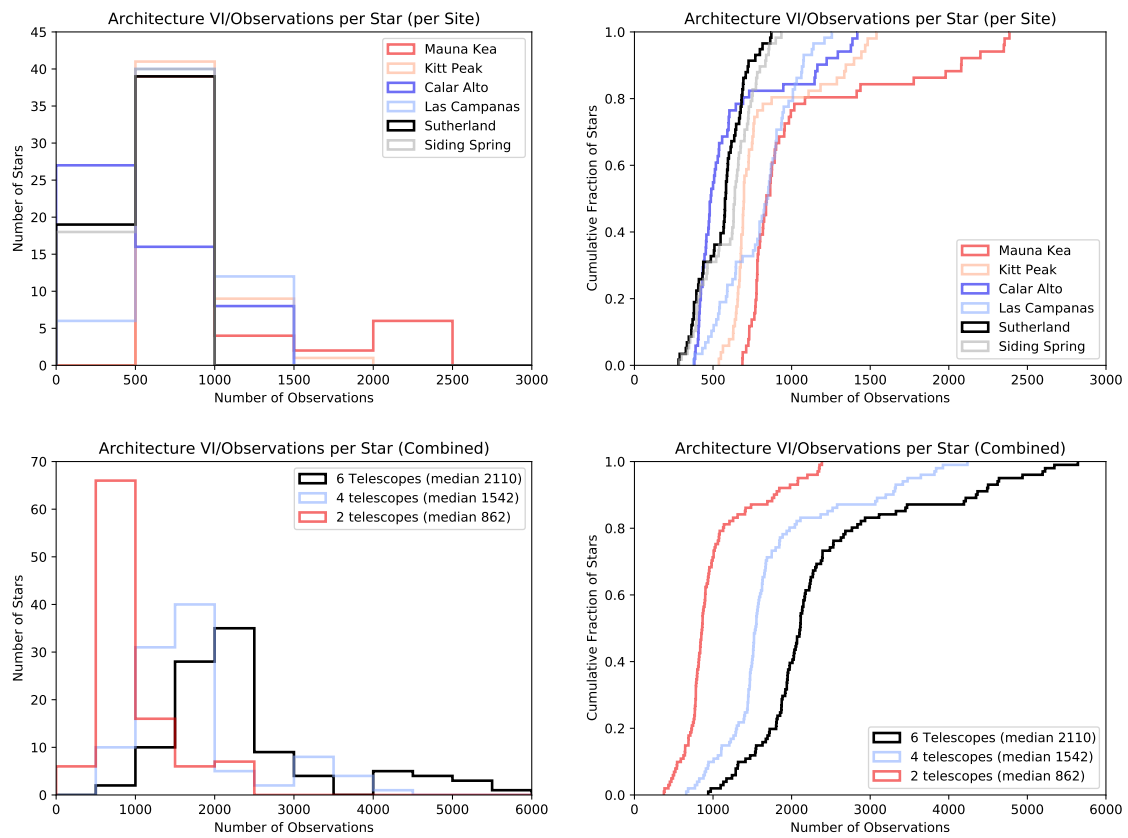


Figure 2.26: Same as figure 2.9, but for architecture VI.

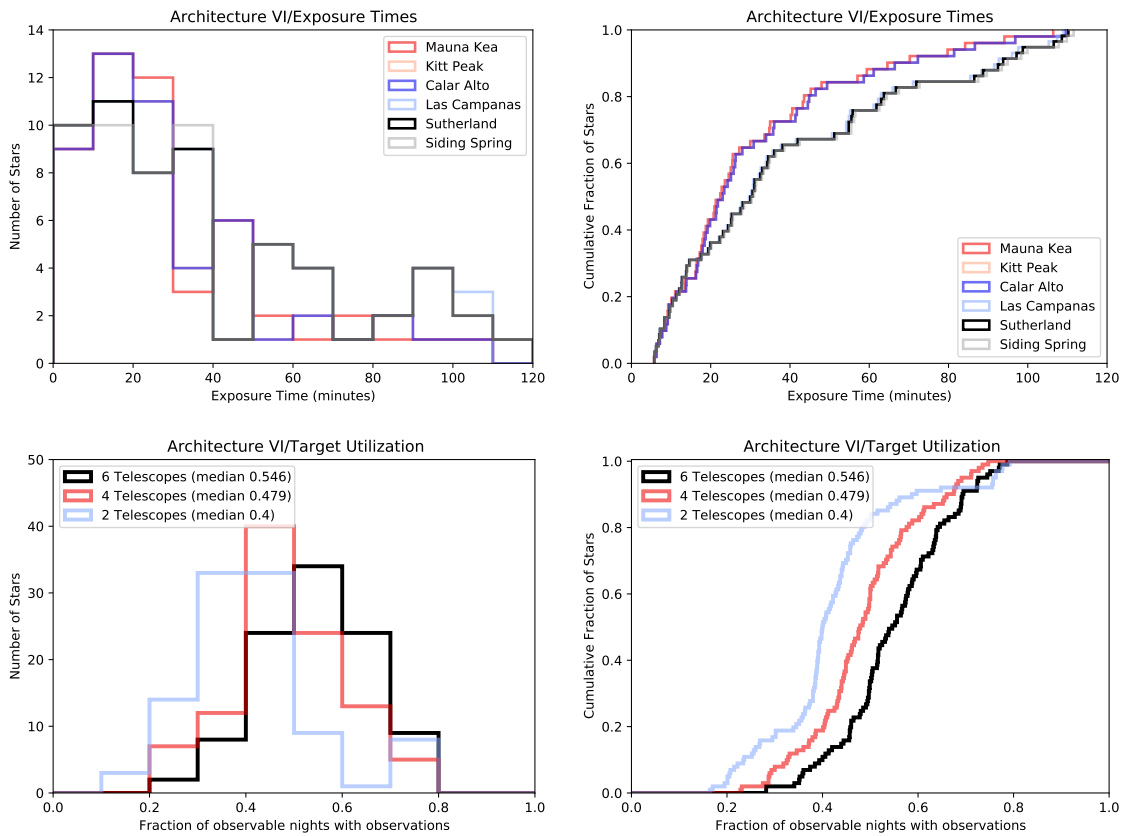


Figure 2.27: Same as figure 2.10, but for architecture VI.

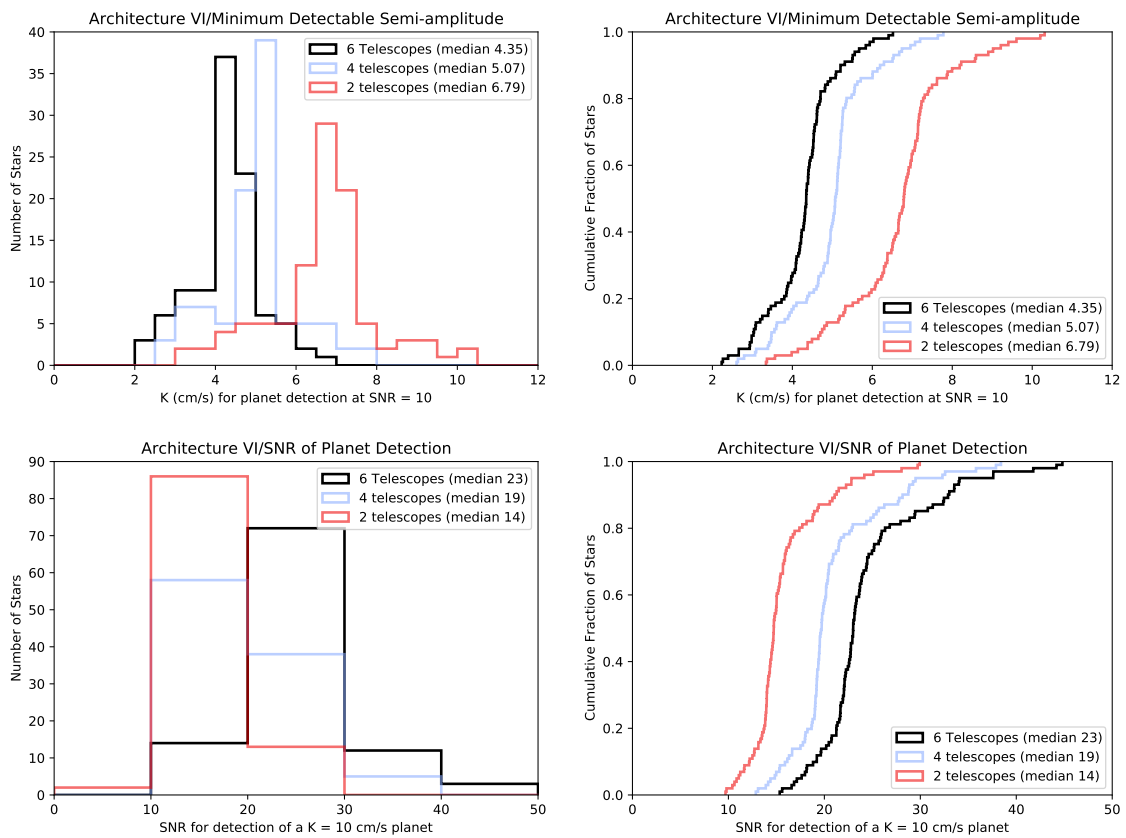


Figure 2.28: Same as figure 2.11, but for architecture VI.

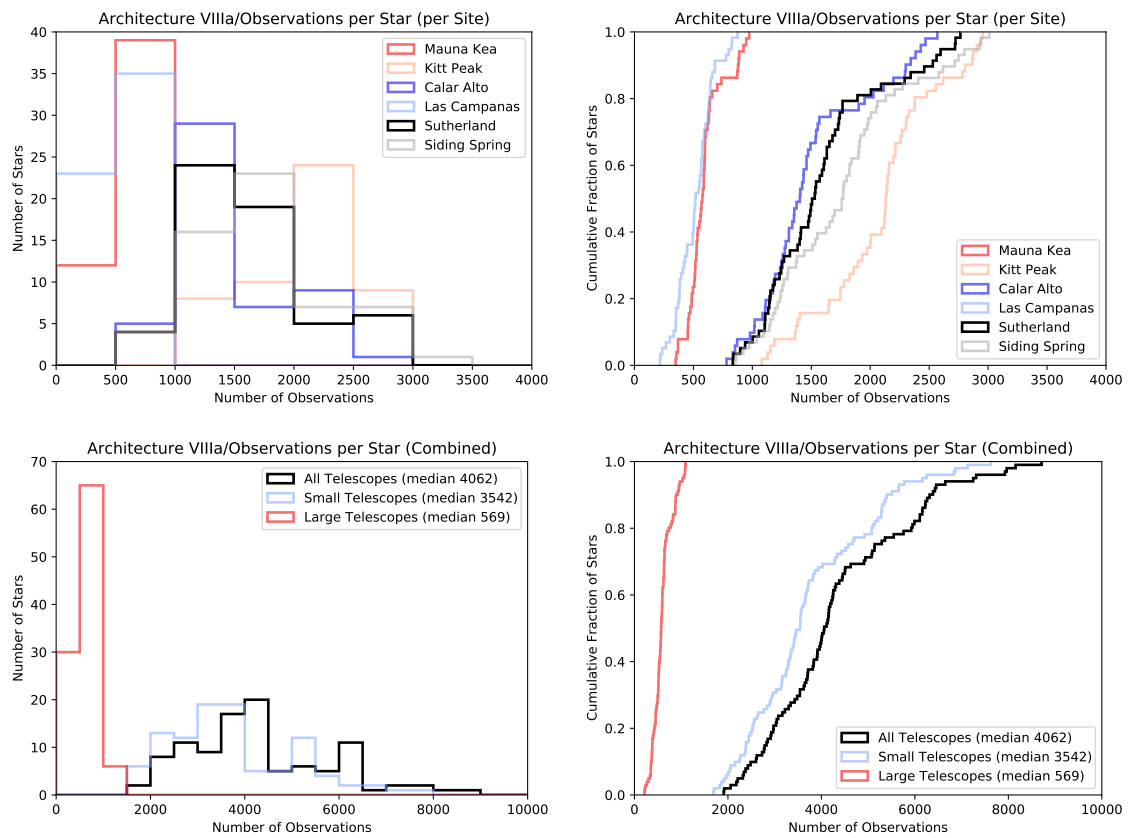


Figure 2.29: Same as figure 2.9, but for architecture VIIIA.

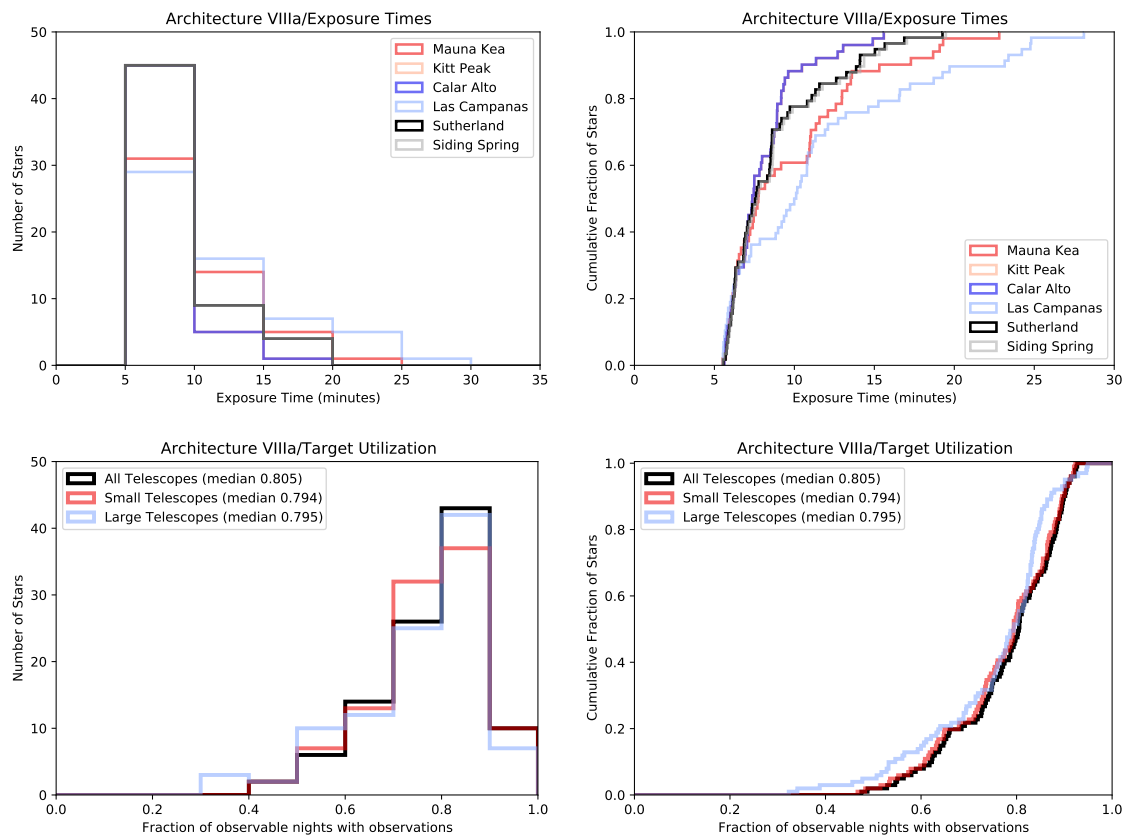


Figure 2.30: Same as figure 2.10, but for architecture VIIia.

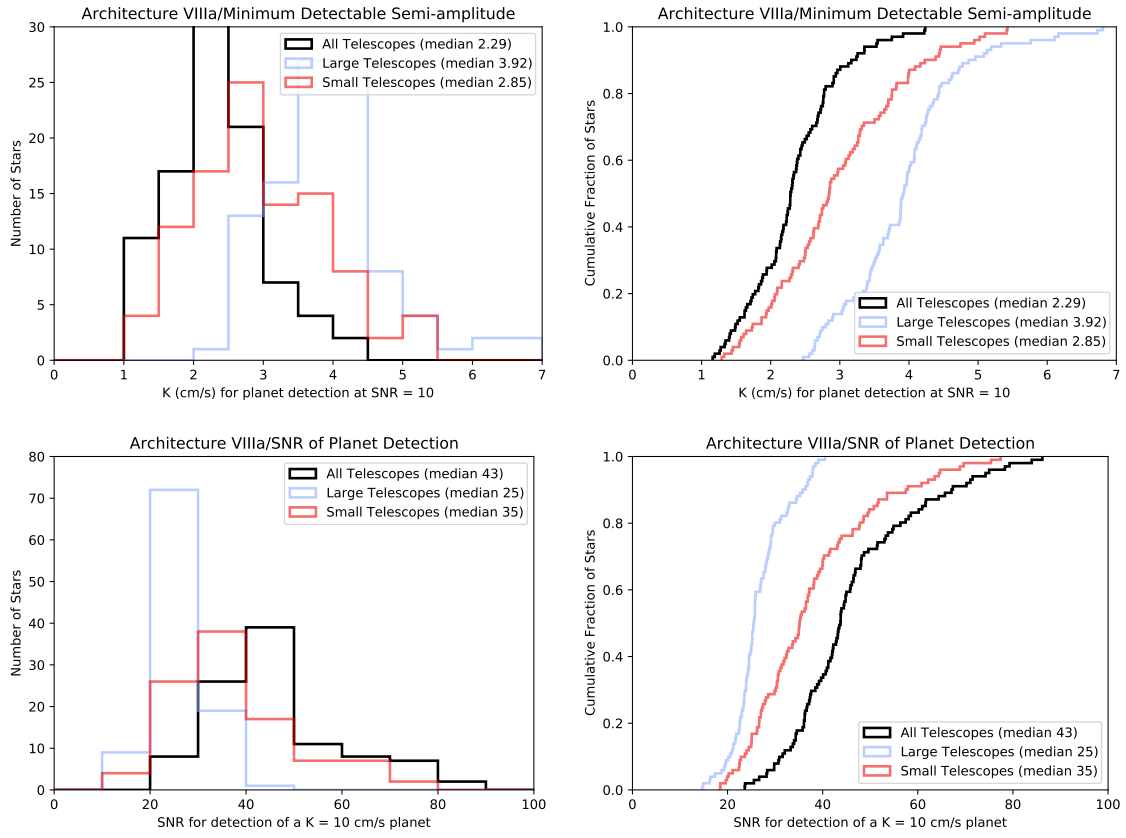


Figure 2.31: Same as figure 2.11, but for architecture VIIIA. This includes using equation 2.2 for finding the sensitivity due to the varying precision of the measurements.

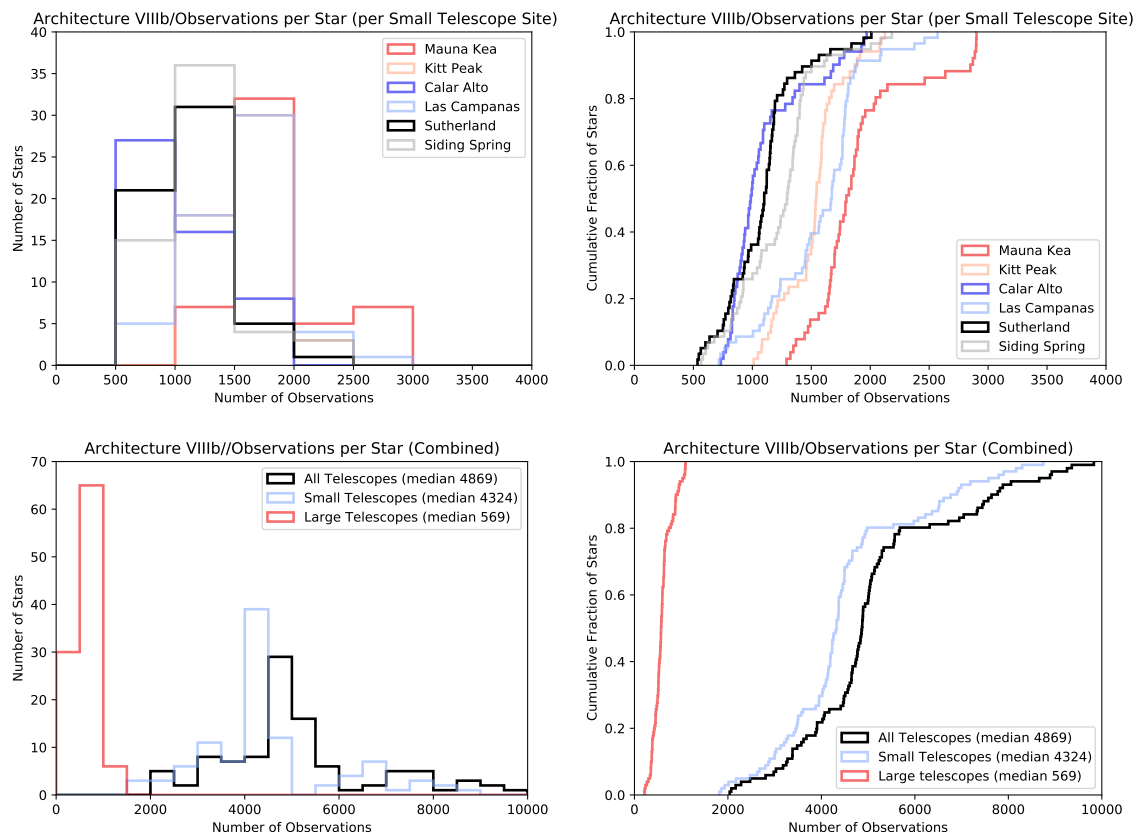


Figure 2.32: Same as figure 2.9, but for architecture VIIIb.

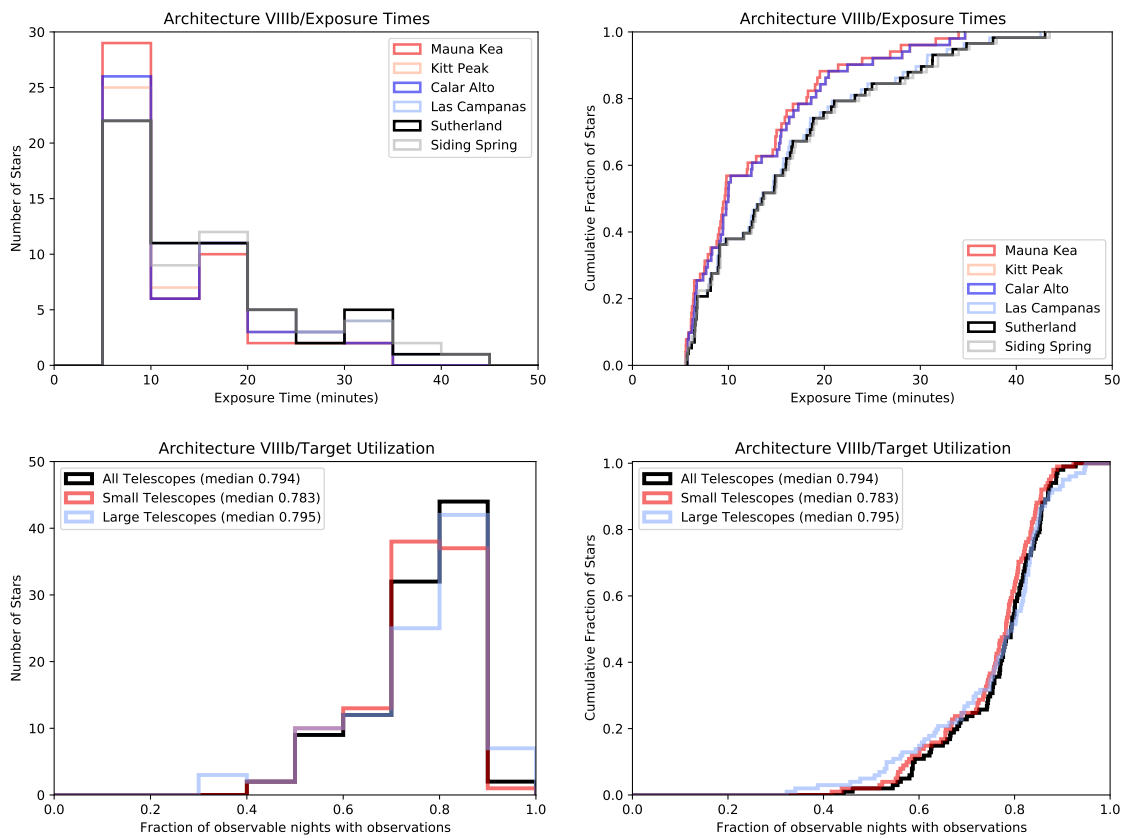


Figure 2.33: Same as figure 2.10, but for architecture VIIlb.

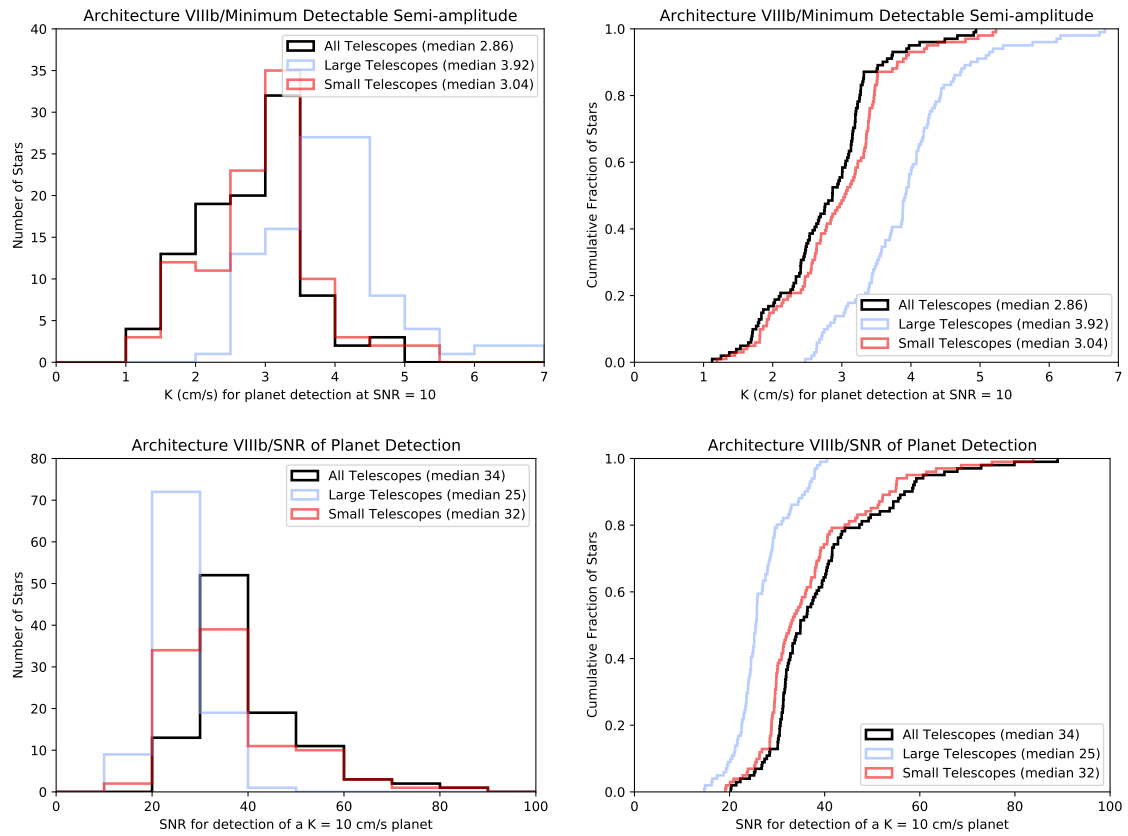


Figure 2.34: Same as figure 2.11, but for architecture VIIIb. This includes using equation 2.2 for finding the sensitivity due to the varying precision of the measurements.

# **Chapter 3: Joint Radial Velocity and Direct Imaging Planet Yield Calculations. II: Radial Velocity Scheduling and Cadence (draft)**

In this chapter, I present a draft of my second paper. It describes the survey simulation code, why I believe it to be trustworthy, and test runs of it on several telescope/spectrograph/target combinations. The combinations herein are different from those in the previous chapter, due to the differing assumptions and goals (these are comparing instruments against each-other, but not full architectures for planning future programs).

## **3.1 Introduction**

### **3.1.1 History**

While planet detection methods have greatly diversified since the first discoveries [5], precision radial velocities remain a key component. The radial velocity method is still the second most common detection method and a key technique to confirm and parameterize exoplanets. It also probes a portion of the mass/radius - distance/period space that is inaccessible to other methods, and has a clear path forwards to achieving the precision needed to detect and characterize an earth-equivalent planet around a sun-equivalent star.

Simulating RV surveys to best determine direct imaging targets have a significant history, though have generally stopped at around the then available precision. eg: [22] performed injection and recovery tests to determine yields and completeness, though were limited what sorts of information could be supplied (since only ice giant and gas giant planets could be firmly detected). Directly detecting terrestrial planets and providing mass estimates may soon be feasible, as opposed to just limiting the parameter space. [130]

looked across multiple spectral types and wavelength ranges (including atmospheric windows), finding brighter, and therefore hotter, stars to generally be more suitable. Less generally, the CARMENES radial velocity survey has developed a highly detailed simulation system related to their spectrograph, telescope, and observation strategy. [131] This simulation is used in part used for night to night planning.

Surveys are increasingly automated, though how to maximize planet yield is only beginning to be studied. [132]

The latest generation of Doppler RV facilities such as: NEID [133], EXPRES [134], ESPRESSO [135], and MAROON-X [136] are reaching into 30 cm/s and lower single measurement precisions. It is currently expected that future ones will get down to around 10 cm/s, though significant obstacles remain.

### 3.1.2 Motivation

There remains considerable debate on the value of  $\eta_{\oplus}$  [137–160], which will be difficult to resolve without characterization of the atmospheres of some tens of terrestrial planets.

Coronographic mission performance in particular is strongly affected by  $\eta_{\oplus}$ . Even for higher values, being able to skip the detection phase and proceed directly to characterization with an optimized observing schedule would improve performance.

Uninformed RV surveys generally choose bright and/or nearby stars due to having more photons to work with. Coronagraphic surveys also do so due to planet brightness, limited inner working angles, and greater angular scale. While early ground-based transit surveys focused on brighter stars, more recent and space-based ones have much reduced restrictions. They have found populations of exoplanets that are largely not amenable to detailed follow-up (especially atmospheric characterization).

Also, both (unlike transit) are looser in geometry requirements. The geometry means that there are nearby planets that are suitable for direct imaging that can be found with RVs, but not transits. The HabEx Interim Report [161] and related results point to a use for finding earth analogs that can be later characterized.

Even for a more general exoplanet demographics mission, masses from a precursor survey greatly assist in constraining atmospheric models. Both mass and radius are required to constrain exoplanet compositions. [162] In particular, more planet mass/radius measurements with smaller error bars and well quantified selection effects are needed to constrain the structure of the transition in between rocky and non-rocky planets. [163]

Planet masses are also important for accurate atmospheric retrievals. Spectroscopy of planetary atmospheres can only find the mass to high precision in limited circumstances, [164] and characterizing secondary atmospheres has considerable uncertainty [165]. Differing compositions (especially for super earths), can produce similar spectra for a wide array of masses. [166] Clouds and high metallicity can make accurate atmospheric retrieval difficult without accurate mass estimates. For JWST, these are  $\pm 50\%$  for initial characterization, and  $\pm 20\%$  for spectroscopic errors to be more important than mass ones. [167] Even in cases where atmospheric retrievals can be done with low quality mass priors, good orbit priors remain useful. [168]

In this paper, we present a multi-part pipeline for: generating a realistic radial velocity survey cadence for a given observing site telescope and properties, instrument and characteristics, desired radial velocity precision, and target list of nearby stars and associated known stellar parameters. However, this paper is focused on the resulting cadence from this level of simulation fidelity compared to more simplistic assumptions. We have developed this software to be re-usable and flexible for considerations of other current and future radial velocity surveys, and the software is available online. For each target star/instrument/telescope/precision combination we estimate exposures times, and resulting radial velocity precision from synthetic spectra after accounting for a typical airmass for observations. We focus on: overall exposure times to get to desired EPRV precision targets, typical numbers of observations per star as a result of the star's position and exposure time, and figures of merit for planet detection. In Section 3.2, we present the inputs to our simulation, and various telescope and instruments considered, as well as the target

---

Available at [https://github.com/pdn4kd/dispatch\\_scheduler](https://github.com/pdn4kd/dispatch_scheduler)

lists considered. In Section 3.3, we present how we calculate the estimated radial velocity precision and requisite exposure times. In Section 3.4, we present how observations are scheduled in a simulated survey for a given target prioritization scheme. In Section 3.5, we present the results of the cadence of observations for the different scenarios we consider. Additionally, we calculate a K/SNR figure of merit for these cadences. In Section 3.9, we discuss the interesting highlights of our resulting cadences, and in Section 3.10 we present our conclusions and plans for future work.

## 3.2 Simulation Inputs

### 3.2.1 Target Catalogs

Testing our code has different requirements from pathfinder EPRV surveys, and the requirements and target lists of the surveys are evolving over time. While most of our simulations are with a single catalog, we construct multiple catalogs for some comparisons.

Our primary catalog uses Habitable Worlds Observatory’s ExEP list (as of 2023-07-26) was also considered. This list [169,170] explicitly selects FGK stars and has cutoffs for  $v \cdot \sin(i)$  and  $R_{hk}$ . This catalog (hereafter called “HWO”) lacks explicit  $v \cdot \sin(i)$  values, so we added them from the literature. [84,171–175]

Our initial star list comes from a modification of a version of the HabEx target list, which contains 72 Hipparcos stars. Given the source, this list has parameters somewhat different from a typical uninformed RV survey. It does not select for low stellar activity, but for distance (consisting entirely of stars within 5 parsecs). Constructing a catalog of the required stellar properties ( $T_{eff}$ , radius, distance,  $v \cdot \sin(i)$ ,  $\log(g)$ ) was done via existing tables in VizieR (see table 3.2). This by necessity makes it somewhat heterogeneous.

For the simulations, this target list was altered by: 1) Adding the companion star in a distant binary (not in Hipparcos); 2) dropping an eclipsing binary; cutting all stars below -30 declination (motivated by all sites currently being considered being in Arizona. Other target lists did not use this cut, though the effect on the simulations was limited due to

nature of the dispatch scheduler.). This left 53 stars. Three sub-lists were also generated: the baseline “full” survey, a “deep” one containing 9 stars of particular interest to the HabEx team, and 47 stars that had no known planets at this time. Many of the stars with known planets have hot jupiters, which are likely to preclude the existence of habitable zone terrestrial planets.

This target list (“HabEx”) was run alongside synthetic catalogs for checking out code’s exposure times, coverage, and precision results to ensure that they were realistic.

A second run of this “HabEx” target list was also done without the declination cut for more directly getting exoplanet yields across our instrument types, sensitivities, and exposure timescales.

As a check, the catalog from [176] (hereafter called the “EPRV target list”) is also used within our revised exposure considerations. This provides an “apples-to-apples” comparison with our previous work, by keeping the targets the same while varying the instruments and exposure parameters.

### 3.2.2 Telescope and Instrument Parameters

The simulations here all use telescopes in Arizona (see table 3.5). These all being northern hemisphere site would normally motivate a declination cut. We do not do so for this survey as a test of what the practical lower limit is. Our site locations are the standard ones listed for each telescope. Our weather is taken from Kitt Peak data (specifically WIYN, see figure 3.1), while MINERVA proper uses records from a survey of Mount Hopkins [42].

We assume constant throughput in our spectrographs, though with values that reflect their actual averages (table 3.1). These throughputs are at or below the low end of commonly reported values to compensate for those being peak values during nights with seeing. That is, they should reflect overall averages of the systems.

Table 3.1: Peak system throughputs for current EPRV spectrographs. These are higher than the averages used in the various architectures, as they largely do not account for performance variations from varying seeing and wavelength.

Spectrograph	Throughput	Source
ESPRESSO	10%	[69]
EXPRES	9-15%	[70]
MAROON-X	7-8%, 11.5%	[71]
NEID	6%	[72]

### 3.3 Radial Velocities

The radial velocity precision code is an implementation and expansion of existing work [63]. The major changes are: including macroturbulence when data is available, and aggregating radial velocity uncertainties across the visible/red/IR ranges if the spectrograph being simulated crosses them. This is expanded somewhat in that the telescope and instrument are simulated to the point of continuum atmospheric absorption/scattering, basic signal to noise considerations on each pixel, and exposure and readout times.

#### 3.3.1 Stellar Properties

For the purpose of simulating RVs, stars are defined by:  $T_{eff}$ ,  $\log(g)$ ,  $v \cdot \sin(i)$ , metallicity, stellar radius, and distance. Effective temperature directly defines the atmosphere model used, while the rest scale RV content ( $\log(g)$ ,  $v \cdot \sin(i)$ , metallicity) or brightness (radius, distance).

While Beatty uses an estimate of macroturbulence based on effective temperature, some catalogs in the literature have measured this parameter [173]. Literature values are used where available.

---

<sup>1</sup> [173], <sup>2</sup> [92], <sup>3</sup> [177], <sup>4</sup> [178], <sup>5</sup> [84], <sup>6</sup> Assumed, <sup>7</sup> [179], <sup>9</sup> [180], <sup>10</sup> [107], <sup>11</sup> [181], <sup>12</sup> [182], <sup>13</sup> [183],  
<sup>14</sup> [184], <sup>15</sup> [185], <sup>16</sup> [186], <sup>17</sup> [187], <sup>18</sup> [188], <sup>19</sup> [189], <sup>20</sup> [190], <sup>21</sup> [191], <sup>22</sup> [192], <sup>23</sup> [193], <sup>24</sup> [86], <sup>25</sup> [121], <sup>99</sup>  
Calculated

Table 3.2: The HabEx stars and their properties used in these simulations.

RA(J2000)	DE(J2000)	HIP	Vmag	Dist (pc)	Rstar	T <sub>eff</sub>	log(g)	[Fe/H]	V <sub>sini</sub>	Mstar	V <sub>mac</sub>
12.095738	5.280615	3765	5.74	7.4604597	0.74 <sup>1</sup>	4937 <sup>1</sup>	4.54 <sup>1</sup>	-0.22 <sup>1</sup>	0.7 <sup>1</sup>	0.69 <sup>1</sup>	1.7 <sup>1</sup>
12.276214	57.815186	3821	3.46	5.952735	1.05 <sup>1</sup>	5919 <sup>1</sup>	4.37 <sup>1</sup>	-0.21 <sup>1</sup>	0.5 <sup>1</sup>	0.94 <sup>1</sup>	4.2 <sup>1</sup>
25.624008	20.268505	7981	5.24	7.467702	0.81 <sup>1</sup>	5190 <sup>1</sup>	4.51 <sup>1</sup>	-0.03 <sup>1</sup>	0.1 <sup>1</sup>	0.78 <sup>1</sup>	2.0 <sup>1</sup>
26.017012	-15.93748	8102	3.49	3.647372	0.82 <sup>1</sup>	5333 <sup>1</sup>	4.6 <sup>1</sup>	-0.44 <sup>1</sup>	0.1 <sup>1</sup>	0.99 <sup>1</sup>	2.2 <sup>1</sup>
26.936811	63.8525	8362	5.63	9.976058	0.84 <sup>1</sup>	5344 <sup>1</sup>	4.54 <sup>1</sup>	0.01 <sup>1</sup>	0.8 <sup>1</sup>	0.89 <sup>1</sup>	2.3 <sup>1</sup>
41.049942	49.228447	12777	4.1	11.232169	1.31 <sup>1</sup>	6196 <sup>1</sup>	4.19 <sup>1</sup>	0.05 <sup>1</sup>	8.0 <sup>1</sup>	0.96 <sup>1</sup>	6.2 <sup>1</sup>
47.26675	49.613277	14632	4.05	10.534078	1.4 <sup>1</sup>	5938 <sup>1</sup>	4.18 <sup>1</sup>	0.13 <sup>1</sup>	3.4 <sup>1</sup>	1.07 <sup>1</sup>	4.3 <sup>1</sup>
55.81209	-9.763394	17378	3.52	9.043226	2.34 <sup>1</sup>	5037 <sup>1</sup>	3.75 <sup>1</sup>	0.15 <sup>1</sup>	0.1 <sup>1</sup>	1.11 <sup>1</sup>	3.4 <sup>1</sup>
63.818	-7.6528707	19849	4.43	5.0443907	0.83 <sup>1</sup>	5092 <sup>1</sup>	4.51 <sup>1</sup>	-0.21	0.5 <sup>1</sup>	0.8 <sup>1</sup>	1.9 <sup>1</sup>
72.460045	6.9612756	22449	3.19	8.025682	1.34 <sup>1</sup>	6398 <sup>1</sup>	4.27 <sup>1</sup>	0.05 <sup>1</sup>	16.4 <sup>1</sup>	1.21 <sup>1</sup>	8.5 <sup>1</sup>
79.78531	40.099052	24813	4.69	12.645422	1.28 <sup>1</sup>	5873 <sup>1</sup>	4.26 <sup>1</sup>	0.11 <sup>1</sup>	0.1 <sup>1</sup>	1.08 <sup>1</sup>	3.9 <sup>1</sup>
143.9146	35.810135	47080	5.4	11.17943	0.97 <sup>1</sup>	5499 <sup>1</sup>	4.44 <sup>1</sup>	0.27 <sup>1</sup>	2.8 <sup>1</sup>	0.95 <sup>1</sup>	2.6 <sup>1</sup>
175.26256	34.201637	56997	5.31	9.541075	0.86 <sup>1</sup>	5502 <sup>1</sup>	4.52 <sup>1</sup>	-0.07 <sup>1</sup>	2.2 <sup>1</sup>	0.9 <sup>1</sup>	2.6 <sup>1</sup>
176.62947	-40.500355	57443	4.89	9.239582	0.94 <sup>1</sup>	5672 <sup>1</sup>	4.51 <sup>1</sup>	-0.27 <sup>1</sup>	0.1 <sup>1</sup>	1.04 <sup>1</sup>	3.1 <sup>1</sup>
188.43561	41.35748	61317	4.24	8.371003	1.06 <sup>1</sup>	5884 <sup>1</sup>	4.42 <sup>1</sup>	-0.18 <sup>1</sup>	0.1 <sup>1</sup>	1.07 <sup>1</sup>	4.0 <sup>1</sup>
199.60132	-18.311195	64924	4.74	8.525149	0.97 <sup>1</sup>	5562 <sup>1</sup>	4.44 <sup>1</sup>	-0.03 <sup>1</sup>	0.8 <sup>1</sup>	0.93 <sup>1</sup>	2.8 <sup>1</sup>
223.34903	19.152798	72848	6.0	11.535356	0.84 <sup>1</sup>	5258 <sup>1</sup>	4.47 <sup>1</sup>	0.06 <sup>1</sup>	4.4 <sup>1</sup>	0.77 <sup>1</sup>	2.1 <sup>1</sup>
236.61089	7.353073	77257	4.42	11.753643	1.38 <sup>1</sup>	5901 <sup>1</sup>	4.22 <sup>1</sup>	0.04 <sup>1</sup>	2.0 <sup>1</sup>	1.15 <sup>1</sup>	4.1 <sup>1</sup>
272.4059	38.457775	88972	6.38	11.097548	0.8 <sup>1</sup>	4970 <sup>1</sup>	4.51 <sup>1</sup>	-0.11	0.1 <sup>1</sup>	0.76 <sup>1</sup>	1.8 <sup>1</sup>
293.08997	69.66118	96100	4.67	5.76668	0.79 <sup>1</sup>	5242 <sup>1</sup>	4.56 <sup>1</sup>	-0.21 <sup>1</sup>	0.5 <sup>1</sup>	0.81 <sup>1</sup>	2.1 <sup>1</sup>
298.8283	6.4067636	98036	3.71	13.70802	3.17 <sup>1</sup>	5081 <sup>1</sup>	3.55 <sup>1</sup>	-0.11 <sup>1</sup>	0.1 <sup>1</sup>	1.3 <sup>1</sup>	3.5 <sup>1</sup>
303.82245	-27.032976	99825	5.73	8.823789	0.82 <sup>1</sup>	5071 <sup>1</sup>	4.5 <sup>1</sup>	0.05 <sup>1</sup>	1.2 <sup>1</sup>	0.78 <sup>1</sup>	1.9 <sup>1</sup>
331.75728	25.345112	109176	3.77	11.756408	1.42 <sup>1</sup>	6565 <sup>1</sup>	4.25 <sup>1</sup>	-0.05 <sup>1</sup>	0.1 <sup>1</sup>	1.31 <sup>1</sup>	11.2 <sup>1</sup>
5.0177503	-64.874794	1599	4.23	8.592542	1.055 <sup>2</sup>	5948 <sup>2</sup>	4.46 <sup>2</sup>	-0.18 <sup>2</sup>	3.0 <sup>2</sup>	1.176 <sup>2</sup>	...
6.4378004	-77.252424	2021	2.82	7.474959	1.802 <sup>2</sup>	5873 <sup>2</sup>	4.08 <sup>2</sup>	-0.09 <sup>2</sup>	4.0 <sup>2</sup>	1.433 <sup>2</sup>	...
9.840858	21.250473	3093	5.88	11.107409	0.879 <sup>2</sup>	5221 <sup>2</sup>	4.45 <sup>2</sup>	0.16 <sup>2</sup>	1.1 <sup>2</sup>	0.799 <sup>2</sup>	...
24.199345	41.40546	7513	4.1	13.468014	1.573 <sup>2</sup>	6213 <sup>2</sup>	4.25 <sup>2</sup>	0.12 <sup>2</sup>	9.6 <sup>2</sup>	1.62 <sup>2</sup>	...
39.02039	6.8868704	12114	5.79	7.208766	0.7348 <sup>2</sup>	4866 <sup>2</sup>	4.66 <sup>2</sup>	0.0 <sup>2</sup>	2.9 <sup>2</sup>	0.909 <sup>2</sup>	...
43.13387	-12.769714	13402	6.05	10.380981	0.7532 <sup>2</sup>	5236 <sup>2</sup>	4.59 <sup>2</sup>	0.11 <sup>2</sup>	4.9 <sup>2</sup>	0.811 <sup>2</sup>	...
49.44235	-62.57532	15330	5.53	12.119742	0.9062 <sup>2</sup>	5699 <sup>2</sup>	4.58 <sup>2</sup>	-0.22 <sup>2</sup>	2.9 <sup>2</sup>	1.128 <sup>2</sup>	...
49.553413	-62.506363	15371	5.24	12.078753	0.9721 <sup>2</sup>	5845 <sup>2</sup>	4.54 <sup>2</sup>	-0.23 <sup>2</sup>	2.6 <sup>2</sup>	1.192 <sup>2</sup>	...
49.8404	3.370198	15457	4.84	9.159186	0.917 <sup>2</sup>	5742 <sup>2</sup>	4.49 <sup>2</sup>	0.1 <sup>2</sup>	5.2 <sup>2</sup>	0.948 <sup>2</sup>	...
49.98188	-43.069782	15510	4.26	6.059871	0.928 <sup>2</sup>	5401 <sup>2</sup>	4.62 <sup>2</sup>	-0.23 <sup>2</sup>	1.5 <sup>2</sup>	1.3 <sup>2</sup>	...
75.20417	-5.7536755	23311	6.22	8.813679	0.7579 <sup>2</sup>	4827 <sup>2</sup>	4.69 <sup>2</sup>	0.3 <sup>2</sup>	1.7 <sup>2</sup>	1.031 <sup>2</sup>	...
92.56031	-74.753044	29271	5.08	10.148163	0.9729 <sup>2</sup>	5587 <sup>2</sup>	4.5 <sup>2</sup>	0.05 <sup>2</sup>	1.7 <sup>2</sup>	1.103 <sup>2</sup>	...
103.07521	-5.173713	32984	6.58	8.7001915	0.665 <sup>2</sup>	4758 <sup>2</sup>	4.92 <sup>2</sup>	-0.01 <sup>2</sup>	1.8 <sup>2</sup>	1.34 <sup>2</sup>	...
114.82549	5.224993	37279	0.4	3.4973595	1.919 <sup>2</sup>	6543 <sup>2</sup>	3.99 <sup>2</sup>	0.03 <sup>2</sup>	5.7 <sup>2</sup>	1.32 <sup>2</sup>	...
157.65659	55.980537	51459	4.82	12.850167	1.12 <sup>2</sup>	6126 <sup>2</sup>	4.34 <sup>2</sup>	-0.05 <sup>2</sup>	2.1 <sup>2</sup>	0.994 <sup>2</sup>	...
177.67383	1.7647179	57757	3.59	10.900371	1.639 <sup>2</sup>	6161 <sup>2</sup>	4.22 <sup>2</sup>	0.16 <sup>2</sup>	4.0 <sup>2</sup>	1.61 <sup>2</sup>	...
178.24487	37.718678	57939	6.42	9.156671	0.659 <sup>2</sup>	4950 <sup>2</sup>	4.65 <sup>2</sup>	-1.16 <sup>2</sup>	0.5 <sup>2</sup>	0.716 <sup>2</sup>	...
197.9683	27.878183	64394	4.23	9.154994	1.063 <sup>2</sup>	6075 <sup>2</sup>	4.57 <sup>2</sup>	0.04 <sup>2</sup>	4.4 <sup>2</sup>	1.54 <sup>2</sup>	...
209.38358	61.492863	68184	6.49	10.104072	0.802 <sup>2</sup>	4757 <sup>2</sup>	4.58 <sup>2</sup>	0.1 <sup>2</sup>	1.3 <sup>2</sup>	0.89 <sup>2</sup>	...
224.36667	-21.415476	73184	5.72	5.905977	0.6754 <sup>2</sup>	4744 <sup>2</sup>	4.76 <sup>2</sup>	0.1 <sup>2</sup>	2.6 <sup>2</sup>	0.951 <sup>2</sup>	...
239.11327	15.661617	78072	3.85	11.120996	1.447 <sup>2</sup>	6262 <sup>2</sup>	4.18 <sup>2</sup>	-0.14 <sup>2</sup>	10.9 <sup>2</sup>	1.16 <sup>2</sup>	...
249.08937	-2.3245835	81300	5.77	9.778039	0.791 <sup>2</sup>	5277 <sup>2</sup>	4.57 <sup>2</sup>	0.05 <sup>2</sup>	2.2 <sup>2</sup>	0.853 <sup>2</sup>	...
259.76596	-46.636234	84720	5.47	8.786574	0.777 <sup>2</sup>	5256 <sup>2</sup>	4.61 <sup>2</sup>	-0.27 <sup>2</sup>	0.3 <sup>2</sup>	0.901 <sup>2</sup>	...
302.1817	-66.18207	99240	3.55	6.1076164	1.178 <sup>2</sup>	5590 <sup>2</sup>	4.31 <sup>2</sup>	0.26 <sup>2</sup>	2.3 <sup>2</sup>	1.045 <sup>2</sup>	...
302.79974	-36.10121	99461	5.32	6.051803	0.7422 <sup>2</sup>	4922 <sup>2</sup>	4.58 <sup>2</sup>	-0.33 <sup>2</sup>	2.7 <sup>2</sup>	0.766 <sup>2</sup>	...
348.32074	57.168354	114622	5.57	6.525711	0.751 <sup>2</sup>	4835 <sup>2</sup>	4.56 <sup>2</sup>	0.09 <sup>2</sup>	1.8 <sup>2</sup>	0.749 <sup>2</sup>	...
53.232685	-9.458262	16537	3.72	3.218021	0.7188 <sup>2</sup>	5146 <sup>2</sup>	4.57 <sup>2</sup>	0.0 <sup>2</sup>	2.4 <sup>2</sup>	0.708 <sup>2</sup>	...
86.11579	-22.448381	27072	3.59	8.969415	1.2 <sup>3</sup>	6241 <sup>4</sup>	4.19 <sup>4</sup>	-0.16 <sup>4</sup>	8.9 <sup>5</sup>	1.4 <sup>6</sup>	...
208.67116	18.397717	67927	2.68	11.341726	2.19 <sup>3</sup>	6201.8 <sup>7</sup>	3.96 <sup>7</sup>	0.13 <sup>7</sup>	11.3 <sup>5</sup>	1.15 <sup>99</sup>	...
247.11726	-70.084404	80686	4.9	12.105072	0.993 <sup>3</sup>	5963 <sup>9</sup>	4.45 <sup>9</sup>	-0.16 <sup>9</sup>	2.4 <sup>5</sup>	1.2 <sup>6,99</sup>	...
4.59542	44.02278	1475	8.13	3.5679882	0.388 <sup>10</sup>	3603 <sup>10</sup>	4.83 <sup>99</sup>	-0.3 <sup>10</sup>	0.6 <sup>11</sup>	0.398 <sup>10</sup>	...
4.60779	44.02734	1475B	11.04	3.5679882	0.1923 <sup>10</sup>	3218 <sup>10</sup>	4.92 <sup>12</sup>	-0.31 <sup>10</sup>	0.1 <sup>11</sup>	0.159 <sup>10</sup>	...
34.26346	34.224243	10644	4.84	10.845987	0.98 <sup>3</sup>	5597 <sup>13</sup>	3.92 <sup>13</sup>	-0.41 <sup>13</sup>	8.6 <sup>5</sup>	1.125 <sup>99</sup>	...
76.37773	-57.472702	23693	4.71	11.650938	1.3 <sup>3</sup>	6069 <sup>9</sup>	4.45 <sup>9</sup>	-0.25 <sup>9</sup>	17.3 <sup>5</sup>	1.2 <sup>6,99</sup>	...
77.91909	-45.018414	24186	8.86	3.9175744	0.43 <sup>3</sup>	3524 <sup>9</sup>	4.87 <sup>9</sup>	-0.5 <sup>9</sup>	5.4 <sup>5</sup>	0.49 <sup>14</sup>	...
82.86415	-3.677229	25878	7.97	5.6908717	0.5735 <sup>15</sup>	3850 <sup>15</sup>	4.71 <sup>12</sup>	0.01 <sup>12</sup>	2.73 <sup>16</sup>	0.633 <sup>10</sup>	...
92.64423	-21.864643	29295	8.15	5.7740054	0.695 <sup>16</sup>	3522 <sup>16</sup>	5.0 <sup>17</sup>	0.06 <sup>16</sup>	1.6 <sup>5</sup>	0.49 <sup>14</sup>	...
152.842425	49.454235	49908	6.6	4.8728194	0.6398 <sup>15</sup>	4176 <sup>15</sup>	4.55 <sup>12</sup>	-0.0512	2.5 <sup>5</sup>	0.707 <sup>10</sup>	...
165.83414	35.96988	54035	7.49	2.54842	0.3924 <sup>15</sup>	3532 <sup>15</sup>	4.82 <sup>12</sup>	-0.4 <sup>12</sup>	1.6 <sup>5</sup>	0.386 <sup>10</sup>	...
217.42896	-62.679485	70890	11.01	1.2947832	0.141 <sup>18</sup>	3054 <sup>19</sup>	5.21 <sup>99</sup>	0.19 <sup>20</sup>	0.0864 <sup>21</sup>	0.118	...
259.05566	-26.546146	84478	6.33	5.9680114	0.72 <sup>3</sup>	4380 <sup>12</sup>	4.71 <sup>12</sup>	-0.2712	3.3 <sup>5</sup>	0.67 <sup>99</sup>	...
297.69583	8.868322	97649	0.76	5.142975	1.5 <sup>3</sup>	7550 <sup>9</sup>	4.13 <sup>9</sup>	-0.24 <sup>9</sup>	211.0 <sup>5</sup>	1.74 <sup>22</sup>	...
316.72476	38.749416	104214	5.2	3.482743	0.728 <sup>3</sup>	4242 <sup>12</sup>	4.7 <sup>12</sup>	-0.3812	2.0 <sup>5</sup>	0.67 <sup>99</sup>	...
316.73026	38.742054	104217	6.05	3.5036085	0.601 <sup>15</sup>	4025 <sup>15</sup>	4.49 <sup>13</sup>	-0.4113	1.6 <sup>5</sup>	0.641 <sup>10</sup>	...
319.31363	-38.867363	105090	6.69								

Table 3.3: The HWO stars and their properties used in these simulations. (1/2)

RA (J2000)	Dec (J2000)	HIP	Vmag	Distance (pc)	Rstar	T <sub>eff</sub>	log(g)	Metallicity	V <sub>sini</sub>	M <sub>star</sub>
129.7987692	65.0209064	42438	5.63	14.4388	0.946	5893	4.53	-0.07	9.3	1.08
137.2127933	33.8822184	44897	5.962	18.9498	1.045	5992	4.5	0.04	4.4	1.08
147.1473806	46.0210074	48113	5.086	18.8226	1.604	5893	4.12	0.1	2.9	1.08
157.6565803	55.9805388	51459 A	4.82	12.9452	1.111	6164	4.43	-0.12	8.6	1.18
178.2448639	37.7186817	57939	6.427	9.1718	0.6	5057	4.64	-1.33	2.9	0.85
188.01761	-16.1960052	61174	4.297	18.2437	1.517	6871	4.242	-0.06	66.8	1.44
188.4356011	41.3574781	61317	4.26	8.4727	1.034	5878	4.42	-0.2	2.8	1.08
198.0132679	-37.8030222	64408	4.847	20.4628	2.116	5688	3.92	0.16	2.7	0.99
218.6700724	29.7451271	71284	4.465	15.756	1.306	6745	4.26	-0.41	8.1	1.39
230.4506246	-48.3176305	75181	5.655	14.7391	1.046	5685	4.37	-0.34	2.4	1.02
238.168921	42.4515175	77760	4.608	15.8975	1.742	5820	4.06	-0.47	3.4	1.08
239.1132612	15.6616168	78072	3.843	11.2537	1.47	6285	4.14	-0.18	9.9	1.25
246.0053797	-39.1929805	80337	5.37	12.8923	0.968	5898	4.53	0.05	2.2	1.07
266.0362631	-51.8340532	86796	5.124	15.6042	1.383	5761	4.25	0.29	3.8	1
271.5988313	-36.0197863	88694 A	5.949	17.1146	0.98	5892	4.38	-0.05	7.3	1.08
272.4059009	38.4577772	88972	6.377	11.0959	0.794	5028	4.5	-0.18	0.6	0.78
291.2424999	11.9444135	95447	5.169	14.922	1.393	5593	4.19	0.38	1.9	0.95
296.6066669	33.7275982	97295 A	5.005	20.9857	1.503	6455	4.26	0.03	8.2	1.29
304.3805338	66.853689	100017	5.922	17.4813	0.999	5930	4.48	-0.1	2.7	1.08
316.730266	38.742044	104217	6.043	3.4964	0.551	4107	4.47	-0.21	1.8	0.63
330.8402234	-56.7859786	108870	4.674	3.6384	0.728	4641	4.29	-0.13	1.4	0.72
2.9334212	-35.1331147	950	5.241	21.7191	1.375	6495	4.3	-0.11	10	1.33
12.5316207	-10.6443289	3909	5.176	15.923	1.153	6208	4.39	-0.12	3.9	1.21
24.9492196	-56.1933179	7751 A	5.764	8.1894	0.775	5025	4.6	-0.24	1.8	0.78
25.6240105	20.2685127	7981	5.241	7.6439	0.828	5204	4.49	-0.04	0.1	0.85
34.7437699	-25.9456872	10798	6.336	12.8347	0.762	5401	4.59	-0.49	2.7	0.94
49.4423477	-62.5753201	15330	5.513	12.0447	0.911	5710	4.5	-0.23	2.7	1.01
49.9817888	-43.069782	15510	4.258	6.0414	0.913	5432	4.46	-0.39	0.9	0.97
56.7120305	-23.2497228	17651	4.21	17.7847	1.678	6685	4.141	0.08	13.2	1.33
71.9012154	-16.9344557	22263	5.489	13.24	0.962	5833	4.49	0	2.9	1.04
84.2911952	-80.4691207	26394	5.666	18.2874	1.153	5982	4.39	0.09	2.7	1.08
86.1157942	-22.4483855	27072 A	3.596	8.905	1.28	6313	4.35	-0.08	7.2	1.23
101.6847372	43.5774246	32480	5.252	16.6106	1.224	6066	4.38	0.11	3.6	1.14
103.0752106	-5.1737127	32984 A	6.562	8.7447	0.687	4767	4.54	0.02	2.7	0.79
105.9888134	-43.608035	34065	5.56	17.0593	1.213	5790	4.33	-0.22	3.6	1.04
108.9589132	47.2399634	35136	5.559	16.8518	1.157	5902	4.32	-0.32	2.9	1.14
103.8277765	25.3756954	33277	5.763	17.4047	1.08	5924	4.44	-0.12	2.9	1.08
219.9020583	-60.8339927	71683	0.002	1.3319	1.231	5776	4.3	0.2	3.2	1.11
240.2610854	33.303511	78459	5.41	17.5108	1.328	5812	4.25	-0.22	1.5	0.97
319.3136211	-38.8673622	105090	6.69	3.9696	0.64	3874	4.78	-0.01	0.9	0.59
12.0957332	5.2806137	3765	5.729	7.4352	0.728	5007	4.62	-0.26	1.8	0.78
72.4600454	6.9612745	22449	3.184	8.0684	1.321	6443	4.3	0.03	15.3	1.25
327.0656298	-47.3036161	107649	5.575	15.5589	1.039	5935	4.41	-0.03	1.8	1.08
156.0987749	-74.0316121	50954	3.99	16.2232	1.587	6905	4.228	0.05	40.7	1.43
199.6013083	-18.3111938	64924	4.735	8.5344	0.982	5552	4.41	-0.01	1.8	0.97
236.6108925	7.3530687	77257	4.422	11.9159	1.356	5898	4.18	-0.01	3.3	1.09
303.8224641	-27.0329754	99825	5.73	8.8116	0.818	5087	4.48	0.03	0.6	0.77
1.6532667	29.0215035	544	6.093	13.7662	0.889	5491	4.55	0.11	3.6	0.94
49.553412	-62.5063624	15371	5.232	12.0394	0.983	5847	4.46	-0.23	2.7	1.07
175.2625678	34.2016338	56997	5.308	9.5762	0.862	5491	4.54	-0.05	2.3	0.94
259.0556767	-26.5461491	84478	6.295	5.9537	0.66	4476	4.57	-0.21	3.3	0.68
261.2504073	67.306708	85235	6.443	12.7919	0.761	5302	4.58	-0.46	1.3	0.87
311.5238859	-25.2708975	102485	4.137	14.6334	1.42	6638	4.238	0.04	42.2	1.33
332.5365841	-32.5484084	109422	4.94	18.4579	1.405	6364	4.2	0.1	12.6	1.25
80.6397108	79.2311507	25110	5.08	20.7858	1.496	6354	4.2	0.12	11.7	1.21
85.334732	53.481058	26779	6.2	12.2701	0.843	5226	4.52	0.1	3	0.88
133.5747796	-5.4344595	43726	6.008	16.8465	0.983	5780	4.49	0.1	2.4	1.02
226.8252747	24.8691943	73996	4.94	19.536	1.451	6435	4.19	-0.02	43	1.33
273.4743034	64.3972849	89348	4.99	23.1569	1.624	6473	4.09	-0.29	9.7	1.33
349.1762648	53.2134748	114924	5.58	20.6102	1.286	6084	4.19	0.03	5.4	1.18
94.1109129	12.2721632	29800	5.04	19.5879	1.364	6480	4.307	-0.03	17.1	1.33
145.5600675	-23.9155672	47592	4.914	14.9515	1.233	6163	4.34	-0.06	5.3	1.14
224.36667	-21.4154798	73184	5.724	5.8864	0.732	4632	4.49	0.02	3.5	0.72
293.0899592	69.6611766	96100	4.672	5.7639	0.782	5298	4.52	-0.21	1.8	0.87
75.2041639	-5.7536734	23311	6.202	8.844	0.776	4810	4.46	0.31	1.4	0.75
81.106097	17.3835351	25278	5.009	14.5792	1.182	6131	4.29	0.01	14.4	1.18
49.8404013	3.3701986	15457	4.85	9.2762	0.946	5709	4.51	0.04	4.5	0.98
118.0652624	-34.7054399	38423 A	5.085	18.3274	1.246	6525	4.276	-0.08	48.4	1.33
41.2758283	-18.5726228	12843	4.465	14.2764	1.345	6330	4.36	0.07	27.3	1.21
321.6108541	-65.3661981	105858	4.229	9.2584	1.086	6095	4.3	-0.7	3.4	1.14
26.9368101	63.8525031	8362	5.626	10.0411	0.834	5358	4.48	0.03	0.9	0.9
272.6089738	-62.00222	89042	5.469	17.7532	1.238	5951	4.29	-0.07	4.2	1.08
5.0177443	-64.8747937	1599	4.223	8.6071	1.063	5932	4.43	-0.21	4.9	1.11
60.6531011	-0.2689222	18859	5.361	18.707	1.206	6268	4.34	0.1	17.7	1.21
62.1525715	38.0397386	19335	5.522	21.1919	1.242	6381	4.61	0.19	16.2	1.18
25.6221438	-53.740831	7978	5.52	17.3488	1.095	6155	4.44	-0.04	5.4	1.14
354.9876724	5.626291	116771	4.132	13.7137	1.591	6200	4.15	-0.14	6.3	1.21
265.8574731	-21.6831941	86736	4.86	17.6523	1.335	6404	4.26	-0.11	11.7	1.33
300.9058545	29.8968035	98767	5.745	16.0035	1.162	5563	4.32	0.22	0.8	0.96
348.320729	57.1683566	114622	5.54	6.5418	0.723	4874	4.56	0.06	1.8	0.75
13.2674852	61.123972	4151	4.8	18.8007	1.656	6105	4.11	0.05	8.6	1.18
349.2403645	-62.0011978	114948	5.655	20.4426	1.16	6280	4.37	-0.03	7.6	1.25

Table 3.4: The HWO stars and their properties used in these simulations. (2/2)

RA (J2000)	Dec (J2000)	HIP	Vmag	Distance (pc)	Rstar	T <sub>eff</sub>	log(g)	Metallicity	Vsin <i>i</i>	Mstar
18.7963393	-45.5316646	5862	4.966	15.2609	1.263	6110	4.34	0.16	4.7	1.14
302.1817036	-66.1820674	99240	3.556	6.0993	1.198	5576	4.29	0.35	2	0.94
165.8341451	35.9698823	54035	7.421	2.5461	0.363	3601	4.87	-0.42	1.6	0.44
209.3835765	61.4928612	68184	6.488	10.0672	0.759	4867	4.56	0.2	0.75	
26.0170131	-15.9374799	8102	3.496	3.6522	0.826	5356	4.53	-0.51	0.9	0.94
87.1455844	-4.0946449	27435	5.973	15.2104	0.922	5731	4.47	-0.22	2.7	1.02
249.0893737	-2.324587	81300	5.764	9.8939	0.818	5262	4.52	0.03	1.6	0.87
125.0160865	27.217705	40843	5.13	18.2233	1.32	6269	4.3	-0.28	4.3	1.25
316.7247483	38.7494173	104214	5.211	3.4966	0.637	4441	4.51	-0.13	1.8	0.68
130.8251265	-38.8823808	42808	6.556	11.1917	0.753	4992	4.6	0.01	2.7	0.76
301.3865229	-67.3208961	98959	6.07	17.9323	1.033	5730	4.42	-0.19	1.8	1.02
11.4399705	-47.5519841	3583 A	5.795	15.0487	0.924	5887	4.65	-0.04	3.6	0.98
55.8120856	-9.7633919	17378	3.537	9.0888	2.245	5045	3.78	0.09	1	0.87
176.6294689	-40.5003572	57443 A	4.893	9.3195	0.97	5618	4.44	-0.31	2.7	1.02
164.8665531	40.4302557	53721	5.037	13.8875	1.21	5880	4.3	0.02	3.1	1.07
260.1648644	32.4677439	84862	5.385	14.5863	1.163	5704	4.33	-0.39	1.6	0.94
346.4668158	-35.8530709	114046	7.33	3.2871	0.47	3680	4.88	-0.22	0.9	0.49
43.1338674	-12.7697133	13402	6.038	10.3605	0.78	5199	4.55	0.07	6.2	0.82
93.7119848	19.1564479	29650	5.2	21.7763	1.335	6539	4.29	0.03	8.6	1.29
79.7853144	40.0909514	24813	4.705	12.5625	1.279	5854	4.24	0.06	1.3	1.08
191.2475207	39.2789162	62207	5.958	17.5565	1.004	5889	4.38	-0.53	1.8	1.14
197.9683076	27.878184	64394	4.23	9.1975	1.079	5996	4.42	0.06	4.5	1.11
152.8422498	49.4542364	49908	6.55	4.8706	0.636	4097	4.64	0.21	2.7	0.63
6.4377932	-77.2542461	2021	2.82	7.4588	1.844	5806	4	-0.12	3.4	1.08
124.599779	-12.6321714	40693	5.951	12.5794	0.883	5423	4.53	-0.03	2.2	0.93
243.9052928	-8.3694395	79672	5.496	14.1369	1.041	5785	4.43	0.03	2.7	1.02
177.6738271	1.7647226	57757	3.602	10.929	1.679	6123	4.13	0.13	3.6	1.14
326.1305414	14.7719398	107350	5.942	18.133	1.006	5939	4.45	-0.06	9.9	1.08
128.2145653	-31.5008514	41926	6.378	12.1643	0.765	5261	4.56	-0.39	1.8	0.85
344.100219	-31.565564	113283	6.446	7.6015	0.697	4601	4.68	0.04	2.6	0.72
40.6394444	-50.8002931	12653	5.395	17.3572	1.158	6157	4.43	0.15	5.4	1.14
53.2326854	-9.458261	16537	3.718	3.2198	0.746	5098	4.55	-0.08	1.9	0.78
54.2182654	0.4016645	16852	4.291	13.9204	1.623	5996	4.1	-0.08	3.7	1.14
265.0992732	-49.4155831	86486	4.762	20.9624	1.621	6620	4.161	-0.22	14	1.39
2.8160752	-15.4679779	910	4.895	18.8861	1.505	6190	4.09	-0.36	4.8	1.18
47.2667471	49.6132784	14632	4.05	10.5774	1.404	5952	4.22	0.09	3.6	1.08
137.5981111	67.1340172	45038 A	4.809	20.5169	1.68	6325	4.07	-0.02	5.8	1.21
157.8409203	-53.7154836	51523	4.897	22.0616	1.845	6155	3.83	-0.4	8.3	1.16
222.8474519	19.1004499	72659 A	4.54	6.7536	0.823	5487	4.54	-0.14	3.5	0.96
258.8374326	-26.602826	84405 B	5.11	5.9478	0.725	5144	4.59	-0.22	4.4	0.85
259.7659898	-46.6362334	84720 A	5.472	8.7911	0.817	5235	4.56	-0.35	1.8	0.9
260.2515605	-21.1129364	84893 A	4.389	17.5187	1.484	6756	4.254	-0.25	18.9	1.44
314.1972153	-26.2963779	103389	5.709	21.1021	1.182	6270	4.35	-0.01	13.7	1.2
336.2348695	-57.7974559	110649 A	5.318	20.3398	1.717	5660	4.13	-0.03	1.8	1.02
338.6734824	-20.7082158	111449 A	5.21	23.0205	1.419	6605	4.274	0.03	34.7	1.35
9.8408558	21.2504758	3093 A	5.863	11.1081	0.898	5203	4.47	0.14	1.8	0.86
41.0499442	49.22844485	12777 A	4.1	11.1501	1.273	6263	4.39	0.01	8.6	1.21
48.0188742	-28.987622	14879 A	3.8	13.999	1.79	6195	3.95	-0.22	5.7	1.25
63.8179984	-7.6528697	19849 A	4.415	5.0098	0.809	5133	4.52	-0.29	0.9	0.86
119.4454762	-60.3030719	38908 A	5.592	16.1718	1.052	5997	4.52	-0.31	2.7	1.11
18.9420379	-68.8759448	5896	4.912	23.2606	1.588	6436	4.021	0.03	61.1	1.35
297.7568487	10.4157201	97675 A	5.122	19.4881	1.491	6134	4.22	0.12	2.8	1.25
92.5603024	-74.753044	29271 A	5.076	10.2129	0.99	5594	4.46	0.1	2.3	0.96
236.8712542	-37.9163119	77358 A	6.012	15.2465	0.959	5602	4.47	0.1	1.8	0.96
271.3644289	2.498947	88601 B	6.061	5.1225	0.674	4475	4.64	0.03	3.7	0.78
24.9481863	-56.1964481	7751 B	5.876	8.1965	0.703	5111	4.63	-0.19	2.5	0.77
112.4831549	49.6724594	36439	5.35	20.4021	1.292	6349	4.29	-0.28	9.7	1.16
157.7696164	82.5586517	51502 A	5.25	22.7302	1.316	6758	4.389	-0.16	94.2	1.39
182.1034022	-24.7288751	59199 A	4.025	14.9365	1.439	6990	4.192	-0.13	23.8	1.5
271.363535	2.5001463	88601 A	4.22	5.1133	0.865	5298	4.52	0.06	4.3	0.88
86.1105697	-22.4218374	27072 B	6.142	8.8916	0.719	4950	4.33	-0.14	4.3	0.81
154.93403	19.4709128	50564	4.792	21.2199	1.669	6410	4.123	0.09	17.5	1.35
199.2127143	17.017178	64797 A	6.55	10.9869	0.781	4843	4.47	-0.18	3.3	0.76
216.2991543	51.8507436	70497 A	4.052	14.5307	1.696	6280	4.23	-0.03	28.6	1.33
12.2762275	57.8151773	3821 A	3.444	5.0098	1.068	5907	4.41	-0.28	3.4	1.14
101.1558951	79.5648107	32439 A	5.44	18.2023	1.17	6204	4.43	-0.1	4.5	1.18
222.8460153	19.1019133	72659 B	6.979	6.7486	0.652	4288	4.636	0.144	4.6	0.67
302.7997449	-36.1012088	99461 A	5.297	6.0122	0.715	4980	4.62	-0.52	0	0.76
150.252737	31.9236703	49081 A	5.378	14.9263	1.186	5743	4.3	0.2	1.8	1
236.0075774	2.5151668	77052 A	5.869	14.7927	0.942	5682	4.47	0.05	4.1	0.94
52.3444893	-62.9375289	16245 A	4.703	21.7816	1.658	6662	4.31	-0.17	13.1	1.32
76.8625232	18.6450499	23835	4.915	15.9172	1.594	5691	4.06	-0.2	2.36	1.04
258.8365985	-26.6016992	84405 A	5.07	5.9523	0.724	5132	4.53	-0.22	4.3	0.85
173.6228602	-32.8313397	56452 A	5.956	9.559	0.751	5196	4.6	-0.4	0.9	0.88
219.8960963	-60.8375276	71681	1.35	1.3319	0.859	5244	4.54	0.24	3.52	0.94
143.9145925	35.8101325	47080 A	5.402	11.2348	0.969	5518	4.44	0.34	2.3	0.94
133.1492129	28.3308208	43587 A	5.96	12.5868	0.948	5292	4.4	0.32	2.2	0.95
198.5631031	-59.1032372	64583 A	4.913	18.24	1.475	6238	4.23	-0.31	13.8	1.25
24.1993398	41.4054587	7513 A	4.1	13.4916	1.611	6154	4.17	0.08	9	1.18
76.377732	-57.4727047	23693	4.701	11.6927	1.064	6158	4.43	-0.18	12	1.14
214.753732	-25.815425	69965 A	5.872	17.9888	0.978	6120	4.41	-0.68	3.6	1.11
341.6732494	12.1728858	112447 A	4.2	16.1509	1.852	6193	4.07	-0.27	7.7	1.25

### 3.3.2 Exposure Time/Precision

In principle, it is possible to figure out exposure times “on the fly”. This is not done due to: the expectation that it would take too long/be too computationally intensive, and that the current atmospheric model does not have a very large effect on precision at high airmass. So a single “good but imperfect” time is used, with assumptions about what that should be.

The aspects of instrumentation considered by Beatty are: wavelength coverage, and the resolution of the spectrograph. This is expanded somewhat in that the telescope and instrument are simulated to the point of basic signal to noise considerations on each pixel, and exposure and readout times.

The readout noise formula is:

$$\frac{photons \cdot gain}{pixels \cdot \sqrt{photons \cdot \frac{gain}{pixels} + (gain \cdot dnoise \cdot 4.4 \cdot exposures)^2 + (gain \cdot darkcurrent \cdot exptime)^2}} \quad (3.1)$$

A generic/other noise term is also included, which describes all unmodeled noise and is treated as an undefined part of an instrument’s noise budget. The generic/other noise is added in quadrature with the (readout) noise to give an overall noise level, which is assumed to be the standard deviation of a Gaussian. A random “measurement” is generated from this overall noise level, and then used for fitting once actual signals have been added in.

Table 3.5: The primary telescope and spectrograph combinations considered. While specific telescopes are listed, these are nominal ones chosen as representative 4/8/12 m class observatories. The collecting area of the 2x8.4 m is simulated as a single 11.78 m telescope.

Telescope	Diameter (m)	Instrument	Wavelength Range (Å)	Nominal Precision (cm/s)
WIYN	3.5	NEID	3800 - 9300	27
LBT	8.4x2	NIRS	9700 - 13000	40
WIYN	3.5	Super NEID	3800 - 9300	3
LBT	8.4x2	Super NEID	3800 - 9300	3
LBT	8.4x2	Super NIRS	9700 - 13000	3

### 3.3.3 Exposure Time Estimation

Exposure time calculation is done via scaling assumptions in the high SNR regime. An initial “guess” is performed by finding the RV precision and SNR at the site when the detector is saturated at whatever wavelength the star is brightest at. To make the guess closer to reality, the signal is attenuated through the airmass at  $10^\circ$  off of zenith, and readout noise is doubled. These seemingly ad-hoc considerations are to consider that the actual exposure is likely to be a co-add of several shorter ones and at more than one airmass.

The actual exposure time is then rescaled by a factor of  $\left(\frac{\text{guessRV}}{\text{targetRV}}\right)^2$ . If there is a signal to noise requirement, SNR is rescaled in the same way, and the longer time of it or radial velocity is used.

Times under a minimum are increased to that minimum so as to average out over p-mode oscillations. This is to minimize the effect of this noise source and convert it from correlated to uncorrelated. In previous work [176], we used a fixed 5-minute (and then for comparison a fixed 10-minute) minimum. A more detailed look is appropriate here, as is calculating the actual p-mode timescales using our in-hand stellar properties.

As these times vary per-star, we look at the effects of instituting two fixed (5 minute and 10 minute), and two variable minimum times per star. The first of the variable versions scales with a star’s dynamical timescale  $\tau \sim \sqrt{R^3/M}$ , where we define the sun as having a time of 300 seconds:

$$T_{min} = 300 \sqrt{\frac{(R/R_\odot)^3}{M/M_\odot}} \quad (3.2)$$

This is in contrast with [66] and [52], which use surface gravity and effective temperature to find the pulsation frequency:

$$\nu = 3100 \mu Hz \left(\frac{g}{g_\odot}\right)^1 \left(\frac{T_{eff}}{T_{eff,\odot}}\right)^{-0.5} \quad (3.3)$$

Here,  $g$  is the actual surface gravity, and not  $\log(g)$ .

Our minimum period is then  $\nu^{-1}$ . For the Sun this is 322 s, which is within 10% of the previous scaling. As shown in sections 3.7, 3.6, 3.8, outside of the short exposure limit, we don't find particularly large differences in results for any p-mode compensation algorithm.

These just generate the “open shutter” time, so the number of exposures to avoid saturating the detector is counted, and the readout times added in to give a total exposure time. We do not impose any upper limit on exposure times, so depending on the input parameters, impractically large ones can be generated. That these stars rarely or never be observed is discussed in section 3.9, and points to how EPRV target selection must be done with care even in the absence of stellar activity.

### 3.3.4 Atmospheric Effects

Our atmospheric absorption/scattering model uses Rayleigh scattering plus a small baseline.

$$\tau = 0.09 + \left( \frac{3080\text{\AA}}{\lambda} \right)^4 \quad (3.4)$$

This relation was found by fitting measurements from CFHT at Mauna Kea, and Texas A&M University [194]. Sky brightness and line absorption are not considered.

The above gives an optical depth at a specific wavelength and 1 airmass. actual absorption considers altitude and zenith angle using simple isothermal (default scale height 8400 m), and slab ( $1/\cos(\theta)$ ) models, respectively.

This is sufficient for ultraviolet, visible, and the nearest infrared wavelengths, but breaks down once water absorption starts to matter (approximately 890 nm). Expanding into this range would be preferable, but would require line-by-line analysis instead of the current continuum model. This is a consideration for future work, but would significantly increase complexity.

---

<https://www.gemini.edu/sciops telescopes-and-sites/observing-condition-constraints/extinction>

Beyond reducing the strength of RV information, line-based absorption also introduces uncertainties which are not modeled here. Scattered/absorbed light is assumed to simply be lost, and any errors in lines from microtellurics are assumed to be perfectly modeled. We partially account for microtelluric errors with nominal noise values in section 3.6.4.

Clouds/hazes are not considered (beyond the wavelength-independent portion of the absorption acting as particulates), nor does the model include weather or season variations in sky quality. A night is assumed to be perfectly clear, or unusable/no observations are possible.

### 3.3.5 Stellar Activity

We do not directly model any form of stellar activity (eg: oscillations, granulation, spots/plages). Indirectly, we both choose a target list to contain relatively inactive stars (eg: low  $R_{HK}$  values), and our exposure times compensate for p-mode oscillations (see 3.3.3). We expect that observation campaigns with high cadence and a large number of observations can better model activity to reduce “jitter”, but this lack of direct modeling can lead to our expected sensitivities and SNRs being optimistic by a factor of several.

In contrast, [52] which models stellar variability with 4 terms: 1 for activity, 1 for oscillation, and 2 for granulation. The active regions use a solar-specific model, while oscillations and granulations consider spectral type. Our p-mode calculations herein substantially addresses the oscillation portion of the noise, as we look at: Luhn’s timescales, an alternate timescale that also scales with spectral type, and 2 fixed ones. Additional strategies are needed for the other forms of stellar variability. Both more realistic active regions, and observing strategies to mitigate active regions and granulation are deferred for future work.

## 3.4 Dispatch Scheduler (Survey Simulations)

The dispatch scheduler simulates an observational campaign to generate observation time series for later use. Our version is derived from the MINERVA scheduler [42, 58]. The scheduler takes a list of targets with name, RA, Dec, and observation times as inputs, and generates a time series of observations for each target (as well as the Sun and each target’s rise and set times). It also generates a nightly summary file containing: start and end of the night, weather, number of times each star was observed, amount of time spent on each star, and if the star was observable at all given our constraints. Constraints define the ordering and prioritization of targets to observe. These observation constraints can be divided into: natural, observatory, and prioritization weights.

For natural constraints, we consider: latitude, longitude, local weather (fraction of clear nights), target acquisition, elevation, and local horizon. Calculated sun-rise/set times are used, and a minimum distance from the Moon is specified (ephemeris via Astropy). For the observatory constraints, we consider local horizon, acquisition/repointing time, and observation/readout time.

As per the name, we use a dispatch scheduler prioritization scheme. The scheduler determines target choices “on the fly”, and we consider several different prioritization weighting options that we discuss in Section 3.4.1.

A typical night works as follows:

- Advance time to “full dark” (configurable, by default astronomical twilight, where the sun is 12 degrees below the horizon)
- Check to see if the night is clear, or lost due to weather
- If the night is cloudy, advance time to dawn
- If the night is clear, prep target list (determining which stars are observable due to sufficient separation from the moon, and being above the horizon)

---

Available at [https://github.com/pdn4kd/dispatch\\_scheduler](https://github.com/pdn4kd/dispatch_scheduler)

- Begin observation loop

Observation loop:

- Generate weightings for the target stars
- Pick highest weighted target
- If the target has a positive weight, observe it for the duration specified
- Wait five minutes (this is done whether or not a target is observed.)
- Repeat until dawn

Observations are recorded as they are taken. If no target has a positive weight, this means that no observations are taken with the telescope, and we record the telescope down-time separately. At dawn, we record the Sun and target rise and set times, a nightly summary of target observations observability and weather, and move to the next night. Dawn can be specified to mean that the sun is still below the horizon, depending on what settings are specified. Days/nights will alternate until the observation campaign is completed.

Finally, we assume that 100% of telescope time is available for a RV survey. Treating the weather as worse/lower probability of a clear night can effectively simulate random queuing without affecting the weighting system. Implementing bright/dark time scheduling would be a subject for future work, as the exact definition varies between observatories.

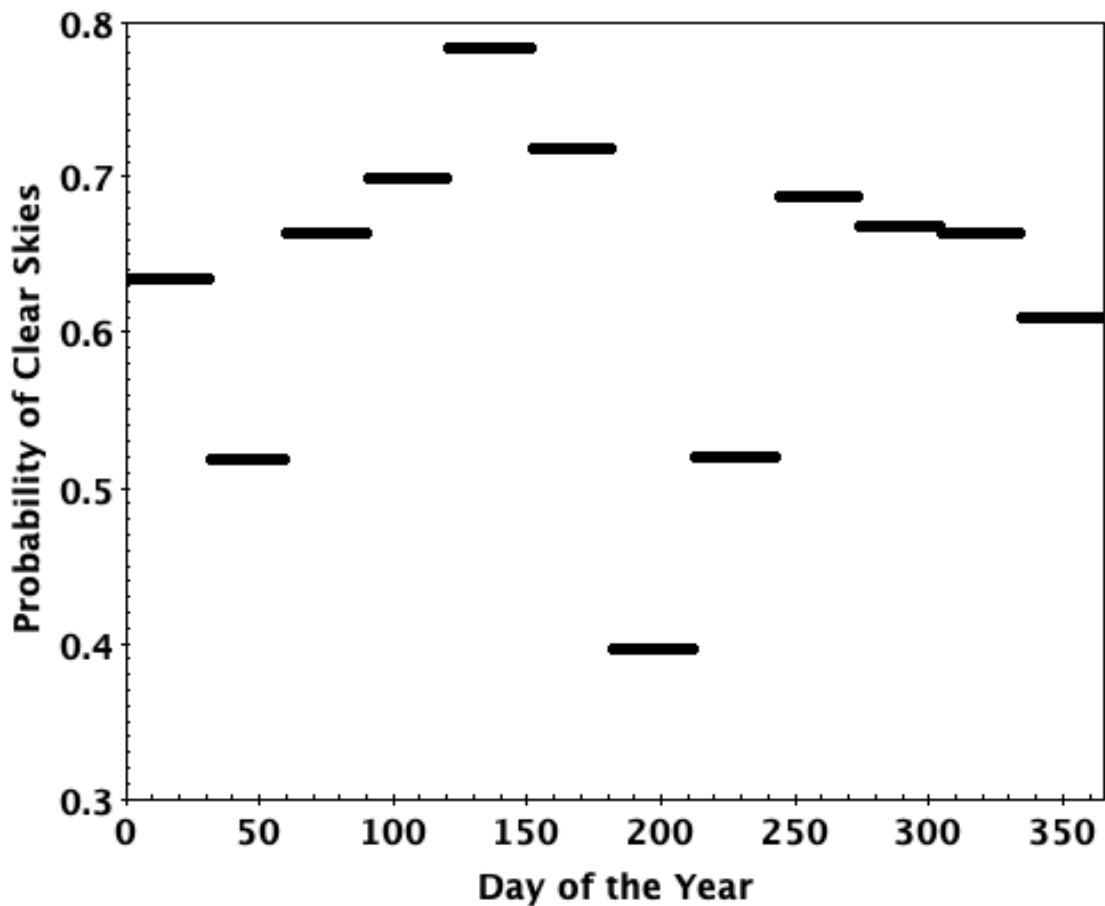


Figure 3.1: Monthly WIYN observing and weather statistics from 1999 to 2006. Adapted from [http://www-kpno.kpno.noao.edu/Images/wiynWeather\\_stats.jpeg](http://www-kpno.kpno.noao.edu/Images/wiynWeather_stats.jpeg)

### 3.4.1 Target Weighting

As we do not plan our observations in advance, we need to figure out which star to observe multiple times per night. Our weighting constraints were chosen to maximize the total number of observations while minimizing the variance between stars. More observations are of obvious value, but we also expect that higher planet yields will be best served by relatively even survey depth. To achieve these, we focused on weighting schemes using hour angle/meridian distance, as well as time since last observation.

Hour angle weighting is an attempt to maximize observation quality without penalizing stars at unfavorable declinations. It varies linearly from 1 at the meridian to 0 at the horizon. The time since last observation weighting is the number of days since last observation after the minimum separation between observations has passed. Before this it is set to 0. Regardless of other considerations, “unobservable” stars are assigned a weight of -999. Observable is defined as: above the nominal horizon for the duration of the observation, sufficiently far from the moon (10 degrees by default), and that the observation will finish before sunrise.

After iterating through different versions of these weightings (see section [3.9.4](#)), we settled on using hour angle multiplied with time since last observation, with a minimum time of 2 hours. These combined weighting will in practice prioritize stars that have not been observed in a given night that are anywhere within a telescope’s pointing limits over ones that have at the zenith.

## 3.5 Results (Overview)

In this section, we discuss the overall outline of the results, and what we look at in terms of outcomes. First we introduce figure of merit we use for detection efficiency (section 3.5.1), which along with exposure times and numbers of observations, we will use for all subsequent simulations that are not directly testing the survey simulation code. We then show a few example outputs before proceeding with the results of different target lists and simulation parameters:

We show example timeseries results in in Figure 3.2, before going into general target list results.

We primarily focus on the HWO target list. All results are for a surface gravity/effective temperature p-mode timescale and hour angle with 2 hour minimum observation separation target weighting. For this we show: exposure times, observations, and how those correlate; exposure times as a function of selected stellar parameters; observations as a function of selected stellar parameters. We show our detection heuristic/figure of merit in some plots, as well as how those detections are degraded by uncorrected telluric effects.

Detailed reasons for why we choose a specific p-mode compensation method and target weighting are described in 3.9.4.

The EPRV and HabEx target lists are then covered briefly, with more of their differences and how target list selection changes results in 3.9.6.

### 3.5.1 Figure of merit: planet semi-amplitude sensitivity and detection SNR

Herein, we use a figure of merit for detecting a plausible planet with some simplifying assumptions: For an uninformed survey where the period observed is much longer than than the planet, the planet's orbit is circular and edge-on, and the distribution of observations

is random/planet phase is unknown [18]:

$$SNR = \frac{K}{\sigma} \sqrt{\frac{N_{\text{obs}}}{2}} \quad (3.5)$$

$$K = SNR \cdot \sigma \sqrt{\frac{2}{N_{\text{obs}}}} \quad (3.6)$$

The noise term,  $\sigma$ , can be broken down into multiple noise sources added in quadrature (photon, instrument, tellurics, etc). eg:

$$SNR = \frac{K}{\sqrt{2}} \sqrt{\frac{N_{\text{obs}}}{\sigma_{\text{instrument}}^2 + \sigma_{\text{photon}}^2 + \sigma_{\text{atmosphere}}^2}} \quad (3.7)$$

$$K = SNR \cdot \sqrt{(\sigma_{\text{instrument}}^2 + \sigma_{\text{photon}}^2 + \sigma_{\text{atmosphere}}^2) \frac{2}{N_{\text{obs}}}} \quad (3.8)$$

For analysis in this paper, we use equations 3.7 and 3.8, with the atmospheric noise term being zero in all sections except for the telluric noise ones.

### 3.5.2 Example Timeseries

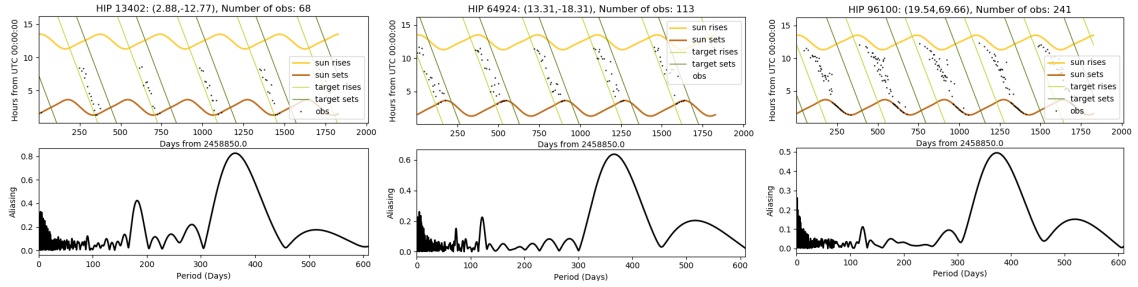


Figure 3.2: Example survey results from a 5 years/100% time with Super NEID (3 cm/s) on the WIYN. The top graph shows target rise and set times, sunrise and sunset times, and target observations over the course of the survey. The bottom graph shows potential aliasing/false planet signals from the distribution of observations over various orbital periods. Patterns in observations as a result of long exposure times and changing weighting are visible, as well sensitivity limitations for some planets.

## 3.6 Results (HWO target list)

### 3.6.1 Exposure Times and Observations

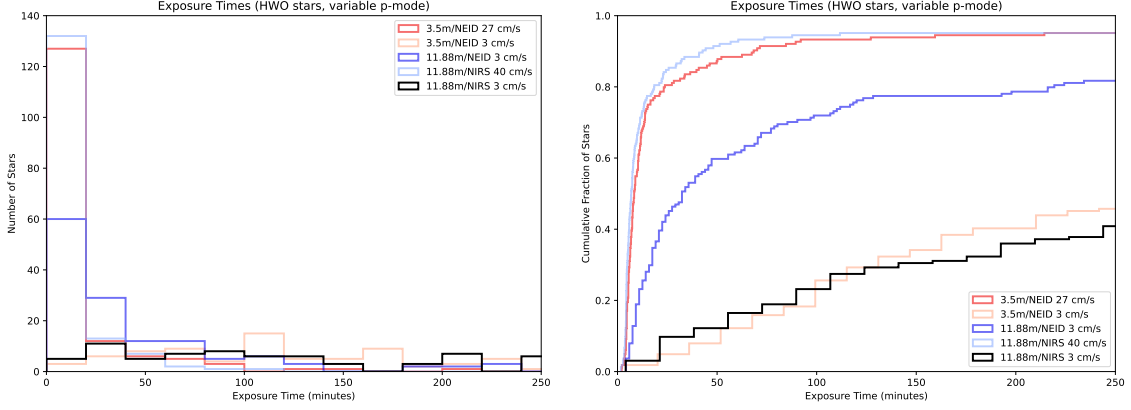


Figure 3.3: Exposure times as histograms (left) and cumulative distribution functions (right) for every star in our telescope/instrument combinations. There is a tail of stars with very long exposure times (and which are therefore difficult to observe at high precision). The PDF appears the same for all 3 sets of stars due to the current bin size of 20 minutes, as whatever chosen p-mode correction has little effect beyond that. Due to finer bin sizes, the CDFs do show that the exact distribution of exposure times is shuffled around somewhat, though the effect is again small (and largely confined to telescope/instrument/precision combinations that skew to shorter exposure times).

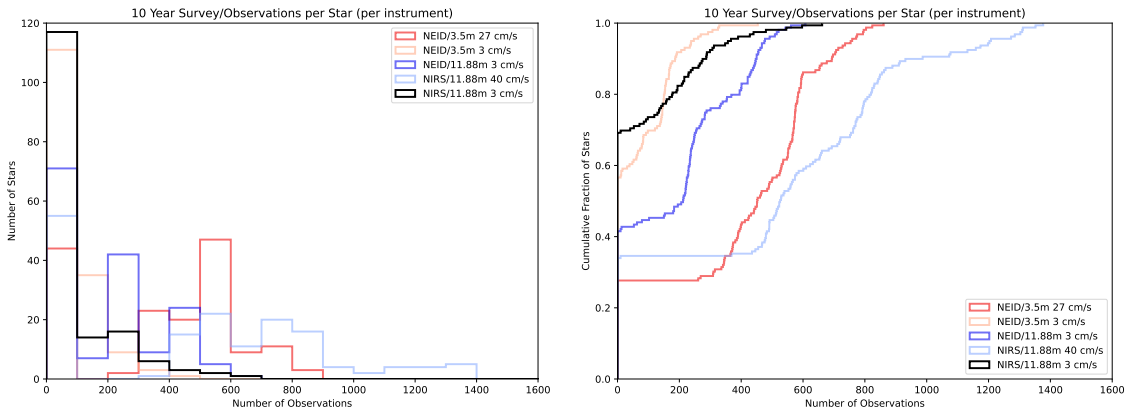


Figure 3.4: Histograms of total number of observations for the different telescope/instrument combinations as both PDFs (left) and CDFs (right). Differences between different architectures are quite obvious, though the ones between different p-mode compensation methods are subtle (and not apparent for the architectures with longer exposure times and fewer observations).

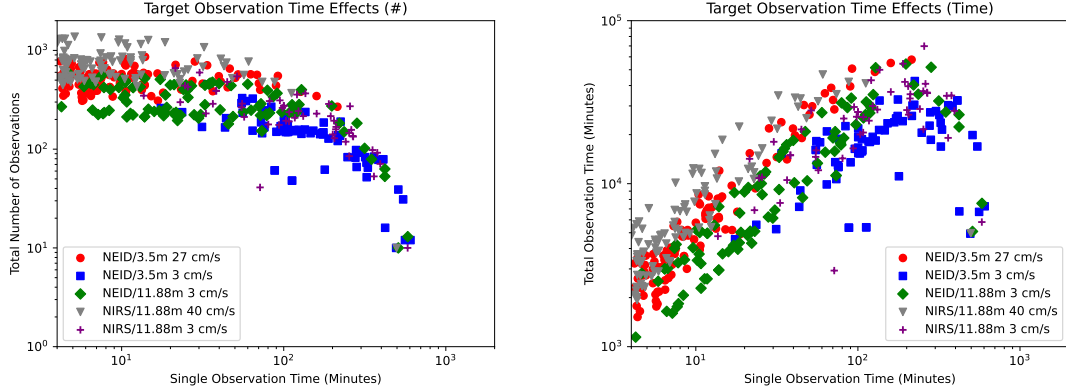


Figure 3.5: Total number of observations (left) and total time spent observing (right) for each star and telescope/instrument combination as a function of exposure time.

### 3.6.2 Exposure Times and Stellar Parameters

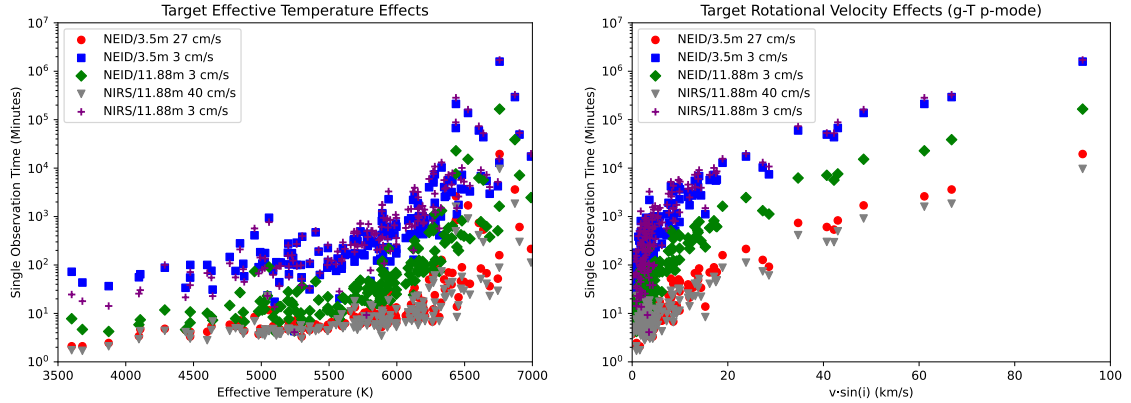


Figure 3.6: Exposure times as a function of effective temperature (left), and rotational velocity (right), for the gravity/effective temperature P-mode compensation. While we see clear trends of hotter/faster rotating stars being harder to observe, the choice of telescope/instrument/precision usually has a larger effect.

### 3.6.3 Right Ascension and Declination

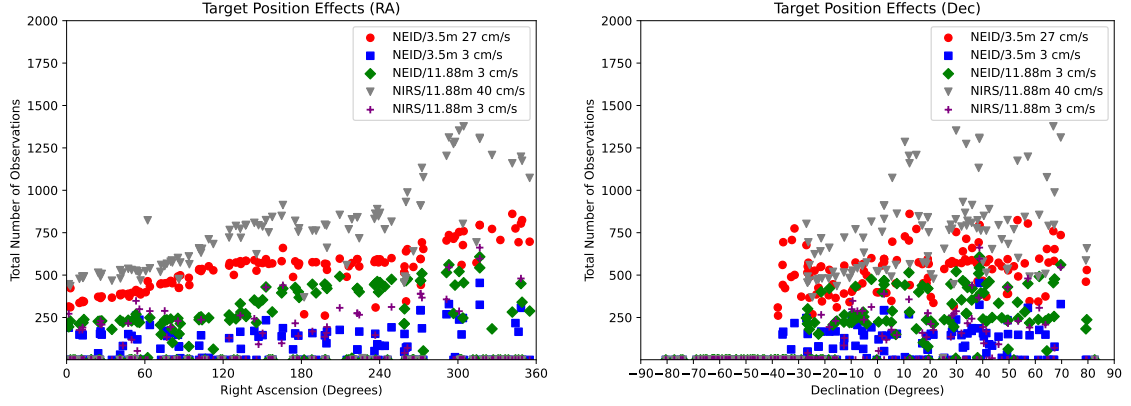


Figure 3.7: Total number of observations per star as a function of Right Ascension (left) and Declination (right). There is a clear trend in right ascension, we believe from a combination of night length and weather (though it is suppressed for longer exposure time telescope/instrument/precision combinations). That the larger peak corresponds with stars that have the longest time above the horizon in late summer (around 300-330 degrees) and not winter/early spring (when the weather is better and nights longer) is surprising. Declination does not show a clear trend, with number of observations per star being relatively flat north of about -40 degrees. Below that, stars are never observed.

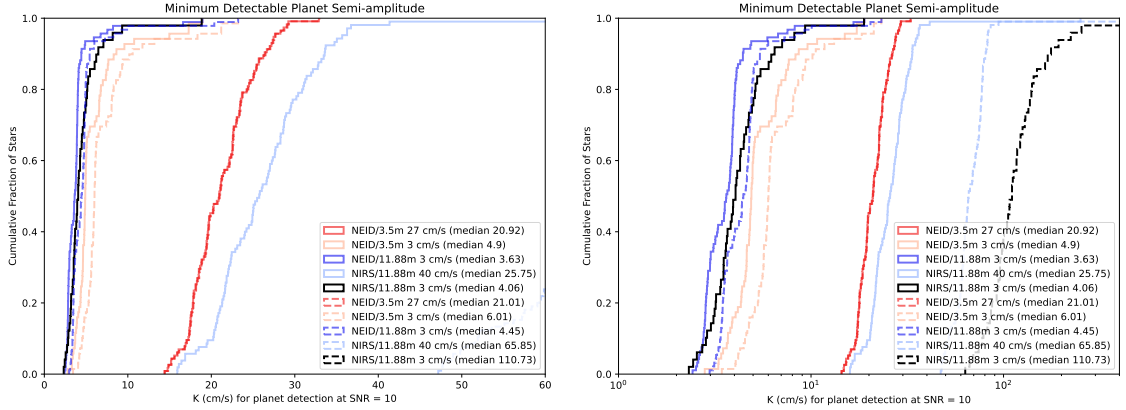


Figure 3.8: CDFs of minimum detectable reflex velocity ( $K$ , in cm/s) of a planet at  $\text{SNR} = 10$  over our telescope/instrument combinations at multiple scales. The results with no microtellurics are shown as solid lines, while the telluric noise are the dotted lines.

### 3.6.4 Telluric Corrections

Despite our earlier atmospheric assumptions, earth's atmosphere has many shallow lines that are difficult to correct for, especially in the infrared. To simulate this, we consider an additional noise term added in quadrature with the instrument and photon noise ones. We choose values of 3 cm/s for the visible spectrograph and 115 cm/s for the NIR spectrograph, which are in line with existing EPRV systems. [195]

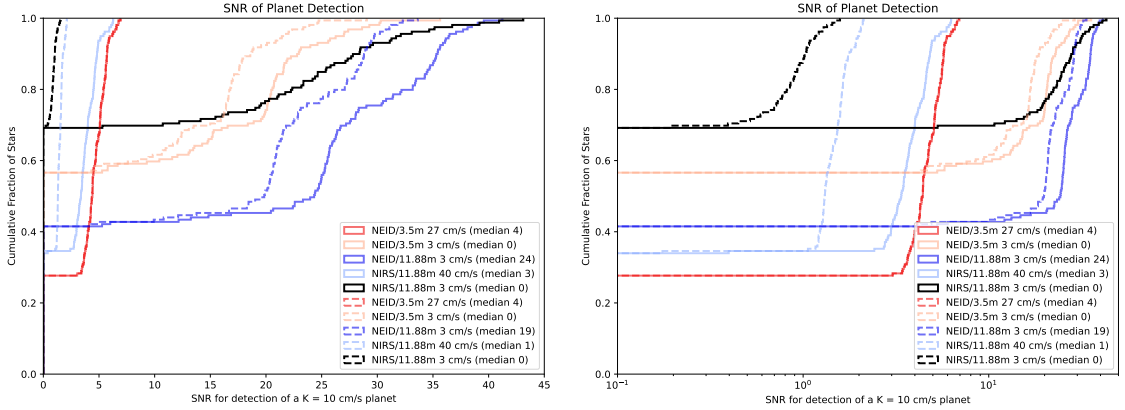


Figure 3.9: CDFs of minimum detectable reflex velocity ( $K$ , in cm/s) of a planet at  $\text{SNR} = 10$  over our telescope/instrument combinations at multiple scales. The results with no microtellurics are shown as solid lines, while the telluric noise are the dotted lines.

As our assumed noise is smaller than the instrument and photon noise sources in all but the most optimistic visible surveys, microtellurics have little effect. In contrast, this noise source dominates over all others in the NIR (being far larger than the instrument or photon components, even in the most pessimistic cases), and must be better accounted for if this wavelength range is to be useful in the EPRV era.

### 3.7 Results (HabEx target list)

While a full set of simulations were done, for brevity we only post the most relevant ones, using the g-T p-mode compensation. We do not go over the results in particular detail, though some of the differences are discussed in section 3.9.

The distributions of observations are largely similar between different p-mode compensation methods, with the exception of the fixed 10-minute case for otherwise short exposure times (NEID, 3.5 m, 27 cm/s and NIRS, 11.88 m, 40 cm/s). For those two telescope/instrument/precision combinations, a long fixed p-mode timescale increases the exposure times for most of the stars, and causes a noticeable reduction in the number of observations.

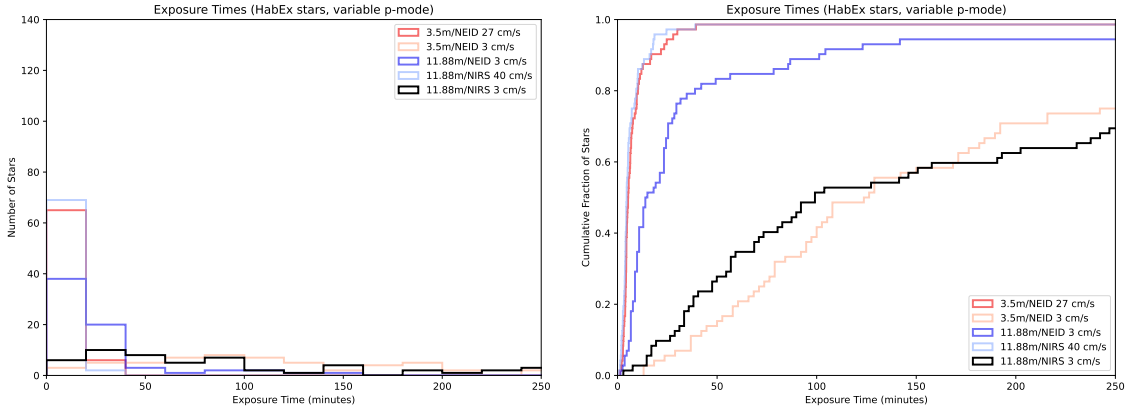


Figure 3.10: Exposure times as histograms (left) and cumulative distribution functions (right) for every star in our telescope/instrument combinations. There is a tail of stars with very long exposure times (and which are therefore difficult to observe at high precision). The PDF appears the same for all 3 sets of stars due to the current bin size of 20 minutes, as whatever chosen p-mode correction has little effect beyond that. Due to finer bin sizes, the CDFs do show that the exact distribution of exposure times is shuffled around somewhat, though the effect is again small (and largely confined to telescope/instrument/precision combinations that skew to shorter exposure times). In all cases, there is a “tail” of stars that have relatively long exposure times, even for favorable telescope/instrument/precision combinations. For less favorable ones, this “tail” can mean that around half of all stars have exposure times of over two hours (and so are difficult to observe).

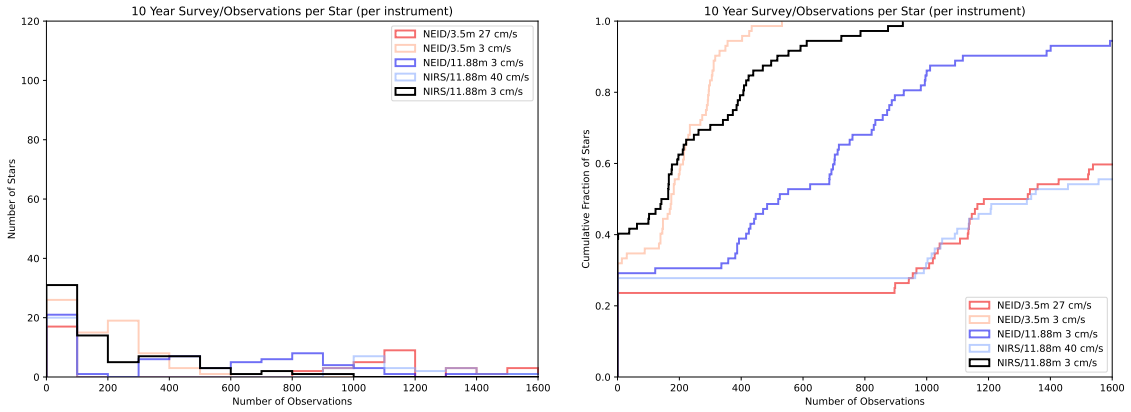


Figure 3.11: Histograms of total number of observations for the different telescope/instrument combinations as both PDFs (left) and CDFs (right). Differences between different architectures are quite obvious, though the ones between different p-mode compensation methods are subtle (and not apparent for the architectures with longer exposure times and fewer observations). Because of the details of the target list (both position and exposure times), between around 25 and 40% percent of the target stars are never observed.

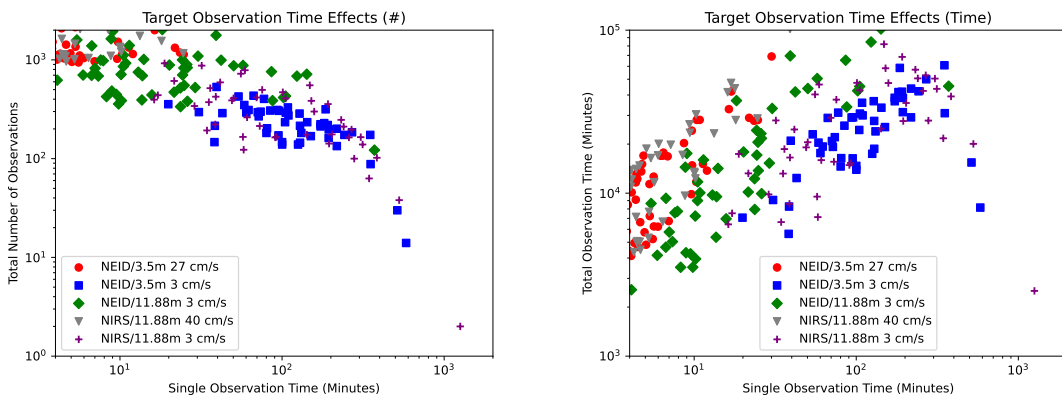


Figure 3.12: Total number of observations (left) and total time spent observing (right) for each star and telescope/instrument combination as a function of exposure time. Number of observations decrease slowly with increasing exposure time (while time spent on a given star increases) until around 300 minutes, and which point both rapidly decrease as the stars become increasingly impractical to observe.

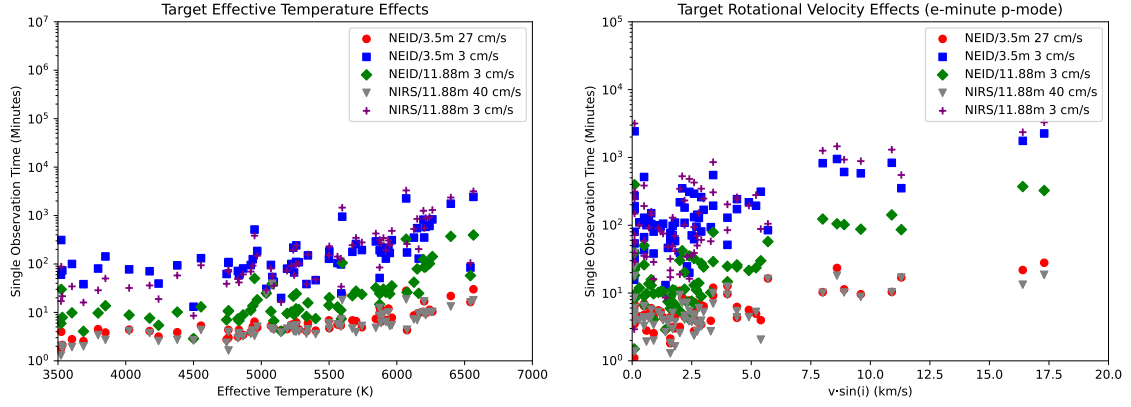


Figure 3.13: Exposure time as a function of effective temperature (left), and rotational velocity (right). This target list shows a clear trend of increasing observation difficulty for hotter stars, though choice of telescope, instrument, and target precision are more important for GKM stars. One star (Altair), is off the top-right corner of the  $v\sin(i)$  plot, due to its unphysically long exposure times at our desired precisions and having a rotational velocity of 211 km/s.

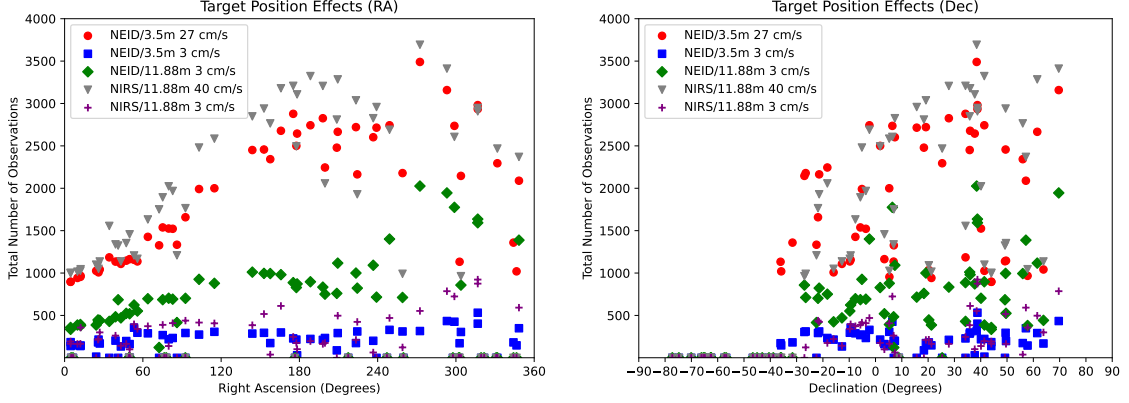


Figure 3.14: Total number of observations per star as a function of Right Ascension (top) and Declination (bottom). There is a clear trend in right ascension, we believe from a combination of night length and weather (though it is suppressed for longer exposure time telescope/instrument/precision combinations). That the peak corresponds with stars that have the longest time above the horizon in late summer (around 300-330 degrees) and not winter or early spring (when the weather is better and nights longer) is surprising. Declination does not show a clear trend, with number of observations per star being relatively flat north of about -40 degrees. Below that, stars are never observed.

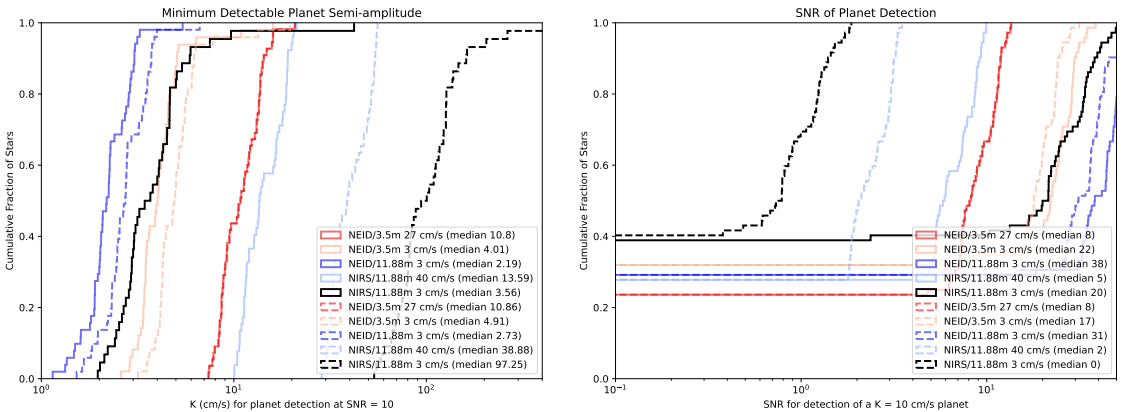


Figure 3.15: How our detection heuristic changes from no microtellurics (solid lines) to nominal microtelluric noise (dotted lines). **Left:** CDFs for the minimum detectable reflex velocity ( $K$ , in cm/s) for a planet at  $\text{SNR} = 10$ . **Right:** CDFs for the SNR for a detection of a  $K = 10$  cm/s planet.

As our assumed noise is smaller than the instrument and photon noise sources in all but the most optimistic visible surveys, microtellurics have little effect. In contrast, this noise source dominates over all others in the NIR (being far larger than the instrument or photon components, even in the most pessimistic cases), and must be better accounted for if this wavelength range is to be useful in the EPRV era.

### **3.8 Results (EPRV target list)**

To avoid redundancy, only the results using the surface gravity/effective temperature variable p-mode correction are shown.

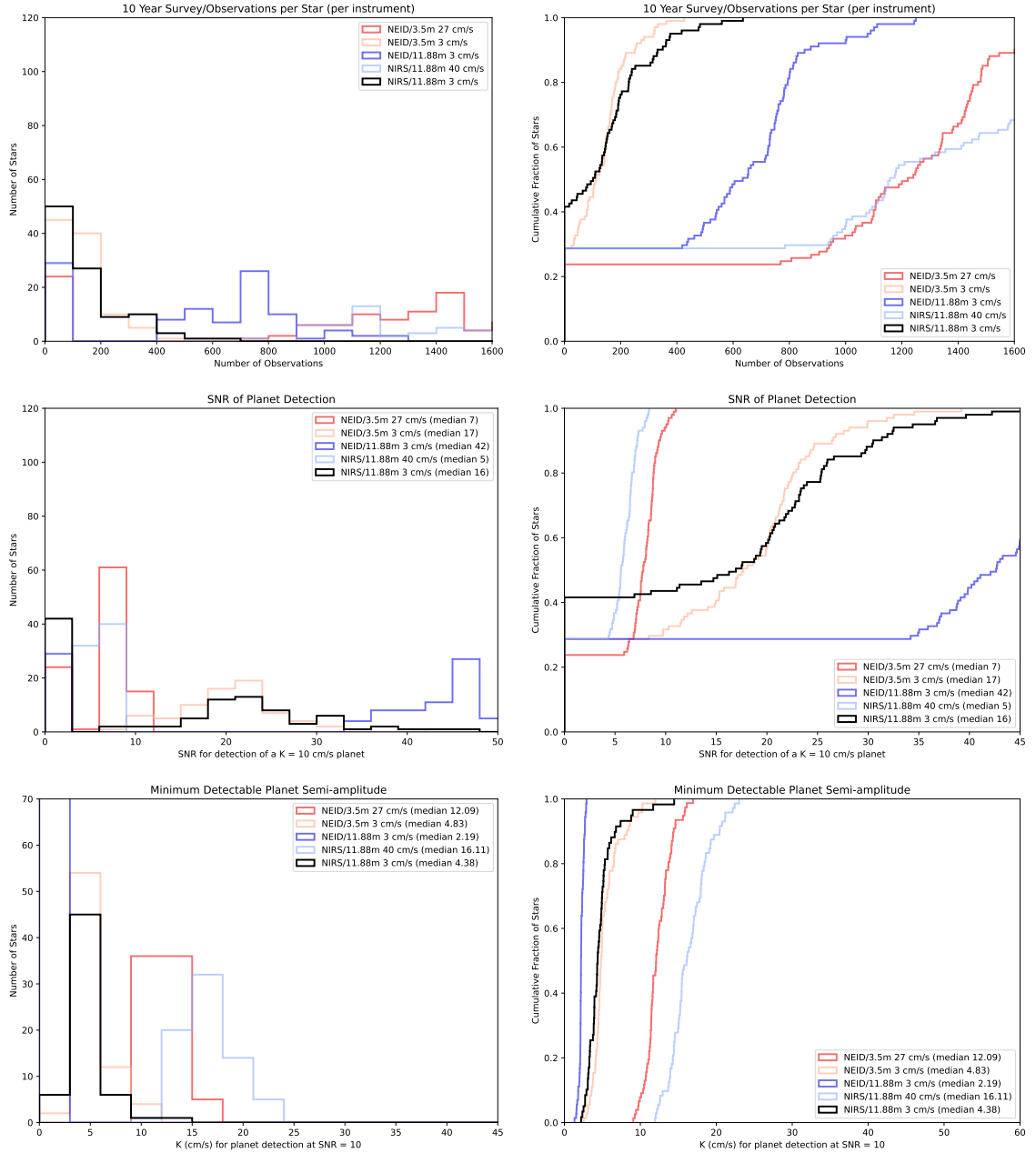


Figure 3.16: Histograms/PDFs (left) and CDFs (right) of the number of observations (top), SNR of a nominal  $10 \text{ cm/s}$  planet detection (middle), and minimum detectable reflex velocity  $k$  of a nominal  $\text{SNR} = 10$  planet detection (bottom).

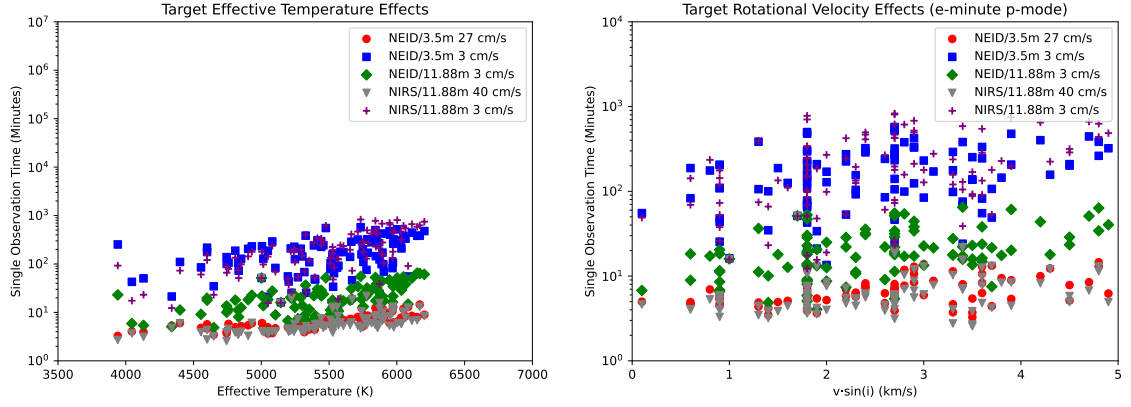


Figure 3.17: Exposure time as a function of effective temperature (left), and rotational velocity (right). This target list shows a clear trend of increasing observation difficulty for hotter stars, though choice of telescope, instrument, and target precision are more important for GKM stars. There is no clear trend in exposure time for  $v\sin(i)$ , possible due to all stars in this sample being slow rotators.

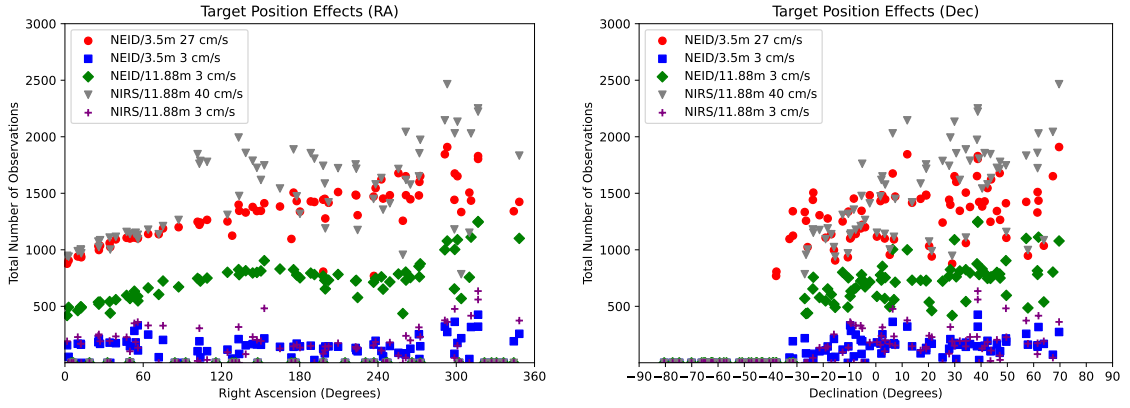


Figure 3.18: Total number of observations per star as a function of Right Ascension (left) and Declination (right). There is a clear trend in right ascension, we believe from a combination of night length and weather (though it is suppressed for longer exposure time telescope/instrument/precision combinations). That the peak corresponds with stars that have the longest time above the horizon in late summer (300-330 degrees) and not winter/early spring (when the weather is better and nights longer) is surprising. Declination does not show a clear trend, with number of observations per star being relatively flat north of about -40 degrees. Below that, stars are never observed.

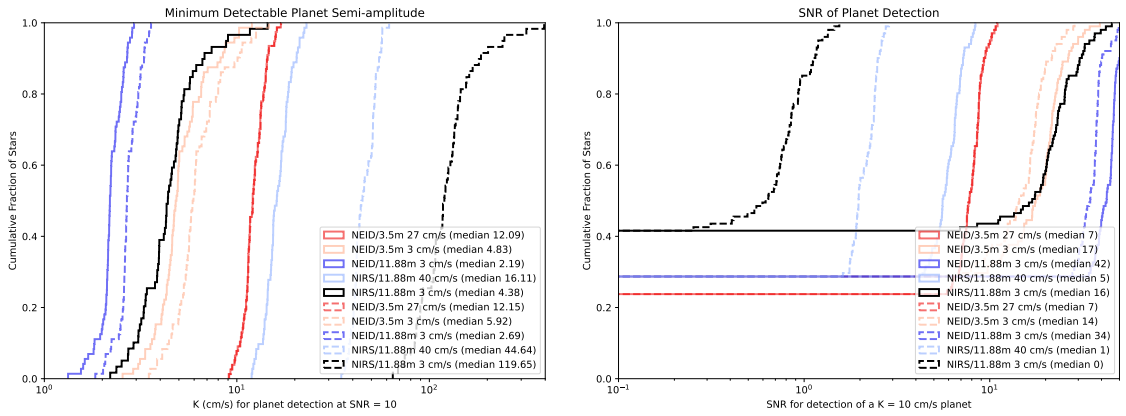


Figure 3.19: How our detection heuristic changes from no microtellurics (solid lines) to nominal microtelluric noise (dotted lines). **Left:** CDFs for the minimum detectable reflex velocity ( $K$ , in cm/s) for a planet at SNR = 10. **Right:** CDFs for the SNR for a detection of a  $K = 10$  cm/s planet.

As our assumed noise is smaller than the instrument and photon noise sources in all but the most optimistic visible surveys, microtellurics have little effect. In contrast, this noise source dominates over all others in the NIR (being far larger than the instrument or photon components, even in the most pessimistic cases), and must be better accounted for if this wavelength range is to be useful in the EPRV era.

## 3.9 Discussion

### 3.9.1 Exposure Time Considerations

Exposure time is an incomplete proxy for ease of observations, with other factors (discussed below) also being relevant. Difficult targets receive fewer exposures, though total time allocated to observing them only falls off when they become almost unobservable. The boundary between difficult and impossible to observe can be fuzzy for actual observations (until one reaches exposure times that are unphysically long), so our exposure time calculator makes no attempt to distinguish these.

Our exposure time calculator can, depending on inputs, generate arbitrarily long exposure times. We do not consider this a problem because: there is no clear cutoff for what makes a star impractical to observe, and the relative times are still useful as figures of merit. Depending on the survey goals, it is possible that they will want to: accept lower precision, tolerate long exposures, or drop the target entirely. We did not impose any limits on what times we accept in our simulations because we both wanted to get a feel for what was impractical within our assumptions, and our code gracefully deals with lists containing unobservable targets.

### 3.9.2 Comparisons to Other Exposure Time Calculators

Herein we compare our ETC considerations and results with some that are used for planning purposes at actual observatories, including one with one of our nominal instruments. As these sorts of ETCs are for planning out approximate time allocation needed, we expect that while results will approximately correlate, they will not be exact. Different systems are optimized for different types of targets, depending on typical observatory usage. Additional features that are subjects of ongoing research (eg: stellar activity) cannot be a-priori described to high detail because we do not yet know them in high detail.

## ESPRESSO ETC

ESPRESSO is an existing EPRV instrument on the VLT at Paranal. Its exposure time calculator[196] is available on the web, and herein we compare the results.

This ETC has a large variety of spectral models, though there is a focus on giant stars and non-blackbody emission. For stars, they use a grid of atmospheric models, with options for their instruments, differing sky conditions, and single vs four telescope observing programs. The calculator is somewhat more focused on faint/low surface brightness (eg: extragalactic) sources, with the inclusion of sky brightness, with limited options in terms of sun-like stars. Though like us they gloss over line effects in the IR. It is well designed for planning with individual targets and specific dates, though the web interface would be a hassle for preparing for a large survey.

For the purposes of trends across spectra type, we look at exposures for a limited subset of stars:

Spectra Type	S/N	RV precision (m/s)
G0	151.882	0.4
G2V	152.606	0.39
K2V	153.587	0.39
K7V	155.971	0.38
M2V	150.353	0.4

There is a similar pattern (at least for constant V-mag) of getting consistent RV precision for a given exposure time across a fairly wide spectra type range. Using their most optimistic Precipitable Water Vapor, seeing, and Moon illumination figures and at the same airmass as we did.

We do not perform other comparisons, given the differences in what our ETCs focus on.

---

<https://www.eso.org/observing/etc/bin/gen/form?INS.NAME=ESPRESSO+INS.MODE=spectro>

## NEID ETC

NEID's ETC is available both in web interface and downloadable forms for observation planning. It is more tightly focused on stellar RVs (in-line with the telescope/instrument's tighter focus). They use a pre-computed grid of stellar models at various effective temperatures, and return precision based on that effective temperature and v-mag. Importantly, they reject any target/precision combination that would have a single observation time longer than 3600 seconds, so our comparisons focus on the lower precision/shorter exposure time end. We specifically look at both synthetic stars for overall trends (3.9.2), and a direct comparison of our target lists (3.9.2).

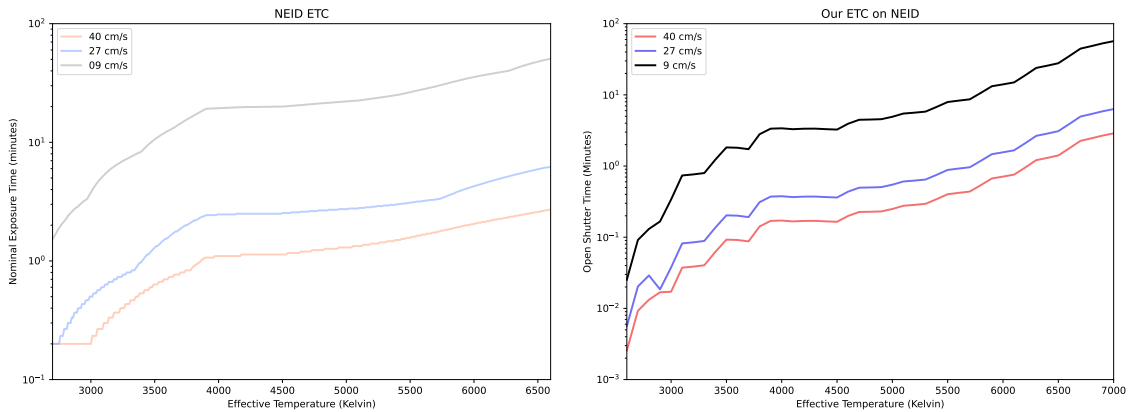


Figure 3.20: **Left:** Nominal exposure times at 3 RV precisions on NEID for synthetic stars that have an apparent V-magnitude of 4.83 as a function of effective temperature (so an unrealistic approximately constant luminosity, thus showing RV information content for a more or less constant number of photons as a function of temperature). The values are calculated with NEID's official ETC over their modeled range (2700 to 6300 K). Lower values are "better" (higher precision). **Right:** Equivalent synthetic stars stars (apparent magnitude 4.83, constant  $v\sin i$ , metallicity, and  $\log(g)$ , but with varying effective temperature) with exposure times calculated by our ETC. Both show similar trends, though the exact times are offset from each-other by about an order of magnitude. Given that none of these stars are especially real, such an offset is not concerning.

Our ETC approximately agrees with NEID's, though there are significant differences

---

[https://bitbucket.org/erik\\_timmermann\\_noao/neid-etc/src/master/](https://bitbucket.org/erik_timmermann_noao/neid-etc/src/master/)

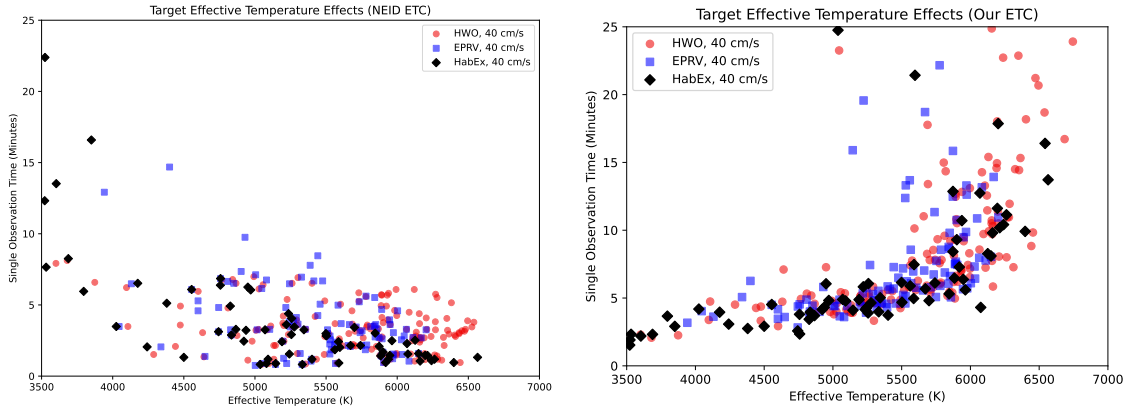


Figure 3.21: **Left:** Exposure times for the stars in our 3 target lists for a nominal single exposure at 40 cm/s, using the NEID ETC. Stars with exposure times longer than one hour are not shown. Depending on the target list, there can be a trend towards shorter exposures for hotter stars, but this is not always the case and it is relatively flat for stars hotter than around 4500-5000 K. If one wanted to choose a target list with a specific exposure time cutoff, they could do so while having stars across a broad temperature range. **Right:** The same target lists at the same scale are shown with our own exposure calculator. The higher “floor” in our times is from our p-mode compensation, and the upwards scatter at high temperatures is from increased  $v\sin i$ .

in details, potentially resulting in a factor of several longer or shorter exposure time. We believe that this is from our considering additional stellar parameters, while also using comparatively simplified atmospheric and instrumental parameters. Given that the spread of exposure times overlap and our surveys all use target lists with a range of exposure times, these differences do not constitute a problem for our general conclusions on survey parameters and viability. They can, however, greatly affect the achievable sensitivity for any specific star. Simulations that consider those additional features may be needed to more tightly define targets, especially for specific (as opposed to our generic) instruments.

### 3.9.3 Dispatch Scheduler considerations

Exposure times, stellar positions, site weather, and how targets are chosen all affect observation counts. Our time since last-observed weighting minimizes RA shadowing issues, so target spacing is not an overly large concern.

More generally, the dispatch scheduler deals relatively well with distributing observations between different targets, getting as many observations for each target as possible, and dealing gracefully with targets being difficult to observe. This combination of “good enough” and being computationally cheap is why we do not look at other weighting options, or more complicated algorithms such as [131]

The “Traveling Telescope Problem” [197] and associated slew concerns are primarily for the short exposure limit. The sorts of exposure times that we have here (including with the p-mode compensation) suggest that we would have fewer observations per hour/per night than they would. However, our assumed slew times are intentionally conservative, so work such as this could improve upon our assumptions.

Exploring how much of an improvement is possible with these sorts of methods, and if they present other limitations would be an avenue for future research.

### 3.9.4 Target Weighting

Number of observations per star were looked at for weighting schemes based on hour angle and/or time since last observation (with minimum delays between observations of 0.5, 1, 2, 4, 8, 16, and 32 hours considered). Variants on relative weighting strength were not otherwise attempted. Due to the difficulties in comparing histograms, the mean, median, and standard deviation of the number of observations were considered as figures of merit.

In general, target selection (number of stars, exposure times, location) had larger effects than the algorithms explored. Which weighting algorithm was more effective also depended on the target list. A small/widely separated one did best with pure hour angle. The full list contains a number of stars that can interfere with each-other, so a method of upweighting that prevents that is preferred.

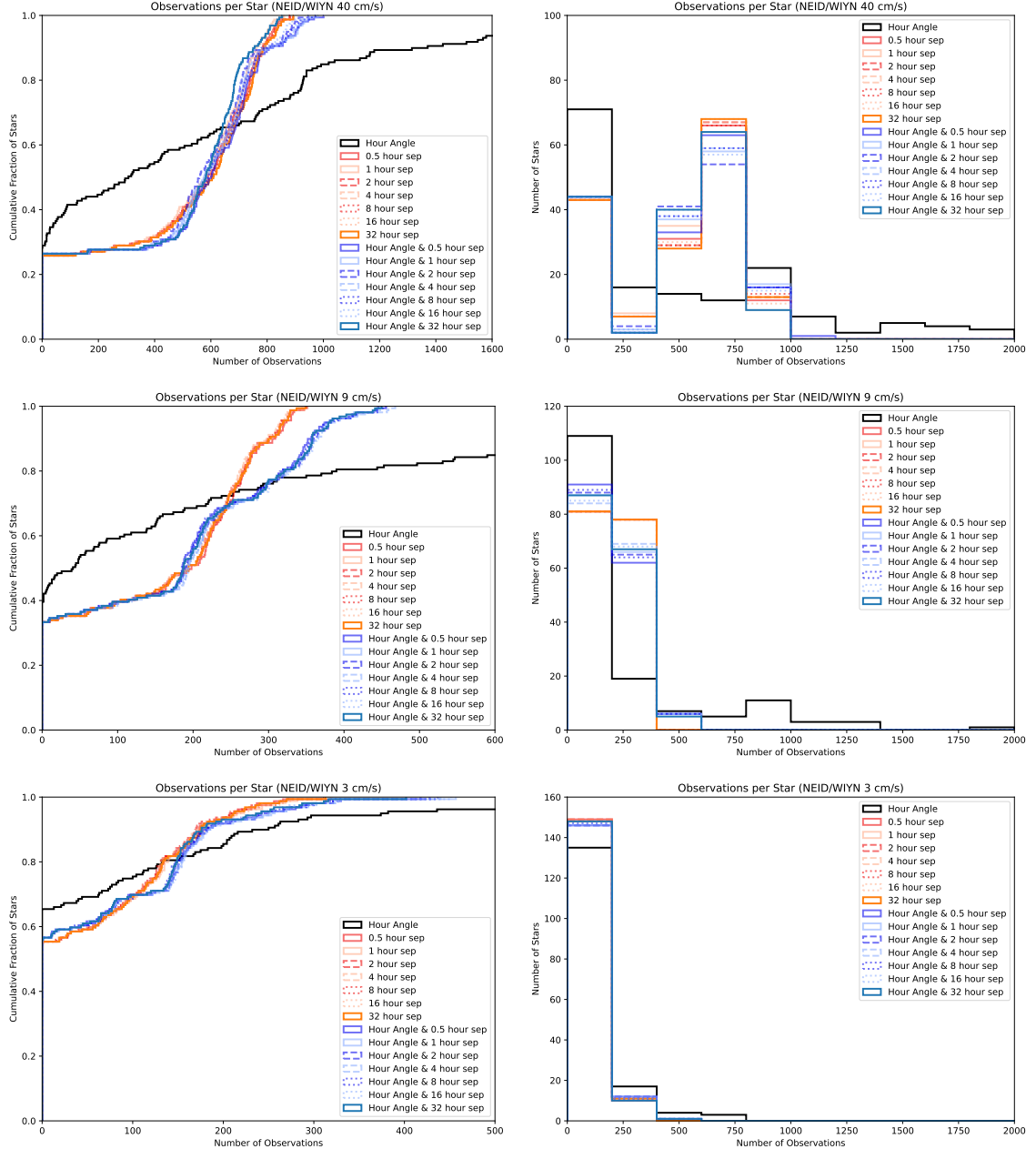


Figure 3.22: PDFs (left), and CDFs (right) of all stars in the HWO target list for different precisions and a large variety of observation weighting strategies. Here we look at 3 main strategies: a simplistic hour-angle weighting, a time since last observation weighting (do not observe the object again at all within the time limit, and then ramp up the weighting), and a combined hour-angle and time since last observation weighting. The last two are relatively similar (especially for shorter exposure times), but we find that the combined weighting is the “best”.

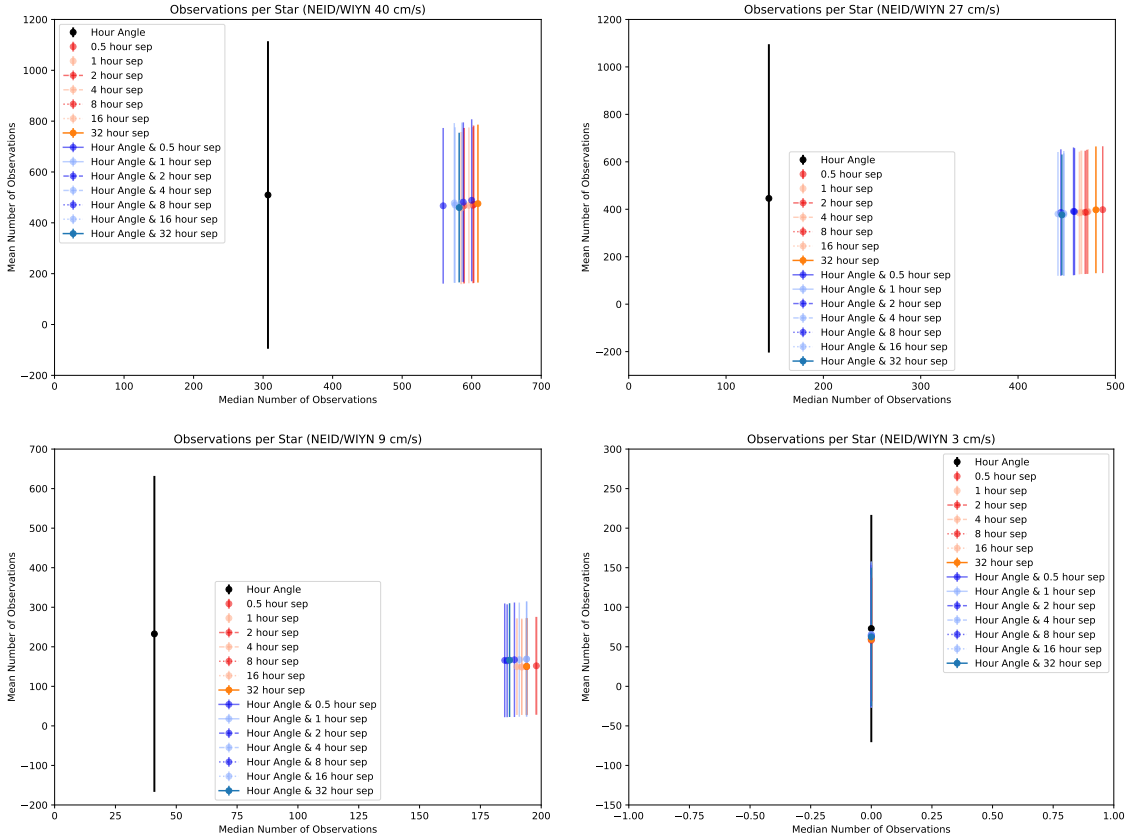


Figure 3.23: Plots of the distribution of results for different precisions and a variety of weighting strategies. We compare median (x-axis) with mean (y-axis) and standard deviation (error bars). Here we look at 3 main strategies: a simplistic hour-angle weighting, a time since last observation weighting (do not observe the object again at all within the time limit, and then ramp up the weighting), and a combined hour-angle and time since last observation weighting. The last two are relatively similar (especially for shorter exposure times), and unlike the broader distributions, it looks like pure time since last observation is the “best”. Notably, for 3 cm/s, we are unable to observe the majority of the stars, hence a median of 0.

### 3.9.5 Do the different P-mode calculation methods affect yields?

The minimum timescale as determined by the p-mode oscillations has a large effect on exposure times only when other factors combine to result in very short exposures. They set a floor which within our constraints is only reached for relatively low precisions, favorable stars, and/or large telescopes.

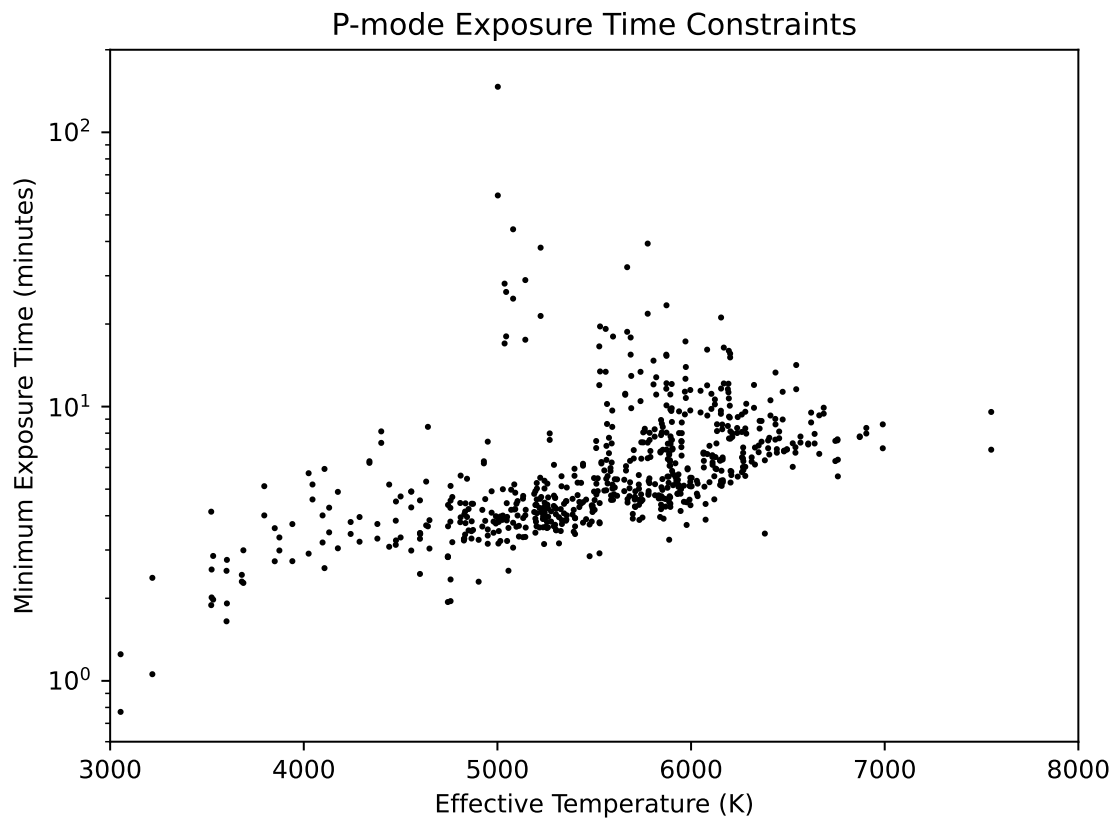


Figure 3.24: All minimum p-mode times across all target lists as a function of effective temperature. Most are shorter than 5 minutes and the vast majority are shorter than 10. The remainder include stars that a direct observation mission may wish to pass over (eg: subgiants).

While both the mass-radius and gravity-temperature methods look similar, it is worthwhile to check to see if they are producing different distributions. To do this, we performed

K-S tests on our distributions of exposure times, observation counts, and K/SNR heuristics. We first look at the extremes of short and long exposure time cases that we simulated, and then at the shortest ones within the preferred instrument/telescope/sensitivity combinations.

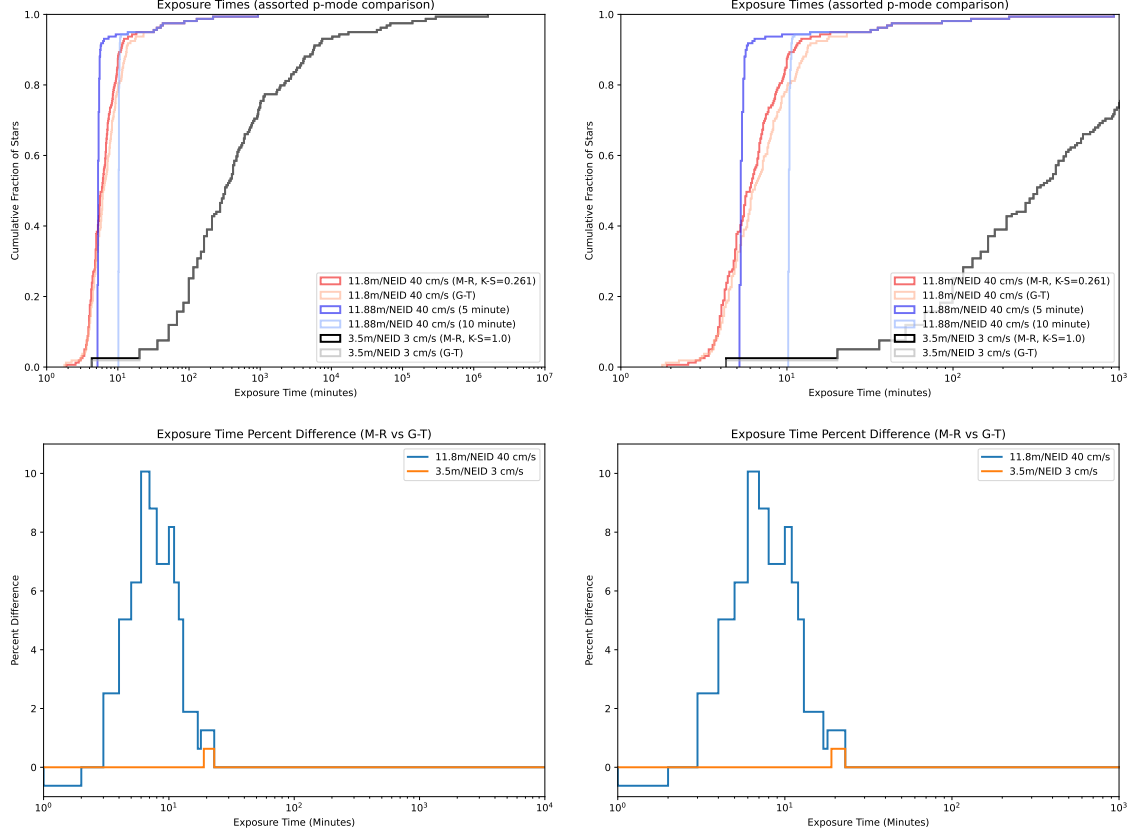


Figure 3.25: Comparison of the exposure time distributions for four kinds of p-mode oscillation compensation measures: fixed 5-minute versus fixed 10-minute versus two kinds of variable (mass-radius and effective temperature-surface gravity). The telescope/precision combinations that otherwise give the shortest exposures (11.8 m and 40 cm/s) and longest exposures (3.5 m and 3 cm/s) using NEID are used. In the CDF graphs (**top**), the p-values for a null result between the two variable exposure modes (the mass-radius and temperature-gravity using distributions are the same) are given in the figure keys. The **bottom** panels show 'percent difference' between the two variable p-mode timescale distributions. The two fixed timescale distributions are not considered, as they are different by inspection (though overlap in some ways with the other distributions). The K-S test does not show these two distributions as statistically different (the p-value for the 40 cm/s case is  $>0.05$ , and for the 3 cm/s case is around 1).

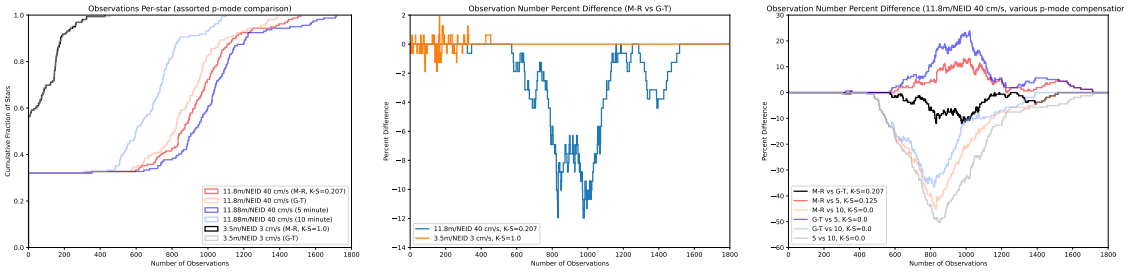


Figure 3.26: Comparison of the same 6 datasets in observation distribution. The left graph is the CDF of the distributions, while the middle is the percent difference for the two variable p-modes, and the right is the percent difference between all combinations for the short exposure time case. Notably unlike the exposure time distributions, these are in some cases distinguishable from each-other.

While we do see some differences, the shortest exposure time we simulated is a “non-canonical” telescope/instrument combination with a telescope size and instrument sensitivity that is at the edge of the trade-space. The shortest exposure time combination that is “canonical” (27 cm/s NEID analog on a 3.5 m telescope) shows a somewhat different pattern.

Any physically-motivated p-mode comparison appears to have similar effects on survey results for a realistic survey, though differences are possible in the short-exposure limit. If a survey spends a relatively long time on each star, then the method will not matter.

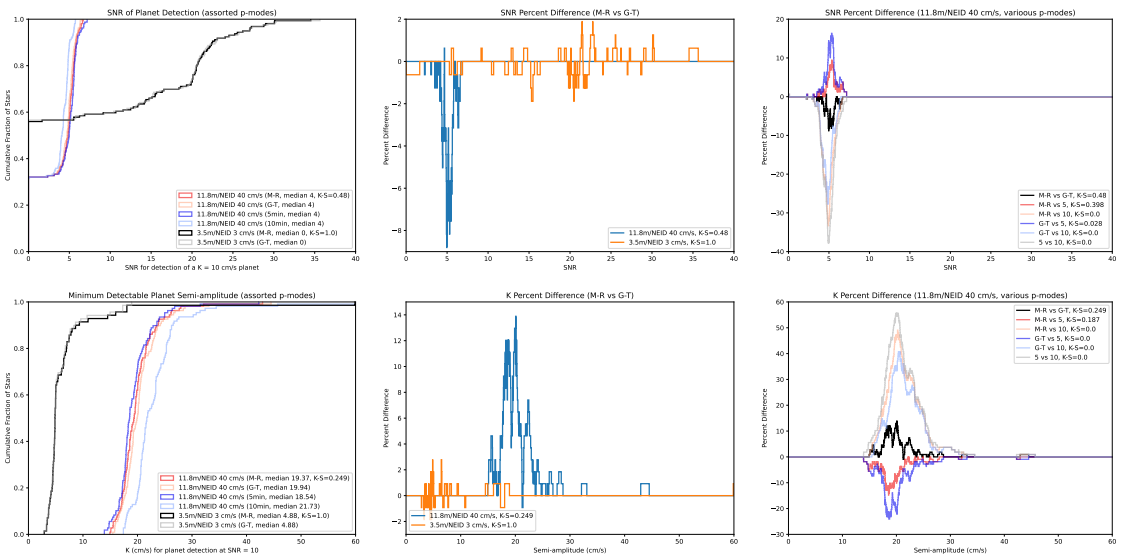


Figure 3.27: Comparison of the same 6 datasets in their distributions for our K/SNR detection heuristic (semi-amplitude sensitivity at an SNR of 10 is top, SNR for a fixed semi-amplitude of 10 cm/s is bottom). The left graphs are the CDF of the distributions, while the middle are the percent difference for the two variable p-modes, and the right is the percent difference between all combinations for the short exposure time case. Using a cutoff of  $p < 0.05$ , we find that the two variable p-mode calculations cannot be distinguished from each-other, nor the mass-radius method from a 5-minute cutoff. All others can be, as can usually be seen by offsets in their CDFs (which appear as peaks/troughs in the percent difference).

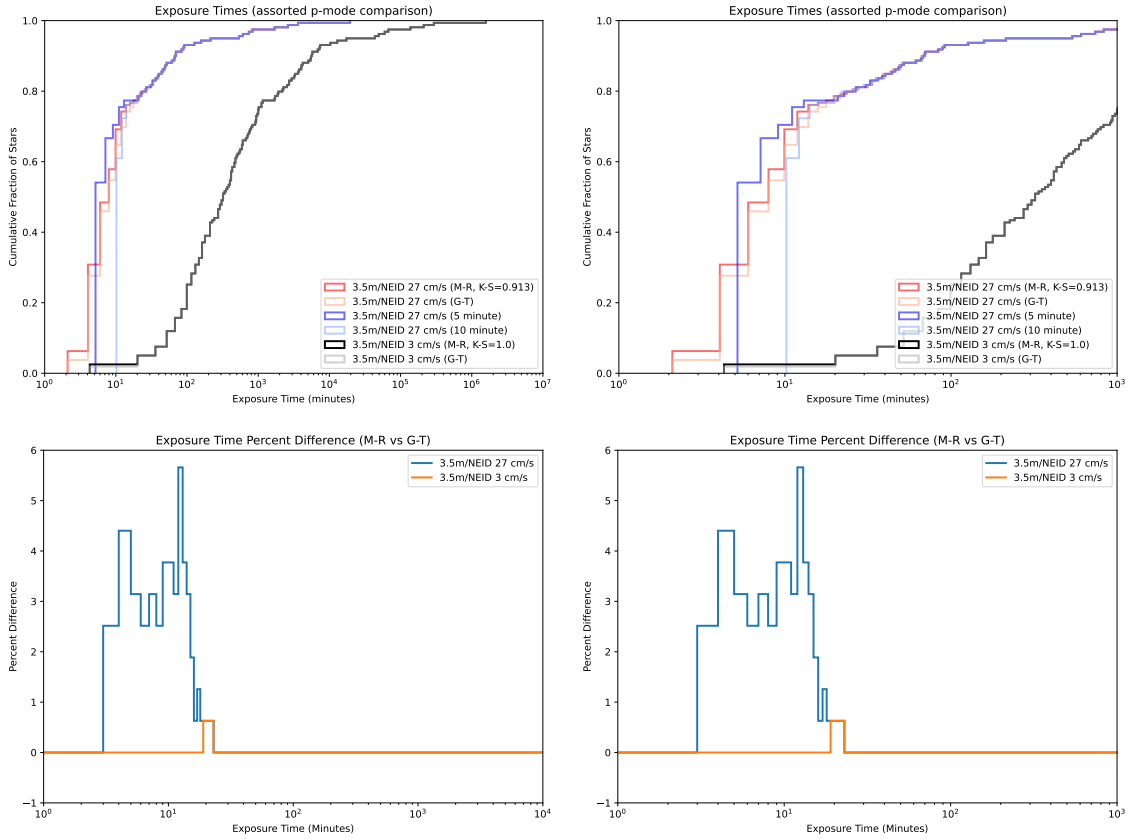


Figure 3.28: Comparison of the exposure time distributions for four kinds of p-mode oscillation compensation measures: fixed 5-minute versus fixed 10-minute versus two kinds of variable (mass-radius and effective temperature-surface gravity). The telescope/precision combinations that are “canonical” and give the shortest exposures (3.5 m and 27 cm/s) and longest exposures (3.5 m and 3 cm/s) using NEID are used. In the CDF graphs (**top**), the p-values for a null result between the two variable exposure modes (the mass-radius and temperature-gravity using distributions are the same) are given in the figure keys. The **bottom** panels show ‘percent difference’ between the two variable p-mode timescale distributions. The two fixed timescale distributions are not considered, as they are different by inspection (though overlap in some ways with the other distributions). The K-S test does not show these two distributions as statistically different (with p-values of near to or exactly 1).

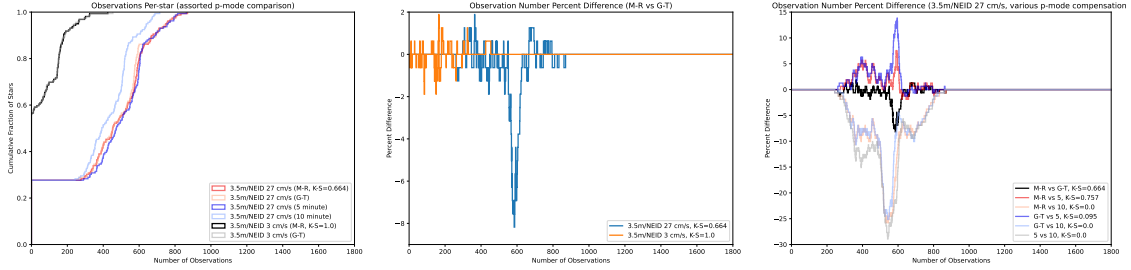


Figure 3.29: Comparison of the same 6 datasets in observation distribution. The left graph is the CDF of the distributions, while the middle is the percent difference for the two variable p-modes, and the right is the percent difference between all combinations for the short exposure time case. The variable p-modes remain indistinguishable from each-other, though the fixed 5-minute is somewhat distinguishable from either. The fixed 10-minute p-mode has a statistically significant and visible offset distribution from the rest.

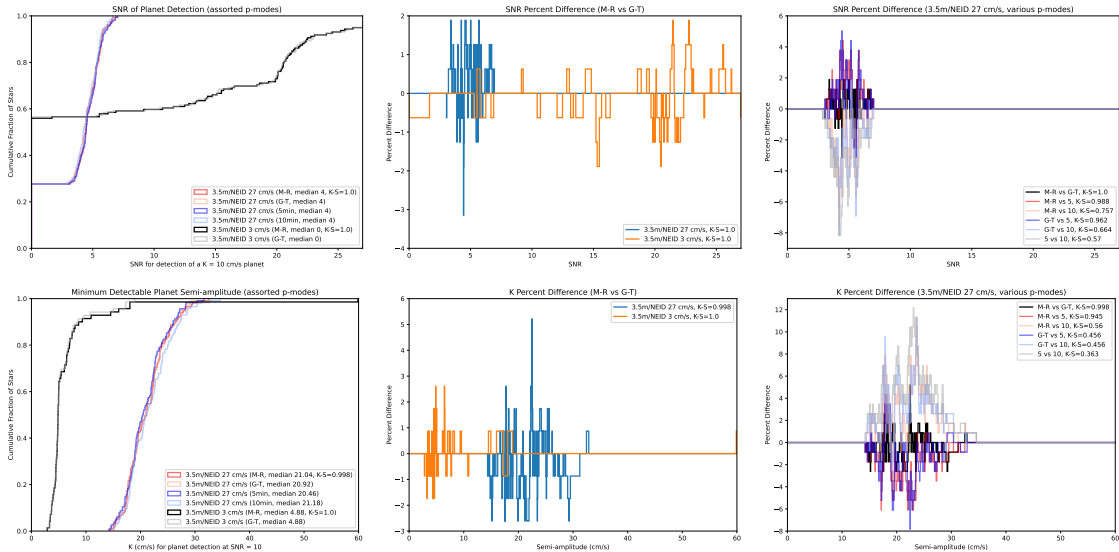


Figure 3.30: Comparison of the same 6 datasets in their distributions for our K/SNR detection heuristic (semi-amplitude sensitivity at an SNR of 10 is top, SNR for a fixed semi-amplitude of 10 cm/s is bottom). The left graphs are the CDF of the distributions, while the middle are the percent difference for the two variable p-modes, and the right is the percent difference between all combinations for the short exposure time case. Using a cutoff of  $p < 0.05$ , we find no p-mode compensation method is different from any other. This is supported by the overlapping CDFs.

Exact details of stellar position are likely to be interacting with the changes in exposure times and/or differences in the weather used (we do not use the same seed for each run), to cause the differences in the observation distributions. That the flat 5-minute floor produces similar results to the variable minimum observation times is potentially interesting, though it may be a result of our assumptions (which give the sun a 300 second, or a 322 second minimum, depending on the method used).

Our detection heuristic has tighter offsets between the CDFs, though due to their near-vertical portion, these are often statistically significant. These suggest that depending on how it is performed, our simulations may have systematic errors from p-mode compensation of up to some tens of percent.

All of these differences are minimized for telescope/instrument/precision combinations that push exposure times longer, and can render them of minor importance for some and no importance for a few of them.

### 3.9.6 Target List Comparison/Target Star Selection

The choice of target stars dramatically affects survey efficiency and efficacy, primarily through exposure time and positional constraints. While our code can deal with some difficult to observe stars, typically due to declination or exposure time, others are impossible to observe at the sorts of precisions necessary to find earth-analogs. Our stellar activity considerations do not greatly affect exposure times, so the variations here are primarily about the information content of spectra and raw number of photons.

While in principle our target list is a volume-limited sample, there are sufficiently many stars that selecting for “easier” ones remains a possibility. Since our most-disfavored stars (hotter ones) are relatively rare, this does not overly constrain us on number of targets. Focusing on “easier” stars may more subtlety bias the survey, though it still reduces the time an eventual direct imaging survey needs to spend on detection/allows more focus on classification.

As we find that an optimistic declination cut does not present issues, this suggests that

they should be chosen more on limiting the number of target stars (assuming that there are too many with short exposure times) than by constraints on observability.

Stars with limited numbers of observations would risk having alias issues. A more subtle aspect of our assumptions is that we want a high cadence to properly model stellar activity. While these simulations use a single site, weather losses (and potentially target list size) would introduce gaps could make this level of activity characterization impossible.

As we have multiple nominally optimized target lists, we can do a degree of comparison.

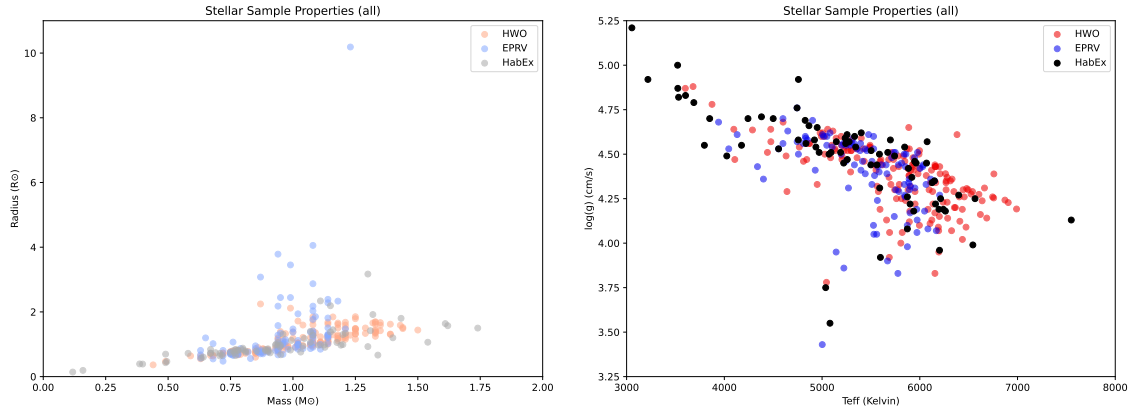


Figure 3.31: A comparison of our 3 target lists in the parameter spaces used for p-mode compensation.

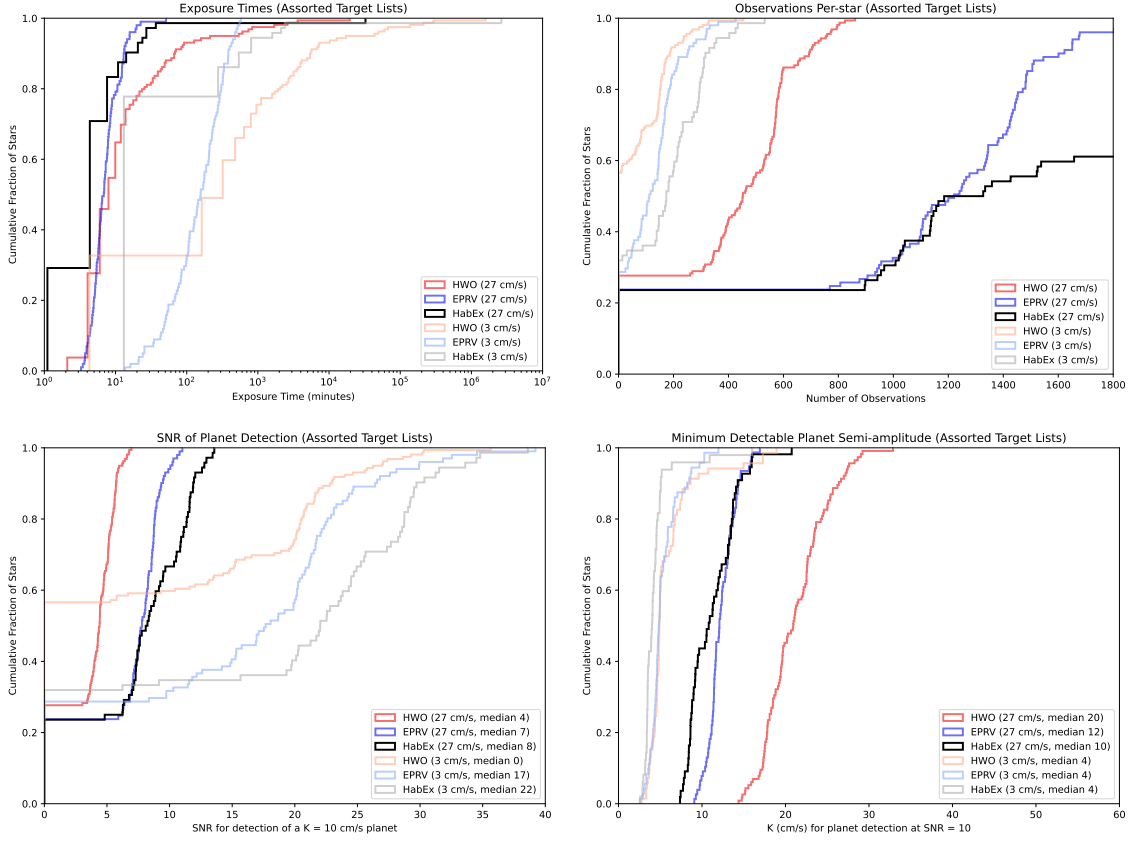


Figure 3.32: A comparison of our 3 target lists (HWO, EPRV, HabEx), for typical high and low precisions using the NEID spectrograph on a 3.5 m telescope. (**top:** CDFs of exposure times and observation counts, **bottom:** CDFs of our K/SNR detection heuristic).

The apparent differences are likely caused by these CDFs glossing over the differing sizes of the target lists, as well as the differing observability. The increased number of stars in general, and “good” stars in particular the HWO list (as compared with the HabEx and EPRV lists) means that observations are spread out over more stars, and everything gets measured to a lower precision.

While we do not quantify the value of target list size (aside from our detection heuristic), this suggests a limit to the target list length for a precursor survey, especially with the large number of observations required. If a survey is to be volume limited, it may need more or larger telescopes to get sufficient numbers.

If our primarily unmodeled noise sources are white noise (as our detection heuristic

assumes), this does point to a smaller / more frequently observed target list as a way to compensate for noise sources that are otherwise larger than we consider.

### 3.9.7 Other/Uncompensated Noise

We do not attempt to directly mitigate any noise beyond oscillations, likely resulting in significant reductions in 'actual' SNR values and higher minimum semi-amplitudes than are shown. (Though longer exposures also likely suffer less from granulation.) Using [52]'s results as a figure of merit, we expect reductions on the order of a factor of 3-6 for correlated noise, and 2 for white noise, for a total reduction in SNR of about 4-9x. There is a great deal of ongoing work to improve on stellar activity, including sun as a star observations. [198–201] These suggest that a NEID-equivalent could find an Earth-analogue around a sun-analogue with on the order of 1000 observations, a number that we reach for many targets. Additional work to mitigate noise may be able to reduce these further, and more realistic simulations of both the noise sources and mitigations thereof would be work for a future paper.

Finally, we do not attempt to model telluric noise, assuming that it will be sufficiently small and/or there will be improvements in mitigation/modeling. Our nominal noise parameters suggest that this is a safe assumption in the visible, but not in the infrared (from their sizes relative to other noise sources). While upcoming EPRV observatories (and the nominal instruments we simulate) will have features like sky fibres, more work is needed.

## 3.10 Conclusions

We (re)introduce a series of codes for calculating exposure times/RV precision, taking into account some degree of atmospheric absorption and compensating for some stellar activity. We also (re)introduce codes for performing realistic dedicated surveys.

We consider multiple target weighting algorithms, settling on a combination of hour angle and time since last observation. Despite the simplicity, does a relatively good job of

making use of the telescope and distributing observations among target stars, with results in line with real-world surveys.

We compare the code with existing exposure time calculators and find (results) broadly similar temperature trends. What parameters various ETCs consider varies enough that other comparisons are difficult, and suggest serious limits on their accuracy without careful per-site/instrument or per-target adjustments. However, our broad trends should be sufficient for “typical” targets.

The important of cadence/multiple sites is highlighted for avoiding poor detection strength from weather.

We have found that target star selection is important for reasons above and beyond stellar activity. eg: Slow-rotating nearby K-dwarfs are much easier to observe than many others. Early M-dwarfs may also work well. G-dwarfs, while more difficult are doable. F and especially A stars are impractical to obtain our desired single measurement precision on. These effects are from: effective temperature being comparatively unimportant over a wide range, but reducing line quantity and increasing microturbulence for hotter stars, as well as increasing rotational velocities (especially past the Kraft Break).

Target star declination is important, though like effective temperature has a relatively broad range where stellar observations are similar in difficulty and number. Right ascension can also matter, though how much and which ones are “best” will vary with the site (from weather and length of night). Even for the “worst” right ascensions, a target list should have some stars, unless exposure times are so long that the list needs to have a minimum of targets.

While previous work showed that one can account for p-mode oscillations approximately (and that they don’t necessarily affect survey results), we show that we can also directly choose exposure times to minimize them. This does not present significant computational overhead or increase in survey difficulty, and so can “just” be done in future EPRV work.

We also show that the p-mode compensation method has little effect on exposure times (and therefore observation rates), outside of the large telescope/low precision limit. The

physically based methods use related scaling methods and are centered at solar ( 5 minute) values, so this is unsurprising. An intentionally different method (10 minutes) does offset things, but again the effect is small and only relevant when exposure times are short (well below 10 minutes).

Finally, we find that telluric noise sources are presently manageable in the visible, but are show-stoppers in the NIR without additional corrections.

## Chapter 4: Orbital Photometric Lightsource Simulations

In this section, I describe a portion of simulation work that I did distinct from the RV simulations.

### 4.1 Motivation

As mentioned earlier, relative photometric precision has seen great advances, though absolute precision is still limited in part because many standard sources are white dwarfs with relatively easy to characterize atmospheres and not anything that can be easily produced in a lab.

Increased photometric precision is now necessary to better characterize transiting exoplanets (by better constraining stellar and by extension planetary diameters). It will also help with answering unsolved problems in cosmology and galaxy evolution.

Exactly what sort of light source (or sources) to fly is not immediately obvious. Blackbody, line emission (LED), and reflected sunlight all are potentially useful, and how bright these will be depends on the emitter power, collimation, distance, and (if the telescope is ground-based) atmosphere.

### 4.2 Project History/My Part

ORCAS/starlite/quasar/CANDLES are a series of projects that looked into flying a spacecraft to act as an absolute photometric light source for improving calibration. These have seen both a test article (ORCASat) flown [202, 203], and have now proceeded to a full probe class mission with Landolt. My own work with this, while not at the scale of a full paper, is sufficient to expand into this chapter.

### 4.3 Simulation Parameters

The simulations used comparatively simple parameters: light sources were either black-bodies (of a specified effective temperature and one of: apparent magnitude or bolometric luminosity), or LEDs (of a specific power output). In both cases, what was seen at the detector was defined using a simple "bucket" model for the detector's bandpass (which required doing numeric integration for the blackbody sources, but the LED ones were assumed to be 100% visible by the detector). Atmospheric effects were ignored by the simulations, though considered to the extent that eg: 1064 nm lasers were not studied.

Exactly what detectors/telescopes and emitted wavelengths were preferred varied over the course of the simulations, as the project developed. Most were of ground-based instruments, though we also considered detectors on JWST and Roman Space Telescope at times.

Dispersion was at a fixed angle. Commonly  $4\pi$  steradians, 1 steradian, or 1 arcsecond. Over the back and forth, exactly which dispersion was preferred varied, finally settling on xxx (corresponding to a bare optical fiber). The beam profiles were assumed to be uniform, and that pointing was never an issue. Falloff from distance as  $\frac{1}{r^2}$  was considered for a range of different distances, corresponding to multiple different orbits, eg: LEO, GEO, HEO, and ESL-2 halo.

Wherever practical, MKS units were used, though some outputs included Angstroms and/or cm for ease of reading.

## 4.4 Procedure/Equations

### 4.4.1 Blackbody

Planck's displacement equation was integrated over the wavelength range of the pass-band to get both photon counts and emitted energy:

$$B d\lambda = \frac{2hc^2/\lambda^5}{e^{(hc/\lambda kT)-1}}$$

### 4.4.2 LED

LED emitters were assumed to be perfectly monochromatic at their specified wavelengths, so bandwidths were defined by the detector. Photon counts were found with:

$$n = \frac{\text{Power} \cdot \lambda}{h \cdot c}$$

### 4.4.3 Filters

Data for Johnson UBVRI and Sloan SDSS band-passes was gathered from [51], While 2MASS JHK, NGRST WFI, and VRO ugrizy were found on their respective websites. I treated the band-passes for all systems as “buckets”, with perfect transmission in the bucket (typically the FWHM of the filter), and zero outside of it.

---

[https://old.ipac.caltech.edu/2mass/releases/allsky/doc/sec3\\_1b.html](https://old.ipac.caltech.edu/2mass/releases/allsky/doc/sec3_1b.html), [https://wfIRST.ipac.caltech.edu/sims/Param\\_db.html](https://wfIRST.ipac.caltech.edu/sims/Param_db.html), and table 2 of <https://github.com/lsst/throughputs>

Table 4.1: A listing of all filters used in the various simulations. For ease of reading, all wavelengths have been converted into Angstroms. Aside from WFI, these are all for ground-based telescopes.

System	Filter	$\lambda_{eff}$	$\Delta\lambda$	$\lambda_{min}$	$\lambda_{max}$
Johnson	U	3663	650		
Johnson	B	4361	890		
Johnson	V	5448	840		
Johnson	R	6407	1580		
Johnson	I	7980	1540		
SDSS	u'	3596	570		
SDSS	g'	4639	1280		
SDSS	r'	6122	1150		
SDSS	i'	7439	1230		
SDSS	z'	8896	1070		
2MASS	J	12550	2900		
2MASS	H	16500	2800		
2MASS	Ks	21550	1550		
WFI	R062	6200	1400		
WFI	Z087	8685	1085		
WFI	Y106	10595	1325		
WFI	J129	12925	1615		
WFI	H158	15770	1970		
WFI	F184	18415	1585		
WFI	W146	14635	5365		
LSST	u	3694	473		
LSST	g	4841	1253		
LSST	r	6358	1207		
LSST	i	7560	1175		
LSST	z	8701	998		
LSST	y	9749	872		

Table 4.2: A listing of all filters used in the various simulations. For ease of reading, all wavelengths have been converted into Angstroms. The JWST filters are most-all NIRCam, while the “NGRST” ones are mostly a repeat of the WFI instrument (though with one filter from GRS and one from PRS added).

System	Filter	$\lambda_{eff}$	$\Delta\lambda$	$\lambda_{min}$	$\lambda_{max}$
NGRST	F062	6200	1400		
NGRST	F087	8690	1085		
NGRST	F106	10600	1325		
NGRST	F129	12930	1615		
NGRST	F158	15770	1970		
NGRST	F184	18420	1585		
NGRST	W146	14640	5150		
NGRST	G150	14650	4650		
NGRST	P120	9750	5250		
JWST	F070W	7088	1213		
JWST	F090W	9083	1773		
JWST	F115W	11624	2055		
JWST	F140M	14074	1367		
JWST	F150W	15104	2890		
JWST	F162M	16297	1626		
JWST	F182M	18494	2251		
JWST	F200W	20028	4190		
JWST	F210M	20982	2055		
JWST	F250M	25049	1783		
JWST	F277W	27845	6615		
JWST	F300M	29940	3256		
JWST	F335M	33675	3389		
JWST	F356W	35935	7239		
JWST	F360M	36298	3585		
JWST	F410M	40887	4263		
JWST	F430M	42829	2295		
JWST	F444W	44394	10676		
JWST	F460M	46316	2309		
JWST	F480M	48213	3141		

Since filter pass-bands are all defined in units of wavelength, their bandwidth was found with:

$$\Delta\nu = \frac{c \cdot \Delta\lambda}{\lambda_{eff}^2 - \Delta\lambda^2/4}$$

#### 4.4.4 F-lambda, Janskys, and Magnitudes

This combined with the aforementioned energy calculations allowed for finding the flux in Janskys:

$$1Jy = 10^{-26} \frac{W}{m^2 \cdot Hz}$$

Flux in wavelength bands was also shown at times with:

$$F_\lambda = \frac{flux}{\Delta\lambda} \frac{W}{m^2 \cdot A}$$

AB magnitudes were found with:

$$m_{AB} = -2.5 \cdot \log_{10}(Janskys) + 8.9$$

This is derived from [46, 47], though exact values for the conversion sometimes varies in the literature (often amounting to if one wants to treat Vega as magnitude 0, or +0.03).

Despite the use of Johnson filters, Vega magnitudes were never used.

## 4.5 Example Graphs

These are typical of what was looked at, with fluxes/magnitudes in differing units to cover what people were familiar with. Displaying all graphs produced would be excessively long and redundant, so only examples that follow the design process are shown.

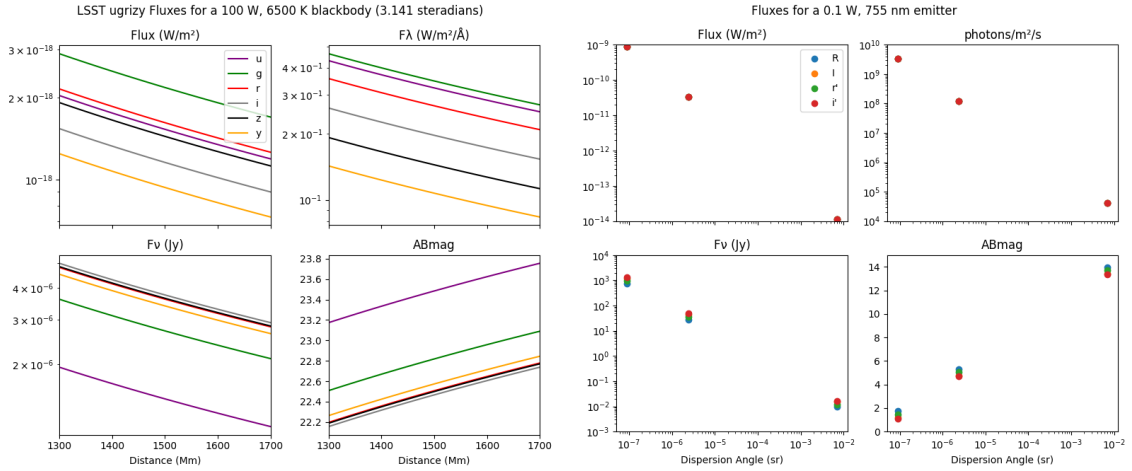


Figure 4.1: Two typical graphs of light source simulations. The left shows what would be seen at the Vera Rubin Observatory from a distant satellite with a 100 W incandescent (black body) source diffused over  $\pi$  steradians. The right shows results from a 755 nm 0.1 W LED source in GEO by several different filters and for several different dispersions.

## 4.6 Light Source Selection

The initial light sources were blackbodies of 2700 K, 3000 K, or 6500 K. Beam dispersal was a full  $4\pi$  steradian sphere, an integrating sphere or bare fibre covering a solid angle of  $\pi$  steradians, or highly focused 1 microsteradian optics. The full sphere was a "worst case" check, with the other two being a comparison of high dispersion and low dispersion systems.

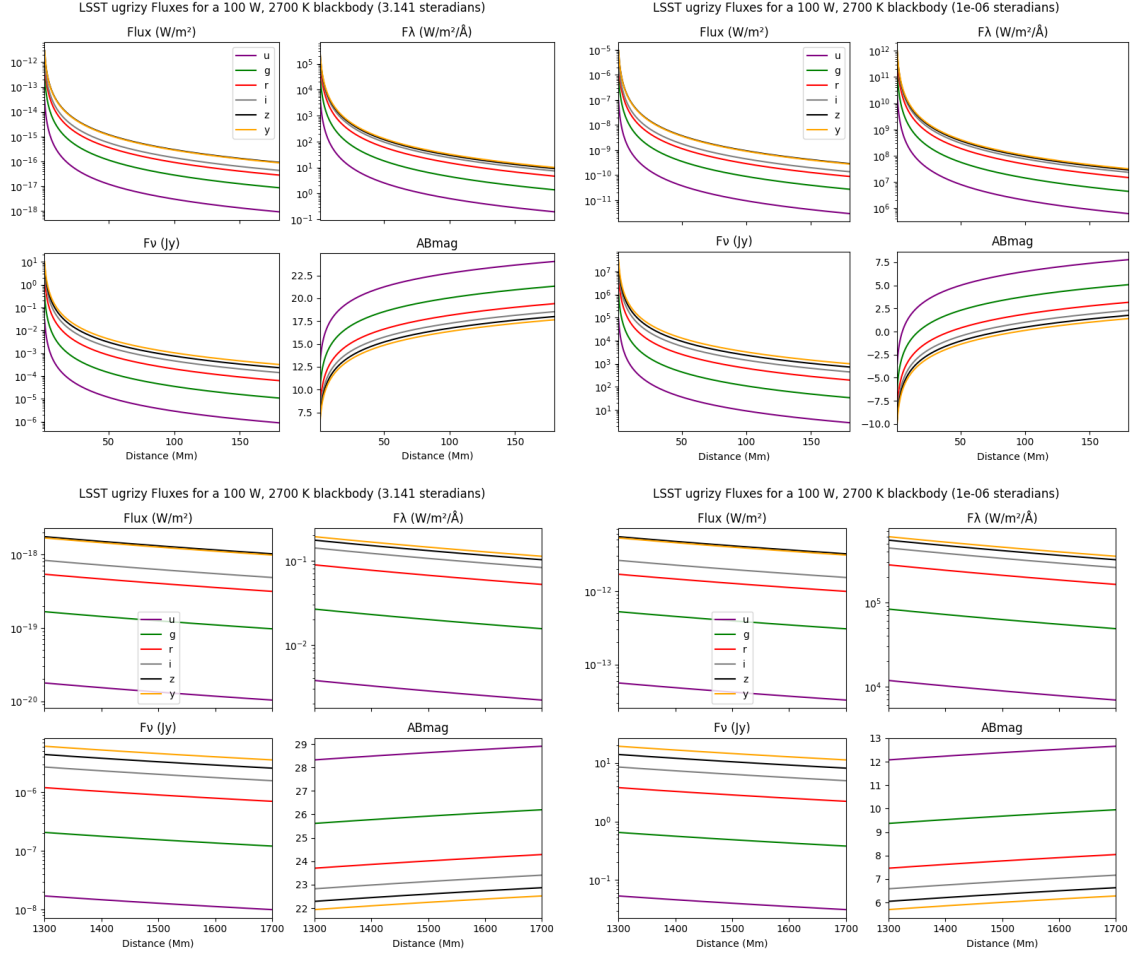


Figure 4.2: Graphs from the initial runs/parameters, looking at a 100 W, 2700 K incandescent source in Vera Rubin Observatory's ugrizy filters at a large range of distances. Despite it being an 8-meter class telescope, the very faint magnitudes (often  $\geq 20$ ), pushed us towards other designs.

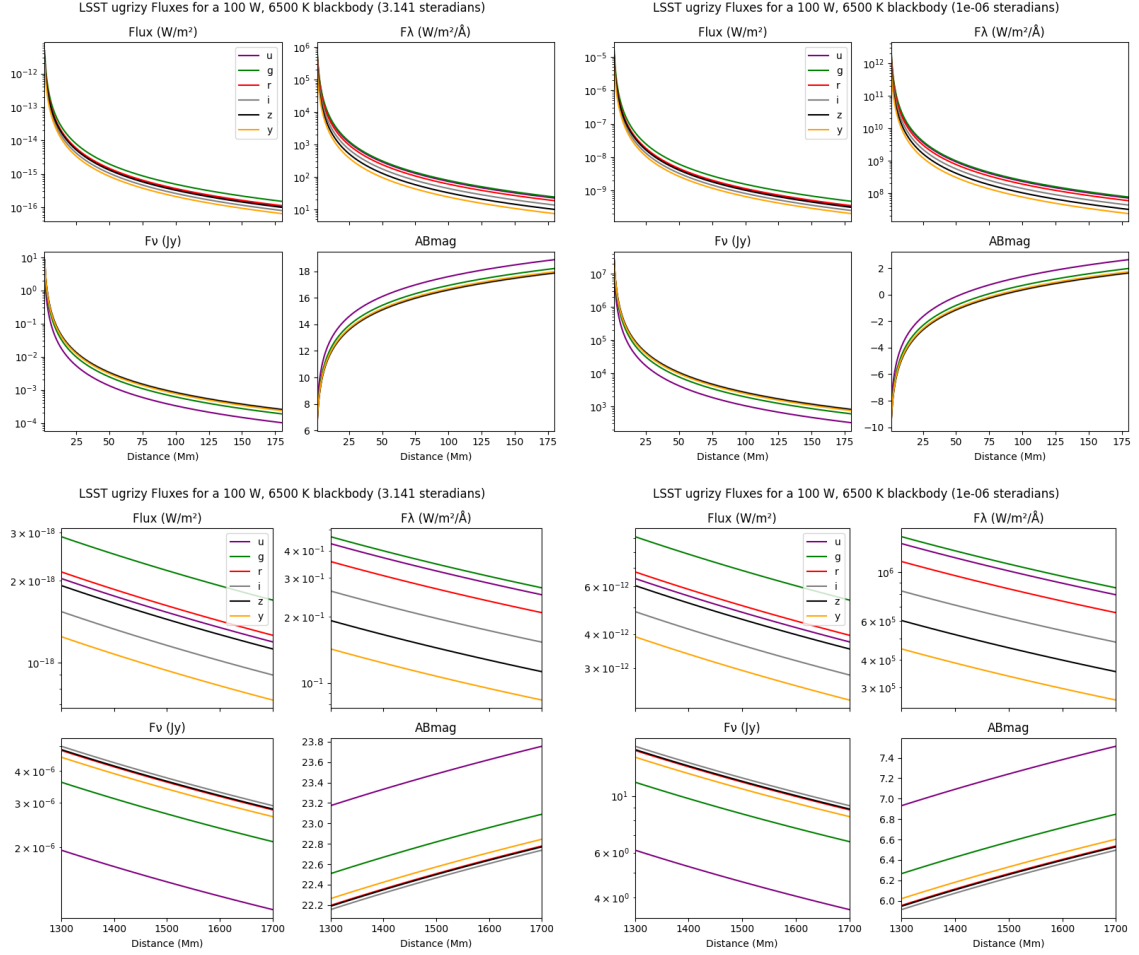


Figure 4.3: Graphs from the initial runs/parameters, looking at a 100 W, 6500 K incandescent source in Vera Rubin Observatory's ugrizy filters at a large range of distances. While the hotter source is substantially brighter in visible light, this would be difficult to do as a true blackbody.

The initial range of orbits included: a low Earth orbit (few hundred km), a highly eccentric geosynchronous orbit, various high Earth orbits, and Earth-Sun L2 halo orbits. Hence the distance ranges here of "near" (1000 km at an implied slant to 180,000 km or a bit less than half the distance to the moon) and "far" (1.3 to 1.9 million km, based off of typical values for JWST). Later on the orbit choices were refined, with L2 dropped and eventually the focus being on GEO.

While the nominal incandescent system was 100 W, for LEDs 1 W and 0.1 W systems were looked at.

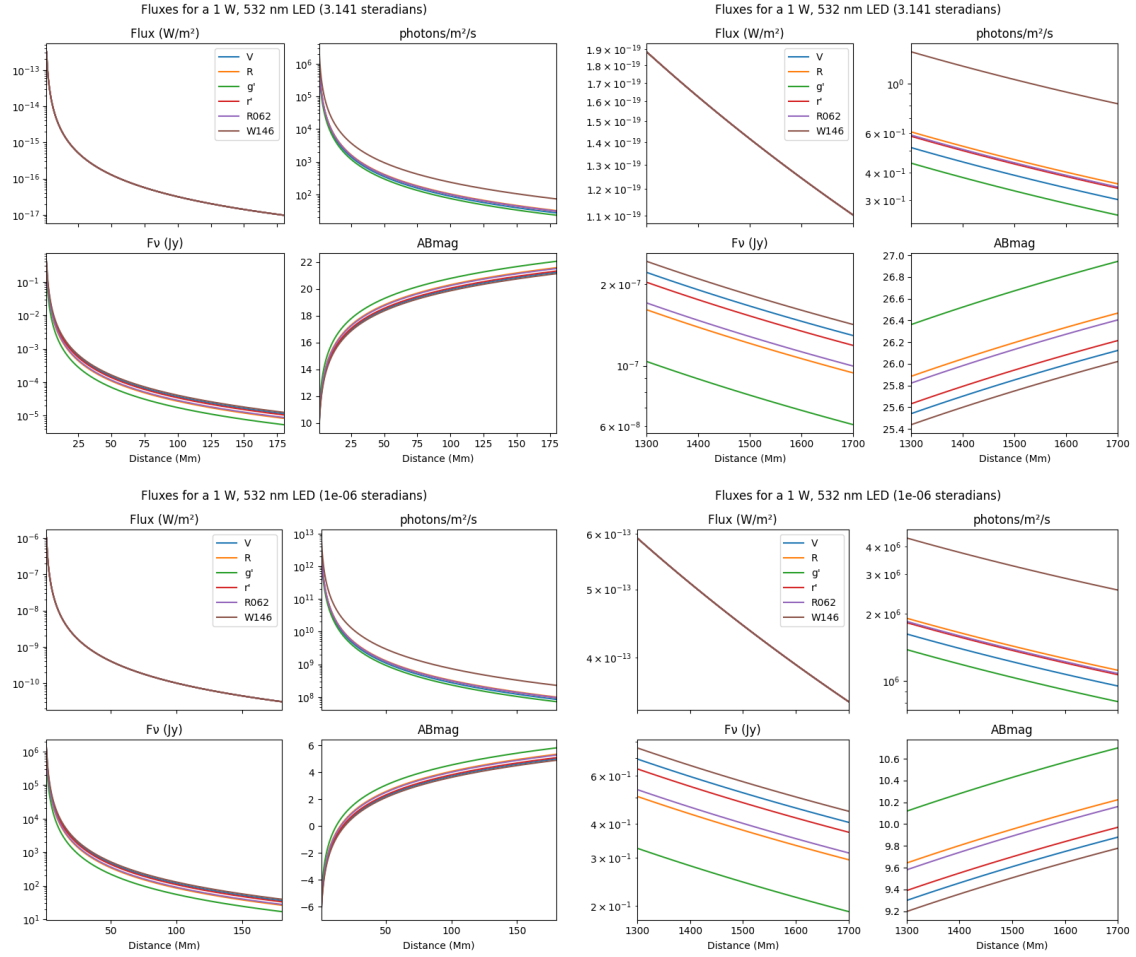


Figure 4.4: A typical LED (532 nm 1 W source), at varying collimations and distances comparable to the incandescent sources. Filters from all of the instruments that we considered that could plausibly detect that wavelength are shown. Again, isotropic emission ( $4\pi$  sr), a stand-in for a bare fibre or possibly an integrating sphere ( $\pi$  sr), and a highly collimated beam ( $1 \mu\text{sr}$ ) are shown. While LEDs offer order of magnitude increases in photons per watt in this wavelength range, the uncollimated beams are again quite faint (below 20th magnitude at the longer distances considered).

Given their small size and potentially smaller beam-width, a decision was made to focus more on bare single mode fibres than integrating spheres. Bare fibres were ultimately used on ORCASat. Follow-up missions like Landolt will look into more collimated optics, atmospheric absorption, solar reflections, etcetera.

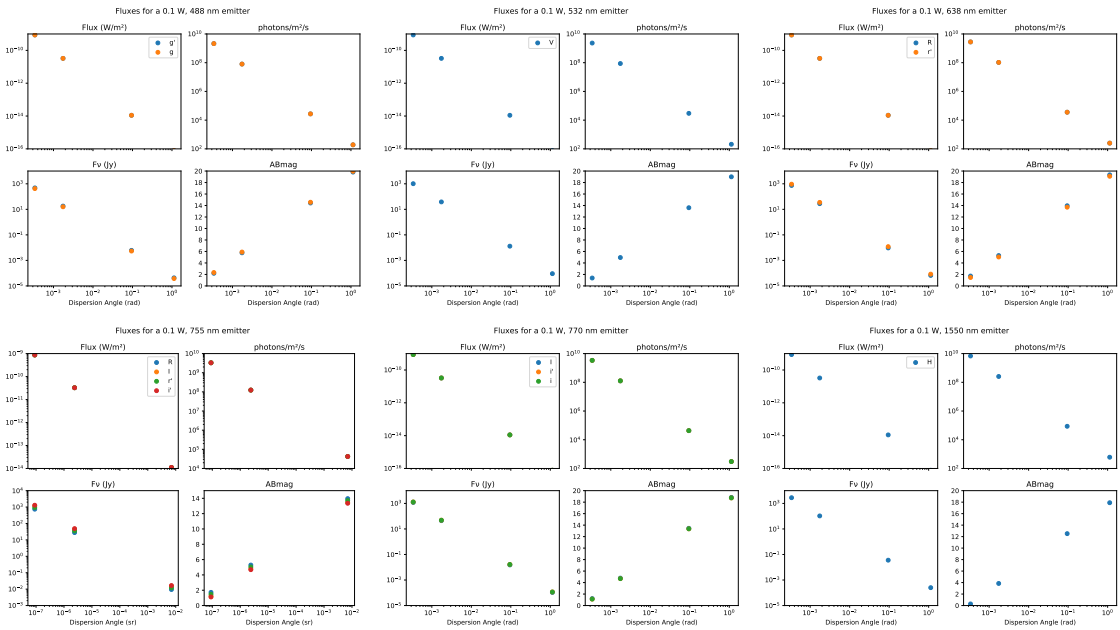


Figure 4.5: Graphs from later runs. Here, the craft would be in GEO (35,768 km), with an LED emitter. Four dispersions were looked at: 338 microradians, 0.1 degrees, 5.42 degrees, and (depending on the run)  $2/\sqrt{\pi}$  radians. At this point, multiple kinds of optics were being considered to get a range of apparent magnitudes, depending on what would be observing the light source.

## **4.7 Conclusions**

I provided calculations that helped to define and refine a project that has become a probe class mission.

They showed that the tradeoffs on distance and brightness meant that somewhat collimated LED light sources were required, and distant (beyond geosynchronous) orbits would be impractical.

## Chapter 5: Overall Conclusions

### 5.1 EPRV Survey Simulations Conclusions

Current and near-future EPRV surveys may be able to find planets around planned direct imaging stars, as well as help characterize their orbits and masses, assisting in atmospheric retrievals. How to best design those surveys to maximize yield is an area of current research.

We (I) developed a pipeline for finding exposure times for stars, simulating a survey with said stars, and calculating the precisions of RV measurements given an observation time-series. This pipeline builds on the MINERVA dispatch scheduler and [63], and makes provisions for a number of physical parameters. We run surveys with multiple stellar target lists, telescope/spectrograph combinations (“architectures”) at multiple site combinations, exposure time constraints, and target weighting algorithms.

#### 5.1.1 Paper 1

Of the architectures in section 2.2.4, all of the 7 configurations that were fully studied can achieve sufficient precision and cadence to (optimistically) detect at  $\text{SNR} = 10$  a  $K = 10$  cm/s planet around most of the stars in the target list. Two of the architectures (IIa/IIb and VIIIa/VIIIb) have more margin than the rest, so would probably be better for decreases in performance from eg: stellar activity. At the same time, that all architectures worked suggests that one can focus on features not considered here (eg: cost) for what would be the “best”. Our nominal p-mode compensation method (a fixed minimum observation time) does not appear to be especially sensitive to the exact value used, with both 5 and 10 minute ones giving similar results. This especially holds for the architectures with smaller telescopes, as they already tend to have longer exposure times.

### 5.1.2 Paper 2

There are a number of survey considerations that not fully considered in paper 1. Specifically, optimizing the target selection algorithm, looking at target observability (in both position and stellar properties), and better addressing both stellar activity and the simplifications of our atmospheric model.

We consider multiple target weighting algorithms, (re)settling on a simple combination of hour angle and time since last observation. This is “good enough”, being relatively efficient and in line with real-world surveys, despite that. We do not try to otherwise optimize on cadence, based on the assumption that a large number of frequent observations for most targets will be sufficiently close to optimal without the computational overhead.

We expand the p-mode compensation methods used (the two nominal ones also used in the first paper, and two physically motivated ones), and find that outside of implausibly short exposure cases, none negatively impact the number of observations or detection sensitivity. As the physically motivated methods are computationally cheap, this suggests that exposure time calculations can ““just” take them into account and that so minimize p-mode oscillations as a noise source for all stars.

We partially account for the limitations of our atmospheric model by comparing errors from uncorrected telluric lines [195] with our target precisions and how they affect the sensitivity heuristic. We find that they introduce an amount of noise that is small compared with our target measurement precision in the visible, and so a manageable part of an error budget. But in the near infrared, they are an order of magnitude larger than the nominal 10 cm/s of an earth-like planet around a sun-like star, and so must be dealt with.

We find that the position in the sky of target stars only matters moderately. The range of declinations that allow for a large number of observations is quite broad at typical mid-latitude sites, and wider than rule of thumb declination cuts. Nominally circumpolar stars also don’t show a boost, possibly because they’re frequently below the telescope’s minimum elevation. Right ascension also matters, with overall number of observations affected by the length of night and weather. This is a relatively weak effect and can be washed out in some

survey architectures.

Exposure times and target list size are (outside of declinations on the edge of observability, and extremes of weather) the driving factor in how often a target is observed and often the overall precision. The biggest factor behind our nominal exposure times (for stars that otherwise make for good RV targets) tends to be target precision. There's a surprisingly large range where changing effective temperatures don't have a large effect on exposure times, though extremes (especially at the hotter end) can still be found.

## 5.2 Orbiting Photometric Light-Source Conclusions

There is a need for better absolute calibration of photometric fluxes, as they have not kept up with relative calibration, and the limitations in precision are hampering many sub-fields of Astronomy. I provided calculations that helped to define and refine a project that has become a probe class mission to do provide a calibration source.

They showed that the trade-offs on distance and brightness meant that somewhat collimated LED light sources were required, and distant (beyond geosynchronous) orbits would be impractical. This drove the final selection of LED illuminated but otherwise bare fibres for the prototype mission.

## Bibliography

## Bibliography

- [1] R. L. Akeson, X. Chen, D. Ciardi, M. Crane, J. Good, M. Harbut, E. Jackson, S. R. Kane, A. C. Laity, S. Leifer, M. Lynn, D. L. McElroy, M. Papin, P. Plavchan, S. V. Ramírez, R. Rey, K. von Braun, M. Wittman, M. Abajian, B. Ali, C. Beichman, A. Beekley, G. B. Berriman, S. Berukoff, G. Bryden, B. Chan, S. Groom, C. Lau, A. N. Payne, M. Regelson, M. Saucedo, M. Schmitz, J. Stauffer, P. Wyatt, and A. Zhang, “The NASA Exoplanet Archive: Data and Tools for Exoplanet Research,” *PASP*, vol. 125, no. 930, p. 989, Aug. 2013.
- [2] N. G. Roman, “Planets of other suns.” *AJ*, vol. 64, pp. 344–345, Jan. 1959.
- [3] O. Struve, “Proposal for a project of high-precision stellar radial velocity work,” *The Observatory*, vol. 72, pp. 199–200, Oct. 1952.
- [4] A. Wolszczan and D. A. Frail, “A planetary system around the millisecond pulsar PSR1257 + 12,” *Nature*, vol. 355, no. 6356, pp. 145–147, Jan. 1992.
- [5] M. Mayor and D. Queloz, “A Jupiter-mass companion to a solar-type star,” *Nature*, vol. 378, pp. 355–359, Nov. 1995.
- [6] D. L. Pollacco, I. Skillen, A. Collier Cameron, D. J. Christian, C. Hellier, J. Irwin, T. A. Lister, R. A. Street, R. G. West, D. R. Anderson, W. I. Clarkson, H. Deeg, B. Enoch, A. Evans, A. Fitzsimmons, C. A. Haswell, S. Hodgkin, K. Horne, S. R. Kane, F. P. Keenan, P. F. L. Maxted, A. J. Norton, J. Osborne, N. R. Parley, R. S. I. Ryans, B. Smalley, P. J. Wheatley, and D. M. Wilson, “The WASP Project and the SuperWASP Cameras,” *PASP*, vol. 118, no. 848, pp. 1407–1418, Oct. 2006.
- [7] J. Pepper, R. W. Pogge, D. L. DePoy, J. L. Marshall, K. Z. Stanek, A. M. Stutz, S. Poindexter, R. Siverd, T. P. O’Brien, M. Trueblood, and P. Trueblood, “The Kilodegree Extremely Little Telescope (KELT): A Small Robotic Telescope for Large-Area Synoptic Surveys,” *PASP*, vol. 119, no. 858, pp. 923–935, Aug. 2007.
- [8] W. J. Borucki, D. Koch, G. Basri, N. Batalha, T. Brown, D. Caldwell, J. Caldwell, J. Christensen-Dalsgaard, W. D. Cochran, E. DeVore, E. W. Dunham, A. K. Dupree, T. N. Gautier, J. C. Geary, R. Gilliland, A. Gould, S. B. Howell, J. M. Jenkins, Y. Kondo, D. W. Latham, G. W. Marcy, S. Meibom, H. Kjeldsen, J. J. Lissauer, D. G. Monet, D. Morrison, D. Sasselov, J. Tarter, A. Boss, D. Brownlee, T. Owen, D. Buzasi, D. Charbonneau, L. Doyle, J. Fortney, E. B. Ford, M. J. Holman, S. Seager, J. H. Steffen, W. F. Welsh, J. Rowe, H. Anderson, L. Buchhave, D. Ciardi, L. Walkowicz, W. Sherry, E. Horch, H. Isaacson, M. E. Everett, D. Fischer, G. Torres, J. A. Johnson, M. Endl, P. MacQueen, S. T. Bryson, J. Dotson, M. Haas, J. Kolodziejczak, J. Van

- Cleve, H. Chandrasekaran, J. D. Twicken, E. V. Quintana, B. D. Clarke, C. Allen, J. Li, H. Wu, P. Tenenbaum, E. Verner, F. Bruhweiler, J. Barnes, and A. Prsa, “Kepler Planet-Detection Mission: Introduction and First Results,” *Science*, vol. 327, no. 5968, p. 977, Feb. 2010.
- [9] G. R. Ricker, “The Transiting Exoplanet Survey Satellite Mission,” *JAAVSO*, vol. 42, no. 1, p. 234, Jun. 2014.
- [10] C. Marois, B. Macintosh, T. Barman, B. Zuckerman, I. Song, J. Patience, D. Lafrenière, and R. Doyon, “Direct Imaging of Multiple Planets Orbiting the Star HR 8799,” *Science*, vol. 322, no. 5906, p. 1348, Nov. 2008.
- [11] The LUVOIR Team, “The LUVOIR Mission Concept Study Final Report,” *arXiv e-prints*, p. arXiv:1912.06219, Dec. 2019.
- [12] B. S. Gaudi, S. Seager, B. Mennesson, A. Kiessling, K. Warfield, K. Cahoy, J. T. Clarke, S. Domagal-Goldman, L. Feinberg, O. Guyon, J. Kasdin, D. Mawet, P. Plavchan, T. Robinson, L. Rogers, P. Scowen, R. Somerville, K. Stapelfeldt, C. Stark, D. Stern, M. Turnbull, R. Amini, G. Kuan, S. Martin, R. Morgan, D. Redding, H. P. Stahl, R. Webb, O. Alvarez-Salazar, W. L. Arnold, M. Arya, B. Balasubramanian, M. Baysinger, R. Bell, C. Below, J. Benson, L. Blais, J. Booth, R. Bourgeois, C. Bradford, A. Brewer, T. Brooks, E. Cady, M. Caldwell, R. Calvet, S. Carr, D. Chan, V. Cormarkovic, K. Coste, C. Cox, R. Danner, J. Davis, L. Dewell, L. Dorsett, D. Dunn, M. East, M. Effinger, R. Eng, G. Freebury, J. Garcia, J. Gaskin, S. Greene, J. Hennessy, E. Hilgemann, B. Hood, W. Holota, S. Howe, P. Huang, T. Hull, R. Hunt, K. Hurd, S. Johnson, A. Kissil, B. Knight, D. Kolenz, O. Kraus, J. Krist, M. Li, D. Lisman, M. Mandic, J. Mann, L. Marchen, C. Marrese-Reading, J. McCready, J. McGown, J. Missun, A. Miyaguchi, B. Moore, B. Nemati, S. Nikzad, J. Nissen, M. Novicki, T. Perrine, C. Pineda, O. Polanco, D. Putnam, A. Qureshi, M. Richards, A. J. Eldorado Riggs, M. Rodgers, M. Rud, N. Saini, D. Scalisi, D. Scharf, K. Schulz, G. Serabyn, N. Sigrist, G. Sikkia, A. Singleton, S. Shaklan, S. Smith, B. Southerd, M. Stahl, J. Steeves, B. Sturges, C. Sullivan, H. Tang, N. Taras, J. Tesch, M. Therrell, H. Tseng, M. Valente, D. Van Buren, J. Villalvazo, S. Warwick, D. Webb, T. Westerhoff, R. Wofford, G. Wu, J. Woo, M. Wood, J. Ziemer, G. Arney, J. Anderson, J. Maíz-Apellániz, J. Bartlett, R. Belikov, E. Bendek, B. Cenko, E. Douglas, S. Dulz, C. Evans, V. Faramaz, Y. K. Feng, H. Ferguson, K. Follette, S. Ford, M. García, M. Geha, D. Gelino, Y. Götberg, S. Hildebrand t, R. Hu, K. Jahnke, G. Kennedy, L. Kreidberg, A. Isella, E. Lopez, F. Marchis, L. Macri, M. Marley, W. Matzko, J. Mazoyer, S. McCandliss, T. Meshkat, C. Mordasini, P. Morris, E. Nielsen, P. Newman, E. Petigura, M. Postman, A. Reines, A. Roberge, I. Roederer, G. Ruane, E. Schwiererman, D. Sirbu, C. Spalding, H. Teplitz, J. Tumlinson, N. Turner, J. Werk, A. Wofford, M. Wyatt, A. Young, and R. Zellem, “The Habitable Exoplanet Observatory (HabEx) Mission Concept Study Final Report,” *arXiv e-prints*, p. arXiv:2001.06683, Jan. 2020.
- [13] R. Morgan, D. Savransky, M. Turmon, B. Mennesson, W. Dula, D. Keithly, E. E. Mamajek, P. Newman, P. Plavchan, T. D. Robinson, G. Roudier, and C. Stark, “Faster Exo-Earth yield for HabEx and LUVOIR via extreme precision radial velocity prior knowledge,” *Journal of Astronomical Telescopes, Instruments, and Systems*, vol. 7, p. 021220, Apr. 2021.

- [14] P. Plavchan, G. Vasisht, C. Beichman, H. Cegla, X. Dumusque, S. Wang, P. Gao, C. Dressing, F. Bastien, S. Basu, T. Beatty, A. Bechter, E. Bechter, C. Blake, V. Bourrier, B. Cale, D. Ciardi, J. Crass, J. Crepp, K. de Kleer, S. Diddams, J. Eastman, D. Fischer, J. Gagné, S. Gaudi, C. Grier, R. Hall, S. Halverson, B. Hamze, E. Herrero Casas, A. Howard, E. Kempton, N. Latouf, S. Leifer, P. Lightsey, C. Lisse, E. Martin, W. Matzko, D. Mawet, A. Mayo, P. Newman, S. Papp, B. Pope, B. Purcell, S. Quinn, I. Ribas, A. Rosich, S. Sanchez-Maes, A. Tanner, S. Thompson, K. Vahala, J. Wang, P. Williams, A. Wise, and J. Wright, “EarthFinder Probe Mission Concept Study: Characterizing nearby stellar exoplanet systems with Earth-mass analogs for future direct imaging,” *arXiv e-prints*, p. arXiv:2006.13428, Jun. 2020.
- [15] NASEM, *Pathways to Discovery in Astronomy and Astrophysics for the 2020s*. Washington, DC: The National Academies Press, 2021. [Online]. Available: <https://nap.nationalacademies.org/catalog/26141/pathways-to-discovery-in-astronomy-and-astrophysics-for-the-2020s>
- [16] ——, *Exoplanet Science Strategy*. Washington, DC: The National Academies Press, 2018. [Online]. Available: <https://www.nap.edu/catalog/25187/exoplanet-science-strategy>
- [17] J. Crass, B. S. Gaudi, S. Leifer, C. Beichman, C. Bender, G. Blackwood, J. A. Burt, J. L. Callas, H. M. Cegla, S. A. Diddams, X. Dumusque, J. D. Eastman, E. B. Ford, B. Fulton, R. Gibson, S. Halverson, R. D. Haywood, F. Hearty, A. W. Howard, D. W. Latham, J. Löhner-Böttcher, E. E. Mamajek, A. Mortier, P. Newman, P. Plavchan, A. Quirrenbach, A. Reiners, P. Robertson, A. Roy, C. Schwab, A. Seifahrt, A. Szentgyorgyi, R. Terrien, J. K. Teske, S. Thompson, and G. Vasishth, “Extreme Precision Radial Velocity Working Group Final Report,” *arXiv e-prints*, p. arXiv:2107.14291, Jul. 2021.
- [18] B. S. Gaudi and J. N. Winn, “Prospects for the Characterization and Confirmation of Transiting Exoplanets via the Rossiter-McLaughlin Effect,” *ApJ*, vol. 655, no. 1, pp. 550–563, Jan. 2007.
- [19] P. Plavchan, D. Latham, S. Gaudi, J. Crepp, X. Dumusque, G. Furesz, A. Vanderburg, C. Blake, D. Fischer, L. Prato, R. White, V. Makarov, G. Marcy, K. Stapelfeldt, R. Haywood, A. Collier-Cameron, A. Quirrenbach, S. Mahadevan, G. Anglada, and P. Muirhead, “Radial Velocity Prospects Current and Future: A White Paper Report prepared by the Study Analysis Group 8 for the Exoplanet Program Analysis Group (ExoPAG),” *ArXiv e-prints*, Mar. 2015.
- [20] S. R. Kane, D. P. Schneider, and J. Ge, “Simulations for multi-object spectrograph planet surveys,” *MNRAS*, vol. 377, no. 4, pp. 1610–1622, Jun. 2007.
- [21] D. A. Fischer, G. Anglada-Escude, P. Arriagada, R. V. Baluev, J. L. Bean, F. Bouchy, L. A. Buchhave, T. Carroll, A. Chakraborty, J. R. Crepp, R. I. Dawson, S. A. Diddams, X. Dumusque, J. D. Eastman, M. Endl, P. Figueira, E. B. Ford, D. Foreman-Mackey, P. Fournier, G. Fűrész, B. S. Gaudi, P. C. Gregory, F. Grundahl, A. P. Hatzes, G. Hébrard, E. Herrero, D. W. Hogg, A. W. Howard, J. A. Johnson, P. Jorden, C. A. Jurgenson, D. W. Latham, G. Laughlin, T. J. Loredo, C. Lovis, S. Mahadevan, T. M.

- McCracken, F. Pepe, M. Perez, D. F. Phillips, P. P. Plavchan, L. Prato, A. Quirrenbach, A. Reiners, P. Robertson, N. C. Santos, D. Sawyer, D. Segransan, A. Sozzetti, T. Steinmetz, A. Szentgyorgyi, S. Udry, J. A. Valenti, S. X. Wang, R. A. Wittenmyer, and J. T. Wright, “State of the Field: Extreme Precision Radial Velocities,” *PASP*, vol. 128, no. 964, p. 066001, Jun. 2016.
- [22] A. W. Howard and B. J. Fulton, “Limits on Planetary Companions from Doppler Surveys of Nearby Stars,” *PASP*, vol. 128, no. 11, p. 114401, Nov. 2016.
- [23] P. Robertson, S. Mahadevan, M. Endl, and A. Roy, “Stellar activity masquerading as planets in the habitable zone of the M dwarf Gliese 581,” *Science*, vol. 345, no. 6195, pp. 440–444, Jul. 2014.
- [24] P. Robertson, A. Roy, and S. Mahadevan, “Stellar Activity Mimics a Habitable-zone Planet around Kapteyn’s Star,” *ApJL*, vol. 805, no. 2, p. L22, Jun. 2015.
- [25] P. Robertson, “Aliasing in the Radial Velocities of YZ Ceti: An Ultra-short Period for YZ Ceti c?” *ApJL*, vol. 864, no. 2, p. L28, Sep. 2018.
- [26] P. Robertson, M. Endl, G. W. Henry, W. D. Cochran, P. J. MacQueen, and M. H. Williamson, “Stellar Activity and its Implications for Exoplanet Detection on GJ 176,” *ApJ*, vol. 801, no. 2, p. 79, Mar. 2015.
- [27] A. P. Hatzes, W. D. Cochran, M. Endl, E. W. Guenther, P. MacQueen, M. Hartmann, M. Zechmeister, I. Han, B. C. Lee, G. A. H. Walker, S. Yang, A. M. Larson, K. M. Kim, D. E. Mkrtchian, M. Döllinger, A. E. Simon, and L. Girardi, “Long-lived, long-period radial velocity variations in Aldebaran: A planetary companion and stellar activity,” *A&A*, vol. 580, p. A31, Aug. 2015.
- [28] R. D. Haywood, “Hide and Seek: Radial-Velocity Searches for Planets around Active Stars,” Ph.D. dissertation, University of St Andrews, Nov. 2015.
- [29] R. F. Díaz, D. Ségransan, S. Udry, C. Lovis, F. Pepe, X. Dumusque, M. Marmier, R. Alonso, W. Benz, F. Bouchy, A. Coffinet, A. Collier Cameron, M. Deleuil, P. Figueira, M. Gillon, G. Lo Curto, M. Mayor, C. Mordasini, F. Motalebi, C. Moutou, D. Pollacco, E. Pompei, D. Queloz, N. Santos, and A. Wyttenbach, “The HARPS search for southern extra-solar planets. XXXVIII. Bayesian re-analysis of three systems. New super-Earths, unconfirmed signals, and magnetic cycles,” *A&A*, vol. 585, p. A134, Jan. 2016.
- [30] S. R. Kane, B. Thirumalachari, G. W. Henry, N. R. Hinkel, E. L. N. Jensen, T. S. Boyajian, D. A. Fischer, A. W. Howard, H. T. Isaacson, and J. T. Wright, “Stellar Activity and Exclusion of the Outer Planet in the HD 99492 System,” *ApJL*, vol. 820, no. 1, p. L5, Mar. 2016.
- [31] E. R. Newton, J. Irwin, D. Charbonneau, Z. K. Berta-Thompson, and J. A. Dittmann, “The Impact of Stellar Rotation on the Detectability of Habitable Planets around M Dwarfs,” *ApJL*, vol. 821, no. 1, p. L19, Apr. 2016.

- [32] A. Vanderburg, P. Plavchan, J. A. Johnson, D. R. Ciardi, J. Swift, and S. R. Kane, “Radial velocity planet detection biases at the stellar rotational period,” *MNRAS*, vol. 459, no. 4, pp. 3565–3573, Jul. 2016.
- [33] J. Lubin, P. Robertson, G. Stefansson, J. Ninan, S. Mahadevan, M. Endl, E. Ford, J. T. Wright, C. Beard, C. Bender, W. D. Cochran, S. A. Diddams, C. Fredrick, S. Halverson, S. Kanodia, A. J. Metcalf, L. Ramsey, A. Roy, C. Schwab, and R. Terrien, “Stellar Activity Manifesting at a One Year Alias Explains Barnard b as a False Positive,” *arXiv e-prints*, p. arXiv:2105.07005, May 2021.
- [34] X. Dumusque, “Radial velocity fitting challenge. I. Simulating the data set including realistic stellar radial-velocity signals,” *A&A*, vol. 593, p. A5, Aug. 2016.
- [35] X. Dumusque, F. Borsa, M. Damasso, R. F. Díaz, P. C. Gregory, N. C. Hara, A. Hatzes, V. Rajpaul, M. Tuomi, S. Aigrain, G. Anglada-Escudé, A. S. Bonomo, G. Boué, F. Dauvergne, G. Frustagli, P. Giacobbe, R. D. Haywood, H. R. A. Jones, J. Laskar, M. Pinamonti, E. Poretti, M. Rainer, D. Ségransan, A. Sozzetti, and S. Udry, “Radial-velocity fitting challenge. II. First results of the analysis of the data set,” *A&A*, vol. 598, p. A133, Feb. 2017.
- [36] R. D. Hall, S. J. Thompson, W. Handley, and D. Queloz, “On the Feasibility of Intense Radial Velocity Surveys for Earth-Twin Discoveries,” *MNRAS*, vol. 479, no. 3, pp. 2968–2987, Sep. 2018.
- [37] C. Nava, M. López-Morales, R. D. Haywood, and H. A. C. Giles, “Exoplanet Imitators: A Test of Stellar Activity Behavior in Radial Velocity Signals,” *AJ*, vol. 159, no. 1, p. 23, Jan. 2020.
- [38] V. Rajpaul, S. Aigrain, and S. Roberts, “Ghost in the time series: no planet for Alpha Cen B,” *MNRAS*, vol. 456, no. 1, pp. L6–L10, Feb. 2016.
- [39] V. Rajpaul, L. A. Buchhave, and S. Aigrain, “Pinning down the mass of Kepler-10c: the importance of sampling and model comparison,” *MNRAS*, vol. 471, no. 1, pp. L125–L130, Oct. 2017.
- [40] A. Leleu, Y. Alibert, N. C. Hara, M. J. Hooton, T. G. Wilson, P. Robutel, J. B. Delisle, J. Laskar, S. Hoyer, C. Lovis, E. M. Bryant, E. Ducrot, J. Cabrera, L. Delrez, J. S. Acton, V. Adibekyan, R. Allart, C. Allende Prieto, R. Alonso, D. Alves, D. R. Anderson, D. Angerhausen, G. Anglada Escudé, J. Asquier, D. Barrado, S. C. C. Barros, W. Baumjohann, D. Bayliss, M. Beck, T. Beck, A. Bekkelien, W. Benz, N. Billot, A. Bonfanti, X. Bonfils, F. Bouchy, V. Bourrier, G. Boué, A. Brandeker, C. Broeg, M. Budre, A. Burdanov, M. R. Burleigh, T. Bárczy, A. C. Cameron, S. Chamberlain, S. Charnoz, B. F. Cooke, C. Corral Van Damme, A. C. M. Correia, S. Cristiani, M. Damasso, M. B. Davies, M. Deleuil, O. D. S. Demangeon, B. O. Demory, P. Di Marcantonio, G. Di Persio, X. Dumusque, D. Ehrenreich, A. Erikson, P. Figueira, A. Fortier, L. Fossati, M. Fridlund, D. Futyan, D. Gandolfi, A. García Muñoz, L. J. Garcia, S. Gill, E. Gillen, M. Gillon, M. R. Goad, J. I. González Hernández, M. Guedel, M. N. Günther, J. Haldemann, B. Henderson, K. Heng, A. E. Hogan, K. Isaak, E. Jehin, J. S. Jenkins, A. Jordán, L. Kiss, M. H. Kristiansen, K. Lam, B. Lavie, A. Lecavelier des Etangs, M. Lendl, J. Lillo-Box, G. Lo Curto, D. Magrin, C. J. A. P. Martins,

- P. F. L. Maxted, J. McCormac, A. Mehner, G. Micela, P. Molaro, M. Moyano, C. A. Murray, V. Nascimbeni, N. J. Nunes, G. Olofsson, H. P. Osborn, M. Oshagh, R. Ottensamer, I. Pagano, E. Pallé, P. P. Pedersen, F. A. Pepe, C. M. Persson, G. Peter, G. Piotto, G. Polenta, D. Pollacco, E. Poretti, F. J. Pozuelos, D. Queloz, R. Ragazzoni, N. Rando, F. Ratti, H. Rauer, L. Raynard, R. Rebolo, C. Reimers, I. Ribas, N. C. Santos, G. Scandariato, J. Schneider, D. Sebastian, M. Sestovic, A. E. Simon, A. M. S. Smith, S. G. Sousa, A. Sozzetti, M. Steller, A. Suárez Mascareño, G. M. Szabó, D. Ségransan, N. Thomas, S. Thompson, R. H. Tilbrook, A. Triaud, O. Turner, S. Udry, V. Van Grootel, H. Venus, F. Verrecchia, J. I. Vines, N. A. Walton, R. G. West, P. J. Wheatley, D. Wolter, and M. R. Zapatero Osorio, “Six transiting planets and a chain of Laplace resonances in TOI-178,” *A&A*, vol. 649, p. A26, May 2021.
- [41] V. M. Rajpaul, L. A. Buchhave, G. Lacedelli, K. Rice, A. Mortier, L. Malavolta, S. Aigrain, L. Borsato, A. W. Mayo, D. Charbonneau, M. Damasso, X. Dumusque, A. Ghedina, D. W. Latham, M. López-Morales, A. Magazzú, G. Micela, E. Molinari, F. Pepe, G. Piotto, E. Poretti, S. Rowther, A. Sozzetti, S. Udry, and C. A. Watson, “A HARPS-N mass for the elusive Kepler-37d: a case study in disentangling stellar activity and planetary signals,” *MNRAS*, Jul. 2021.
  - [42] J. J. Swift, M. Bottom, J. A. Johnson, J. T. Wright, N. McCrady, R. A. Wittenmyer, P. Plavchan, R. Riddle, P. S. Muirhead, E. Herzig, J. Myles, C. H. Blake, J. Eastman, T. G. Beatty, S. I. Barnes, S. R. Gibson, B. Lin, M. Zhao, P. Gardner, E. Falco, S. Criswell, C. Nava, C. Robinson, D. H. Sliski, R. Hedrick, K. Ivarsen, A. Hjelstrom, J. de Vera, and A. Szentgyorgyi, “Miniature Exoplanet Radial Velocity Array (MINERVA) I. Design, Commissioning, and First Science Results,” *Journal of Astronomical Telescopes, Instruments, and Systems*, vol. 1, no. 2, p. 027002, Apr. 2015.
  - [43] R. C. Bohlin, “Comparison of White Dwarf Models with STIS Spectrophotometry,” *AJ*, vol. 120, no. 1, pp. 437–446, Jul. 2000.
  - [44] R. C. Bohlin, M. E. Dickinson, and D. Calzetti, “Spectrophotometric Standards from the Far-Ultraviolet to the Near-Infrared: STIS and NICMOS Fluxes,” *AJ*, vol. 122, no. 4, pp. 2118–2128, Oct. 2001.
  - [45] R. C. Bohlin, “STIS Flux Calibration,” in *HST Calibration Workshop : Hubble after the Installation of the ACS and the NICMOS Cooling System*, S. Arribas, A. Koekemoer, and B. Whitmore, Eds., Jan. 2003, p. 115.
  - [46] J. B. Oke and J. E. Gunn, “Secondary standard stars for absolute spectrophotometry.” *ApJ*, vol. 266, pp. 713–717, Mar. 1983.
  - [47] M. Fukugita, T. Ichikawa, J. E. Gunn, M. Doi, K. Shimasaku, and D. P. Schneider, “The Sloan Digital Sky Survey Photometric System,” *AJ*, vol. 111, p. 1748, Apr. 1996.
  - [48] R. C. Bohlin and R. L. Gilliland, “Absolute Flux Distribution of the SDSS Standard BD +17°4708,” *AJ*, vol. 128, no. 6, pp. 3053–3060, Dec. 2004.
  - [49] R. C. Bohlin, I. Hubeny, and T. Rauch, “New Grids of Pure-hydrogen White Dwarf NLTE Model Atmospheres and the HST/STIS Flux Calibration,” *AJ*, vol. 160, no. 1, p. 21, Jul. 2020.

- [50] R. C. Bohlin, S. Deustua, G. Narayan, A. Saha, A. Calamida, K. D. Gordon, J. B. Holberg, I. Hubeny, T. Matheson, and A. Rest, “Faint White Dwarf Flux Standards: Data and Models,” *AJ*, vol. 169, no. 1, p. 40, Jan. 2025.
- [51] M. S. Bessell, “Standard Photometric Systems,” *ARA&A*, vol. 43, pp. 293–336, Sep. 2005.
- [52] J. K. Luhn, E. B. Ford, Z. Guo, C. Gilbertson, P. Newman, P. Plavchan, J. A. Burt, J. Teske, and A. F. Gupta, “Impact of Correlated Noise on the Mass Precision of Earth-analog Planets in Radial Velocity Surveys,” *AJ*, vol. 165, no. 3, p. 98, Mar. 2023.
- [53] M. Cretignier, X. Dumusque, R. Allart, F. Pepe, and C. Lovis, “Measuring precise radial velocities on individual spectral lines. II. Dependence of stellar activity signal on line depth,” *A&A*, vol. 633, p. A76, Jan. 2020.
- [54] A. F. Lanza, A. Collier Cameron, and R. D. Haywood, “Reducing activity-induced variations in a radial-velocity time series of the Sun as a star,” *MNRAS*, vol. 486, no. 3, pp. 3459–3464, Jul. 2019.
- [55] X. Dumusque, “Measuring precise radial velocities on individual spectral lines. I. Validation of the method and application to mitigate stellar activity,” *A&A*, vol. 620, p. A47, Nov. 2018.
- [56] A. Wise, P. Plavchan, X. Dumusque, H. Cegla, and D. Wright, “Spectral Line Depth Variability in Radial Velocity Spectra,” *ApJ*, vol. 930, no. 2, p. 121, May 2022.
- [57] J. Burt, B. Holden, A. Wolfgang, and L. G. Bouma, “Simulating the M-R Relation from APF Follow-up of TESS Targets: Survey Design and Strategies for Overcoming Mass Biases,” *AJ*, vol. 156, no. 6, p. 255, Dec. 2018.
- [58] C. Nava, S. Johnson, N. McCrady, and Minerva, “Optimization of the MINERVA Exoplanet Search Strategy via Simulations,” in *American Astronomical Society Meeting Abstracts #225*, ser. American Astronomical Society Meeting Abstracts, vol. 225, Jan 2015, p. 258.26.
- [59] P.-Y. Bely, “Weather and seeing on Mauna Kea,” *PASP*, vol. 99, pp. 560–570, Jun. 1987.
- [60] D. Barrado, U. Thiele, J. Aceituno, S. Pedraz, S. F. Sánchez, A. Aguirre, M. Alises, G. Bergond, D. Galadí, A. Guijarro, F. Hoyo, D. Mast, L. Montoya, C. Sengupta, E. de Guindos, and E. Solano, “The Calar Alto Observatory: current status and future instrumentation,” in *Highlights of Spanish Astrophysics VI*, M. R. Zapatero Osorio, J. Gorgas, J. Maíz Apellániz, J. R. Pardo, and A. Gil de Paz, Eds., Nov. 2011, pp. 637–646.
- [61] P. Väisänen, C. Coetzee, A. Schroeder, S. M. Crawford, D. A. H. Buckley, J. Brink, É. Depagne, A. Kniazev, T. Koen, P. Kotze, F. Marang, B. Miszalski, E. Romero Colmenero, O. Strydom, V. Van Wyk, and T. B. Williams, “Worth its SALT: four

- years of full science operations with the Southern African Large Telescope,” in *Observatory Operations: Strategies, Processes, and Systems VI*, ser. Society of Photo-Optical Instrumentation Engineers (SPIE) Conference Series, A. B. Peck, R. L. Seaman, and C. R. Benn, Eds., vol. 9910, Jul. 2016, p. 99100T.
- [62] P. D. Newman, “Simulations for Planning Upcoming Exoplanet Radial Velocity Surveys II: Planet Injection and Recovery,” in prep.
  - [63] T. G. Beatty and B. S. Gaudi, “Astrophysical Sources of Statistical Uncertainty in Precision Radial Velocities and Their Approximations,” *PASP*, vol. 127, p. 1240, Dec. 2015.
  - [64] É. Artigau, L. Malo, R. Doyon, P. Figueira, X. Delfosse, and N. Astudillo-Defru, “Optical and Near-infrared Radial Velocity Content of M Dwarfs: Testing Models with Barnard’s Star,” *AJ*, vol. 155, no. 5, p. 198, May 2018.
  - [65] A. Reiners and M. Zechmeister, “Radial Velocity Photon Limits for the Dwarf Stars of Spectral Classes F-M,” *ApJS*, vol. 247, no. 1, p. 11, Mar. 2020.
  - [66] W. J. Chaplin, H. M. Cegla, C. A. Watson, G. R. Davies, and W. H. Ball, “Filtering Solar-Like Oscillations for Exoplanet Detection in Radial Velocity Observations,” *AJ*, vol. 157, no. 4, p. 163, Apr. 2019.
  - [67] P. M. Robertson, F. R. Hearty, T. B. Anderson, G. K. Stefánsson, E. I. Levi, C. F. Bender, S. Mahadevan, S. P. Halverson, A. J. Monson, L. W. Ramsey, A. Roy, C. Schwab, R. C. Terrien, M. J. Nelson, and B. Blank, “A system to provide sub-milliKelvin temperature control at T 300K for extreme precision optical radial velocimetry,” in *Proc. SPIE*, ser. Society of Photo-Optical Instrumentation Engineers (SPIE) Conference Series, vol. 9908, Aug. 2016, p. 990862.
  - [68] C. Schwab, A. Rakich, Q. Gong, S. Mahadevan, S. P. Halverson, A. Roy, R. C. Terrien, P. M. Robertson, F. R. Hearty, E. I. Levi, A. J. Monson, J. T. Wright, M. W. McElwain, C. F. Bender, C. H. Blake, J. Stürmer, Y. V. Gurevich, A. Chakraborty, and L. W. Ramsey, “Design of NEID, an extreme precision Doppler spectrograph for WIYN,” in *Proc. SPIE*, ser. Society of Photo-Optical Instrumentation Engineers (SPIE) Conference Series, vol. 9908, Aug. 2016, p. 99087H.
  - [69] F. Pepe, S. Cristiani, R. Rebolo, N. C. Santos, H. Dekker, A. Cabral, P. Di Martantonio, P. Figueira, G. Lo Curto, C. Lovis, M. Mayor, D. Mégevand, P. Molaro, M. Riva, M. R. Zapatero Osorio, M. Amate, A. Manescau, L. Pasquini, F. M. Zerbi, V. Adibekyan, M. Abreu, M. Affolter, Y. Alibert, M. Aliverti, R. Allart, C. Allende Prieto, D. Álvarez, D. Alves, G. Avila, V. Baldini, T. Bandy, S. C. C. Barros, W. Benz, A. Bianco, F. Borsa, V. Bourrier, F. Bouchy, C. Broeg, G. Calderone, R. Cirami, J. Coelho, P. Conconi, I. Coretti, C. Cumani, G. Cupani, V. D’Odorico, M. Damasso, S. Deiries, B. Delabre, O. D. S. Demangeon, X. Dumusque, D. Ehrenreich, J. P. Faria, A. Fragoso, L. Genolet, M. Genoni, R. Génova Santos, J. I. González Hernández, I. Hughes, O. Iwert, F. Kerber, J. Knudstrup, M. Landoni, B. Lavie, J. Lillo-Box, J. L. Lizon, C. Maire, C. J. A. P. Martins, A. Mehner, G. Micela, A. Modigliani, M. A. Monteiro, M. J. P. F. G. Monteiro, M. Moschetti, M. T. Murphy, N. Nunes, L. Oggioni, A. Oliveira, M. Oshagh, E. Pallé, G. Pariani, E. Poretti,

- J. L. Rasilla, J. Rebordão, E. M. Redaelli, S. Santana Tschudi, P. Santin, P. Santos, D. Ségransan, T. M. Schmidt, A. Segovia, D. Sosnowska, A. Sozzetti, S. G. Sousa, P. Spanò, A. Suárez Mascareño, H. Tabernero, F. Tenegi, S. Udry, and A. Zanutta, “ESPRESSO at VLT. On-sky performance and first results,” *A&A*, vol. 645, p. A96, Jan. 2021.
- [70] R. T. Blackman, D. A. Fischer, C. A. Jurgenson, D. Sawyer, T. M. McCracken, A. E. Szymkowiak, R. R. Petersburg, J. M. J. Ong, J. M. Brewer, L. L. Zhao, C. Leet, L. A. Buchhave, R. Tronsgaard, J. Llama, T. Sawyer, A. B. Davis, S. H. C. Cabot, M. Shao, R. Trahan, B. Nemati, M. Genoni, G. Pariani, M. Riva, P. Fournier, and R. Pawluczyk, “Performance Verification of the EXtreme PREcision Spectrograph,” *AJ*, vol. 159, no. 5, p. 238, May 2020.
- [71] A. Seifahrt, J. L. Bean, J. Stürmer, D. Kasper, L. Gers, C. Schwab, M. Zechmeister, G. Stefánsson, B. Montet, L. A. Dos Santos, A. Peck, J. White, and E. Tapia, “On-sky commissioning of MAROON-X: a new precision radial velocity spectrograph for Gemini North,” in *Society of Photo-Optical Instrumentation Engineers (SPIE) Conference Series*, ser. Society of Photo-Optical Instrumentation Engineers (SPIE) Conference Series, vol. 11447, Dec. 2020, p. 114471F.
- [72] C. Schwab, C. Bender, C. Blake, Q. Gong, S. Halverson, F. Hearty, E. Hunting, S. Kanodia, M. Liang, S. E. Logsdon, E. Lubar, S. Mahadevan, M. McElwain, A. Monson, J. Rajagopal, L. Ramsey, P. Robertson, A. Roy, G. K. Stefansson, R. Terrien, and J. T. Wright, “The NEID Doppler spectrometer at WIYN,” in *American Astronomical Society Meeting Abstracts #233*, ser. American Astronomical Society Meeting Abstracts, vol. 233, Jan. 2019, p. 408.03.
- [73] S. S. Vogt, M. Radovan, R. Kibrick, R. P. Butler, B. Alcott, S. Allen, P. Arriagada, M. Bolte, J. Burt, J. Cabak, K. Chloros, D. Cowley, W. Deich, B. Dupraw, W. Earthman, H. Epps, S. Faber, D. Fischer, E. Gates, D. Hilyard, B. Holden, K. Johnston, S. Keiser, D. Kanto, M. Katsuki, L. Laiterman, K. Lanclos, G. Laughlin, J. Lewis, C. Lockwood, P. Lynam, G. Marcy, M. McLean, J. Miller, T. Misch, M. Peck, T. Pfister, A. Phillips, E. Rivera, D. Sand ford, M. Saylor, R. Stover, M. Thompson, B. Walp, J. Ward, J. Wareham, M. Wei, and C. Wright, “APF—The Lick Observatory Automated Planet Finder,” *PASP*, vol. 126, no. 938, p. 359, Apr. 2014.
- [74] A. Szentgyorgyi, D. Baldwin, S. Barnes, J. Bean, S. Ben-Ami, P. Brennan, J. Budynkiewicz, D. Catropa, M.-Y. Chun, C. Conroy, A. Contos, J. D. Crane, D. Durusky, H. Epps, I. Evans, J. Evans, V. Fishman, A. Frebel, T. Gauron, D. Guzman, T. Hare, B.-H. Jang, J.-G. Jang, A. Jordan, J. Kim, K.-M. Kim, Y. Kim, S. Lee, M. Lopez-Morales, C. Mendes de Oliveira, K. McCracken, S. McMuldroch, J. Miller, M. Mueller, J. S. Oh, C. Onyuksel, B.-G. Park, C. Park, S.-J. Park, C. Paxson, D. Phillips, D. Plummer, W. Podgorski, A. Rubin, A. Seifahrt, D. Stark, J. Steiner, A. Uomoto, R. Walsworth, and Y.-S. Yu, “The GMT-consortium large earth finder (G-CLEF): an optical echelle spectrograph for the Giant Magellan Telescope (GMT),” in *Ground-based and Airborne Instrumentation for Astronomy VII*, ser. Society of Photo-Optical Instrumentation Engineers (SPIE) Conference Series, C. J. Evans, L. Simard, and H. Takami, Eds., vol. 10702, Jul. 2018, p. 107021R.

- [75] R. K. Gibson, R. Oppenheimer, C. T. Matthews, and G. Vasisht, “Characterization of the C-RED 2: a high-frame rate near-infrared camera,” *Journal of Astronomical Telescopes, Instruments, and Systems*, vol. 6, p. 011002, Jan. 2020.
- [76] J. R. Crepp, J. Crass, D. King, A. Bechter, E. Bechter, R. Ketterer, R. Reynolds, P. Hinz, D. Kopon, D. Cavalieri, L. Fantano, C. Koca, E. Onuma, K. Stapelfeldt, J. Thomas, S. Wall, S. Macenka, J. McGuire, R. Korniski, L. Zugby, J. Eisner, B. S. Gaudi, F. Hearty, K. Kratter, M. Kuchner, G. Micela, M. Nelson, I. Pagano, A. Quirrenbach, C. Schwab, M. Skrutskie, A. Sozzetti, C. Woodward, and B. Zhao, “iLocater: a diffraction-limited Doppler spectrometer for the Large Binocular Telescope,” in *Ground-based and Airborne Instrumentation for Astronomy VI*, ser. Society of Photo-Optical Instrumentation Engineers (SPIE) Conference Series, C. J. Evans, L. Simard, and H. Takami, Eds., vol. 9908, Aug. 2016, p. 990819.
- [77] D. Mawet, M. Fitzgerald, Q. Konopacky, C. Beichman, N. Jovanovic, R. Dekany, D. Hover, E. Chisholm, D. Ciardi, É. Artigau, R. Banyal, T. Beatty, B. Benneke, G. A. Blake, A. Burgasser, G. Canalizo, G. Chen, T. Do, G. Doppmann, R. Doyon, C. Dressing, M. Fang, T. Greene, L. Hillenbrand, A. Howard, S. Kane, T. Kataria, E. Kempton, H. Knutson, T. Kotani, D. Lafrenière, C. Liu, S. Nishiyama, G. Pandey, P. Plavchan, L. Prato, S. P. Rajaguru, P. Robertson, C. Salyk, B. Sato, E. Schlawin, S. Sengupta, T. Sivarani, W. Skidmore, M. Tamura, H. Terada, G. Vasisht, J. Wang, and H. Zhang, “High-resolution Infrared Spectrograph for Exoplanet Characterization with the Keck and Thirty Meter Telescopes,” in *Bulletin of the American Astronomical Society*, vol. 51, Sep. 2019, p. 134.
- [78] B. J. Rauscher, “Teledyne H1RG, H2RG, and H4RG Noise Generator,” *PASP*, vol. 127, no. 957, p. 1144, Nov. 2015.
- [79] E. B. Bechter, A. J. Bechter, J. R. Crepp, and J. Crass, “Assessing the suitability of H4RG near-infrared detectors for precise Doppler radial velocity measurements,” *Journal of Astronomical Telescopes, Instruments, and Systems*, vol. 5, p. 038004, Jul. 2019.
- [80] G. Mosby, B. J. Rauscher, C. Bennett, E. S. Cheng, S. Cheung, A. Cillis, D. Content, D. Cottingham, R. Foltz, J. Gygax, R. J. Hill, J. W. Kruk, J. Mah, L. Meier, C. Merchant, L. Miko, E. C. Piquette, A. Waczynski, and Y. Wen, “Properties and characteristics of the Nancy Grace Roman Space Telescope H4RG-10 detectors,” *Journal of Astronomical Telescopes, Instruments, and Systems*, vol. 6, p. 046001, Oct. 2020.
- [81] B. Addison, D. J. Wright, R. A. Wittenmyer, J. Horner, M. W. Mengel, D. Johns, C. Marti, B. Nicholson, J. Soutter, B. Bowler, I. Crossfield, S. R. Kane, J. Kielkopf, P. Plavchan, C. G. Tinney, H. Zhang, J. T. Clark, M. Clerete, J. D. Eastman, J. Swift, M. Bottom, P. Muirhead, N. McCrady, E. Herzig, K. Hogstrom, M. Wilson, D. Sliski, S. A. Johnson, J. T. Wright, J. A. Johnson, C. Blake, R. Riddle, B. Lin, M. Cornachione, T. R. Bedding, D. Stello, D. Huber, S. Marsden, and B. D. Carter, “Minerva-Australis. I. Design, Commissioning, and First Photometric Results,” *PASP*, vol. 131, no. 1005, p. 115003, Nov. 2019.

- [82] S. Seager, N. J. Kasdin, J. Booth, M. Greenhouse, D. Lisman, B. Macintosh, S. Shaklan, M. Vess, S. Warwick, D. Webb, S. D'Amico, J. Debes, S. Domagal-Goldman, S. Hildebrandt, R. Hu, M. Hughes, A. Kiessling, N. Lewis, J. Rhodes, M. Rizzo, A. Roberge, T. Robinson, L. Rogers, D. Savransky, D. Scharf, C. Stark, M. Turnbull, A. Romero-Wolf, J. Ziemer, A. Gray, M. Hughes, G. Agnes, J. Arenberg, S. C. Bradford, M. Fong, J. Gregory, S. Matousek, J. Murphy, J. Rhodes, D. Scharf, and P. Willems, "Starshade Rendezvous Probe Mission," in *Bulletin of the American Astronomical Society*, vol. 51, Sep. 2019, p. 106.
- [83] Gaia Collaboration, A. G. A. Brown, A. Vallenari, T. Prusti, J. H. J. de Bruijne, C. Babusiaux, C. A. L. Bailer-Jones, M. Biernmann, D. W. Evans, L. Eyer, F. Jansen, C. Jordi, S. A. Klioner, U. Lammers, L. Lindegren, X. Luri, F. Mignard, C. Panem, D. Pourbaix, S. Randich, P. Sartoretti, H. I. Siddiqui, C. Soubiran, F. van Leeuwen, N. A. Walton, F. Arenou, U. Bastian, M. Cropper, R. Drimmel, D. Katz, M. G. Lattanzi, J. Bakker, C. Cacciari, J. Castañeda, L. Chaoul, N. Cheek, F. De Angeli, C. Fabricius, R. Guerra, B. Holl, E. Masana, R. Messineo, N. Mowlavi, K. Nienartowicz, P. Panuzzo, J. Portell, M. Riello, G. M. Seabroke, P. Tanga, F. Thévenin, G. Gracia-Abril, G. Comoretto, M. Garcia-Reinaldos, D. Teyssier, M. Altmann, R. Andrae, M. Audard, I. Bellas-Velidis, K. Benson, J. Berthier, R. Blomme, P. Burgess, G. Busso, B. Carry, A. Cellino, G. Clementini, M. Clotet, O. Creevey, M. Davidson, J. De Ridder, L. Delchambre, A. Dell'Oro, C. Ducourant, J. Fernández-Hernández, M. Fouesneau, Y. Frémat, L. Galluccio, M. García-Torres, J. González-Núñez, J. J. González-Vidal, E. Gosset, L. P. Guy, J. L. Halbwachs, N. C. Hambly, D. L. Harrison, J. Hernández, D. Hestroffer, S. T. Hodgkin, A. Hutton, G. Jasniewicz, A. Jean-Antoine-Piccolo, S. Jordan, A. J. Korn, A. Krone-Martins, A. C. Lanzafame, T. Lebzelter, W. Löffler, M. Manteiga, P. M. Marrese, J. M. Martín-Fleitas, A. Moitinho, A. Mora, K. Muinonen, J. Osinde, E. Pancino, T. Pauwels, J. M. Petit, A. Recio-Blanco, P. J. Richards, L. Rimoldini, A. C. Robin, L. M. Sarro, C. Siopis, M. Smith, A. Sozzetti, M. Süveges, J. Torra, W. van Reeven, U. Abbas, A. Abreu Aramburu, S. Accart, C. Aerts, G. Altavilla, M. A. Álvarez, R. Alvarez, J. Alves, R. I. Anderson, A. H. Andrei, E. Anglada Varela, E. Antiche, T. Antoja, B. Arcay, T. L. Astraatmadja, N. Bach, S. G. Baker, L. Balaguer-Núñez, P. Balm, C. Barache, C. Barata, D. Barbato, F. Barblan, P. S. Barklem, D. Barrado, M. Barros, M. A. Barstow, S. Bartholomé Muñoz, J. L. Bassilana, U. Becciani, M. Bellazzini, A. Berihuete, S. Bertone, L. Bianchi, O. Bienaymé, S. Blanco-Cuaresma, T. Boch, C. Boeche, A. Bombrun, R. Borrachero, D. Bossini, S. Bouquillon, G. Bourda, A. Bragaglia, L. Bramante, M. A. Breddels, A. Bressan, N. Brouillet, T. Brüsemeister, E. Brugaletta, B. Bucciarelli, A. Burlacu, D. Busonero, A. G. Butkevich, R. Buzzi, E. Cafau, R. Cancelliere, G. Cannizzaro, T. Cantat-Gaudin, R. Carballo, T. Carlucci, J. M. Carrasco, L. Casamiquela, M. Castellani, A. Castro-Ginard, P. Charlot, L. Chemin, A. Chiavassa, G. Cocozza, G. Costigan, S. Cowell, F. Crifo, M. Crosta, C. Crowley, J. Cuypers, C. Dafonte, Y. Damerdji, A. Dapergolas, P. David, M. David, P. de Laverny, F. De Luise, R. De March, D. de Martino, R. de Souza, A. de Torres, J. Debosscher, E. del Pozo, M. Delbo, A. Delgado, H. E. Delgado, P. Di Matteo, S. Diakite, C. Diener, E. Distefano, C. Dolding, P. Drazinos, J. Durán, B. Edvardsson, H. Enke, K. Eriksson, P. Esquej, G. Eynard Bontemps, C. Fabre, M. Fabrizio, S. Faigler, A. J. Falcão, M. Farràs Casas, L. Federici, G. Fedorets, P. Fernique, F. Figueras, F. Filippi,

K. Findeisen, A. Fonti, E. Fraile, M. Fraser, B. Frézouls, M. Gai, S. Galleti, D. Garabato, F. García-Sedano, A. Garofalo, N. Garralda, A. Gavel, P. Gavras, J. Gerssen, R. Geyer, P. Giacobbe, G. Gilmore, S. Girona, G. Giuffrida, F. Glass, M. Gomes, M. Granvik, A. Gueguen, A. Guerrier, J. Guiraud, R. Gutiérrez-Sánchez, R. Haigron, D. Hatzidimitriou, M. Hauser, M. Haywood, U. Heiter, A. Helmi, J. Heu, T. Hilger, D. Hobbs, W. Hofmann, G. Holland, H. E. Huckle, A. Hypki, V. Icardi, K. Janßen, G. Jevardat de Fombelle, P. G. Jonker, Á. L. Juhász, F. Julbe, A. Karampelas, A. Kewley, J. Klar, A. Kochoska, R. Kohley, K. Kolenberg, M. Kontizas, E. Kontizas, S. E. Koposov, G. Kordopatis, Z. Kostrzewska-Rutkowska, P. Koubsky, S. Lambert, A. F. Lanza, Y. Lasne, J. B. Lavigne, Y. Le Fustec, C. Le Poncin-Lafitte, Y. Lebreton, S. Leccia, N. Leclerc, I. Lecoeur-Taibi, H. Lenhardt, F. Leroux, S. Liao, E. Licata, H. E. P. Lindstrøm, T. A. Lister, E. Livanou, A. Lobel, M. López, S. Managau, R. G. Mann, G. Mantelet, O. Marchal, J. M. Marchant, M. Marconi, S. Marinoni, G. Marschalkó, D. J. Marshall, M. Martino, G. Marton, N. Mary, D. Massari, G. Matijević, T. Mazeh, P. J. McMillan, S. Messina, D. Michalik, N. R. Millar, D. Molina, R. Molinaro, L. Molnár, P. Montegriffo, R. Mor, R. Morbidelli, T. Morel, D. Morris, A. F. Mulone, T. Muraveva, I. Musella, G. Nelemans, L. Nicastro, L. Noval, W. O'Mullane, C. Ordénovic, D. Ordóñez-Blanco, P. Osborne, C. Pagani, I. Pagano, F. Pailler, H. Palacin, L. Palaversa, A. Panahi, M. Pawlak, A. M. Piersimoni, F. X. Pineau, E. Plachy, G. Plum, E. Poggio, E. Poujoulet, A. Prša, L. Pulone, E. Racero, S. Ragaini, N. Rambaux, M. Ramos-Lerate, S. Regibo, C. Reylé, F. Riclet, V. Ripepi, A. Riva, A. Rivard, G. Rixon, T. Roegiers, M. Roelens, M. Romero-Gómez, N. Rowell, F. Royer, L. Ruiz-Dern, G. Sadowski, T. Sagristà Sellés, J. Sahlmann, J. Salgado, E. Salguero, N. Sanna, T. Santana-Ros, M. Sarasso, H. Savietto, M. Schultheis, E. Sciacca, M. Segol, J. C. Segovia, D. Ségransan, I. C. Shih, L. Siltala, A. F. Silva, R. L. Smart, K. W. Smith, E. Solano, F. Solitro, R. Sordo, S. Soria Nieto, J. Souchay, A. Spagna, F. Spoto, U. Stampa, I. A. Steele, H. Steidelmüller, C. A. Stephenson, H. Stoev, F. F. Suess, J. Surdej, L. Szabados, E. Szegedi-Elek, D. Tapiador, F. Taris, G. Tauran, M. B. Taylor, R. Teixeira, D. Terrett, P. Teyssandier, W. Thuillot, A. Titarenko, F. Torra Clotet, C. Turon, A. Ulla, E. Utrilla, S. Uzzi, M. Vailant, G. Valentini, V. Valette, A. van Elteren, E. Van Hemelryck, M. van Leeuwen, M. Vaschetto, A. Vecchiato, J. Veljanoski, Y. Viala, D. Vicente, S. Vogt, C. von Essen, H. Voss, V. Votruba, S. Voutsinas, G. Walmsley, M. Weiler, O. Wertz, T. Wevers, L. Wyrzykowski, A. Yoldas, M. Žerjal, H. Ziaeepour, J. Zorec, S. Zschocke, S. Zucker, C. Zurbach, and T. Zwitter, “Gaia Data Release 2. Summary of the contents and survey properties,” *A&A*, vol. 616, p. A1, Aug. 2018.

- [84] R. Glebocki and P. Gnacinski, “VizieR Online Data Catalog: Catalog of Stellar Rotational Velocities (Glebocki+ 2005),” *VizieR Online Data Catalog*, p. III/244, Mar 2005.
- [85] P. C. Keenan and R. C. McNeil, “The Perkins Catalog of Revised MK Types for the Cooler Stars,” *ApJS*, vol. 71, p. 245, Oct. 1989.
- [86] I. Ramírez, C. Allende Prieto, and D. L. Lambert, “Oxygen Abundances in Nearby FGK Stars and the Galactic Chemical Evolution of the Local Disk and Halo,” *ApJ*, vol. 764, no. 1, p. 78, Feb 2013.

- [87] M. Tsantaki, S. G. Sousa, V. Z. Adibekyan, N. C. Santos, A. Mortier, and G. Israelian, “Deriving precise parameters for cool solar-type stars. Optimizing the iron line list,” *A&A*, vol. 555, p. A150, Jul. 2013.
- [88] F. van Leeuwen, “Validation of the new Hipparcos reduction,” *A&A*, vol. 474, no. 2, pp. 653–664, Nov. 2007.
- [89] R. da Silva, A. d. C. Milone, and H. J. Rocha-Pinto, “Homogeneous abundance analysis of FGK dwarf, subgiant, and giant stars with and without giant planets,” *A&A*, vol. 580, p. A24, Aug. 2015.
- [90] P. Jofré, U. Heiter, C. Soubiran, S. Blanco-Cuaresma, C. C. Worley, E. Pancino, T. Cantat-Gaudin, L. Magrini, M. Bergemann, J. I. González Hernández, V. Hill, C. Lardo, P. de Laverny, K. Lind, T. Masseron, D. Montes, A. Mucciarelli, T. Nordlander, A. Recio Blanco, J. Sobeck, R. Sordo, S. G. Sousa, H. Tabernero, A. Vallenari, and S. Van Eck, “Gaia FGK benchmark stars: Metallicity,” *A&A*, vol. 564, p. A133, Apr. 2014.
- [91] R. O. Gray, C. J. Corbally, R. F. Garrison, M. T. McFadden, E. J. Bubar, C. E. McGahee, A. A. O’Donoghue, and E. R. Knox, “Contributions to the Nearby Stars (NStars) Project: Spectroscopy of Stars Earlier than M0 within 40 pc-The Southern Sample,” *AJ*, vol. 132, no. 1, pp. 161–170, Jul. 2006.
- [92] J. A. Valenti and D. A. Fischer, “Spectroscopic Properties of Cool Stars (SPOCS). I. 1040 F, G, and K Dwarfs from Keck, Lick, and AAT Planet Search Programs,” *ApJS*, vol. 159, pp. 141–166, Jul. 2005.
- [93] N. C. Santos, G. Israelian, and M. Mayor, “Spectroscopic [Fe/H] for 98 extra-solar planet-host stars. Exploring the probability of planet formation,” *A&A*, vol. 415, pp. 1153–1166, Mar. 2004.
- [94] T. V. Mishenina, C. Soubiran, V. V. Kovtyukh, M. M. Katsova, and M. A. Livshits, “Activity and the Li abundances in the FGK dwarfs\*,” *A&A*, vol. 547, p. A106, Nov. 2012.
- [95] G. Gonzalez, M. K. Carlson, and R. W. Tobin, “Parent stars of extrasolar planets - X. Lithium abundances and v sini revisited,” *MNRAS*, vol. 403, no. 3, pp. 1368–1380, Apr. 2010.
- [96] S. G. Sousa, N. C. Santos, M. Mayor, S. Udry, L. Casagrande, G. Israelian, F. Pepe, D. Queloz, and M. J. P. F. G. Monteiro, “Spectroscopic parameters for 451 stars in the HARPS GTO planet search program. Stellar [Fe/H] and the frequency of exo-Neptunes,” *A&A*, vol. 487, no. 1, pp. 373–381, Aug. 2008.
- [97] E. Jofré, R. Petrucci, C. Saffe, L. Saker, E. Artur de la Villarmois, C. Chavero, M. Gómez, and P. J. D. Mauas, “Stellar parameters and chemical abundances of 223 evolved stars with and without planets,” *A&A*, vol. 574, p. A50, Feb. 2015.
- [98] H. M. Tabernero, D. Montes, and J. I. González Hernández, “Chemically tagging the Hyades Supercluster. A homogeneous sample of F6-K4 kinematically selected northern stars,” *A&A*, vol. 547, p. A13, Nov. 2012.

- [99] I. Ramírez, J. Meléndez, J. Bean, M. Asplund, M. Bedell, T. Monroe, L. Casagrande, L. Schirbel, S. Dreizler, J. Teske, M. Tucci Maia, A. Alves-Brito, and P. Baumann, “The Solar Twin Planet Search. I. Fundamental parameters of the stellar sample,” *A&A*, vol. 572, p. A48, Dec. 2014.
- [100] R. O. Gray, C. J. Corbally, R. F. Garrison, M. T. McFadden, and P. E. Robinson, “Contributions to the Nearby Stars (NStars) Project: Spectroscopy of Stars Earlier than M0 within 40 Parsecs: The Northern Sample. I.” *AJ*, vol. 126, no. 4, pp. 2048–2059, Oct. 2003.
- [101] U. Heiter and R. E. Luck, “Abundance Analysis of Planetary Host Stars. I. Differential Iron Abundances,” *AJ*, vol. 126, no. 4, pp. 2015–2036, Oct. 2003.
- [102] Y. Takeda, M. Ohkubo, B. Sato, E. Kambe, and K. Sadakane, “Spectroscopic Study on the Atmospheric Parameters of Nearby F–K Dwarfs and Subgiants,” *PASJ*, vol. 57, pp. 27–43, Feb. 2005.
- [103] M. Ammler-von Eiff and A. Reiners, “New measurements of rotation and differential rotation in A-F stars: are there two populations of differentially rotating stars?” *A&A*, vol. 542, p. A116, Jun. 2012.
- [104] L. da Silva, L. Girardi, L. Pasquini, J. Setiawan, O. von der Lühe, J. R. de Medeiros, A. Hatzes, M. P. Döllinger, and A. Weiss, “Basic physical parameters of a selected sample of evolved stars,” *A&A*, vol. 458, no. 2, pp. 609–623, Nov. 2006.
- [105] K. Fuhrmann, “Nearby stars of the Galactic disc and halo - IV,” *MNRAS*, vol. 384, no. 1, pp. 173–224, Feb. 2008.
- [106] J. D. Kirkpatrick, T. J. Henry, and J. McCarthy, Donald W., “A Standard Stellar Spectral Sequence in the Red/Near-Infrared: Classes K5 to M9,” *ApJS*, vol. 77, p. 417, Nov. 1991.
- [107] A. W. Mann, G. A. Feiden, E. Gaidos, T. Boyajian, and K. von Braun, “How to Constrain Your M Dwarf: Measuring Effective Temperature, Bolometric Luminosity, Mass, and Radius,” *ApJ*, vol. 804, no. 1, p. 64, May 2015.
- [108] S. C. Marsden, P. Petit, S. V. Jeffers, J. Morin, R. Fares, A. Reiners, J. D. do Nascimento, M. Aurière, J. Bouvier, B. D. Carter, C. Catala, B. Dintrans, J. F. Donati, T. Gastine, M. Jardine, R. Konstantinova-Antova, J. Lanoux, F. Lignières, A. Morgenthaler, J. C. Ramírez-Vélez, S. Théado, V. Van Grootel, and BCool Collaboration, “A BCool magnetic snapshot survey of solar-type stars,” *MNRAS*, vol. 444, no. 4, pp. 3517–3536, Nov. 2014.
- [109] W. W. Morgan and P. C. Keenan, “Spectral Classification,” *ARA&A*, vol. 11, p. 29, Jan. 1973.
- [110] I. Ramírez, J. Meléndez, and M. Asplund, “Chemical signatures of planets: beyond solar-twins,” *A&A*, vol. 561, p. A7, Jan. 2014.
- [111] E. E. Mamajek, M. R. Meyer, and J. Liebert, “Post-T Tauri Stars in the Nearest OB Association,” *AJ*, vol. 124, no. 3, pp. 1670–1694, Sep. 2002.

- [112] S. G. Lee, “Spectral classification of high-proper-motion stars.” *AJ*, vol. 89, pp. 702–719, May 1984.
- [113] A. P. Cowley, W. A. Hiltner, and A. N. Witt, “Spectral classification and photometry of high proper motion stars.” *AJ*, vol. 72, pp. 1334–1340, Dec. 1967.
- [114] S. G. Sousa, N. C. Santos, A. Mortier, M. Tsantaki, V. Adibekyan, E. Delgado Mena, G. Israelian, B. Rojas-Ayala, and V. Neves, “Homogeneous spectroscopic parameters for bright planet host stars from the northern hemisphere . The impact on stellar and planetary mass,” *A&A*, vol. 576, p. A94, Apr. 2015.
- [115] T. J. Henry, L. M. Walkowicz, T. C. Barto, and D. A. Golimowski, “The Solar Neighborhood. VI. New Southern Nearby Stars Identified by Optical Spectroscopy,” *AJ*, vol. 123, no. 4, pp. 2002–2009, Apr. 2002.
- [116] I. Ramírez and J. Meléndez, “The Effective Temperature Scale of FGK Stars. I. Determination of Temperatures and Angular Diameters with the Infrared Flux Method,” *ApJ*, vol. 626, no. 1, pp. 446–464, Jun. 2005.
- [117] G. Takeda, E. B. Ford, A. Sills, F. A. Rasio, D. A. Fischer, and J. A. Valenti, “Structure and Evolution of Nearby Stars with Planets. II. Physical Properties of ~1000 Cool Stars from the SPOCS Catalog,” *ApJS*, vol. 168, no. 2, pp. 297–318, Feb. 2007.
- [118] R. O. Gray, M. G. Napier, and L. I. Winkler, “The Physical Basis of Luminosity Classification in the Late A-, F-, and Early G-Type Stars. I. Precise Spectral Types for 372 Stars,” *AJ*, vol. 121, no. 4, pp. 2148–2158, Apr. 2001.
- [119] N. C. Santos, G. Israelian, M. Mayor, J. P. Bento, P. C. Almeida, S. G. Sousa, and A. Ecuvillon, “Spectroscopic metallicities for planet-host stars: Extending the samples,” *A&A*, vol. 437, no. 3, pp. 1127–1133, Jul. 2005.
- [120] C. Allende Prieto, P. S. Barklem, D. L. Lambert, and K. Cunha, “S<sup>4</sup>N: A spectroscopic survey of stars in the solar neighborhood. The Nearest 15 pc,” *A&A*, vol. 420, pp. 183–205, Jun. 2004.
- [121] A. Gáspár, G. H. Rieke, and N. Ballering, “The Correlation between Metallicity and Debris Disk Mass,” *ApJ*, vol. 826, no. 2, p. 171, Aug 2016.
- [122] J. Maldonado, E. Villaver, and C. Eiroa, “The metallicity signature of evolved stars with planets,” *A&A*, vol. 554, p. A84, Jun. 2013.
- [123] J. D. Twicken, J. M. Jenkins, S. E. Seader, P. Tenenbaum, J. C. Smith, L. S. Brownston, C. J. Burke, J. H. Catanzarite, B. D. Clarke, M. T. Cote, F. R. Girouard, T. C. Klaus, J. Li, S. D. McCauliff, R. L. Morris, B. Wohler, J. R. Campbell, A. Kamal Uddin, K. A. Zamudio, A. Sabale, S. T. Bryson, D. A. Caldwell, J. L. Christiansen, J. L. Coughlin, M. R. Haas, C. E. Henze, D. T. Sanderfer, and S. E. Thompson, “Detection of Potential Transit Signals in 17 Quarters of Kepler Data: Results of the Final Kepler Mission Transiting Planet Search (DR25),” *AJ*, vol. 152, no. 6, p. 158, Dec. 2016.

- [124] J. M. Jenkins, D. A. Caldwell, and W. J. Borucki, “Some Tests to Establish Confidence in Planets Discovered by Transit Photometry,” *ApJ*, vol. 564, no. 1, pp. 495–507, Jan. 2002.
- [125] L. A. Rogers and S. Seager, “A Framework for Quantifying the Degeneracies of Exo-planet Interior Compositions,” *ApJ*, vol. 712, no. 2, pp. 974–991, Apr. 2010.
- [126] N. E. Batalha, T. Lewis, J. J. Fortney, N. M. Batalha, E. Kempton, N. K. Lewis, and M. R. Line, “The Precision of Mass Measurements Required for Robust Atmospheric Characterization of Transiting Exoplanets,” *ApJL*, vol. 885, no. 1, p. L25, Nov. 2019.
- [127] D.-R. Harbeck, C. McCully, A. Pickles, N. Volgenau, P. Conway, and B. Taylor, “Long-term monitoring of the throughput in Las Cumbres Observatory’s fleet of telescopes,” in *Observatory Operations: Strategies, Processes, and Systems VII*, ser. Society of Photo-Optical Instrumentation Engineers (SPIE) Conference Series, vol. 10704, Jul. 2018, p. 1070401.
- [128] Z.-H. Cao, L.-Y. Liu, Y.-H. Zhao, L. Feng, H. R. A. Jones, H. Shen, J.-X. Hao, Y.-J. Xue, Y.-Q. Yao, J. Xu, A. Esamdin, Z.-X. Qi, J.-R. Shi, J. Li, Y. Tian, Z. Wang, T.-S. Yan, X. Wang, J.-P. Xiong, S.-C. Yu, J.-B. Zhang, Z.-X. Shen, Y.-Y. Jiang, J. Yin, G.-X. Pu, P. Wei, C.-H. Bai, G.-J. Feng, L. Ma, T.-F. Song, J.-F. Wang, J.-F. Tian, X.-Q. Zeng, Z.-G. Hou, S.-L. Liao, Z.-S. Cao, D.-W. Fan, Y.-F. Xu, C.-H. Li, and Y.-H. Tao, “Long-term analysis of clear nights using satellite data considering astronomical sites in western China,” *Research in Astronomy and Astrophysics*, vol. 20, no. 6, p. 081, Jun. 2020.
- [129] A. Roy, S. Halverson, S. Mahadevan, G. Stefansson, A. Monson, S. E. Logsdon, C. F. Bender, C. H. Blake, E. Golub, A. Gupta, K. P. Jaehnig, S. Kanodia, K. Kaplan, M. W. McElwain, J. P. Ninan, J. Rajagopal, P. Robertson, C. Schwab, R. C. Terrien, S. X. Wang, M. J. Wolf, and J. T. Wright, “Solar Contamination in Extreme-precision Radial-velocity Measurements: Deleterious Effects and Prospects for Mitigation,” *AJ*, vol. 159, no. 4, p. 161, Apr. 2020.
- [130] M. Bottom, P. S. Muirhead, J. A. Johnson, and C. H. Blake, “Optimizing Doppler Surveys for Planet Yield,” *PASP*, vol. 125, p. 240, Mar. 2013.
- [131] A. Garcia-Piquer, J. C. Morales, I. Ribas, J. Colomé, J. Guàrdia, M. Perger, J. A. Caballero, M. Cortés-Contreras, S. V. Jeffers, A. Reiners, P. J. Amado, A. Quirrenbach, and W. Seifert, “Efficient scheduling of astronomical observations. Application to the CARMENES radial-velocity survey,” *A&A*, vol. 604, p. A87, Aug. 2017.
- [132] L. B. Handley, E. A. Petigura, V. V. Mišić, J. Lubin, and H. Isaacson, “Automated Scheduling of Doppler Exoplanet Observations at Keck Observatory,” *AJ*, vol. 167, no. 3, p. 122, Mar. 2024.
- [133] S. Halverson, R. Terrien, S. Mahadevan, A. Roy, C. Bender, G. K. Stefánsson, A. Monson, E. Levi, F. Hearty, C. Blake, M. McElwain, C. Schwab, L. Ramsey, J. Wright, S. Wang, Q. Gong, and P. Roberston, “A comprehensive radial velocity error budget for next generation Doppler spectrometers,” in *Ground-based and Airborne Instrumentation for Astronomy VI*, ser. Society of Photo-Optical Instrumentation Engineers

- (SPIE) Conference Series, C. J. Evans, L. Simard, and H. Takami, Eds., vol. 9908, Aug. 2016, p. 99086P.
- [134] C. Jurgenson, D. Fischer, T. McCracken, D. Sawyer, A. Szymkowiak, A. Davis, G. Muller, and F. Santoro, “EXPRES: a next generation RV spectrograph in the search for earth-like worlds,” in *Ground-based and Airborne Instrumentation for Astronomy VI*, ser. Society of Photo-Optical Instrumentation Engineers (SPIE) Conference Series, C. J. Evans, L. Simard, and H. Takami, Eds., vol. 9908, Aug. 2016, p. 99086T.
  - [135] F. Pepe, S. Cristiani, R. Rebolo, N. C. Santos, H. Dekker, A. Cabral, P. Di Marcantonio, P. Figueira, G. Lo Curto, C. Lovis, M. Mayor, D. Mégevand, P. Molero, M. Riva, M. R. Zapatero Osorio, M. Amate, A. Manescau, L. Pasquini, F. M. Zerbi, V. Adibekyan, M. Abreu, M. Affolter, Y. Alibert, M. Aliverti, R. Allart, C. Allende Prieto, D. Álvarez, D. Alves, G. Avila, V. Baldini, T. Bandy, S. C. C. Barros, W. Benz, A. Bianco, F. Borsa, V. Bourrier, F. Bouchy, C. Broeg, G. Calderone, R. Cirami, J. Coelho, P. Conconi, I. Coretti, C. Cumani, G. Cupani, V. D’Odorico, M. Damasso, S. Deiries, B. Delabre, O. D. S. Demangeon, X. Dumusque, D. Ehrenreich, J. P. Faria, A. Fragoso, L. Genolet, M. Genoni, R. Génova Santos, J. I. González Hernández, I. Hughes, O. Iwert, F. Kerber, J. Knudstrup, M. Landoni, B. Lavie, J. Lillo-Box, J. L. Lizon, C. Maire, C. J. A. P. Martins, A. Mehner, G. Micela, A. Modigliani, M. A. Monteiro, M. J. P. F. G. Monteiro, M. Moschetti, M. T. Murphy, N. Nunes, L. Oggioni, A. Oliveira, M. Oshagh, E. Pallé, G. Pariani, E. Poretti, J. L. Rasilla, J. Rebordão, E. M. Redaelli, S. Santana Tschudi, P. Santin, P. Santos, D. Ségransan, T. M. Schmidt, A. Segovia, D. Sosnowska, A. Sozzetti, S. G. Sousa, P. Spanò, A. Suárez Mascareño, H. Tabernero, F. Tenegi, S. Udry, and A. Zanutta, “ESPRESSO at VLT. On-sky performance and first results,” *A&A*, vol. 645, p. A96, Jan. 2021.
  - [136] A. Seifahrt, J. Stürmer, J. L. Bean, and C. Schwab, “MAROON-X: a radial velocity spectrograph for the Gemini Observatory,” in *Ground-based and Airborne Instrumentation for Astronomy VII*, ser. Society of Photo-Optical Instrumentation Engineers (SPIE) Conference Series, C. J. Evans, L. Simard, and H. Takami, Eds., vol. 10702, Jul. 2018, p. 107026D.
  - [137] G. J. Bergsten, I. Pascucci, G. D. Mulders, R. B. Fernandes, and T. T. Koskinen, “The Demographics of Kepler’s Earths and Super-Earths into the Habitable Zone,” *AJ*, vol. 164, no. 5, p. 190, Nov. 2022.
  - [138] S. Bryson, M. Kunimoto, R. K. Kopparapu, J. L. Coughlin, W. J. Borucki, D. Koch, V. S. Aguirre, C. Allen, G. Barentsen, N. M. Batalha, T. Berger, A. Boss, L. A. Buchhave, C. J. Burke, D. A. Caldwell, J. R. Campbell, J. Catanzarite, H. Chandrasekaran, W. J. Chaplin, J. L. Christiansen, J. Christensen-Dalsgaard, D. R. Ciardi, B. D. Clarke, W. D. Cochran, J. L. Dotson, L. R. Doyle, E. S. Duarte, E. W. Dunham, A. K. Dupree, M. Endl, J. L. Fanson, E. B. Ford, M. Fujieh, I. Gautier, Thomas N., J. C. Geary, R. L. Gilliland, F. R. Girouard, A. Gould, M. R. Haas, C. E. Henze, M. J. Holman, A. W. Howard, S. B. Howell, D. Huber, R. C. Hunter, J. M. Jenkins, H. Kjeldsen, J. Kolodziejczak, K. Larson, D. W. Latham, J. Li, S. Mathur,

- S. Meibom, C. Middour, R. L. Morris, T. D. Morton, F. Mullally, S. E. Mullally, D. Pletcher, A. Prsa, S. N. Quinn, E. V. Quintana, D. Ragozzine, S. V. Ramirez, D. T. Sanderfer, D. Sasselov, S. E. Seader, M. Shabram, A. Shporer, J. C. Smith, J. H. Steffen, M. Still, G. Torres, J. Troeltzsch, J. D. Twicken, A. K. Uddin, J. E. Van Cleve, J. Voss, L. M. Weiss, W. F. Welsh, B. Wohler, and K. A. Zamudio, “The Occurrence of Rocky Habitable-zone Planets around Solar-like Stars from Kepler Data,” *AJ*, vol. 161, no. 1, p. 36, Jan. 2021.
- [139] M. Kunimoto and J. M. Matthews, “Searching the Entirety of Kepler Data. II. Occurrence Rate Estimates for FGK Stars,” *AJ*, vol. 159, no. 6, p. 248, Jun. 2020.
- [140] S. Bryson, J. Coughlin, N. M. Batalha, T. Berger, D. Huber, C. Burke, J. Dotson, and S. E. Mullally, “A Probabilistic Approach to Kepler Completeness and Reliability for Exoplanet Occurrence Rates,” *AJ*, vol. 159, no. 6, p. 279, Jun. 2020.
- [141] S. D. Dulz, P. Plavchan, J. R. Crepp, C. Stark, R. Morgan, S. R. Kane, P. Newman, W. Matzko, and G. D. Mulders, “Joint Radial Velocity and Direct Imaging Planet Yield Calculations. I. Self-consistent Planet Populations,” *ApJ*, vol. 893, no. 2, p. 122, Apr. 2020.
- [142] I. Pascucci, G. D. Mulders, and E. Lopez, “The Impact of Stripped Cores on the Frequency of Earth-size Planets in the Habitable Zone,” *ApJL*, vol. 883, no. 1, p. L15, Sep. 2019.
- [143] D. C. Hsu, E. B. Ford, D. Ragozzine, and K. Ashby, “Occurrence Rates of Planets Orbiting FGK Stars: Combining Kepler DR25, Gaia DR2, and Bayesian Inference,” *AJ*, vol. 158, no. 3, p. 109, Sep. 2019.
- [144] J. K. Zink and B. M. S. Hansen, “Accounting for multiplicity in calculating eta Earth,” *MNRAS*, vol. 487, no. 1, pp. 246–252, Jul. 2019.
- [145] D. Garrett, D. Savransky, and R. Belikov, “Planet Occurrence Rate Density Models Including Stellar Effective Temperature,” *PASP*, vol. 130, no. 993, p. 114403, Nov. 2018.
- [146] R. K. Kopparapu, E. Hébrard, R. Belikov, N. M. Batalha, G. D. Mulders, C. Stark, D. Teal, S. Domagal-Goldman, and A. Mandell, “Exoplanet Classification and Yield Estimates for Direct Imaging Missions,” *ApJ*, vol. 856, no. 2, p. 122, Apr. 2018.
- [147] G. D. Mulders, I. Pascucci, D. Apai, and F. J. Ciesla, “The Exoplanet Population Observation Simulator. I. The Inner Edges of Planetary Systems,” *AJ*, vol. 156, no. 1, p. 24, Jul. 2018.
- [148] C. J. Burke, J. L. Christiansen, F. Mullally, S. Seader, D. Huber, J. F. Rowe, J. L. Coughlin, S. E. Thompson, J. Catanzarite, B. D. Clarke, T. D. Morton, D. A. Caldwell, S. T. Bryson, M. R. Haas, N. M. Batalha, J. M. Jenkins, P. Tenenbaum, J. D. Twicken, J. Li, E. Quintana, T. Barclay, C. E. Henze, W. J. Borucki, S. B. Howell, and M. Still, “Terrestrial Planet Occurrence Rates for the Kepler GK Dwarf Sample,” *ApJ*, vol. 809, no. 1, p. 8, Aug. 2015.

- [149] D. Foreman-Mackey, D. W. Hogg, and T. D. Morton, “Exoplanet Population Inference and the Abundance of Earth Analogs from Noisy, Incomplete Catalogs,” *ApJ*, vol. 795, no. 1, p. 64, Nov. 2014.
- [150] E. A. Petigura, A. W. Howard, and G. W. Marcy, “Prevalence of Earth-size planets orbiting Sun-like stars,” *Proceedings of the National Academy of Science*, vol. 110, no. 48, pp. 19 273–19 278, Nov. 2013.
- [151] S. Dong and Z. Zhu, “Fast Rise of “Neptune-size” Planets ( $4\text{-}8 R_{\oplus}$ ) from  $P \sim 10$  to  $\sim 250$  Days—Statistics of Kepler Planet Candidates up to  $\sim 0.75$  AU,” *ApJ*, vol. 778, no. 1, p. 53, Nov. 2013.
- [152] A. N. Youdin, “The Exoplanet Census: A General Method Applied to Kepler,” *ApJ*, vol. 742, no. 1, p. 38, Nov. 2011.
- [153] X. Bonfils, X. Delfosse, S. Udry, T. Forveille, M. Mayor, C. Perrier, F. Bouchy, M. Gillon, C. Lovis, F. Pepe, D. Queloz, N. C. Santos, D. Ségransan, and J. L. Bertaux, “The HARPS search for southern extra-solar planets. XXXI. The M-dwarf sample,” *A&A*, vol. 549, p. A109, Jan. 2013.
- [154] R. K. Kopparapu, “A Revised Estimate of the Occurrence Rate of Terrestrial Planets in the Habitable Zones around Kepler M-dwarfs,” *ApJL*, vol. 767, no. 1, p. L8, Apr. 2013.
- [155] C. D. Dressing and D. Charbonneau, “The Occurrence of Potentially Habitable Planets Orbiting M Dwarfs Estimated from the Full Kepler Dataset and an Empirical Measurement of the Detection Sensitivity,” *ApJ*, vol. 807, no. 1, p. 45, Jul. 2015.
- [156] G. J. Bergsten, I. Pascucci, K. K. Hardegree-Ullman, R. B. Fernandes, J. L. Christiansen, and G. D. Mulders, “No Evidence for More Earth-sized Planets in the Habitable Zone of Kepler’s M versus FGK Stars,” *AJ*, vol. 166, no. 6, p. 234, Dec. 2023.
- [157] A. Kaminski, S. Sabotta, J. Kemmer, P. Chaturvedi, R. Burn, J. C. Morales, J. A. Caballero, I. Ribas, A. Reiners, A. Quirrenbach, P. J. Amado, V. J. S. Béjar, S. Dreizler, E. W. Guenther, A. P. Hatzes, T. Henning, M. Kürster, D. Montes, E. Nagel, E. Pallé, V. Pinter, S. Reffert, M. Schlecker, Y. Shan, T. Trifonov, M. R. Z. Osorio, and M. Zechmeister, “The CARMENES search for exoplanets around M dwarfs: Occurrence rates of Earth-like planets around very low-mass stars,” *A&A*, vol. 696, p. A101, Apr. 2025.
- [158] S. Bryson, M. Kunimoto, R. Belikov, G. J. Bergsten, S. Bhure, W. J. Borucki, D. A. Caldwell, A. Chakrabarty, R. B. Fernandes, M. Y. He, J. M. Jenkins, K. Ment, M. R. Meyer, G. D. Mulders, I. Pascucci, and P. Plavchan, “Why Estimating  $\eta_{\oplus}$  is Difficult: A Kepler-Centric Perspective,” *arXiv e-prints*, p. arXiv:2511.05658, Nov. 2025.
- [159] R. B. Fernandes, S. Johnson, G. J. Bergsten, S. Bhure, K. M. Boley, A. P. Boss, S. Bryson, W. DeRocco, J. Dietrich, A. Duck, S. Giacalone, A. F. Gupta, M. Y. He, M. Kunimoto, K. Ment, S. Sagear, M. L. Silverstein, K. Sullivan, E. Halley Vrijmoet, K. Wagner, R. F. Wilson, L. Brefka, R. Belikov, A. Chakrabarty, J. L. Christiansen, D. R. Ciardi, A. Dattilo, E. Fitzmaurice, E. B. Ford, A. Hotnisky,

- S. Jones, A. Kar, R. Kopparapu, N. Lawson, E. E. Mamajek, B. Mennesson, M. R. Meyer, S. Millholland, G. D. Mulders, S. E. Mullally, A. Murlidhar, I. Pascucci, D. Ragozzine, P. Robertson, K. Stapelfeldt, and J. Wright, “Are We There Yet? Challenges in Quantifying the Frequency of Earth Analogs in the Habitable Zone,” *arXiv e-prints*, p. arXiv:2511.05660, Nov. 2025.
- [160] A. Silburt, E. Gaidos, and Y. Wu, “A Statistical Reconstruction of the Planet Population around Kepler Solar-type Stars,” *ApJ*, vol. 799, no. 2, p. 180, Feb. 2015.
- [161] B. S. Gaudi, S. Seager, B. Mennesson, A. Kiessling, K. Warfield, G. Kuan, K. Cahoy, J. T. Clarke, S. Domagal-Goldman, L. Feinberg, O. Guyon, J. Kasdin, D. Mawet, T. Robinson, L. Rogers, P. Scowen, R. Somerville, K. Stapelfeldt, C. Stark, D. Stern, M. Turnbull, S. Martin, O. Alvarez-Salazar, R. Amini, W. Arnold, B. Balasubramanian, M. Baysinger, L. Blais, T. Brooks, R. Calvet, V. Cormarkovic, C. Cox, R. Danner, J. Davis, L. Dorsett, M. Effinger, R. Eng, J. Garcia, J. Gaskin, J. Harris, S. Howe, B. Knight, J. Krist, D. Levine, M. Li, D. Lisman, M. Mandic, L. Marchen, C. Marrese-Reading, J. McGowen, A. Miyaguchi, R. Morgan, B. Nemati, S. Nikzad, J. Nissen, M. Novicki, T. Perrine, D. Redding, M. Richards, M. Rud, D. Scharf, G. Serabyn, S. Shaklan, S. Smith, M. Stahl, P. Stahl, H. Tang, D. Van Buren, J. Villalvazo, S. Warwick, D. Webb, R. Wofford, J. Woo, M. Wood, J. Ziemer, E. Douglas, V. Faramaz, S. Hildebrandt, T. Meshkat, P. Plavchan, G. Ruane, and N. Turner, “The Habitable Exoplanet Observatory (HabEx) Mission Concept Study Interim Report,” *arXiv e-prints*, Sep. 2018.
- [162] L. A. Rogers and S. Seager, “A Framework for Quantifying the Degeneracies of Exoplanet Interior Compositions,” *ApJ*, vol. 712, no. 2, pp. 974–991, Apr. 2010.
- [163] L. A. Rogers, “Most 1.6 Earth-radius Planets are Not Rocky,” *ApJ*, vol. 801, no. 1, p. 41, Mar. 2015.
- [164] J. de Wit and S. Seager, “Constraining Exoplanet Mass from Transmission Spectroscopy,” *Science*, vol. 342, no. 6165, pp. 1473–1477, Dec. 2013.
- [165] Q. Changeat, L. Keyte, I. P. Waldmann, and G. Tinetti, “Impact of Planetary Mass Uncertainties on Exoplanet Atmospheric Retrievals,” *ApJ*, vol. 896, no. 2, p. 107, Jun. 2020.
- [166] N. E. Batalha, E. M. R. Kempton, and R. Mbarek, “Challenges to Constraining Exoplanet Masses via Transmission Spectroscopy,” *ApJL*, vol. 836, no. 1, p. L5, Feb. 2017.
- [167] N. E. Batalha, T. Lewis, J. J. Fortney, N. M. Batalha, E. Kempton, N. K. Lewis, and M. R. Line, “The Precision of Mass Measurements Required for Robust Atmospheric Characterization of Transiting Exoplanets,” *ApJL*, vol. 885, no. 1, p. L25, Nov. 2019.
- [168] A. Salvador, T. D. Robinson, J. J. Fortney, and M. S. Marley, “Influence of Orbit and Mass Constraints on Reflected Light Characterization of Directly Imaged Rocky Exoplanets,” *ApJL*, vol. 969, no. 1, p. L22, Jul. 2024.

- [169] E. Mamajek and K. Stapelfeldt, “NASA ExEP Mission Star List of Plausible Targets for a Future IROUV Direct Imaging Space Observatory,” in *American Astronomical Society Meeting Abstracts*, ser. American Astronomical Society Meeting Abstracts, vol. 55, Jan. 2023, p. 116.07.
- [170] ——, “NASA Exoplanet Exploration Program (ExEP) Mission Star List for the Habitable Worlds Observatory (2023),” *arXiv e-prints*, p. arXiv:2402.12414, Feb. 2024.
- [171] R. Martínez-Arnáiz, J. Maldonado, D. Montes, C. Eiroa, and B. Montesinos, “Chromospheric activity and rotation of FGK stars in the solar vicinity. An estimation of the radial velocity jitter,” *A&A*, vol. 520, p. A79, Sep. 2010.
- [172] M. Ammler-von Eiff and A. Reiners, “New measurements of rotation and differential rotation in A-F stars: are there two populations of differentially rotating stars?” *A&A*, vol. 542, p. A116, Jun. 2012.
- [173] J. M. Brewer, D. A. Fischer, J. A. Valenti, and N. Piskunov, “Spectral Properties of Cool Stars: Extended Abundance Analysis of 1,617 Planet-search Stars,” *The Astrophysical Journal Supplement Series*, vol. 225, p. 32, Aug. 2016.
- [174] R. E. Luck, “Abundances in the Local Region II: F, G, and K Dwarfs and Subgiants,” *AJ*, vol. 153, no. 1, p. 21, Jan. 2017.
- [175] S. Hojjatpanah, P. Figueira, N. C. Santos, V. Adibekyan, S. G. Sousa, E. Delgado-Mena, Y. Alibert, S. Cristiani, J. I. González Hernández, A. F. Lanza, P. Di Marantonio, J. H. C. Martins, G. Micela, P. Molaro, V. Neves, M. Oshagh, F. Pepe, E. Poretti, B. Rojas-Ayala, R. Rebolo, A. Suárez Mascareño, and M. R. Zapatero Osorio, “Catalog for the ESPRESSO blind radial velocity exoplanet survey,” *A&A*, vol. 629, p. A80, Sep. 2019.
- [176] P. D. Newman, P. Plavchan, J. A. Burt, J. Teske, E. E. Mamajek, S. Leifer, B. S. Gaudi, G. Blackwood, and R. Morgan, “Simulations for Planning Next-generation Exoplanet Radial Velocity Surveys,” *AJ*, vol. 165, no. 4, p. 151, Apr. 2023.
- [177] L. E. Pasinetti Fracassini, L. Pastori, S. Covino, and A. Pozzi, “Catalogue of Apparent Diameters and Absolute Radii of Stars (CADARS) - Third edition - Comments and statistics,” *A&A*, vol. 367, pp. 521–524, Feb 2001.
- [178] E. A. Rich, J. P. Wisniewski, M. W. McElwain, J. Hashimoto, T. Kudo, N. Kusakabe, Y. K. Okamoto, L. Abe, E. Akiyama, W. Brandner, T. D. Brandt, P. Cargile, J. C. Carson, T. M. Currie, S. Egner, M. Feldt, M. Fukagawa, M. Goto, C. A. Grady, O. Guyon, Y. Hayano, M. Hayashi, S. S. Hayashi, L. Hebb, K. G. Hehminiak, T. Henning, K. W. Hodapp, M. Ishii, M. Iye, M. Janson, R. Kandori, G. R. Knapp, M. Kuzuhara, J. Kwon, T. Matsuo, S. Mayama, S. Miyama, M. Momose, J.-I. Morino, A. Moro-Martin, T. Nakagawa, T. Nishimura, D. Oh, T.-S. Pyo, J. Schlieder, E. Serabyn, M. L. Sitko, T. Suenaga, H. Suto, R. Suzuki, Y. H. Takahashi, M. Takami, N. Takato, H. Terada, C. Thalmann, D. Tomono, E. L. Turner, M. Watanabe, T. Yamada, H. Takami, T. Usuda, and M. Tamura, “The fundamental stellar parameters of FGK stars in the SEEDS survey Norman, OK 73071, USA,” *MNRAS*, vol. 472, no. 2, pp. 1736–1752, Dec. 2017.

- [179] A. Kunder, G. Kordopatis, M. Steinmetz, T. Zwitter, P. J. McMillan, L. Casagrande, H. Enke, J. Wojno, M. Valentini, C. Chiappini, G. Matijević, A. r. Siviero, P. de Laverny, A. Recio-Blanco, A. Bijaoui, R. F. G. Wyse, J. Binney, E. K. Grebel, A. Helmi, P. Jofre, T. Antoja, G. Gilmore, A. Siebert, B. Famaey, O. Bienaymé, B. K. Gibson, K. C. Freeman, J. F. Navarro, U. Munari, G. Seabroke, B. Anguiano, M. Žerjal, I. Minchev, W. Reid, J. Bland-Hawthorn, J. Kos, S. Sharma, F. Watson, Q. A. Parker, R.-D. Scholz, D. Burton, P. Cass, M. Hartley, K. Fiegert, M. Stupar, A. Ritter, K. Hawkins, O. Gerhard, W. J. Chaplin, G. R. Davies, Y. P. Elsworth, M. N. Lund, A. Miglio, and B. Mosser, “The Radial Velocity Experiment (RAVE): Fifth Data Release,” *AJ*, vol. 153, no. 2, p. 75, Feb 2017.
- [180] C. Soubiran, J.-F. Le Campion, N. Brouillet, and L. Chemin, “The PASTEL catalogue: 2016 version,” *A&A*, vol. 591, p. A118, Jun 2016.
- [181] E. R. Newton, J. Irwin, D. Charbonneau, Z. K. Berta-Thompson, J. A. Dittmann, and A. A. West, “The Rotation and Galactic Kinematics of Mid M Dwarfs in the Solar Neighborhood,” *ApJ*, vol. 821, no. 2, p. 93, Apr 2016.
- [182] P. Prugniel, I. Vauglin, and M. Koleva, “The atmospheric parameters and spectral interpolator for the MILES stars,” *A&A*, vol. 531, p. A165, Jul 2011.
- [183] P. Prugniel, C. Soubiran, M. Koleva, and D. Le Borgne, “New release of the ELODIE library: Version 3.1,” *arXiv e-prints*, pp. astro-ph/0703658, Mar 2007.
- [184] L. Kaltenegger and W. A. Traub, “Transits of Earth-like Planets,” *ApJ*, vol. 698, no. 1, pp. 519–527, Jun. 2009.
- [185] E. R. Newton, D. Charbonneau, J. Irwin, and A. W. Mann, “An Empirical Calibration to Estimate Cool Dwarf Fundamental Parameters from H-band Spectra,” *ApJ*, vol. 800, no. 2, p. 85, Feb 2015.
- [186] E. R. Houdebine, “Observation and modelling of main-sequence star chromospheres - XIV. Rotation of dM1 stars,” *MNRAS*, vol. 407, no. 3, pp. 1657–1673, Sep 2010.
- [187] A. S. Rajpurohit, C. Reylé, F. Allard, D. Homeier, M. Schultheis, M. S. Bessell, and A. C. Robin, “The effective temperature scale of M dwarfs,” *A&A*, vol. 556, p. A15, Aug 2013.
- [188] B. O. Demory, D. Ségransan, T. Forveille, D. Queloz, J. L. Beuzit, X. Delfosse, E. di Folco, P. Kervella, J. B. Le Bouquin, C. Perrier, M. Benisty, G. Duvert, K. H. Hofmann, B. Lopez, and R. Petrov, “Mass-radius relation of low and very low-mass stars revisited with the VLTI,” *A&A*, vol. 505, no. 1, pp. 205–215, Oct 2009.
- [189] T. S. Boyajian, H. A. McAlister, G. van Belle, D. R. Gies, T. A. ten Brummelaar, K. von Braun, C. Farrington, P. J. Goldfinger, D. O’Brien, J. R. Parks, N. D. Richardson, S. Ridgway, G. Schaefer, L. Sturmann, J. Sturmann, Y. Touhami, N. H. Turner, and R. White, “Stellar Diameters and Temperatures. I. Main-sequence A, F, and G Stars,” *ApJ*, vol. 746, no. 1, p. 101, Feb 2012.

- [190] B. Edvardsson, J. Andersen, B. Gustafsson, D. L. Lambert, P. E. Nissen, and J. Tomkin, “The Chemical Evolution of the Galactic Disk - Part One - Analysis and Results,” *A&A*, vol. 275, p. 101, Aug. 1993.
- [191] M. Kiraga and K. Stepien, “Age-Rotation-Activity Relations for M Dwarf Stars,” *AcA*, vol. 57, pp. 149–172, Jun 2007.
- [192] S. J. Adelman, “The physical properties of normal A stars,” in *The A-Star Puzzle*, J. Zverko, J. Ziznovsky, S. J. Adelman, and W. W. Weiss, Eds., vol. 224, Dec. 2004, pp. 1–11.
- [193] M. Koleva and A. Vazdekis, “Stellar population models in the UV. I. Characterisation of the New Generation Stellar Library,” *A&A*, vol. 538, p. A143, Feb 2012.
- [194] R. W. Schmude, Jr., “Atmospheric Extinction Coefficients Measured at Texas A&M University Observatory,” *International Amateur-Professional Photoelectric Photometry Communications*, vol. 57, p. 12, Sep. 1994.
- [195] S. X. Wang, N. Latouf, P. Plavchan, B. Cale, C. Blake, É. Artigau, C. M. Lisse, J. Gagné, J. Crass, and A. Tanner, “Characterizing and Mitigating the Impact of Telluric Absorption in Precise Radial Velocities,” *AJ*, vol. 164, no. 5, p. 211, Nov. 2022.
- [196] H. M. J. Boffin, J. Vinther, G. Bazin, D. Huerta, Y. Jung, L. K. Lundin, and M. Stellert, “ESO’s new generation of Exposure Time Calculators,” *arXiv e-prints*, p. arXiv:2407.02972, Jul. 2024.
- [197] L. B. Handley, E. A. Petigura, and V. V. Mišić, “Solving the Traveling Telescope Problem with Mixed-integer Linear Programming,” *AJ*, vol. 167, no. 1, p. 33, Jan. 2024.
- [198] R. A. Rubenzahl, S. Halverson, J. Walawender, G. M. Hill, A. W. Howard, M. Brown, E. Ida, J. Tehero, B. J. Fulton, S. R. Gibson, M. Kassis, B. Smith, T. Wold, and J. Payne, “Staring at the Sun with the Keck Planet Finder: An Autonomous Solar Calibrator for High Signal-to-noise Sun-as-a-star Spectra,” *PASP*, vol. 135, no. 1054, p. 125002, Dec. 2023.
- [199] J. Llama, L. L. Zhao, J. M. Brewer, A. Szymkowiak, D. A. Fischer, M. Collins, J. Tiegs, and F. Cornelius, “The Lowell Observatory Solar Telescope: A fiber feed into the EXtreme PREcision Spectrometer,” *arXiv e-prints*, p. arXiv:2407.07967, Jul. 2024.
- [200] E. B. Ford, C. F. Bender, C. H. Blake, A. F. Gupta, S. Kanodia, A. S. J. Lin, S. E. Logsdon, J. K. Luhn, S. Mahadevan, I. Palumbo, Michael L., R. C. Terrien, J. T. Wright, J. Zhao, S. Halverson, E. Hunting, P. Robertson, A. Roy, and G. Stefansson, “Earths within Reach: Evaluation of Strategies for Mitigating Solar Variability using 3.5 years of NEID Sun-as-a-Star Observations,” *arXiv e-prints*, p. arXiv:2408.13318, Aug. 2024.

- [201] B. Klein, S. Aigrain, M. Cretignier, K. Al Moulla, X. Dumusque, O. Barragán, H. Yu, A. Mortier, F. Rescigno, A. C. Cameron, M. López-Morales, N. Meunier, A. Sozzetti, and N. K. O’Sullivan, “Investigating stellar activity through eight years of Sun-as-a-star observations,” *MNRAS*, vol. 531, no. 4, pp. 4238–4262, Jul. 2024.
- [202] J. Albert and Orcasat, “ORCASat: Status Since Deployment out of the International Space Station into LEO on Dec. 29, 2022,” in *American Astronomical Society Meeting Abstracts*, ser. American Astronomical Society Meeting Abstracts, vol. 242, Jun. 2023, p. 317.02.
- [203] J. O’Meara, P. Wizinowich, E. Peretz, J. Chin, G. Fillion, J. Fowler, L. Gers, S. Kwok, S. Lilley, E. Marin, J. Mather, M. Miller-Blanchaer, B. Pasquale, S. Ragland, K. Tsubota, and E. Wetherell, “Enabling high resolution visible adaptive optics with ORCAS at the W.M. Keck Observatory,” in *American Astronomical Society Meeting Abstracts*, ser. American Astronomical Society Meeting Abstracts, vol. 242, Jun. 2023, p. 116.01.

## **Biography**

Patrick Newman received their Bachelor's in Physics from University of Missouri Kansas City in 2015. While at George Mason University, they have acted in roles of Graduate Teaching Assistant, Graduate Research Assistant, and Observatory Operator. As an observatory operator, they have assisted in education, outreach, and exoplanet transit follow-up for both the Kepler K2 and TESS missions. Their primary research was in simulations, including surveys for the NN-EXPLORE EPRV Initiative, Earthfinder, and ORCASat. They will receive their Ph.D. in December 2025.